# SHORT-CIRCUIT CURRENTS IN WIND-TURBINE GENERATOR NETWORKS

A Dissertation
Presented to
The Academic Faculty

by

Dustin F. Howard

In Partial Fulfillment
of the Requirements for the Degree
Doctor of Philosophy in the
School of Electrical and Computer Engineering

Georgia Institute of Technology
December 2013

# SHORT-CIRCUIT CURRENTS IN WIND-TURBINE GENERATOR NETWORKS

Approved by:

Dr. Ronald G. Harley, Advisor
School of Electrical and Computer Engineering
*Georgia Institute of Technology*

Dr. Chuanyi Ji
School of Electrical and Computer Engineering
*Georgia Institute of Technology*

Dr. Miroslav Begovic
School of Electrical and Computer Engineering
*Georgia Institute of Technology*

Dr. Shui-Nee Chow
School of Mathematics
*Georgia Institute of Technology*

Dr. Thomas G. Habetler
School of Electrical and Computer Engineering
*Georgia Institute of Technology*

Date Approved: November 12, 2013

*To my wife*

# ACKNOWLEDGEMENTS

I would like to thank my advisor, Professor Ron Harley, for his guidance throughout the process of my research. It has been an honor to work under him the last few years. I have learned from him that acute attention to detail and a thorough work ethic leads one to truly understand the subject of interest. I would also like to thank Professor Tom Habetler, who has given me much valuable feedback on this work. I would also like to thank Professor Miroslav Begovic, Professor Chuanyi Ji, and Professor Shui-Nee Chow for taking the time to review my dissertation and provide valuable feedback.

I would like to thank my fellow graduate students, particularly Andrew Paquette, Dr. Diogenes Molina, Dr. Stefan Grubic, and Dr. Jiaqi Liang for their valuable feedback throughout the course of my research. Their eager willingness to discuss the problems that arose during my research helped to refine my research more than any other source. Their day-to-day companionship in the lab has also helped maintain my sanity when the work of the Ph.D. became stressful.

For the experimental work presented in this dissertation, the help of Dr. Jose Restrepo was invaluable. Without all of his circuit design experience and tutorials for using the equipment, the experimental portion of this work would not have been possible. Additionally, Dr. Restrepo assisted me remotely from Venezuela as questions arose in my work. I would also like to thank Dr. Jiaqi Liang for his assistance in building the experimental setup and his help on designing the control software. I am also thankful for

James Steinberg, who (somehow) always made himself available to help when I needed to build another piece of equipment.

I would like to thank Travis Smith and Dr. Michael Starke at Oak Ridge National Laboratory for their guidance and expertise in forming the scope of this work. Travis Smith provided me with a strong foundation in wind plant collector systems and protection considerations. Therefore, the quality of this work is much credited to his help.

Most importantly, I would like to thank my wife, Lindsay, for her unwavering support and encouragement throughout the course of this work.

# TABLE OF CONTENTS

Page

**ACKNOWLEDGEMENTS** ..... **IV**
**LIST OF TABLES** ..... **X**
**LIST OF FIGURES** ..... **XII**
**LIST OF ABBREVIATIONS** ..... **XXI**
**LIST OF SYMBOLS** ..... **XXII**
**SUMMARY** ..... **XXIV**
**CHAPTER 1: INTRODUCTION** ..... **1**
1.1. Origin of the Problem ..... 1
1.2. Research Scope and Objectives ..... 6
1.3. Outline of Chapters ..... 6
**CHAPTER 2: BACKGROUND AND PREVIOUS WORK** ..... **9**
2.1. Introduction ..... 9
2.2. Overview of Short-Circuit Calculations in Power Networks ..... 9
2.3. Symmetrical Components and Sequence-Network Circuits ..... 13
2.3.1. Symmetrical-Component Theory ..... 14
2.3.2. Sequence-Network Circuits ..... 15
2.4. Three-Phase Induction Machines ..... 17
2.5. Type 1 WTG Short-Circuit Behavior ..... 20
2.5.1. Balanced Short Circuit ..... 20
2.5.2. Unbalanced Short Circuit ..... 23
2.6. Type 2 WTG Short-Circuit Behavior ..... 25
2.7. Type 3 WTG ..... 26
2.7.1. Overview of Type 3 WTG System ..... 27
2.7.2. Effects of RSC Voltage Limitations ..... 28
2.7.3. RSC Protection ..... 28
2.7.4. Control of GSC and RSC ..... 30
2.7.5. Short-Circuit Behavior ..... 34
2.8. Type 4 WTG ..... 34

2.9. Wind Plant Collector System ..... 36
2.9.1. WTG Step-Up Transformer ..... 36
2.9.2. Collector Cables ..... 37
2.9.3. Substation Transformer ..... 37
2.9.4. Collector System Protection ..... 38
2.9.5. Phasor Estimation in Protective Relays ..... 40
2.10. Conclusions ..... 42
**CHAPTER 3: TYPE 1 AND 2 WIND-TURBINE GENERATORS ..... 44**
3.1. Introduction ..... 44
3.2. Comparison of Transient Simulation Software Packages ..... 45
3.3. Comparison of Transient Simulations and Sequence-Network Calculations ..... 46
3.4. Improved Sequence-Network Model of Induction Machine ..... 51
3.5. Experimental Waveforms vs. PSCAD Simulations ..... 55
3.5.1. Machine Parameter Identification: No-Load Test ..... 56
3.5.2. Machine Parameter Identification: Blocked-Rotor Test ..... 58
3.5.3. Measured vs. Simulated Short-Circuit Currents ..... 60
3.5.4. Effects of Leakage Saturation ..... 63
3.6. Single-Machine Infinite-Bus Studies ..... 66
3.7. Multi-Machine Studies with a Type 1 Wind Farm ..... 74
3.8. Multi-Machine Studies with a Type 2 Wind Farm ..... 79
3.9. Conclusions ..... 83
**CHAPTER 4: TYPE 3 WIND-TURBINE GENERATOR ..... 85**
4.1. Introduction ..... 85
4.2. GSC and RSC Controller Design ..... 86
4.2.1. GSC Inner Current-Loop Controllers ..... 87
4.2.2. DC-Link Voltage Controller ..... 91
4.2.3. RSC Inner Current-Loop Controllers ..... 96
4.2.4. Rotor-Speed Controller ..... 100
4.2.5. Reactive-Power Controllers ..... 104
4.2.6. Effects of Mutual-Flux Saturation on Controls ..... 107

4.3. Proposed Sequence-Network Model of the Type 3 WTG ..... 110
4.3.1. Steady-State Equivalent Circuit ..... 110
4.3.2. Sequence-Network Circuits ..... 116
4.4. Effects of RSC Voltage Limitations ..... 119
4.4.1. Transient Over Voltages ..... 120
4.4.2. Overvoltages Due to Stator Voltage Unbalance ..... 122
4.5. Experimental Results vs. Transient Simulations ..... 124
4.5.1. Experimental Testbed ..... 124
4.5.2. Simulation and Measurement Comparison: Three-phase Fault ..... 127
4.5.3. Simulation and Measurement Comparison: Single Phase Fault ..... 129
4.6. Experimental Results vs. Sequence-Network Calculations ..... 131
4.6.1. Three-Phase Fault Case ..... 131
4.6.2. Single-Phase Fault Case ..... 135
4.7. Single Machine Infinite Bus Studies ..... 138
4.8. System Studies of Multi-Machine Type 3 Wind Farm ..... 148
4.9. Conclusions ..... 152
**CHAPTER 5: TYPE 4 WIND-TURBINE GENERATOR ..... 154**
5.1. Introduction ..... 154
5.2. GSC and MSC Control Design ..... 155
5.2.1. GSC Control Design ..... 156
5.2.2. MSC Control Design ..... 162
5.2.3. Rotor Speed Control Design ..... 165
5.3. Proposed Sequence-Network Model of Type 4 WTG ..... 167
5.3.1. Steady-State Equivalent Circuit ..... 167
5.3.2. Sequence-Network Circuits ..... 169
5.4. Experimental Results vs. Transient Simulations ..... 171
5.4.1. Three-Phase Short-Circuit Case ..... 173
5.4.2. Single-Phase Fault Case ..... 175
5.5. Single-Machine Infinite Bus Studies ..... 177

5.6. Multi-Machine Network Studies ..... 185
5.7. Conclusion ..... 190
**CHAPTER 6: CONCLUSIONS, CONTRIBUTIONS, AND RECOMMENDATIONS FOR FUTURE WORK ..... 191**
6.1. Conclusions ..... 191
6.2. Summary of Contributions ..... 193
6.3. Future Work ..... 196
6.3.1. Control Topology Effect on Sequence-Network Models ..... 196
6.3.2. Incorporation into Existing Protection and Short-Circuit Software ..... 196
6.3.3. Study of Temporary Over Voltages in Wind Plant Collector System ..... 197
6.3.4. Protection Considerations with Short Time Constants of Decay ..... 197
**APPENDIX A: WIND-TURBINE GENERATOR PARAMETERS ..... 200**
**APPENDIX B: CLOSED-FORM SOLUTION OF INDUCTION MACHINE SHORT-CIRCUIT CURRENTS ..... 205**
**APPENDIX C: COLLECTOR SYSTEM PARAMETERS ..... 216**
**APPENDIX D: SENSOR CALIBRATION AND MEASUREMENT UNCERTAINTY ..... 218**
**APPENDIX E: STATOR-FLUX ESTIMATION IN TYPE 3 WTG ..... 223**
**APPENDIX F: EQUIVALENT IMPEDANCES FOR SHORT-CIRCUIT CALCULATIONS ..... 225**
**APPENDIX G: TYPE 3 WTG ROTOR OVERVOLTAGES ..... 226**
**APPENDIX H: AC-CROWBAR AND DC-CHOPPER CONTROL LOGIC ..... 229**
**APPENDIX I: COMPARISON OF AVERAGED AND SWITCHING WTG MODELS ..... 232**
**REFERENCES ..... 240**
**VITA ..... 248**

# LIST OF TABLES

Page


Table 2.1: Various RSC protection techniques in the Type 3 WTG. ..... 29
Table 2.2: Substation transformer winding options and zero-sequence circuits [57]..... 38
Table 3.1: Comparison of calculated and simulated short-circuit currents for a TLG fault..... 50
Table 3.2: Comparison of calculated and simulated short-circuit currents for a SLG fault..... 50
Table 3.3: Comparison of conventional and improved sequence-network calculations..... 55
Table 4.1: Pre-fault conditions for three-phase fault on experimental testbed (all parameters in per unit). ..... 131
Table 4.2: Calculated pre-fault rotor current considering saturation effects. ..... 132
Table 4.3: Pre-fault conditions for single-phase fault on experimental testbed (all parameters in per unit). ..... 135
Table 4.4: Calculated pre-fault rotor current considering saturation effects (current in per unit). ..... 136
Table 4.5: Pre-fault conditions of Type 3 WTG and parameters for short-circuit calculations (all parameters in per unit)..... 141
Table A.1: Lab-scale Type 1 wind-turbine generator parameters. ..... 200
Table A.2: Utility-scale Type 1 and Type 2 wind-turbine generator parameters. ..... 200
Table A.3: Lab-scale Type 3 wind-turbine generator parameters. ..... 201
Table A.4: Utility-scale Type 3 WTG parameters..... 202
Table A.5: Lab-scale Type 4 WTG parameters. ..... 203
Table A.6: Utility-scale Type 4 WTG parameters..... 204

Table A.7: Steady State Current Calculation Results from Circuits of Fig. A.3 and Fig. A.4 (Magnitude in pu and Angle in Degrees)..... 214
Table A.8: Underground cable parameters used in the networks in Fig. 3.18, Fig. 3.25, Fig. 4.40, Fig. 4.47, Fig. 5.18, Fig. 5.24. ..... 216
Table A.9: Generator step-up transformer parameters used in the networks in Fig. 3.18, Fig. 3.25, Fig. 4.40, Fig. 4.47, Fig. 5.18, Fig. 5.24..... 216
Table A.10: Substation step-up transformer parameters used in the networks in Fig. 3.18, Fig. 3.25, Fig. 4.40, Fig. 4.47, Fig. 5.18, Fig. 5.24..... 216
Table A.11: Transmission system parameters used in the networks in Fig. 3.18, Fig. 3.25, Fig. 4.40, Fig. 4.47, Fig. 5.18, Fig. 5.24. ..... 217
Table A.12: Summary of Measurement Uncertainty from Current Transducers ..... 220
Table A.13: Summary of Measurement Uncertainty from Voltage Transducers ..... 222
Table A.14: Equivalent Impedances for Short-Circuit Calculation in (4.65) ..... 225

# LIST OF FIGURES

Page


Fig. 1.1: (a) Conventional power plant with large synchronous generator and (b) simplified equivalent circuit for short-circuit calculations. ..... 2

Fig. 1.2: Typical wind plant collector system layout. ..... 3

Fig. 1.3: Various WTG types. ..... 4

Fig. 2.1: Simplified circuit for short-circuit calculations. ..... 11

Fig. 2.2: Components of the short-circuit current in an *R-L* circuit. ..... 11

Fig. 2.3: Simple three phase network with some common fault types. ..... 14

Fig. 2.4: Sequence-network circuit for SLG fault. ..... 16

Fig. 2.5: Sequence-network circuit for a LL fault. ..... 16

Fig. 2.6: Three-phase induction machine winding configuration [8]. ..... 18

Fig. 2.7: Voltage behind transient reactance model of induction machine. ..... 21

Fig. 2.8: Positive and negative sequence circuits of induction machine (a) for steady-state and (b) initial short-circuit calculations. ..... 24

Fig. 2.9: Circuit diagram of Type 2 WTG. ..... 25

Fig. 2.10: Control diagram of Type 2 WTG. ..... 25

Fig. 2.11: Circuit diagram of Type 3 WTG. ..... 27

Fig. 2.12: Control signal measurement and calculation for RSC and GSC. ..... 30

Fig. 2.13: Control diagram of GSC in Type 3 WTG. ..... 31

Fig. 2.14: Control diagram of RSC in Type 3 WTG. ..... 32

Fig. 2.15: General Type 4 WTG topology. ..... 35

Fig. 2.16: Typical wind plant collector system. ..... 36

Fig. 2.17: Phasor estimation of a transient signal. (a) Arbitrary transient signal and (b) comparison of actual and estimated RMS magnitude of signal. ..... 41

Fig. 3.1: Comparison of transient simulation results in PSCAD, EMTP-RV, and SimPowerSystems for a (a) three-phase fault and (b) single-phase fault. ..... 46
Fig. 3.2: Simple network for simulating induction machine transients. ..... 48
Fig. 3.3: Short-circuit current for a TLG fault and envelopes defining current decay. ..... 48
Fig. 3.4: Short-circuit current for a SLG fault and fitted waveform. ..... 48
Fig. 3.5: Comparison of calculated and simulated RMS short-circuit current for a (a) TLG fault and (b) SLG fault (solid = simulated, dashed = calculated). ..... 51
Fig. 3.6: Comparison of simulated short-circuit current and closed-form solution (calculated current) for a SLG fault. ..... 53
Fig. 3.7: Improved sequence-network model of induction machine for unbalanced fault. ..... 54
Fig. 3.8: Photo of experimental wound-rotor induction machine used for testing. ..... 56
Fig. 3.9: Steady-state equivalent circuit of induction machine. ..... 57
Fig. 3.10: No-load saturation curve of induction machine. ..... 58
Fig. 3.11: Blocked-rotor test result curve. ..... 59
Fig. 3.12: Induction machine circuit for applying fault. ..... 61
Fig. 3.13: Photo of control circuitry for applying a fault to the induction machine. ..... 61
Fig. 3.14: Experimental and simulation results for a three-phase fault on the induction machine. ..... 62
Fig. 3.15: Experimental and simulation results for a phase-A-to-neutral fault on the induction machine. ..... 63
Fig. 3.16: Experimental and simulation results for a three-phase short-circuit test at reduced voltage. ..... 65
Fig. 3.17: Comparison of measured short-circuit currents to simulated currents with a reduction in the winding leakage reactances. ..... 66
Fig. 3.18: Single-machine infinite bus network. ..... 67

Fig. 3.19: Transient sequence-network circuit of the single-machine network for a three-phase fault on the transmission system. ..... 68
Fig. 3.20: Steady-state sequence-network circuit of the single-machine network for a three-phase fault on the transmission system. ..... 68
Fig. 3.21: (a) Transient simulation results of the voltages and currents for a three-phase fault on the transmission system and (b) comparison of the calculated and simulated positive-sequence components of these voltages and currents. ..... 71
Fig. 3.22: Transient sequence-network circuit for a single-phase fault on the single machine system. ..... 72
Fig. 3.23: Steady-state sequence-network circuit for a single-phase fault on the single machine system. ..... 73
Fig. 3.24: (a) Transient simulation results of the voltages and currents for a single-phase fault on the transmission system and (b) comparison of the calculated and simulated sequence components of these voltages and currents (solid = simulated, dashed = calculated). ..... 74
Fig. 3.25: Multi-machine Type 1 wind farm used for short-circuit studies. ..... 75
Fig. 3.26: (a) Transient simulation results of the voltages and currents for a single-phase fault on the collector system of the multi-machine system and (b) comparison of the calculated and simulated sequence components of these voltages and currents (solid = simulated, dashed = calculated). ..... 77
Fig. 3.27: (a) Transient simulation results of the voltages and currents for a two-phase-to-ground fault on the transmission system of the multi-machine system and (b) comparison of the calculated and simulated sequence components of these voltages and currents (solid = simulated, dashed = calculated). ..... 78
Fig. 3.28: (a) Transient simulation results of the voltages and currents for a three-phase fault on the transmission system of the multi-machine system and (b) comparison of the calculated and

simulated positive-sequence components of these voltages and currents (solid = simulated, dashed = calculated). ..... 81
Fig. 3.29: (a) Transient simulation results of the voltages and currents for a line-to-line fault on the transmission system of the multi-machine system and (b) comparison of the calculated and simulated sequence components of these voltages and currents (solid = simulated, dashed = calculated). ..... 82
Fig. 4.1: Circuit diagram of Type 3 WTG. ..... 86
Fig. 4.2: Simplified three-phase circuit of GSC. ..... 87
Fig. 4.3: GSC inner-current control loops. ..... 88
Fig. 4.4: Block diagram of GSC inner current-control loop. ..... 90
Fig. 4.5: Bode plot of GSC closed-loop current control system. ..... 91
Fig. 4.6: Step response of GSC closed-loop current control system. ..... 91
Fig. 4.7: DC-link circuit. ..... 93
Fig. 4.8: Two options for DC-link voltage control loop. ..... 93
Fig. 4.9: Block diagram of DC-link voltage-control loop. ..... 94
Fig. 4.10: Bode plot of closed-loop DC-link voltage controller. ..... 96
Fig. 4.11: Step response of closed-loop DC-link voltage controller. ..... 96
Fig. 4.12: Simplified three-phase circuit of RSC. ..... 97
Fig. 4.13: RSC inner current control loops. ..... 98
Fig. 4.14: Block diagram of RSC current-control loop. ..... 99
Fig. 4.15: Bode plot of closed-loop RSC current controller. ..... 100
Fig. 4.16: Step response of closed-loop RSC current controller. ..... 100
Fig. 4.17: Block diagram of rotor speed controller. ..... 102
Fig. 4.18: Bode plot of closed-loop rotor speed controller. ..... 103
Fig. 4.19: Step response of speed controller. ..... 103
Fig. 4.20: Block diagram of the stator reactive power control loop. ..... 106
Fig. 4.21: Bode plot of closed-loop stator reactive-power controller. ..... 106
Fig. 4.22: Step response of closed-loop stator reactive-power controller. ..... 106
Fig. 4.23: Block diagram of GSC reactive-power control loop. ..... 107

Fig. 4.24. No-load saturation characteristics of wound-rotor induction machine. ..... 109
Fig. 4.25: Steady-state equivalent circuit of the Type 3 WTG. ..... 112
Fig. 4.26. Approximation of the steady-state real-power output of the Type 3 WTG. ..... 113
Fig. 4.27: Single-machine infinite bus network for steady-state calculations. ..... 114
Fig. 4.28: Proposed sequence-network circuits of the Type 3 WTG for uninterrupted control of the RSC. ..... 117
Fig. 4.29: Proposed sequence-network circuits of the Type 3 WTG with crowbar protection (a) immediately after fault and (b) in steady-state after the fault. ..... 119
Fig. 4.30: Space vector of rotor voltage during transients. ..... 121
Fig. 4.31: Space vector of induced rotor voltages during stator voltage unbalance. ..... 123
Fig. 4.32. Circuit diagram of Type 3 WTG testbed. ..... 125
Fig. 4.33. Photo of Type 3 WTG experimental testbed. ..... 126
Fig. 4.34: Comparison of experimental and transient simulation results for a three-phase fault on a Type 3 WTG ($\omega_r$* = 1.1 pu). ..... 128
Fig. 4.35: Comparison of experimental and transient simulation results for a single-phase fault on a Type 3 WTG ($\omega_r$* = 0.92 pu). ..... 130
Fig. 4.36: Equivalent circuit for short-circuit calculations on testbed Type 3 WTG. ..... 133
Fig. 4.37: (a) Instantaneous currents from the Type 3 WTG and (b) comparison of measured and calculated positive-sequence currents. ..... 135
Fig. 4.38: Sequence-network circuit for a phase-A-to-neutral fault in experimental setup. ..... 136
Fig. 4.39: (a) Instantaneous current after a phase A to neutral fault and (b) comparison of measured and calculated sequence currents

(measured: solid, calculated: dotted -> $X_m = X_{m1}$, dashed -> $X_m = X_{m2}$, dot/dash -> $X_m = X_{m3}$). ..... 138
Fig. 4.40. Single-machine network for analyzing the short-circuit behavior of a Type 3 WTG. ..... 139
Fig. 4.41: Simulation results for a (a) three-phase fault and (b) single-phase fault. ..... 140
Fig. 4.42: Sequence-network circuit for a three-phase fault for no crowbar operation. ..... 141
Fig. 4.43: (a) Instantaneous waveforms of SMIB network voltages and currents for a three-phase fault and (b) comparison of simulated and calculated positive-sequence components of these voltages and currents. ..... 143
Fig. 4.44: Sequence-network circuit for calculating the short-circuit currents in the SMIB system for a single-phase fault on the transmission system. ..... 144
Fig. 4.45: (a) Instantaneous simulation waveforms of SMIB system for a single-phase fault and (b) comparison of calculation and simulated sequence currents (solid = simulated, dashed = calculated). ..... 145
Fig. 4.46: (a) Transient simulation results of various system voltage and currents for the case of a three-phase fault and AC crowbar activation and (b) comparison of the calculated and simulated positive-sequence components of these voltages and currents. ..... 147
Fig. 4.47: Multi-machine network used for system studies of Type 3 WTG wind farm. ..... 149
Fig. 4.48: (a) Simulation results for a three-phase fault on the transmission system and (b) comparison of the calculated and simulated positive-sequence voltages and currents in the network. ..... 150
Fig. 4.49: (a) Simulation results for a phase-B-and-C-to-ground fault on the transmission system and (b) comparison of calculated and

simulated sequence quantities (solid = simulated, dashed = calculated). ..... 152
Fig. 5.1: Circuit diagram of Type 4 WTG. ..... 155
Fig. 5.2: Block diagram of GSC controls. ..... 156
Fig. 5.3: Block diagram of GSC current controller. ..... 157
Fig. 5.4: GSC hysteresis buffer output logic. ..... 158
Fig. 5.5: Bode plot of the low-pass filter for current-limiting controller. ..... 159
Fig. 5.6: Step response of the low-pass filter used in current-limiting controller for a unit step change in the peak instantaneous voltage. ..... 159
Fig. 5.7: Approximation of turn-on time of the current-limiting controller for a 50% drop in the GSC terminal voltage. ..... 161
Fig. 5.8: Approximation of turn-off time of the current-limiting controller after the recovery of the GSC terminal voltage from a 50% drop in voltage. ..... 161
Fig. 5.9: Machine-side converter control block diagram. ..... 163
Fig. 5.10: Block diagram of MSC inner current-control loop. ..... 165
Fig. 5.11: Block diagram of speed control loop in MSC. ..... 166
Fig. 5.12: Steady-state equivalent circuit of Type 4 WTG. ..... 168
Fig. 5.13: Sequence-network circuits of a Type 4 WTG. ..... 171
Fig. 5.14: Photo of experimental testbed of Type 4 wind turbine generator. ..... 172
Fig. 5.15: Circuit diagram of Type 4 WTG experimental testbed. ..... 172
Fig. 5.16: Comparison of experimental and simulation results for a three-phase fault. ..... 174
Fig. 5.17: Comparison of experimental and simulation results for a single-phase fault. ..... 176
Fig. 5.18: Single-machine infinite bus network for simulating the Type 4 WTG. ..... 177
Fig. 5.19: Simulation results for a three-phase and single-phase fault on the transmission system of the SMIB network. ..... 179

Fig. 5.20: Sequence-network circuit for a three-phase fault on the transmission system. ..... 180
Fig. 5.21: (a) Simulation results of network voltages and currents for a three-phase fault and (b) comparison of calculated and simulated positive-sequence components of these voltages and currents. ..... 182
Fig. 5.22: Sequence-network circuit for single-phase fault on the transmission system. ..... 183
Fig. 5.23: (a) Simulation results of network voltages and currents for a single-phase fault and (b) comparison of the simulated and calculated sequence components of these voltages and currents (solid = simulated, dashed = calculated). ..... 184
Fig. 5.24: Type 4 wind farm with seven WTGs. ..... 186
Fig. 5.25: (a) Transient simulation results of network voltages and currents for a three-phase fault and (b) comparison of simulated and calculated positive-sequence components of these voltages and currents. ..... 188
Fig. 5.26: (a) Transient simulation results of network voltages and currents for a two-phase-to-ground fault and (b) comparison of simulated and calculated sequence components of these voltages and currents (solid = simulated, dashed = calculated). ..... 189
Fig. A.1: (a) Steady-state equivalent circuit of induction machine and (b) steady-state sequence-network representation of induction machine. ..... 212
Fig. A.2: Single induction machine network for simulation of stator short-circuit faults. ..... 214
Fig. A.3: Steady-state sequence network for a phase-A-to-ground fault on the network of Fig. A.2. ..... 214
Fig. A.4: Per-phase steady state equivalent circuit of the network in Fig. A.2. ..... 215
Fig. A.5: Circuit for calibrating current transducers. ..... 219

Fig. A.6: Circuit for calibrating voltage transducers. ..... 221
Fig. A.7: AC crowbar circuit used in Type 3 WTG..... 230
Fig. A.8: Control logic for AC crowbar IGBT gate signal. ..... 230
Fig. A.9: DC-link circuit for Type 3 and Type 4 WTG. ..... 231
Fig. A.10: Control logic of the DC-chopper in the Type 3 and Type 4 WTG. ..... 231
Fig. A.11: Circuit diagram of power electronics converter used in Type 3 and 4 WTGs. ..... 233
Fig. A.12: Circuit diagram of averaged power electronics converter. ..... 233
Fig. A.13: Comparison of averaged and switching models of the Type 3 WTG for a three-phase fault. ..... 235
Fig. A.14: Comparison of averaged and switching models of the Type 3 WTG for a single-phase fault..... 236
Fig. A.15: Comparison of averaged and switching models of the Type 3 WTG for a single-phase fault..... 237
Fig. A.16: Comparison of averaged and switching models of the Type 4 WTG for a three-phase fault. ..... 238
Fig. A.17: Comparison of averaged and switching models of the Type 4 WTG for a single-phase fault..... 239

# LIST OF ABBREVIATIONS

| | |
|---|---|
| ASPEN | Advanced systems for power engineering |
| CAPE | Computer aided protection engineering |
| DLG | Double line to ground |
| FERC | Federal Energy Regulatory Commission |
| GSC | Grid side converter |
| IGBT | Insulated gate bipolar transistor |
| LGIP | Large generator interconnection procedure |
| LL | Line to line |
| MSC | Machine side converter |
| PFCC | Power factor correction capacitors |
| PI | Proportional Integral |
| PIR | Proportional Integral Resonant |
| PLL | Phase locked loop |
| PSCAD | Power system computer aided design |
| PWM | Pulse width modulation |
| RSC | Rotor side converter |
| SCIG/SCIM | Squirrel cage induction generator/machine |
| SG | Synchronous generator |
| SLG | Single line to ground |
| SMIB | Single machine infinite bus |
| TLG | Three line to ground |
| WRIG/WRIM | Wound rotor induction generator/machine |
| WTG | Wind-turbine generator |

# LIST OF SYMBOLS

| Symbol | Definition | Units |
|---|---|---|
| $\lambda, \Lambda$ | Flux linkage | Weber Turns |
| $\omega$ | Frequency | rad/s |
| $F$ | Friction Constant | kg*m$^2$/sec |
| $i, I$ | Current | amperes |
| $J$ | Inertia | kg*m$^2$ |
| $L$ | Inductance | Henry |
| $p$ | Time derivative | -- |
| $P$ | Real Power | Watts |
| $Q$ | Reactive Power | Volt-Amperes Reactive |
| $R$ | Resistance | ohms |
| $s$ | slip or Laplace variable | -- |
| $T$ | Torque | N-m |
| $t, T$ | Time | seconds |
| $v,V$ | Voltage | volts |
| $X$ | Reactance | ohms |

| Subscripts | Meaning |
|---|---|
| $c$ | Underground cable |
| $d$ | d-axis |
| $f$ | fault |
| $g$ | grid-side converter |
| $gt$ | generator transformer |
| $l$ | Leakage |
| $m$ | magnetizing or mutual or Machine-side Converter |
| $p$ | plant or point-of-common-coupling |

| | |
|---|---|
| *q* | q-axis |
| *r* | Rotor |
| *s* | Stator |
| *st* | Substation Transformer |
| *L* | Transmission System Parameter |

| **Superscripts** | **Meaning** |
|---|---|
| + | Positive-sequence |
| - | Negative-sequence |
| *0* | Zero-sequence |
| *s* | Stator-flux oriented |
| *v* | Stator-voltage oriented |

# SUMMARY

Protection of both the wind plant and the interconnecting transmission system during short-circuit faults is imperative for maintaining system structural integrity and reliability. The circuit breakers and protective relays used to protect the power system during such events are designed based upon calculations of the current that will flow in the circuit during the fault. Sequence-network models of various power-system components, such as synchronous generators, transformers, transmission lines, etc., are often used to perform these calculations. However, there are no such models widely accepted for certain types of wind-turbine generators used in modern wind plants.

The problem with developing sequence-network models of wind plants is that several different wind-turbine generator designs exist; yet, each exhibit very different short-circuit behavior. Therefore, a "one size fits all" approach is not appropriate for modeling wind plants, as has been the case for conventional power plants based on synchronous-generator technology. Further, many of the newer wind-turbine designs contain proprietary controls that affect the short-circuit behavior, and wind-turbine manufacturers are often not willing to disclose these controls. Thus, protection engineers do not have a standard or other well-established model for calculating short-circuit currents in power systems with wind plants. Therefore, the research described in this dissertation involves the development of such models for calculating short-circuit currents from wind-turbine generators.

The focus of this dissertation is on the four existing wind-turbine generator designs (identified as Types 1 – 4). Only AC-transmission-interconnected wind-turbine generators are considered in this dissertation. The primary objective of this research is the development of sequence-network models, which are frequency-domain analysis tools, for each wind-turbine generator design. The time-domain behavior of each wind-

turbine generator is thoroughly analyzed through transient simulations, experimental tests on scaled wind-turbine generator test beds, and solutions to the system dynamic equations. These time-domain analyses are used to support the development of the sequence-network models.

# CHAPTER 1: INTRODUCTION

## 1.1. Origin of the Problem

The amount of installed wind-power capacity is expected to increase over the next few decades due to higher energy costs from conventional sources, financial incentives from state and federal governments, and renewable portfolio standards required by some state and federal government agencies. Installed wind-power capacity could supply 2.5% of the world's electricity demand as of 2010, and many European countries currently supply 10-20% of their electricity demand with wind power [1]. The United States has seen a rapid growth in installed wind-power capacity over the past decade, and government planning has commenced to reach an aggressive goal of 20% wind energy by the year 2030 [2]. Such rapid growth in wind-power capacity has led to an industry re-examination of the power system operation and reliability during electrical faults, since some types of wind plants behave fundamentally different than conventional power plants. Government regulations have been enacted that require wind plants to remain online and support the power system during electrical faults, particularly low-voltage conditions caused by short-circuit events [3] [4] [5]. Protection systems in the wind plant must be designed in such a way to adhere to the aforementioned grid codes while adequately protecting the wind plant and interconnecting system. Because wind plants differ in many ways from conventional power plants, existing techniques for characterizing short-circuit currents are not necessarily appropriate for all types of wind plants.

Conventional power plants typically consist of a large synchronous generator (SG) connected to the transmission system through a step-up transformer, as shown in Fig. 1.1(a). Stages of gas or steam turbines are directly coupled to the generator rotor. A governor (not shown in Fig. 1.1(a) ) regulates the amount of gas/steam in the turbines to

control the rotor speed to a constant value [6] [7]. The plant step-up transformer and transmission interconnection are typically at the same physical location of the power plant to minimize transmission losses. An excitation system supplies DC current to the field winding that is wound on the rotor shaft. The excitation system controls the DC field current $I_f$ to regulate the AC stator terminal voltage of the SG [6] [7]. Synchronous generator short-circuit currents are often calculated from simplified models using a voltage behind sub-transient reactance [6] [8], as shown in Fig. 1.1(b). The sub-transient reactance $X''$ can be calculated based on the SG winding inductances. The circuit of Fig. 1.1(b) is used to calculate the initial short-circuit currents after a fault, and these currents are known to decay with time constants based on the winding inductances and resistances [6] [8]. This type of model is required from the Federal Energy Regulatory Commission's (FERC) Standard Large Generator Interconnection Procedure (LGIP), which is a required agreement for all power plants over 20 MW interconnecting to the transmission system [9]. Commercially-available protection software, such as CAPE and ASPEN, calculate short-circuit currents based on IEEE recommended practices [10] that are also based on this voltage behind reactance representation of a power plant. Because the short-circuit characteristics of some types of wind-turbine generators (WTGs) are different from SGs, this type of model is not appropriate for all types of wind plants.

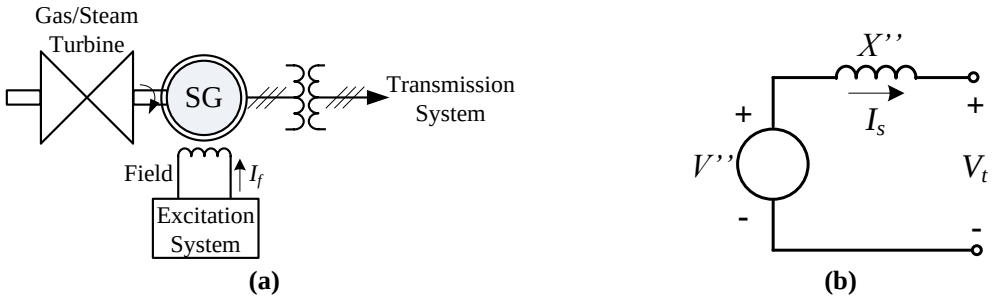


**Fig. 1.1: (a) Conventional power plant with large synchronous generator and (b) simplified equivalent circuit for short-circuit calculations.**

A one-line diagram of a typical wind plant is shown in Fig. 1.2. WTGs used in transmission interconnected wind plants are usually rated from one to three MVA. Each WTG has a step-up transformer which steps the voltage up from low voltage (typically 575-690 V) to medium voltage (typically 12.1 kV - 34.5 kV) [11]. A wind plant covers a large geographic area with up to hundreds of WTGs interconnected through miles of underground cables known as the wind plant collector system [12]. A wind plant may have several collector "feeders," which are the underground cables connecting a string of WTGs to the wind plant substation transformer. Each feeder is usually limited to carrying 25-30 MVA of power. The substation transformer connects the wind plant to the transmission system.

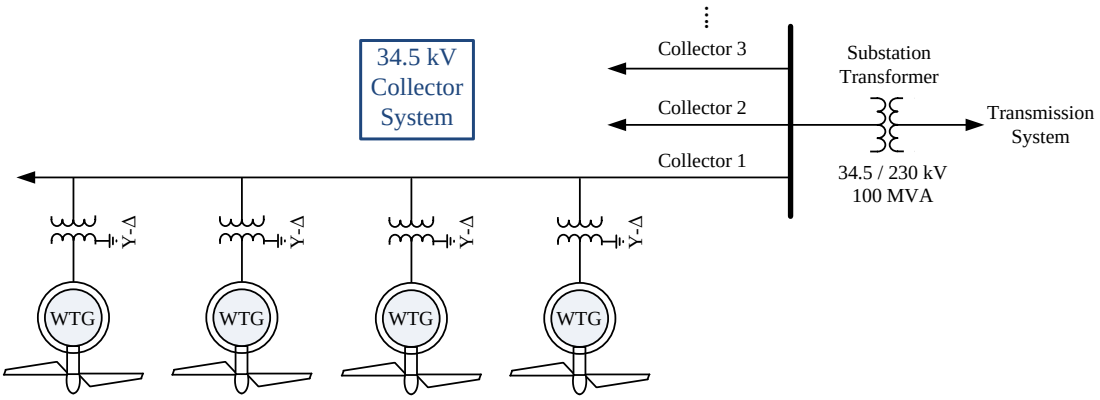


**Fig. 1.2: Typical wind plant collector system layout.**

WTGs are typically classified into four types [13-18], and a diagram of each type is shown in Fig. 1.3. The Type 1 WTG is a squirrel-cage induction generator (SCIG) with stator windings connected directly to the grid. A soft starter is connected in series with the generator with a bypass contactor for normal (non-starting) operating conditions. Several stages of power-factor-correction capacitors (PFCC) are connected to the stator windings, and are switched in/out based on the WTG power output. The Type 1 operates at a fixed rotational speed slightly above grid frequency. The Type 2 WTG is a wound-rotor induction generator (WRIG) with a variable resistance connected to the rotor

windings through brushes and slip rings. Type 2 WTGs require a soft starter and PFCC, similar to the Type 1; but the external rotor resistance allows for a wider operating speed range than the Type 1. Super-synchronous rotational speeds of 1 – 1.1 pu are possible with the Type 2. The Type 3 WTG is a WRIG with the stator windings connected directly to the grid and the rotor windings connected to the grid through an AC-AC power-electronic converter. The AC-AC converter allows for a wider operating speed range than both Type 1 and Type 2 WTGs, and also allows for sub-synchronous and super-synchronous operating speeds (typically 0.7 – 1.3 pu). The Type 4 WTG is connected to the grid through a fully-rated AC-AC converter. Several variations in the drive train of the Type 4 are available, with options including: gearbox or no gearbox, synchronous or induction generator, permanent-magnet synchronous or wound-rotor synchronous generator [13]. The rotational speed of the Type 4 is decoupled from the grid frequency, and a similar operating speed range as the Type 3 is possible with the Type 4 configuration.

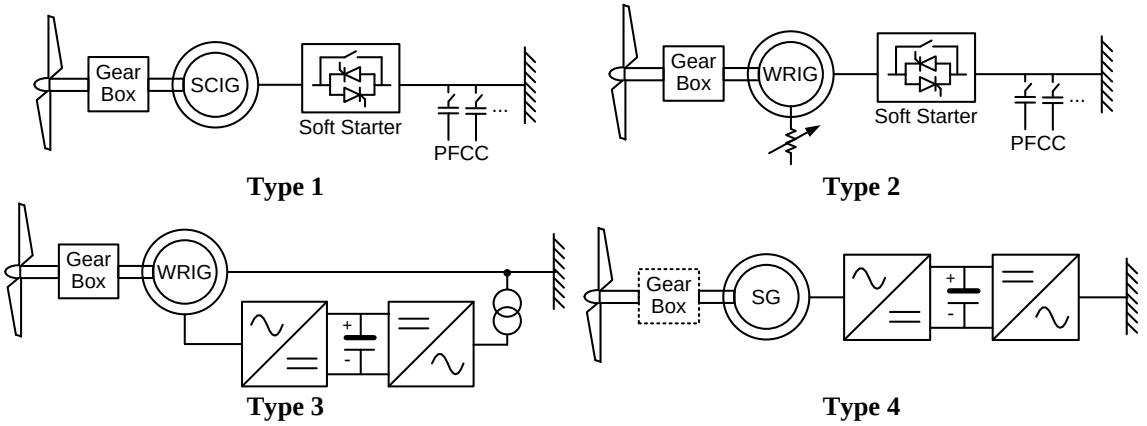


**Fig. 1.3: Various WTG types.**

Early grid-connected WTGs consisted of Types 1 and 2. As technology improved, the market for wind power moved toward Type 3 and 4 concepts [19]. Variable speed wind turbines are capable of extracting more power from the wind and

reduce mechanical stresses on the generator and turbine drivetrain [20]; therefore, Type 3 and 4 WTGs are now the preferred choice in new wind plant projects. Additionally, the added control capability of the Type 3 and 4 make wind plants of this type more able to meet the aforementioned grid-interconnection requirements often imposed on the wind plant.

The short-circuit behavior of Type 1 and 2 WTGs is primarily dependent on the physical characteristics of the machine, since no active control is implemented with these WTG types during a short circuit. Therefore, Types 1 and 2 exhibit similar physical dynamics as the SG, and can be modeled as voltages behind a reactance in short-circuit calculations. The behavior of Types 3 and 4 during faults, however, is dominated by the controls of the AC-AC converters. The control circuits in the AC-AC converters in the Type 3 and Type 4 WTG contain high-bandwidth current-control loops that can respond rapidly to changes in the WTG terminal voltage. Thus, the short-circuit current contributed by these types of WTGs can be directly controlled. Herein lays the stark difference between conventional SGs and modern WTGs. The conventional short-circuit model of SGs, using a generic, "one size fits all" voltage-behind-reactance type model, is a *physics-based* model to calculate the short-circuit currents. Whereas, the short-circuit model of a Type 3 and Type 4 WTG must be a *control-based* model. Because the short-circuit current contributed by these types of WTGs can be controlled, the specific short-circuit current contributed by different WTGs can vary between different manufacturers. Additionally, manufacturers may be reluctant to share certain characteristics of their control for proprietary reasons. Therefore, a new, generic short-circuit model of modern wind turbines is needed which can *incorporate* this control behavior without *requiring* proprietary control information.

## 1.2. Research Scope and Objectives

The research presented in this dissertation focuses on AC-interconnected WTGs for utility-scale applications. The response of WTGs to short-circuit faults on the interconnecting power system is investigated in this work using transient simulations and experimental tests carried out on lab-scale equipment. The results of this work are intended to provide equations, models, and procedures for calculating short-circuit currents from different types of WTGs. Thus, the primary audience for this work includes utility protection engineers and wind-turbine manufacturers. While the primary application of this work relates to power-system protection, the focus of the work is to develop the short-circuit models of the WTGs, and not on the appropriate protection practices for wind plants.

The objectives of this research are:

1. To validate and improve upon existing short-circuit models of Type 1 and Type 2 WTGs, as necessary.
2. To develop short-circuit models of Type 3 and Type 4 WTGs using typical control strategies.
3. To validate the Type 1, 3, and 4 WTG transient simulation models using hardware test beds with ratings of about 10 kVA.
4. To validate the developed short-circuit models of WTG Types 1-4 WTGs using transient simulations of utility-scale WTGs within a realistic WTG network.

## 1.3. Outline of Chapters

**Chapter 1:** The background and motivation behind the research are discussed, and the scope and objectives of the research are outlined.

**Chapter 2:** Background information regarding short-circuit calculation considerations in existing IEEE standards is discussed in this Chapter. A brief review of symmetrical-component theory and sequence-network circuits is provided. The existing short-circuit

models of Type 1 and Type 2 WTGs are reviewed in this chapter, as well as the control strategies used in Type 3 and Type 4 WTGs. An outline of the wind-plant collector system components and layouts is provided, including protection considerations and typical transformer connections.

**Chapter 3:** In this chapter, the Type 1 and Type 2 WTGs are discussed together since their short-circuit behavior is similar. Transient-simulation results of an induction machine are compared with short-circuit calculations using an existing short-circuit model of the Type 1 WTG. The existing short-circuit model of the Type 1 WTG is shown to give accurate results for a three-phase fault, but is shown to give some error for unbalanced fault calculations. An improved short-circuit model of the Type 1 WTG is proposed in this chapter which gives more accurate calculations for unbalanced faults on a Type 1 WTG. Experimental short-circuit tests on a lab-scale Type 1 WTG are described in this chapter and compared to transient simulation results. Transient simulations are described for a single-machine system and a multi-machine system, and compared with calculations using the existing short-circuit model of the Type 1 WTG. The existing short-circuit model is shown to have good agreement to the transient simulation results. Transient simulations are also described for a multi-machine system consisting of Type 2 WTGs, and compared to short-circuit calculations using the same model as the Type 1 WTG. It is shown that the key difference between the Type 1 and Type 2 WTG's short-circuit response is the rapid decay in the Type 2 WTG currents, which are due to the high rotor resistance.

**Chapter 4:** A design methodology for the dynamic controls of the Type 3 WTG is introduced in this chapter and implementations of these controls in both transient simulations and hardware is described and typical results provided. Simulation and experimental tests are presented for both balanced and unbalanced faults. The effects of magnetic saturation on the short-circuit currents of the Type 3 WTG are described. The theoretical approach to development of the short-circuit model of the Type 3 WTG is

provided, and calculation results using the short-circuit model are compared with both transient simulations and experimental results.

**Chapter 5:** A design methodology for the dynamic controls of the Type 4 WTG is discussed in this chapter, and implementations of these controls in both transient simulations and hardware are described together with results. Simulation and experimental results include both balanced and unbalanced faults. The theoretical approach to development of the short-circuit model of the Type 4 is discussed, and calculation results using the short-circuit model are compared with both transient simulations and experimental results.

**Chapter 6:** The conclusions that can be drawn from the work presented in this dissertation are discussed, as well as the new contributions of this work and recommendations for future work.

# CHAPTER 2: BACKGROUND AND PREVIOUS WORK

## 2.1. Introduction

A review of short-circuit calculation methods and conventions are given in this chapter. Symmetrical-component theory and sequence-network circuits, which are often used to calculate short-circuit currents from generators, are also introduced in this chapter. A review of previous work on wind-turbine generator (WTG) short-circuit analysis is described, as well as various control methods for the Type 3 and Type 4 WTGs. Wind plant collector system characteristics are briefly described, particularly those related to the short-circuit behavior of the plant, including transformer winding connections and collector system protection practices.

## 2.2. Overview of Short-Circuit Calculations in Power Networks

A review of short-circuit calculation techniques is given in this section for the simplest case of a three-line-to-ground (TLG) fault. Because a balanced three-phase power network remains symmetrical and balanced during a TLG fault, the network can be analyzed on a per-phase basis. The more general case of unbalanced faults is considered in later sections. The simple case of an *R-L* circuit with constant voltage source is studied first to introduce common terms and conventions used in short-circuit analysis. The material in this section draws heavily upon IEEE Standard 551 [10] entitled "IEEE Recommended Practice for Calculating Short-Circuit Currents in Industrial and Commercial Power Systems."

A practical power system is a large, complex, and non-linear dynamic system. Precise calculation of the short-circuit currents in such a system would be a time consuming and complex computation. Simplified circuits, as shown in Fig. 2.1, are often used to calculate conservative estimates of the short-circuit currents at different points in

the power system. These simplified circuits often provide a sufficiently accurate estimate of the short-circuit current. Because the power system consists of mostly inductive components, the circuit of Fig. 2.1 gives insight into the behavior of the short-circuit currents. The differential equation describing the dynamics of the circuit of Fig. 2.1 is given by

$$\sqrt{2}V\sin(\omega t) = Ri + L\frac{di}{dt}. \tag{2.1}$$

The current flowing in the circuit after $T_0$ is displayed in Fig. 2.2. The current waveform is described by the solution to the differential equation of (2.1), the final result of which is given by

$$i(t) = \frac{\sqrt{2}V}{\sqrt{R^2 + X^2}}\sin(\omega t - \alpha) + \left[ i(T_0) - \frac{\sqrt{2}V}{\sqrt{R^2 + X^2}}\sin(\omega T_0 - \alpha) \right] e^{-\omega(t-T_0)R/X}, \tag{2.2}$$

where $X = \omega L$ and $\alpha = \tan^{-1}(X/R)$. Equation (2.2) indicates the short-circuit current consists of an alternating component and a transient DC component that decays exponentially to zero. The transient DC component magnitude depends on the time $T_0$ the switch in Fig. 2.1 closes and the pre-short-circuit current $i(T_0)$. Often, the load (pre-short-circuit) current is neglected since it is considered small compared to the short-circuit current. Thus, (2.2) can be written more concisely as

$$i(t) = i_{ac}(t) + i_{dc}(t) = \sqrt{2}I_{ac,rms}[\sin(\omega t - \alpha) - \sin(\omega T_0 - \alpha)e^{-\omega(t-T_0)R/X}], \tag{2.3}$$

where the AC RMS current is given by

$$I_{ac,rms} = \frac{V}{\sqrt{R^2 + X^2}}. \tag{2.4}$$

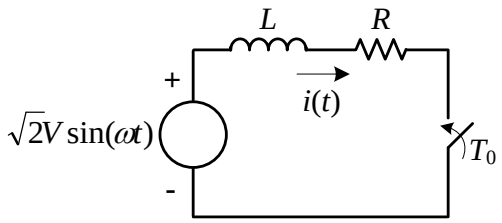


**Fig. 2.1: Simplified circuit for short-circuit calculations.**

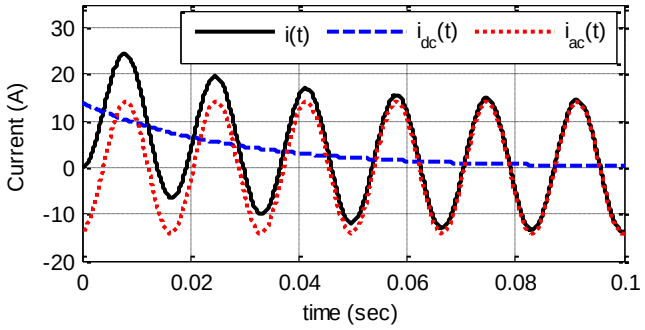


**Fig. 2.2: Components of the short-circuit current in an *R*-*L* circuit.**

Various components of the short-circuit current are of interest depending on the particular application. Some of the key components of interest are listed below in the context of the circuit shown in Fig. 2.1:

1. **Maximum Instantaneous Current**: This value is based upon the worst-case scenario that the short circuit occurs at a point in time that produces the maximum DC offset in the short-circuit current. Assuming the X/R ratio of the circuit is large, then the angle $\alpha$ in (2.3) is approximately 90°. Therefore, a rough approximation is that the maximum peak occurs one-half cycle after the short circuit ($T_0$ + 1/120 seconds), and can be calculated from (2.3) as

$$I_{pk} = \sqrt{2} I_{ac,rms} (1 + e^{-\omega R/(120X)}) . \qquad (2.5)$$

However, because the actual current maximum occurs before one-half cycle, the calculation in (2.5) is a non-conservative estimate. To account for this error,

various modifications of (2.5) have been formed to provide better estimates of the peak current, and are given in [10].

2. **First-Cycle RMS Current**: This value also corresponds to the worst-case scenario of maximum DC offset in the short-circuit current. Because the initial short-circuit current is not periodic (due to the exponentially decaying DC component), the DC offset is taken to be the value at one-half cycle ($T_0$ + 1/120 seconds) after the short circuit as an approximation. Thus, the first-cycle RMS current is approximated by

$$I_{rms} = I_{ac,rms}\sqrt{1+2e^{-\omega R/(60X)}}\ . \tag{2.6}$$

3. **Interrupting Current**: This value corresponds to the RMS current a circuit breaker must interrupt to open the circuit at a specified point in time after the short-circuit event. Interrupting times vary depending on the application, but may range from 1.5 to several cycles after the fault. The following equation can be used to calculate the interrupting current based on the interrupting time $T_{\text{int}}$ of interest:

$$I_{rms}(T_{\text{int}}) = I_{ac,rms}\sqrt{1+2e^{-2\omega(T_{\text{int}}-T_0)R/X}}\ . \tag{2.7}$$

4. **Steady-State Current**: This is the current that remains after transients have died away, and for the circuit of Fig. 2.1 is simply $I_{ac,rms}$.

5. **Fundamental-Frequency Short-Circuit Current**: This value corresponds to the RMS short-circuit current excluding the DC offset. For the circuit of Fig. 2.1, this is simply $I_{ac,rms}$. However, in general, short-circuit currents have a decaying AC component in addition to a decaying DC component. Thus, the fundamental-frequency short-circuit current includes both the steady-state and transient AC components that decay over time.

Short-circuit currents in a power system are, in general, more complicated than can be described using the circuit of Fig. 2.1 and (2.2). Electric machines contribute decaying AC components to the short-circuit currents as well as decaying DC components. The short-circuit currents of induction machines, which are used in WTG

Types 1-3, are discussed in later sections. The analysis presented in this section is valid for networks subject to a TLG fault that have no AC decay in the short-circuit currents. Unbalanced faults are more common, and analysis of power systems on a per-phase basis for unbalanced faults requires the use of symmetrical components, which are discussed in the next section.

## 2.3. Symmetrical Components and Sequence-Network Circuits

Most electric power is generated and transmitted in three-phase circuits. Under ideal conditions, the voltage and current in each phase are balanced and symmetrical, having identical magnitudes and angles separated by 120° phase shifts. However, in realistic operating conditions, the three-phase circuits have some amount of asymmetry. During fault conditions, the asymmetry can be severe if the fault only involves one or two phases in the three-phase circuit. Thus, a means for analyzing the short-circuit currents under asymmetrical conditions is necessary to protect the system against these conditions.

A simple three-phase network is shown in Fig. 2.3. Common faults that can occur in a power system (in order of frequency of occurrence [21]) are the single-line-to-ground (SLG) fault, line-to-line (LL) fault, double-line-to-ground (DLG) fault, and a three-line-to-ground (TLG) fault. Each of these fault types are illustrated in Fig. 2.3. While they are shown in Fig. 2.3 as solid short circuits, in general, the fault may have some impedance. Calculating the phase currents in Fig. 2.3 for the unsymmetrical faults would be quite tedious if done using conventional circuit analysis techniques. As discussed in the previous section, for a TLG fault the three-phase circuit can be reduced to a per-phase circuit, which greatly simplifies the calculations. However, under unsymmetrical conditions, these calculations are best performed using the theory of symmetrical components.

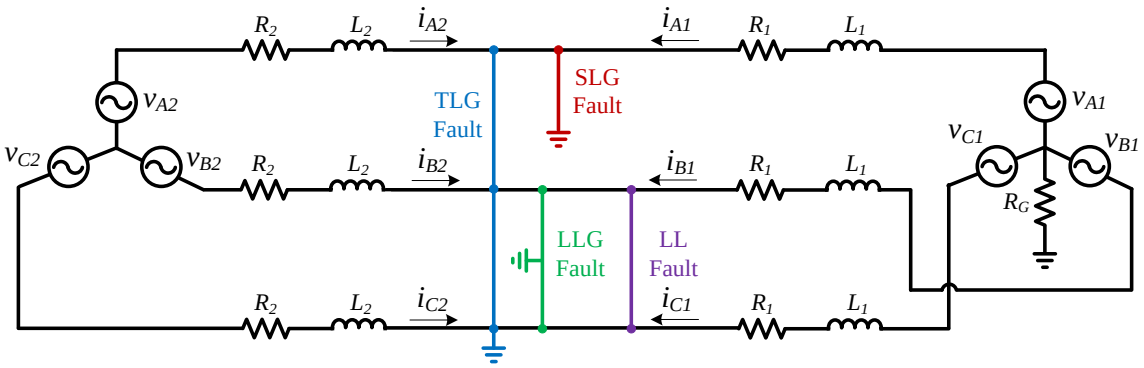


**Fig. 2.3: Simple three phase network with some common fault types.**

### *2.3.1. Symmetrical-Component Theory*

Symmetrical-component theory, originally developed by Charles Legeyt Fortescue in the early part of the 20th century, states that an arbitrary set of *n* unbalanced phasors can be resolved into *n* – 1 balanced *n*-phase systems of different phase sequence and one zero-phase sequence system [21], where the zero-phase sequence is a set where all three phases are of equal phase and magnitude. While this theory applies to an arbitrary *n*-phase system, a three-phase system is of particular interest in this work. Mathematically, symmetrical-component theory is described using an arbitrary three-phase set $\vec{I}_a$, $\vec{I}_b$, and $\vec{I}_c$ as

$$\begin{bmatrix} \vec{I}_a \\ \vec{I}_b \\ \vec{I}_c \end{bmatrix} = \begin{bmatrix} \vec{I}_{a0} \\ \vec{I}_{b0} \\ \vec{I}_{c0} \end{bmatrix} + \begin{bmatrix} \vec{I}_{a1} \\ \vec{I}_{b1} \\ \vec{I}_{c1} \end{bmatrix} + \begin{bmatrix} \vec{I}_{a2} \\ \vec{I}_{b2} \\ \vec{I}_{c2} \end{bmatrix}, \tag{2.8}$$

where $\vec{I}_{a1}$, $\vec{I}_{b1}$, and $\vec{I}_{c1}$ are known as the positive-sequence set, $\vec{I}_{a2}$, $\vec{I}_{b2}$, and $\vec{I}_{c2}$ are known as the negative-sequence set, and $\vec{I}_{a0}$, $\vec{I}_{b0}$, and $\vec{I}_{c0}$ are known as the zero-sequence set. Thus, from symmetrical-component theory, an unbalanced three-phase set is resolved into two balanced three-phase sets (positive and negative sequence) and one zero-sequence set. Taking into account the symmetry of the positive- and negative-sequence sets, and the equality of the zero-sequence set, (2.8) can be written as [7]

$$\begin{bmatrix} \vec{I}_a \\ \vec{I}_b \\ \vec{I}_c \end{bmatrix} = \vec{I}_{a0}\begin{bmatrix} 1 \\ 1 \\ 1 \end{bmatrix} + \vec{I}_{a1}\begin{bmatrix} 1 \\ \alpha^2 \\ \alpha \end{bmatrix} + \vec{I}_{a2}\begin{bmatrix} 1 \\ \alpha \\ \alpha^2 \end{bmatrix} = \begin{bmatrix} 1 & 1 & 1 \\ 1 & \alpha^2 & \alpha \\ 1 & \alpha & \alpha^2 \end{bmatrix}\begin{bmatrix} \vec{I}_{a0} \\ \vec{I}_{a1} \\ \vec{I}_{a2} \end{bmatrix}, \tag{2.9}$$

where $\alpha = e^{\,j120°}$. The matrix in (2.9) is known as the symmetrical components transformation matrix [7]. The inverse relationship also exists, and is found by inverting the symmetrical components transformation matrix, with a final result given by

$$\begin{bmatrix} \vec{I}_{a0} \\ \vec{I}_{a1} \\ \vec{I}_{a2} \end{bmatrix} = \frac{1}{3}\begin{bmatrix} 1 & 1 & 1 \\ 1 & \alpha & \alpha^2 \\ 1 & \alpha^2 & \alpha \end{bmatrix}\begin{bmatrix} \vec{I}_a \\ \vec{I}_b \\ \vec{I}_c \end{bmatrix}. \tag{2.10}$$

It can be shown from (2.10) that if $\vec{I}_a$, $\vec{I}_b$, and $\vec{I}_c$ are a balanced and symmetrical set, then the negative- and zero-sequence components are zero. Thus, only the positive-sequence components are of interest under balanced, symmetrical conditions. The symmetry of the positive-, negative-, and zero-sequence sets simplifies the analysis of unsymmetrical three-phase systems by breaking the system up into two balanced systems and one zero-sequence system.

### *2.3.2. Sequence-Network Circuits*

Sequence-network circuits are a direct application of the symmetrical-component theory described in the previous section. Well-established positive-, negative-, and zero-sequence circuits of various power system components are available and given in [7] and [21]. For analyzing a fault on a particular point in a network, these equivalent sequence-network circuits of the interconnecting network are connected in various ways depending on the fault type, and calculations of the voltages and currents are performed on these per-phase sequence-network circuits. The actual phase currents flowing in the faulted network are then calculated using the symmetrical-components transformation matrix described in the previous section. It is shown in [7] how to connect the sequence-network circuits of a three-phase system under the various faults shown in Fig. 2.3. To

calculate the currents in the circuit of Fig. 2.3 under a SLG fault, the sequence-network circuit of Fig. 2.4 is used. The circuit of Fig. 2.4 is the per-phase equivalent circuit to calculate the symmetrical components of the fault currents flowing in the network of Fig. 2.3. Similarly, the sequence-network circuit for a LL fault is shown in Fig. 2.5. Sequence-network circuits for other types of faults are given in [7] and [21].

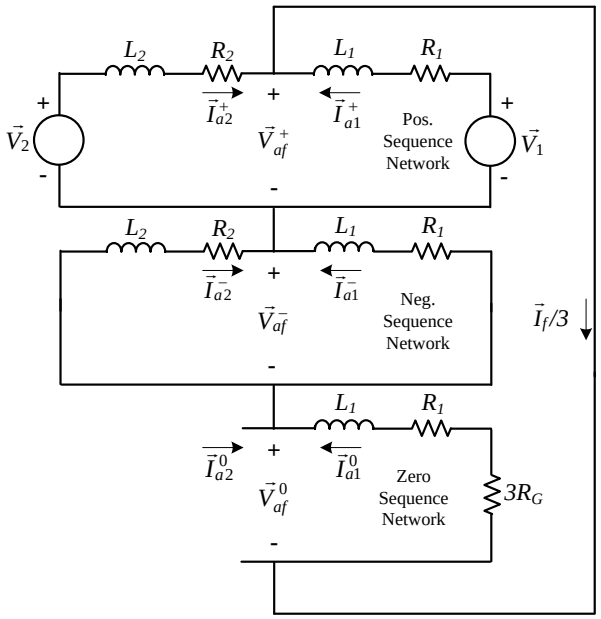


**Fig. 2.4: Sequence-network circuit for SLG fault.**

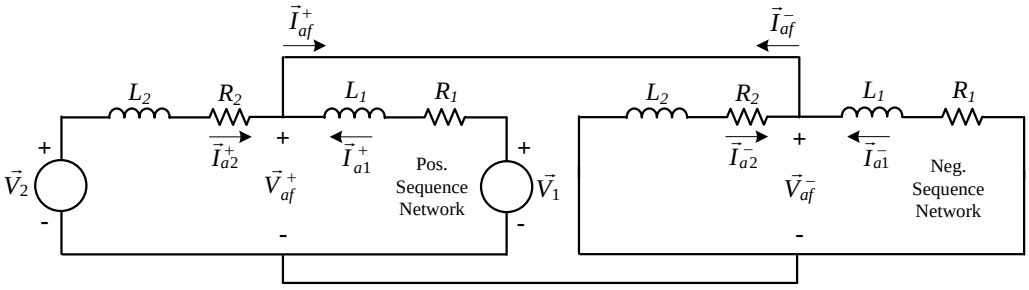


**Fig. 2.5: Sequence-network circuit for a LL fault.**

While standard sequence-network models are available for many power system components, such as transformers, transmission lines, synchronous machines, etc., well-established models of WTGs have not yet been formed, with the exception of the Type 1

WTG [10] [21]. In [22], a sequence-network model of a Type 3 wind plant is proposed for both balanced and unbalanced load-flow calculations. However, no such model has been developed for Type 3 WTGs for short-circuit analysis.

A brief review of induction machines is given in the next section, since these machines are used in WTG Types 1, 2, and 3. This discussion is followed by a review of sequence-network models developed in previous work of the Type 1 WTG.

## 2.4. Three-Phase Induction Machines

Three-phase induction machines are widely used today, predominantly as motors. WTG Types 1-3 use induction machines as a generator. A diagram of the physical winding layout of a three-phase induction machine is shown in Fig. 2.6 [8]. A set of three-phase windings is wound on the stator magnetic core as well as the rotor. The three-phase rotor windings rotate with the rotor shaft. Induction machines are classified as either squirrel-cage machines, where the rotor windings are short circuited through end rings directly on the rotor, or wound-rotor machines, where the windings are brought out from the rotor through brushes and slip rings. Type 1 WTGs are squirrel-cage induction machines and Types 2 and 3 are wound-rotor induction machines.

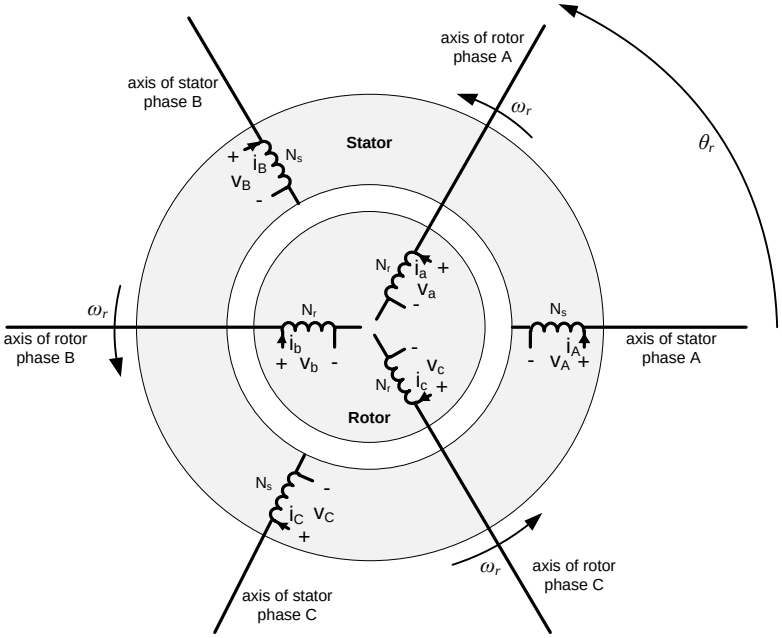


**Fig. 2.6: Three-phase induction machine winding configuration [8].**

The electrical dynamic equations describing the three-phase induction machine of Fig. 2.6 in physical (abc) variables [8] [23] are given by

$$\begin{array}{ll} \text{Stator} & \text{Rotor} \\ v_{as} = R_s i_{as} + p\lambda_{as} & v_{ar} = R_r i_{ar} + p\lambda_{ar} \\ v_{bs} = R_s i_{bs} + p\lambda_{bs} & v_{br} = R_r i_{br} + p\lambda_{br} \\ v_{cs} = R_s i_{cs} + p\lambda_{cs} & v_{cr} = R_r i_{cr} + p\lambda_{cr} \end{array}, \tag{2.11}$$

where $p = d/dt$, $R_r$ and $R_s$ are the stator and rotor winding resistances, and $\lambda$ is flux linkage. The flux linkages in (2.11) consist of self- and mutual-flux linkages between all the other windings; thus, the mutual-flux linkages between the stator and rotor windings depend on the rotor angle of rotation. If the induction machine is symmetrical, the dynamic equations can be greatly simplified from (2.11). These simpler dynamic equations are based on the two-axis theory of induction machines [8] [23], and are given by

$$\begin{array}{ll} \text{Stator} & \text{Rotor} \\ v_{ds} = R_s i_{ds} - \omega_p \lambda_{qs} + p\lambda_{ds} & v_{dr} = R_r i_{dr} - (\omega_p - \omega_r)\lambda_{qr} + p\lambda_{dr} \\ v_{qs} = R_s i_{qs} + \omega_p \lambda_{ds} + p\lambda_{qs} & v_{qr} = R_r i_{qr} + (\omega_p - \omega_r)\lambda_{dr} + p\lambda_{qr} \\ v_{0s} = R_s i_{0s} + p\lambda_{0s} & v_{0r} = R_r i_{0r} + p\lambda_{0r} \end{array} . \tag{2.12}$$

where the *abc* quantities are transformed to *dq0* quantities using the transformation given by

$$\begin{bmatrix} v_{ds} \\ v_{qs} \\ v_{0s} \end{bmatrix} = \frac{2}{3} \begin{bmatrix} \sin\theta_p & \sin(\theta_p - 120°) & \sin(\theta_p + 120°) \\ \cos\theta_p & \cos(\theta_p - 120°) & \cos(\theta_p + 120°) \\ 0.5 & 0.5 & 0.5 \end{bmatrix} \begin{bmatrix} v_{as} \\ v_{bs} \\ v_{cs} \end{bmatrix} . \tag{2.13}$$

where $\theta_p$ is the angle of the arbitrary reference frame rotating at frequency $\omega_p$. The stator currents and flux linkages are transformed using the same transformation. The rotor quantities are transformed using the same transformation, except the angle $\theta_p - \theta_r$ is used in place of the angle $\theta_p$. The *d* and *q* subscripts denote artificial direct- and quadrature-axis quantities obtained by transforming the sinusoidal three-phase quantities in the induction machine to a reference frame rotating at some arbitrary frequency $\omega_p$. The flux linkages in (2.12) are given by

$$\begin{array}{ll} \lambda_{ds} = L_s i_{ds} + L_m i_{dr} & \lambda_{dr} = L_r i_{dr} + L_m i_{ds} \\ \lambda_{qs} = L_s i_{qs} + L_m i_{qr} & \lambda_{qr} = L_r i_{qr} + L_m i_{qs} \\ \lambda_{0s} = L_{ls} i_{0s} & \lambda_{0r} = L_{lr} i_{0r} \end{array} , \tag{2.14}$$

where $L_m$ is the mutual (or magnetizing) inductance, $L_{ls}$ and $L_{lr}$ are the leakage inductances of the stator and rotor, and $L_s = L_{ls} + L_m$ and $L_r = L_{lr} + L_m$. The equations in (2.12) and (2.14) with a '0' subscript represent the zero-sequence component, and can often be neglected since the stator and rotor winding neutral points are typically left floating. Thus, the six dynamics equations in (2.11) with time-varying inductances are reduced to four dynamic equations in (2.12) (assuming the '0' components can be neglected) with constant inductances using the two-axis theory. This theory simplifies the steady-state analysis of induction machines and permits high-performance control techniques often used in Type 3 WTGs and Type 4 WTGs, as discussed in later sections.

The machine equations in (2.12) can alternatively be written in space-vector (complex) notation, given by

$$\begin{array}{cc} \text{Stator} & \text{Rotor} \\ \vec{v}_s = R_s\vec{i}_s + j\omega_p\vec{\lambda}_s + p\vec{\lambda}_s & \vec{v}_r = R_r\vec{i}_r + j(\omega_p - \omega_r)\vec{\lambda}_r + p\vec{\lambda}_r \end{array} \tag{2.15}$$

where the zero-sequence quantities have been neglected and

$$\vec{v}_s = v_{ds} + jv_{qs}\,. \tag{2.16}$$

Similar relationships exist between the other voltage, current, and flux-linkage space-vector quantities and the *dq* quantities. Both the *dq* notation and space-vector notation are used throughout this dissertation.

The real and reactive power delivered to an induction machine in terms of the *dq* notation are given by

$$\begin{aligned} P_s &= \frac{3}{2}(v_{qs}i_{qs} + v_{ds}i_{ds}) \\ Q_s &= \frac{3}{2}(v_{qs}i_{ds} - v_{ds}i_{qs}) \end{aligned}\,. \tag{2.17}$$

The mechanical differential equation governing the rotor speed is given by

$$Jp\omega_r = T_e - F\omega_r - T_L\,, \tag{2.18}$$

where $J$ is the rotor shaft inertia, $T_e$ is the electric torque developed by the machine, $T_L$ is the load torque, and $F$ is the friction constant. The electric torque developed by the machine can be expressed in terms of the *dq* currents as

$$T_e = \frac{3}{2}\frac{poles}{2}L_m(i_{qs}i_{dr} - i_{ds}i_{qr})\,. \tag{2.19}$$

## 2.5. Type 1 WTG Short-Circuit Behavior

### *2.5.1. Balanced Short Circuit*

A voltage-behind-reactance model of a squirrel-cage induction machine (SCIM) is described in [8] and [24], and is based upon the *theory of constant flux linkages*. This

theory is easily understood by examination of the rotor voltage equations in (2.15). Assuming a rotor reference frame ($\omega_p = \omega_r$) and neglecting the voltage drop across the rotor resistance, the rotor voltage equations can be written in complex notation as

$$0 = p\vec{\lambda}_r\,, \tag{2.20}$$

where the rotor voltages are zero in a SCIM since the rotor windings are short circuited. Equation (2.20) indicates that the rotor flux linkage cannot change instantly after a disturbance. Since the rotor resistance is actually non zero, the rotor flux does eventually change after a disturbance. Under this simplification, however, the rotor flux linkage immediately after the short circuit can be assumed unchanged from the rotor flux linkage before the short circuit. References [8] and [24] show that the stator voltage equations in (2.15) can then be written as

$$\vec{V}_s = R_s\vec{I}_s + jX_s'\vec{I}_s + \vec{V}'\,, \tag{2.21}$$

where $X_s$' is the *stator transient reactance* or just *transient reactance*, given by

$$X_s' = X_{ls} + \frac{X_{lr}X_m}{X_{lr} + X_m}\,, \tag{2.22}$$

and $\vec{V}'$ is known as the *voltage behind transient reactance,* which is directly proportional to the rotor flux linkages $\vec{\lambda}_r$ [8] [24]. Thus, from the constant flux linkage theorem, following a sudden change in the stator voltage $v_s$ the voltage behind transient reactance remains constant. Therefore, the voltage behind reactance model for the SCIM is based on (2.21), and shown in Fig. 2.7. This circuit is valid for a brief period following a short circuit before the rotor flux begins to decay.

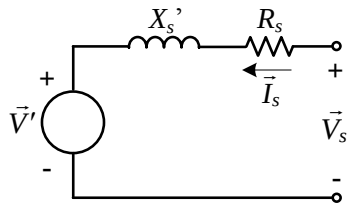


**Fig. 2.7: Voltage behind transient reactance model of induction machine.**

Some induction machines have specially designed rotors known as double-cage rotors or deep-bar rotors. For induction machines of this type, an additional sub-transient circuit is required in addition to the circuit of Fig. 2.7. Induction machines with this type of rotor are described in [25], and can be represented with a similar circuit as shown in Fig. 2.7 except using a *sub-transient reactance* and *voltage behind sub-transient reactance*.

The response of a SCIM to a three-phase short circuit at the machine terminals is discussed in [26]. A solution for the stator currents after the short circuit is derived from the dynamic equations, and found to follow the general form given by

$$i(t) = I_{tac} e^{-t/T_r'} \sin(\omega_s t + \theta) + I_{tdc} e^{-t/T_s'}, \tag{2.23}$$

where, in the development of this equation, it is assumed that the stator and rotor resistance can be neglected in the initial short-circuit calculation and the rotor speed is equal to synchronous frequency. Equation (2.23) indicates that the induction machine short-circuit currents consist of a decaying AC component and a decaying DC component. The decaying DC component is shown in [26] to depend on the instant the fault occurs. The time constants of decay in (2.23) are known as the rotor transient time constant, given by

$$T_r' = \frac{L_r'}{R_r}, \tag{2.24}$$

and the stator transient time constant, given by

$$T_s' = \frac{L_s'}{R_s}. \tag{2.25}$$

The rotor transient inductance $L_r$' in (2.24) is given by

$$L_r' = L_r - \frac{L_m^2}{L_s} = L_{lr} + \frac{L_{ls} L_m}{L_{ls} + L_m}. \tag{2.26}$$

Equation (2.23) indicates that the AC component of the short-circuit current decays approximately with time constant $T_r$'; thus, the voltage behind transient reactance in Fig.

2.7 decays with time constant $T_r$' since this is the voltage that drives this AC component in the short-circuit current.

### *2.5.2. Unbalanced Short Circuit*

The response of a SCIM during unbalanced faults is described in [27] using a similar approach as in [26], and the general form of the short-circuit current under an unbalanced fault is given as

$$i(t) = I_{tac} e^{-t/T_r'} \sin(\omega_r t + \theta) + I_{tdc} e^{-t/T_s'} + I_{ss} \sin(\omega_s t + \varphi). \tag{2.27}$$

The components $I_{tac}$, $I_{tdc}$, and $I_{ss}$ for the unbalanced fault case depend on the pre-fault voltage, post-fault positive-sequence voltage, and post-fault negative-sequence voltage at the machine terminals. This solution is reached by taking the pre- and post-fault steady-state conditions, and calculating a "natural" transient component which ensures continuity of the stator and rotor fluxes before and after the short circuit. The assumptions in this solution are that the winding resistances only contribute to the decay of the currents (and not the magnitude) and that the rotor speed $\omega_r$ is equal to synchronous frequency $\omega_s$ (slip $s$ = 0). Additionally, it is assumed that the pre- and post-fault voltages are known and fixed. The positive- and negative-sequence post-fault steady-state currents and fluxes are calculated in [27] using the sequence-network circuits shown in Fig. 2.8(a). The positive-sequence circuit in Fig. 2.8(a) is the regular per-phase steady-state equivalent circuit of an induction machine, and the negative-sequence circuit differs from the positive-sequence circuit by the slip [21], where the negative-sequence slip $s_n$ in the negative-sequence circuit is given by

$$s_n = \frac{-\omega_s - \omega_r}{-\omega_s} = 1 + \frac{\omega_r}{\omega_s} = 2 - s, \tag{2.28}$$

where the synchronous frequency in negative sequence is $-\omega_s$.

The voltage behind transient reactance model of the induction machine in Fig. 2.7 is used in the positive-sequence circuit for initial short-circuit calculations in unbalanced faults. The negative-sequence circuit is typically represented as an impedance equal to

the positive sequence impedance [21], as shown in Fig. 2.8(b). From the solution given in (2.27), the voltage behind transient reactance, in addition to the post-fault terminal voltage, drives the transient AC component of the current. The steady-state AC current remaining after transients have died away is independent of the initial flux before the fault, and is only driven by the post-fault terminal voltage.

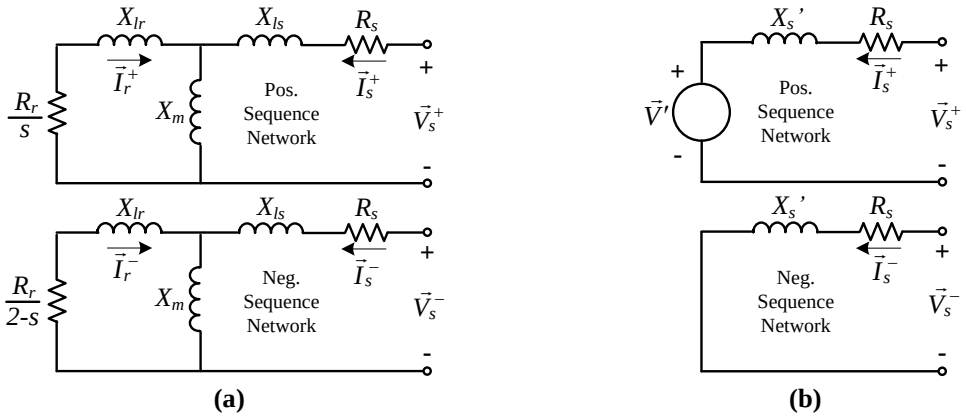


**Fig. 2.8: Positive and negative sequence circuits of induction machine (a) for steady-state and (b) initial short-circuit calculations.**

Short-circuit calculations of a Type 1 wind farm are carried out in [28] for the purpose of finding an equivalent voltage behind reactance representation for an entire wind farm. Short-circuit calculations are performed in DigSilent software, where the induction machines are represented as a 1 pu voltage source behind the machine's locked-rotor impedance. The short-circuit currents calculated from the entire wind farm are used to calculate an equivalent impedance of the wind farm that can be used in series with a 1 pu voltage to calculate the short-circuit currents into the interconnecting transmission network. However, the calculated currents from the developed equivalent circuit were not compared against detailed transient simulations to see the accuracy of the proposed model.

## 2.6. Type 2 WTG Short-Circuit Behavior

The variable rotor resistance of the Type 2 WTG is achieved by modulating the insulated-gate bipolar transistor (IGBT) switch shown in Fig. 2.9 [16]. The combination of the external resistance $R_{ext}$ in Fig. 2.9 and the IGBT modulation produce an effective rotor resistance $R_{r,eff}$. If the IGBT has a duty cycle $D$ of 100%, the switch stays on and the Type 2 WTG resembles the Type 1 WTG since the rotor windings are short circuited. If the duty cycle is 0%, all the rotor current flows through the fixed external resistance. In [13] and [16], the duty cycle of the IGBT switch is reportedly controlled as shown in Fig. 2.10. The inner current control loop consists of a PI controller which drives the error between the rotor current magnitude command and the actual rotor current magnitude to zero. The rotor current command is generated by the outer control loop, which consists of another PI controller which drives the error between the power output reference and the measured power output to zero.

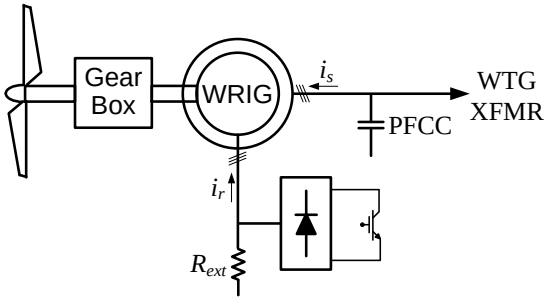


**Fig. 2.9: Circuit diagram of Type 2 WTG.**

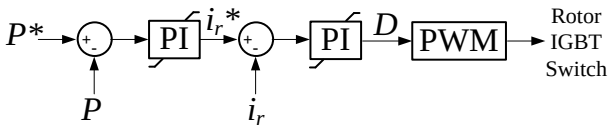


**Fig. 2.10: Control diagram of Type 2 WTG.**

Different control techniques of the rotor resistance during faults have been reported in literature. In [16], it is assumed that the inner current loop in Fig. 2.10 drives the duty cycle of the IGBT switch to zero fast enough that all the rotor current flows through the external rotor resistance during a fault. In other words, a short circuit on the grid causes the rotor current to sharply increase, which causes the inner current loop PI controller output to decrease. However, in [14, 29, 30], it is implied that the rotor resistance is not controlled during short-circuit conditions. The case of no external rotor resistance (duty cycle = 100% in Fig. 2.9) is simply taken to be the worst-case scenario. In either case, the time constant of decay in the AC component of the short-circuit current can be approximated by [14]

$$T_r' = \frac{L_r'}{R_{r,eff}}. \tag{2.29}$$

This time constant of decay is similar to that of the Type 1 WTG given in (2.24), except that $R_{r,eff}$ depends on the rotor winding resistance, the external resistance, and the IGBT control. The Type 2 WTG is assumed to behave similarly to the Type 1 in all aspects with the exception of the time constant in (2.29). Under this assumption, short-circuit calculations can be carried out in a similar way for the Type 2 as described in the previous section for the Type 1, and is typically assumed to behave as a Type 1 as a worst-case scenario.

## 2.7. Type 3 WTG

The Type 3 WTG provides numerous benefits over Types 1 and 2, including [31]

- Higher energy yield.
- Less mechanical stress to generator drive train during wind gusts.
- Improved power quality, including dynamic reactive power compensation.

A brief overview of the Type 3 WTG system is given in this section, along with a review of previous work regarding the response of these systems to short-circuit faults. This

section also includes a review of the electrical controls of the Type 3 WTG, since these controls significantly affect the response of this type of WTG.

### *2.7.1. Overview of Type 3 WTG System*

A circuit diagram of a Type 3 WTG is shown in Fig. 2.11. The grid-side converter (GSC) and rotor-side converter (RSC) are three-phase inverters [13] [32] connected together through a DC link. Each converter contains IGBT switches controlled by a pulse-width modulation (PWM) scheme. The RSC is connected to the three-phase rotor windings of the wound-rotor induction generator (WRIG). The GSC is connected to the stator terminal voltages of the WRIG. The back-to-back GSC and RSC fulfill various control objectives, as discussed in the next sections. Power can flow in both directions through the converter depending on the operating speed of the WRIG. The AC crowbar and DC chopper are designed to protect the RSC and DC link capacitor from overcurrent and overvoltage conditions, respectively. The control of the RSC, GSC, AC crowbar, and DC chopper all affect the short-circuit behavior of the Type 3 WTG, and are discussed in the following sections.

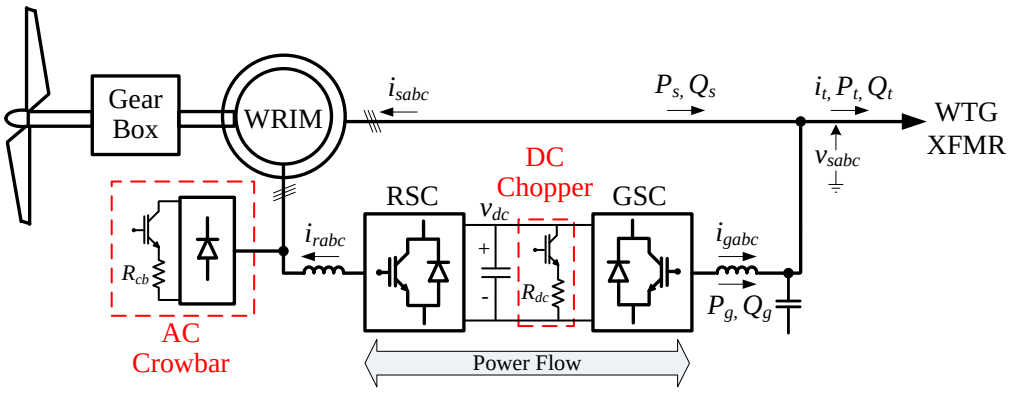


**Fig. 2.11: Circuit diagram of Type 3 WTG.**

### *2.7.2. Effects of RSC Voltage Limitations*

During steady-state and balanced conditions, the per-unit RSC voltage magnitude is a function of the slip, given by [33]

$$V_r = |s| V_s . \tag{2.30}$$

Since the Type 3 WTG operates in a range of slip from -0.3 to 0.3, the rated voltage of the RSC only needs to be roughly 0.3 per unit (assuming the stator voltage is one per unit). In practice, this RSC rated voltage is slightly higher than this for better dynamic controls of the rotor current [33], but the rated voltage of the RSC is intentionally designed to be as low as possible to save on the cost of the power electronics. However, much higher voltages are induced in the rotor windings during three-phase faults [33] [34] [35] and unbalanced faults [36] [37]. During these conditions, high currents can flow in the rotor windings and the RSC, which can possibly damage the RSC components if not properly protected. Hence, various methods for protecting the RSC from these over-voltage conditions have been devised, and are often referred to as "crowbar" circuits.

### *2.7.3. RSC Protection*

Protection techniques of the RSC can be categorized into four cases, as described in Table 2.1. Before grid-code requirements were imposed on wind plants, the AC crowbar circuit of Type 3 WTGs would turn on during a voltage dip and remain on until the wind plant tripped offline [38] or until the voltage recovered. Case 1 in Table 2.1 identifies this protection technique. A grid voltage dip causes the stator current to increase, which also causes the rotor current to increase due to the electromagnetic coupling. Turning the AC crowbar on while also disabling the RSC IGBT gate signals diverts this high rotor current away from the RSC. The short-circuit behavior of Type 3 WTGs in this case has been analyzed in [26] and [27] assuming the crowbar is applied

immediately after the short circuit occurs. Under this protection technique, the Type 3 WTG behaves like a Type 1 or Type 2 WTG since the rotor windings are short-circuited and the RSC is disabled. Rotor current control interruptions can be reduced by applying the AC crowbar for short periods of time during the voltage dip until the rotor current has decayed, and then re-enabling the RSC [39]. This technique (Case 2 in Table 2.1) may cause the AC crowbar circuit to turn on and off several time during the short circuit, resulting in highly non-linear behavior of the stator currents during the fault [38].

Some Type 3 WTG designs do not contain AC crowbar circuits, but implement the same function of the AC crowbar using a DC chopper circuit (Case 3 in Table 2.1) [16]. In this case, the RSC control is disabled during the fault, and the induced currents flow through the diode rectifier of the RSC. The DC chopper dissipates the excess power in the resistance.

Some control techniques for the RSC have been proposed to reduce the currents flowing in the rotor circuit during faults, thus allowing un-interrupted control of the rotor currents during a short circuit [40] (Case 4 in Table 2.1). Performing this type of control requires a RSC with oversized IGBT modules. In this case, the controls of the RSC dominate the response of the WRIG stator currents during the short-circuit fault. The RSC controls that perform this function are described in the next section.

**Table 2.1: Various RSC protection techniques in the Type 3 WTG.**

| | Case | Description |
|---|---|---|
| With AC Crowbar | 1 | AC crowbar is enabled at the onset of the fault and remains enabled for the duration of the fault with the RSC disabled [26] [27] |
| | 2 | AC crowbar is enabled at the onset of the fault, and is discontinuously enabled and disabled for the duration of the fault as the rotor current magnitude crosses an upper and lower threshold [39] [38] |
| Without AC Crowbar | 3 | DC chopper circuit is enabled after the fault while the RSC is disabled [16] |
| | 4 | RSC maintains control of the rotor currents during the fault with no interruption [40] |

### *2.7.4. Control of GSC and RSC*

Control of the RSC and GSC is often performed using vector control techniques originally applied to AC motor control [24]. Control of the RSC in Type 3 WTGs often involves transforming the stator voltages, stator currents, and rotor currents to a synchronous *dq* reference frame with the d-axis aligned with the stator flux [41] [42] or stator voltage [31] [43]. A stator voltage orientation is normally chosen for the GSC control signals [41] [42]. The control signals for the RSC and GSC are obtained as shown in Fig. 2.12 assuming a stator-flux-oriented synchronous reference frame is used for the RSC and a stator-voltage-oriented reference frame is used for the GSC. The DC-link voltage is also measured, but is not shown in Fig. 2.12.

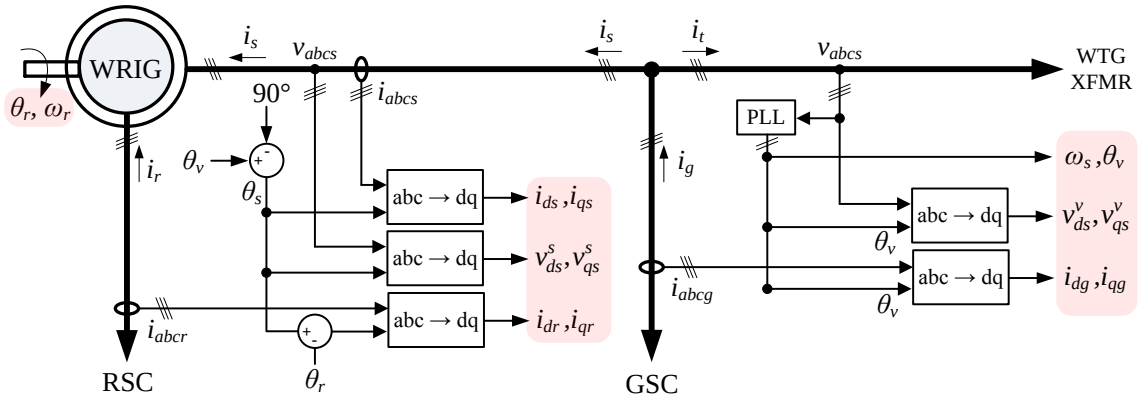


**Fig. 2.12: Control signal measurement and calculation for RSC and GSC.**

Independent control of the d- and q-axis components of the GSC current can be implemented in Type 3 WTGs using feed-forward compensation terms in the control loops [33] [41], as shown in Fig. 2.13. The inner current loops controlling the GSC currents $i_{dg}$ and $i_{qg}$ have a much higher bandwidth than the outer control loops for the DC-link voltage $V_{dc}$ and reactive power $Q_g$. The reactive power delivered by the GSC is proportional to $i_{qg}$ under steady-state conditions [41], and in some cases the outer control loop for the reactive power in Fig. 2.13 is eliminated and either a zero or constant control

reference for $i_{qg}$ is applied [42]. The signals used for control in Fig. 2.13 are obtained as shown in Fig. 2.12.

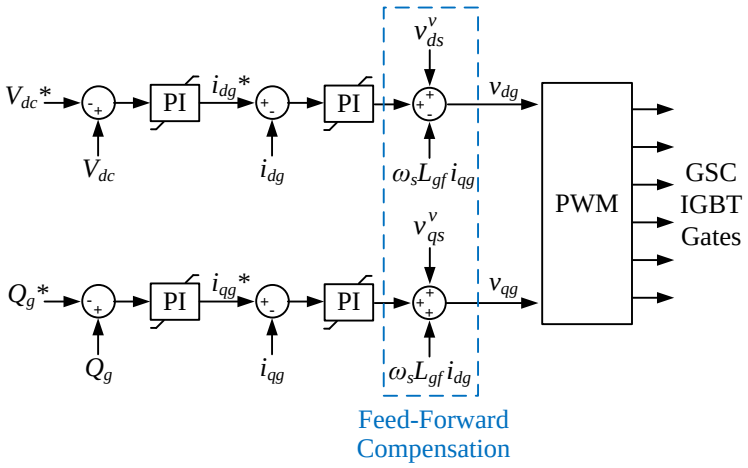


**Fig. 2.13: Control diagram of GSC in Type 3 WTG.**

A similar feed-forward compensating controller is typically used for the RSC to enable decoupled control of the d- and q-axis components of the rotor current [33] [41]. A block diagram of the RSC control is shown in Fig. 2.14. Similar to the GSC, high-bandwidth inner current loops are present in the RSC for controlling the d- and q-axis rotor currents $i_{dr}$ and $i_{qr}$. The outer control loop for the reactive power can be eliminated and replaced by a constant q-axis rotor current command [42]. The outer control loops can alternatively be used to control the real power and terminal voltage, instead of the rotor speed and reactive power, respectively.

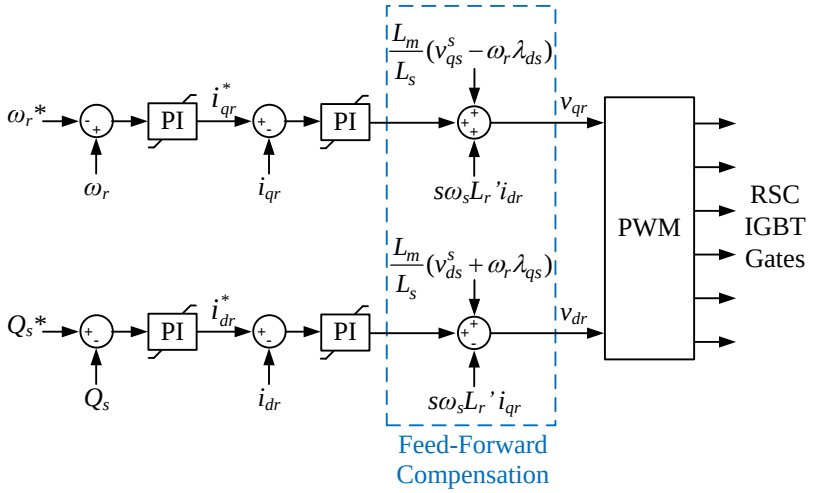


**Fig. 2.14: Control diagram of RSC in Type 3 WTG.**

In steady-state conditions, the d- and q-axis control quantities in Fig. 2.13 and Fig. 2.14 are DC quantities, which is ideal for control purposes. However, under unbalanced conditions, a second harmonic component appears in the d- and q-axis currents and voltages due to the presence of negative sequence [40]. The negative-sequence current and voltage cause second harmonic ripples in the electromagnetic torque, real power, reactive power, and DC-link voltage [43] [44]. Torque oscillations cause additional wear on the WTG drive train, and power oscillations are undesirable for power quality reasons. The controls shown in Fig. 2.13 and Fig. 2.14 are intended to only control the positive-sequence (DC) quantities. Therefore, various improvements in the WTG controllers have been developed to limit the negative-sequence currents that flow in the Type 3 WTG.

Several control techniques have been proposed to limit the negative-sequence currents in the Type 3 WTG. In [43], feed-forward control loops for the RSC are designed to reduce the second-harmonic ripple in the electric torque and WRIG reactive power by injecting a negative-sequence voltage control signal into the RSC voltage control signal. This negative-sequence voltage control signal is obtained using an additional control loop with the desired second harmonic torque as a reference (set to

zero) and a feedback component which consists of the calculated torque which has been passed through a band-pass filter centered at second harmonic. Thus, this additional control loop is only active under unbalanced conditions, i.e. when second harmonic is present in the torque. In [44] and [45], the positive- and negative-sequence components of the rotor currents and GSC currents are controlled separately. The positive- and negative-sequence components of the current are extracted from the measured quantities using two synchronous reference frames, one rotating in the positive direction and the other rotating in the negative direction. The number of current controllers doubles when using this scheme since positive- and negative-sequence currents must be controlled for each of the d- and q-axis currents. Proportional-integral-resonant (PIR) controllers have been proposed [40] [46] to control the negative-sequence currents in the inner current loops. In this technique, a resonant path is inserted in parallel with the positive sequence PI controller shown in Fig. 2.14. The resonant frequency of this controller is set at the second harmonic, and thus only operates when negative-sequence currents are present. The gain and phase angle of the closed-loop system are set to have unity gain and approximately zero phase shift at second harmonic. A PIR controller is implemented in [40] which has two resonant paths: one for the 120 Hz component caused by negative-sequence currents and one for the 60 Hz component induced by temporary DC components in the rotor currents that occur after disturbances. This controller decreases the high rotor currents caused by both unbalanced conditions and transient conditions, thus reducing the need for crowbar interruptions.

The control of the negative-sequence currents in the Type 3 WTG using any of the above mentioned control schemes is severely limited, however, due to the limitations of the RSC voltage [37] [47]. Complete control of the negative-sequence currents in the DFIG for unbalanced faults would require a RSC with a much higher voltage rating than 30% of the induction machine's rated rotor voltage, which is unfavorable due to the increase in cost of such a converter.

### *2.7.5. Short-Circuit Behavior*

The short-circuit characteristics of Type 3 WTGs have been studied through transient simulations in [14], [29], [16], and [38]. However, no details of the modeling and control of the WTG are given in those studies. Approximate values for the maximum and minimum short-circuit currents contributed by a Type 3 WTG are given in the form of simplified equations [14] or lookup tables as a function of the system voltage [38] in those studies. Detailed analysis of a Type 3 WTG under balanced faults and unbalanced faults has been described in [26] and [27], respectively, for the special case that the crowbar activates immediately after the fault and remains activated. In each of these papers, closed-form solutions are given for the short-circuit currents of the Type 3 WTG without considering the contribution of the GSC currents. In practice, however, the GSC currents must also be considered since additional currents are injected by the GSC during the fault.

## 2.8. Type 4 WTG

Type 4 WTGs encompass the same advantages over the Type 1 and 2 WTGs as the Type 3, including a wide operating-speed range and higher energy yield. The Type 4 WTGs achieve the variable-speed operation using a fully-rated power electronic converter in series with the generator, as shown in Fig. 2.15. The advantage of the Type 4 WTG configuration over the Type 3 is that the gearbox can sometimes be eliminated, which improves the overall turbine efficiency and reduces maintenance costs [48]. Additionally, the short-circuit current contributed by Type 4 WTGs can be limited to roughly 1.1 to 1.4 pu [49] [50]. However, the generator and fully-rated power electronics generally result in a higher initial cost when compared with the Type 3.

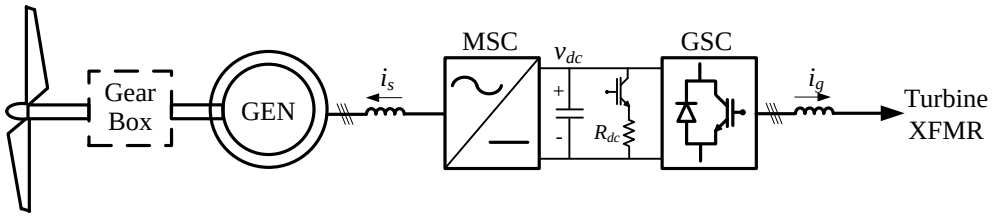


**Fig. 2.15: General Type 4 WTG topology.**

The power electronics convert the fixed-voltage, fixed-frequency grid voltage into variable voltage, variable frequency for the generator stator windings. For this reason, many types of generators can be used in the Type 4 configuration, including induction machines, wound-rotor synchronous machines, and permanent-magnet synchronous machines [13]. Additionally, the machine-side converter (MSC) in Fig. 2.15 can be a three-phase inverter [51] or a diode rectifier with DC-DC converter [52]. Because the generator is decoupled from the grid through the power-electronic converter, the response of the Type 4 WTG to short-circuit faults on the grid is based on the control of the grid-side converter (GSC) [49] [50].

Under balanced conditions, the GSC of the Type 4 WTG is controlled in the same way as the GSC of the Type 3 WTG. Thus, the positive-sequence controller for the GSC of the Type 4 is given by the GSC control already described in the previous section and shown in Fig. 2.13 [16] [53] [54]. However, under unbalanced conditions, some manufacturers design the controls of the Type 4 GSC to output only positive-sequence currents [49] [50] to reduce oscillations in the DC-link voltage and power output of the WTG. This type of control can be achieved in the Type 4 in similar ways described for the Type 3, such as using separate controllers for the positive- and negative-sequence currents in the vector control scheme [51]. During the first cycle following a fault, the GSC output may reach 2.5 pu in magnitude, but the controller quickly enters current-limiting mode, which generally limits the current output between 1.1 and 1.4 pu [49] [50]. In the case where the Type 4 WTG outputs only positive-sequence current, the

negative- and zero-sequence circuits can simply be represented as open circuits and as a current source in the positive-sequence circuit with a magnitude equal to the current limit set by the manufacturer [49]. With this type of model, the primary problem is determining the proportion of the real and reactive components (magnitude and phase angle) of this current source.

## 2.9. Wind Plant Collector System

A one-line diagram of a typical wind plant collector system is shown in Fig. 2.16. The wind plant collector system is made up of WTG transformers, cables, and substation transformers, among many other components, including switchgear and protection equipment. A brief description of these components is presented below.

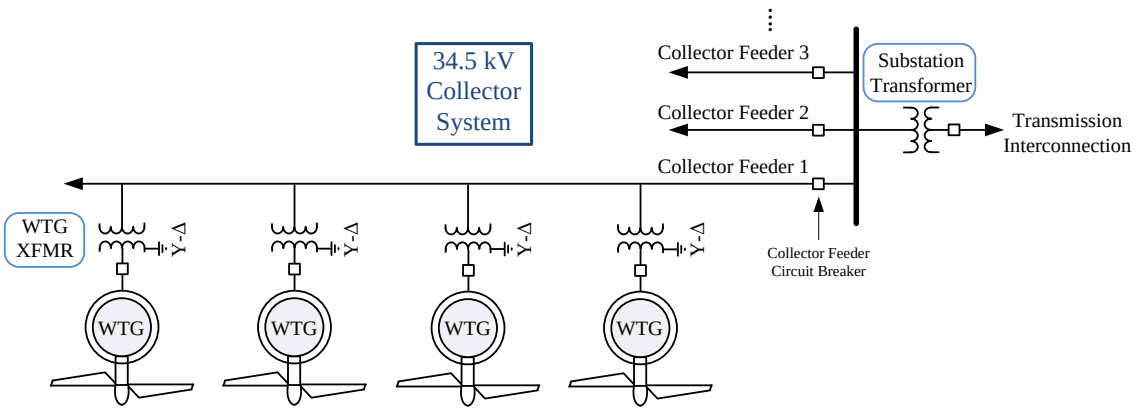


**Fig. 2.16: Typical wind plant collector system.**

### *2.9.1. WTG Step-Up Transformer*

The WTG step-up transformer connects the low-voltage (LV) WTG terminals to the medium-voltage (MV) collector system (typically 12.1 - 34.5 kV). This transformer can either be in the nacelle of the turbine or at the base of the turbine. The most common winding connection for this transformer is grounded wye on the LV side and delta on the MV side, although other connections have been reported [12] [11]. The reason for this

particular connection is to provide grounding for the LV side and to isolate the WTG from the collector system zero-sequence behavior [12]. Common values of the WTG step-up transformer impedance are 5%-6% of the transformer's base impedance [11] [12].

### *2.9.2. Collector Cables*

The wind plant collector cables connect the WTG step-up transformers to the wind plant main substation transformer. These cables are often direct-buried underground cables, but can also be overhead cables [12] [55]. The conductor sizes of the collector cables are based on the number of WTGs connected to a particular cable and the soil resistivity [11] [12]. A wind plant may have several different conductor sizes on a single collector feeder [11], with the conductors decreasing in size towards the end of the feeder (toward the last WTG on the feeder). An underground collector cable can be several miles in length, and can have significant distributed capacitance [11].

### *2.9.3. Substation Transformer*

Most wind plants today connect to a high-voltage (HV) transmission system. The wind-plant substation transformer steps up the MV collector system to the HV transmission system. The substation transformer MVA rating can sometimes be less than that of the entire wind farm since the transformer is usually only under partial load [56]. The winding configuration of the substation transformer varies among wind plants, and is often determined based on the interconnecting transmission operator's requirements, particularly regarding ground-source and zero-sequence-isolation requirements [56] [57]. The substation transformer is typically required to provide grounding for both the transmission system and collector system. Common winding configuration options for the substation transformer are shown in Table 2.2. The Y-Δ and Δ-Y options provide complete zero-sequence isolation of the MV and HV systems, but leave either the MV

system ungrounded or provide no ground source for the HV system. Thus, these types of transformers often require additional grounding transformers on either the MV or HV system [56] [57] [58]. The Y-Y configuration provides no ground source for the transmission system nor zero-sequence isolation of the MV and HV system, except when particular transformer core designs are used [56] [57]. The Y-Δ-Y configuration is the most common winding connection because it provides a ground source for both the MV and HV system, and provides some zero-sequence isolation between the systems [56] [57].

**Table 2.2: Substation transformer winding options and zero-sequence circuits [57].**

| Winding Configuration | Zero-Sequence Circuit | Zero-Sequence Isolation? | MV Ground Source? | HV Ground Source? |
|---|---|---|---|---|
| 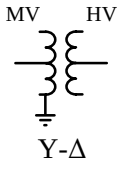 Y-Δ | 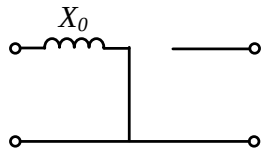 | Yes | Yes | No |
| 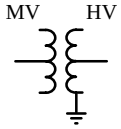 Δ-Y | 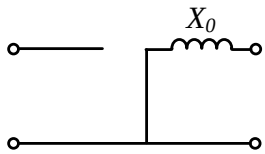 | Yes | No | Yes |
| 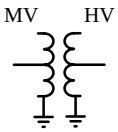 Y-Y | 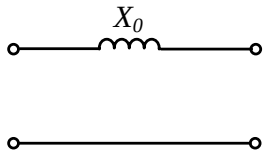 | No | No | No |
| 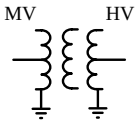 Y-Δ-Y | 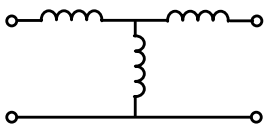 | No | Yes | Yes |

## *2.9.4. Collector System Protection*

The protection objectives of a wind-plant collector system are no different than the protection objectives of any other electrical system. Namely, these objectives include

(but are not limited to) preventing damage to collector system components and preventing injury to wind-plant personnel, while achieving these objectives in an economical manner. This means the protective relays should operate when needed and *only* when needed. In other words, the protective relay should not operate incorrectly under normal conditions or for faults outside its realm of protection.

The general zones of protection in a wind plant are classified [59] as the utility interconnection, substation, collector cables, and WTGs. The protective relaying functions used in each of these zones of protection are discussed in detail in [59] and [60], and typically consist of instantaneous overcurrent, time overcurrent, differential, directional, impedance, distance, over/under voltage, and frequency relaying functions, among others. In [61], simulation studies were performed on an offshore wind farm with a long, radial transmission interconnection, and it was found that some impedance, overcurrent, and distance protective relaying functions did not operate correctly for some types of faults on the transmission interconnection.

A specific condition addressed in literature involves the case of a phase-to-ground fault on the collector system cables within the wind plant, which can cause severe over voltages on the unfaulted phases during the fault [58] [62] if the collector system is not effectively grounded. Overvoltages can also occur if the collector feeder breaker trips in response to a ground fault inside the wind plant, and the WTGs continue "feeding" the fault after the breaker has tripped. This condition results in particularly severe overvoltages if the collector system has no ground reference after the breaker trips, in which the distributed cable capacitance causes the unfaulted phase voltages to rise further [62]. For this reason, careful coordination between the wind-plant grounding scheme and arrestor selection is required to prevent damage to the system caused by these overvoltages [62].

### *2.9.5. Phasor Estimation in Protective Relays*

Modern protective relays estimate the voltage and current phasors of the system based on sampled data collected from instrument transformers. Numerical techniques have been developed to estimate the phasor values of the voltages/currents based on these data samples [63] [64]. These techniques are intended to calculate *steady-state* phasor quantities, and provide only a rough approximation to the phasor quantity of a voltage/current during a transient. A cosine filter algorithm [63] is used in this research to determine the phasor values of the voltages and currents during a short-circuit transient, and a summary of this technique is given in this section.

A cosine filter algorithm is often implemented in modern digital relays to extract the fundamental-frequency components of measured currents and voltages [63] [64]. The cosine filter output is calculated by

$$i_f[k] = \frac{2}{N}\sum_{n=1}^{N} i_m[k-N+n]\cos\left(\frac{2\pi(n-0.5)}{N}\right), \tag{2.31}$$

where $i_f$ is the digital filter output, $i_m$ is the sampled signal, and $N$ is the number of samples per cycle, which is commonly 16. The corresponding phasor can be found from the output of the cosine filter using

$$I_c[k] = \frac{1}{\sqrt{2}}\left(i_f[k] + j\frac{i_f[k-1] - i_f[k]\cos(\omega\Delta T_s)}{\sin(\omega\Delta T_s)}\right), \tag{2.32}$$

where $I_c$ is the calculated phasor, $\Delta T_s$ is the sampling period, and $\omega$ is the frequency of the signal. The output of (2.32) is a rotating phasor estimation of the sampled signal.

As an example of the phasor calculation from (2.31) and (2.32), take the arbitrary waveform defined by the following equation:

$$x(t) = \begin{cases} \sqrt{2}\sin(\omega t + 60°), & t \le 0 \\ 5e^{-t/0.05} - 8\sqrt{2}e^{-t/0.05}\sin(\omega t + 30°), & t > 0 \end{cases}. \tag{2.33}$$

This waveform is displayed in Fig. 2.17(a). Note that this waveform consists of a decaying DC component and a decaying AC component, which is *qualitatively* similar to the short-circuit-current waveforms from an AC machine. Assuming a sampling rate of 16 samples per cycle, the output of the cosine filter of (2.31) at a point in time is based upon the most recent sampled data point and the 15 previous data points collected. Thus, the calculation is made using a "sliding window" approach. The magnitude of the AC component (RMS value) of $x(t)$ in (2.33) is known to be

$$\left|\vec{X}(t)\right| = \begin{cases} 1, & t \le 0 \\ 8e^{-t/0.05}, & t > 0 \end{cases}. \tag{2.34}$$

This value is plotted in Fig. 2.17(b), along with the output of the phasor estimation algorithm using the cosine filter of (2.31) on the sampled data and then calculating the phasor quantity using (2.32). The phasor estimation technique provides a rough estimate of the phasor magnitude of this arbitrary waveform. However, this algorithm is very good at estimating the phasor magnitude during steady state (provided the signal oscillates at 60 Hz), as shown in Fig. 2.17(b) before $t = 0$. When the "transient" occurs in the waveform, the calculated phasor provides only a rough estimate of the phasor magnitude.

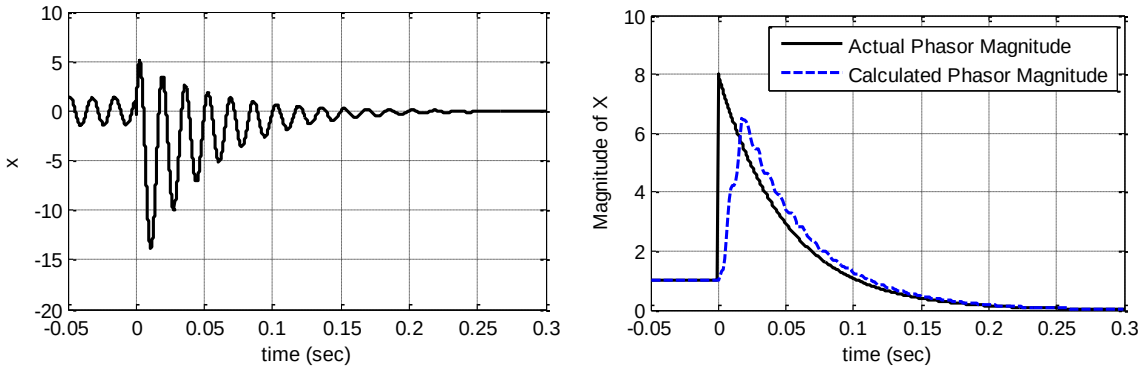


**Fig. 2.17: Phasor estimation of a transient signal. (a) Arbitrary transient signal and (b) comparison of actual and estimated RMS magnitude of signal.**

## 2.10. Conclusions

Commercially-available short-circuit and protection software uses models and equations derived from existing standards from IEEE or other governing organizations. These models have been well-established and proven effective for many years, particularly for conventional power system components such as synchronous generators. However, because newer technologies are being introduced into the power system at higher rates, the existing standard models are not adequate to represent these new technologies, particularly wind turbines based on Type 3 and Type 4 technology. Therefore, new models that adequately represent these types of wind turbines are required.

The previous research by others on the short-circuit behavior of the Type 3 WTG has focused on the control of the RSC and GSC during balanced and unbalanced faults. The objective of those studies was to reduce the torque oscillations, reduce the AC crowbar interruptions, reduce the negative-sequence currents, and improve the low-voltage ride through capability of Type 3 WTGs. However, little attention has been given to the effects of the Type 3 WTG controls on the protective relaying in power systems, particularly on how to model these types of wind turbines in commercial short-circuit software that uses frequency-domain (sequence-network) analysis. Previous work investigating the short-circuit contribution of WTGs has focused on transient simulation studies, which, in general, are much too detailed for protection studies and only give the time-domain behavior of the WTGs. Therefore, it is not straightforward to obtain insight into the positive-, negative-, and zero-sequence behavior of the system using transient simulations.

A short-circuit model for the Type 3 and Type 4 WTGs must account for the controls of the WTG, but must not require proprietary control information that a WTG manufacturer may be reluctant to provide. Such a "generic" model, which would be

suitable for protection-software calculations, has not been established in current literature or by standards organizations. Thus, the goal of this research is to develop short-circuit models of these types of WTGs appropriate for phasor calculations using sequence-network circuits.

# CHAPTER 3: TYPE 1 AND 2 WIND-TURBINE GENERATORS

## 3.1. Introduction

The short-circuit behavior of induction machines has been discussed thoroughly in previous literature. Therefore, the primary goal of this chapter is to verify the existing short-circuit models of wind-turbine generators (WTGs) using induction machines, which include Types 1 and 2. Because the governing principles behind the short-circuit behavior of Type 1 and Type 2 WTGs are the same, they are discussed in conjunction in this chapter. The initial analysis presented in this Chapter is focused on the Type 1 WTG; but, at the end of the Chapter, transient simulation results of a small wind farm of Type 2 WTGs are provided. These results are compared with calculations using the same short-circuit model for the Type 2 as the Type 1 WTG, except the high rotor resistance of the Type 2 is accounted for in the calculations.

Comparisons of experimental short-circuit tests, power system computer aided design (PSCAD) transient simulations, and sequence-network calculations for Type 1 WTGs have been performed and are described in this chapter. It is found that, in most cases, the conventional sequence-network model of Type 1 and Type 2 WTGs gives satisfactory results for short-circuit calculations of WTGs of this type. However, some of the simplifying assumptions made in the conventional sequence-network model may not give satisfactory results in some cases. Two effects that are not considered in the conventional sequence-network model are investigated in this chapter, and they include leakage-flux saturation in the induction machine and the negative-sequence voltage induced in the machine during unbalanced faults.

## 3.2. Comparison of Transient Simulation Software Packages

One of the primary tools engineers use to analyze the short-circuit currents in WTG networks is electromagnetic transient (EMT) simulation software. Many EMT simulation packages are commercially available, and all have their distinct advantages and disadvantages. Additionally, different software packages use different numerical integration methods to iteratively solve the nonlinear differential equations of the induction machine. Most simulation packages represent the induction machine dynamic equations in the *dq* notation discussed in the previous chapter. In practice, the stator winding neutral point is rarely grounded; therefore, the zero-sequence components in the induction machine dynamic equations are sometimes neglected. As an initial study, three transient simulation packages were compared: PSCAD/EMTDC, SimPowerSystems, and EMTP-RV. The purpose of this study was to verify that these simulation packages give the same results for various types of faults on the induction machine. The results of this study are shown in Fig. 3.1. The phase A stator and rotor current waveforms of the induction machine are shown in Fig. 3.1(a) for the case of a three-phase fault at the machine terminals. Similarly, the results for a single-phase-to-ground fault are shown in Fig. 3.1(b). In each case, the induction machine is run with no mechanical load and an ideal voltage source is connected to its terminals (with no additional impedance). The fault is manually applied to the machine by programming the voltage source to be set to zero at a specific time in the simulation. For the single-phase fault case, only the faulted phase was set to zero, while the other phases remained unchanged. The stator winding neutral point was left floating in these studies; thus, no zero-sequence current flows in the induction machine. Good agreement between the transient waveforms of the different simulation packages can be seen in the results in Fig. 3.1. It was found from these studies, however, that using a simulation time step of less than 10 microseconds results in the best agreement among the different software packages.

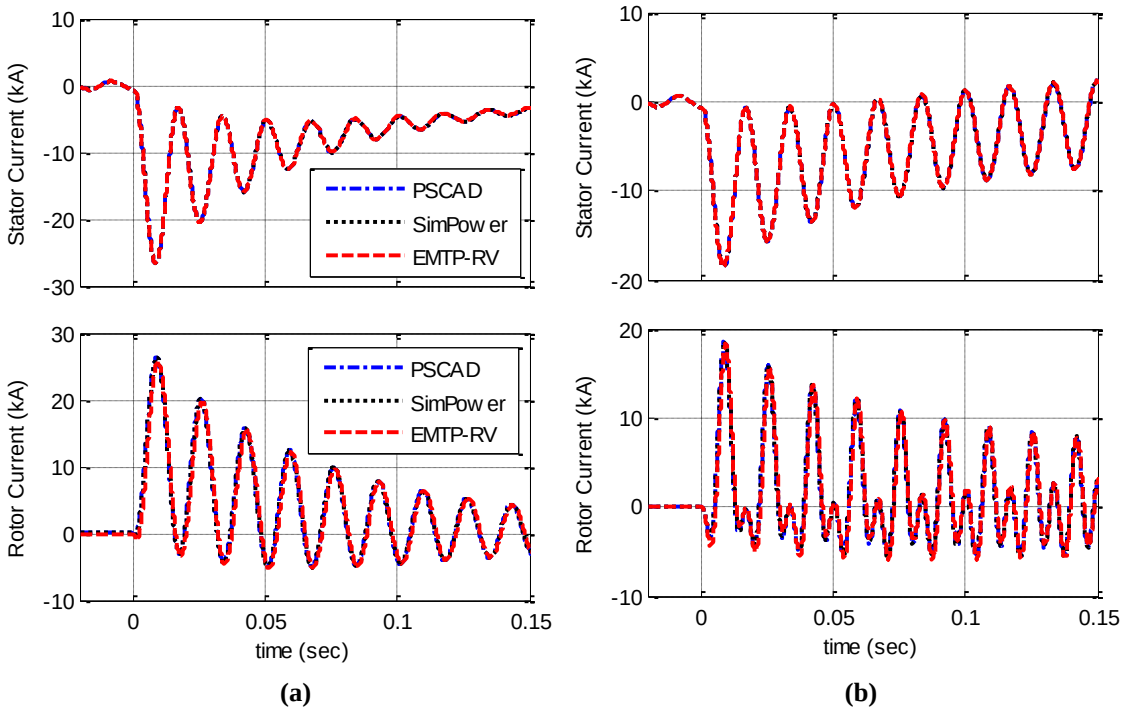


**Fig. 3.1: Comparison of transient simulation results in PSCAD, EMTP-RV, and SimPowerSystems for a (a) three-phase fault and (b) single-phase fault.**

## 3.3. Comparison of Transient Simulations and Sequence-Network Calculations

Transient simulation software is a detailed and accurate tool for representing the short-circuit characteristics of WTGs. However, the goal of this research is to develop RMS, phasor-type models of WTGs for short-circuit calculations. Because phasor-type calculations are based on the assumption of steady-state conditions, attempting to represent the short-circuit behavior of machines (which is inherently a dynamic phenomenon) with steady-state models has significant limitations. The voltage-behind-transient-reactance model of the induction machine is a quasi-steady-state model which captures the behavior of the machine in the brief instant of time after a short circuit occurs. Thus, this type of model provides a "snapshot" of the short-circuit behavior for one point in time. The machine time constants of decay provide estimates of the current

in the time after the fault. Transient simulations are used to verify the phasor-type models of the WTG, but comparing transient simulation waveforms to phasor calculations is not immediately straightforward. Thus, techniques for extracting phasor values from the short-circuit waveforms are described in this section.

Transient simulations are run in PSCAD using the simple circuit shown in Fig. 3.2, with machine parameters given in Appendix A. Two techniques can be used to extract the initial phasor value of the short-circuit current from the transient waveforms. The first technique, as displayed in Fig. 3.3 for the case of a three line-to-ground (TLG) fault, uses the peaks of the short-circuit current waveform to define decaying exponential envelopes [65]. The envelopes define the peak-to-peak short-circuit current magnitude. Extrapolating these curves to the instant of the fault ($t$ = 0 in Fig. 3.3) gives the short-circuit current at the instant of the fault, which is theoretically the same value calculated using the voltage-behind-transient-reactance model of the induction machine. This technique works well for analysis of a TLG fault, but not as well for unsymmetrical faults. For unsymmetrical faults, the magnitude *and* angle of the short-circuit currents are important.

The second technique also involves a curve-fitting technique, except the short-circuit waveforms from PSCAD are fit using the closed-form expression of the short-circuit currents in (2.27) [66]. The curve-fitting is performed using Matlab's curve-fitting toolbox. By entering the PSCAD simulation data, the Matlab function calculates the various magnitudes, angles, and time constants in (2.27) that give the best fit for the input data. The resulting short-circuit waveform from PSCAD and corresponding curve fit from Matlab are shown in Fig. 3.4 for the case of a single line-to-ground (SLG) fault in the circuit of Fig. 3.2. The results in Fig. 3.4 show that the fitted curve closely matches the simulation waveform.

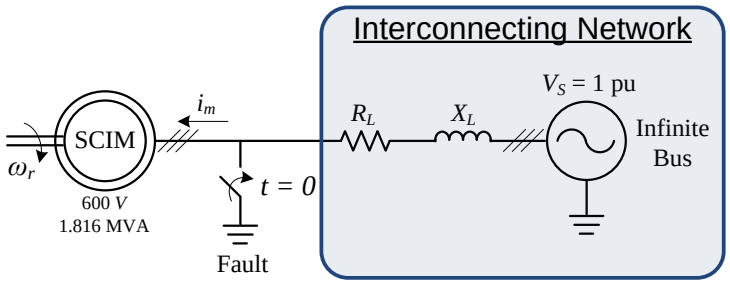


**Fig. 3.2: Simple network for simulating induction machine transients.**

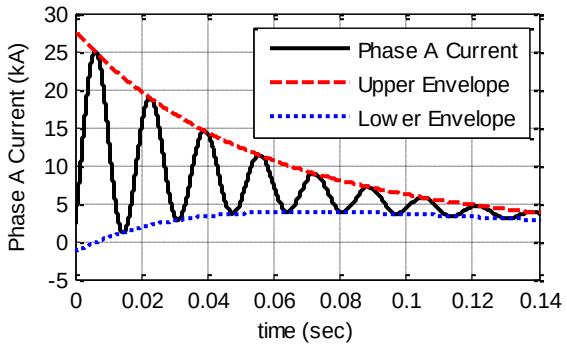


**Fig. 3.3: Short-circuit current for a TLG fault and envelopes defining current decay.**

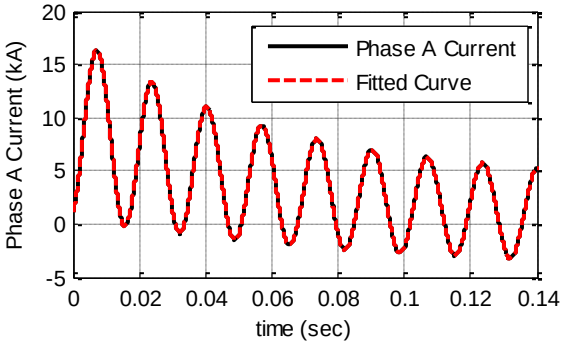


**Fig. 3.4: Short-circuit current for a SLG fault and fitted waveform.**

Using the values of $I_{tac}$, $I_{ss}$, $T_r'$, etc. in (2.27) extracted from the Matlab curve fit of the simulated short-circuit currents, the phasor value of the short-circuit currents can be calculated using

$$\left|I_{sc}(t)\right| = \left|\frac{I_{tac}}{\sqrt{2}} e^{j\theta} e^{-t/T_r'} + \frac{I_{ss}}{\sqrt{2}} e^{j\phi}\right|. \tag{3.1}$$

The DC component in the general solution in (2.27) is neglected in (3.1) since the fundamental-frequency, RMS component of the current is of interest. The RMS value of the short-circuit current at the instant of the fault is found by setting $t = 0$ in (3.1). In the case of a TLG fault, the steady-state component $I_{ss}$ in (3.1) is zero since the voltages become zero and flux cannot be maintained in the machine. However, under unbalanced faults, one or more of the phases remain connected to the network, and flux can be maintained in the machine from the un-faulted phase(s). Hence, $I_{ss}$ is non-zero in the case of unbalanced faults.

Calculation of the RMS short-circuit current in (3.1) can be done using the sequence-network circuits of the induction machine described in the previous chapter (see Fig. 2.8) by connecting the sequence-network circuits for the particular fault type and calculating the currents. Using these sequence-network circuits, the short-circuit current from an induction machine can be estimated using

$$\left|\vec{I}_{sc}(t)\right| = \left|(\vec{I}_t - \vec{I}_{ss})e^{-t/T_r'} + \vec{I}_{ss}\right|, \tag{3.2}$$

where $\vec{I}_t$ is the transient short-circuit current phasor calculated using the circuits of Fig. 2.8(b), $\vec{I}_{ss}$ is the steady-state current phasor calculated using the circuits of Fig. 2.8(a), and $T_r'$ is calculated using (2.24).

Comparing the initial short-circuit currents from the curve fitting of the PSCAD waveforms and the sequence-network calculations gives the results in Table 3.1 and Table 3.2 [66]. Table 3.1 lists the magnitude and angle of the short-circuit currents for a TLG fault at the machine terminals. A comparison of the magnitudes of the simulation results and the sequence-network calculations gives less than 1% error in each phase-current calculation, indicating the sequence-network calculations match closely with the PSCAD simulations. Table 3.2 lists the same results for a phase-A-to-ground fault. In

this case, the magnitude of the phase A short-circuit current is close to the value from PSCAD simulations, but the magnitudes in phases B and C show some error between the sequence-network calculations and PSCAD simulations.

**Table 3.1: Comparison of calculated and simulated short-circuit currents for a TLG fault.**

| | Seq. Net. Calc. | | Sim. Results | | |
|---|---|---|---|---|---|
| | Mag. (pu) | Ang. (deg) | Mag. (pu) | Ang. (deg) | % Error |
| $\vec{I}_a$ | **5.95** | -76.7 | **5.91** | -80.6 | **0.7 %** |
| $\vec{I}_b$ | **5.95** | 163.3 | **5.90** | 159.4 | **0.8 %** |
| $\vec{I}_c$ | **5.95** | 43.3 | **5.92** | 39.4 | **0.6 %** |

**Table 3.2: Comparison of calculated and simulated short-circuit currents for a SLG fault.**

| | Seq. Net. Calc. | | Sim. Results | | |
|---|---|---|---|---|---|
| | Mag. (pu) | Ang. (deg) | Mag. (pu) | Ang. (deg) | % Error |
| $\vec{I}_a$ | **3.54** | -69.5 | **3.51** | -71.1 | **0.8 %** |
| $\vec{I}_b$ | **0.91** | 105.4 | **1.06** | 102.0 | **13.8 %** |
| $\vec{I}_c$ | **2.63** | 112.3 | **2.46** | 111.6 | **6.8 %** |

The RMS short-circuit currents for several cycles after the fault occurrence are shown in Fig. 3.5 for a TLG fault and a SLG fault. Again, calculation results from the sequence-network circuits using (3.2) and simulation results curve fitting using (3.1) are compared in the plots of Fig. 3.5. For the TLG fault case shown in Fig. 3.5(a), there is good agreement between the simulation and calculation results for the first several cycles after the fault occurrence. Similarly, for the SLG fault case shown in Fig. 3.5(b), the calculated values are a good approximation to the PSCAD simulation results, but some error is present, particularly for the first 30 msec after the fault in the phase B current. This discrepancy is due to the error in the initial short-circuit current as displayed in Table 3.2 for the phase B current.

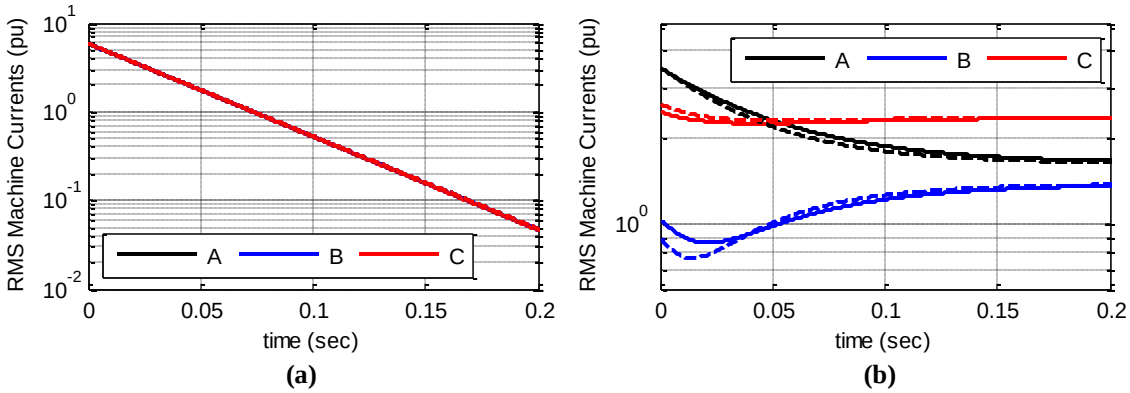


**Fig. 3.5: Comparison of calculated and simulated RMS short-circuit current for a (a) TLG fault and (b) SLG fault (solid = simulated, dashed = calculated).**

The calculation results presented in this section were based upon a sequence-network circuit of the induction machine described in previous work by others [8] [25]. Thus, the results in this section simply verified that existing sequence-network models of Type 1 WTGs give a good approximation to the RMS currents found from transient simulations, with the exception of some errors in the unbalanced fault calculations. The work presented in the next section describes a more general solution of the induction machine short-circuit currents, and also provides some insight into the cause of the errors in the unbalanced short-circuit calculations seen in the results of this section. A new sequence-network model of the induction machine is proposed based on this general solution.

## 3.4. Improved Sequence-Network Model of Induction Machine

The errors in the sequence-network calculations described in the previous section for the *unbalanced* fault led to further research to improve the sequence-network model to reduce the error in the calculations. Detailed mathematical analyses were performed to describe the induction machine short-circuit currents for both balanced and unbalanced short circuits. The mathematical techniques developed are more general than approaches taken thus far in the literature [26] [27]. A closed-form solution of the stator short-circuit

currents in the induction machine is developed from a linearized model of the machine dynamic equations that makes the following assumptions:

- The rotor speed remains unchanged for a short period after the fault occurrence.
- The stator voltages at the machine terminals after the fault are known and fixed.

The first assumption is valid for a short period of time after a fault for machines with a large inertia, as in the case of a large wind turbine. The second assumption is valid if the machine is connected to a "stiff" grid, where the magnitude of current flowing in the machine does not affect the terminal voltages significantly. Thus, it can be assumed that the terminal voltage magnitude and angle in the un-faulted phases remain unchanged after the fault. For example, if a phase-A-to-ground fault occurs at the machine terminals, the phase A terminal voltage is zero, but the magnitude and angle of the phase B and C voltages remain unchanged from their pre-fault values. The work presented in this section is a summary of this mathematical derivation of the short-circuit currents and the improved sequence-network model that can be derived from it.

Assuming a stationary reference frame ($\omega_p$ = 0), the stator and rotor voltage equations in (2.15) can be written in state-space form as

$$\frac{d}{dt}\begin{bmatrix}\vec{\lambda}_s \\ \vec{\lambda}_r\end{bmatrix} = \begin{bmatrix} -\frac{R_s}{L_s'} & \frac{R_s}{L_s'}\frac{L_m}{L_r} \\ \frac{R_r}{L_r'}\frac{L_m}{L_s} & -\frac{R_r}{L_r'} + j\omega_r \end{bmatrix}\begin{bmatrix}\vec{\lambda}_s \\ \vec{\lambda}_r\end{bmatrix} + \begin{bmatrix}\vec{v}_s \\ \vec{v}_r\end{bmatrix}, \tag{3.3}$$

where the parameters in (3.3) are defined in Chapter 2. Equation (3.3) is the general form for a set of linear differential equations with constant coefficients (provided the rotor speed $\omega_r$ is assumed constant). Therefore, a closed-form solution for the stator and rotor flux linkages can be found from the equations in (3.3). The closed-form solution can be determined from the homogeneous and particular solutions, where the homogeneous solution is found from the eigenvalues of the state matrix and the matrix exponential [67]. The particular solution is found from the method of undetermined coefficients [68] using the known stator voltage and setting the rotor voltage to zero. The closed-form solution

derivation is given in detail in [69] and is also provided in Appendix B for convenience. The resulting waveforms comparing the closed-form solution (calculated current) to simulation results from PSCAD are shown in Fig. 3.6. One phase of the machine currents for a phase A to ground fault is shown in Fig. 3.6 and shows the closed-form solution follows the simulated current closely for the first several cycles.

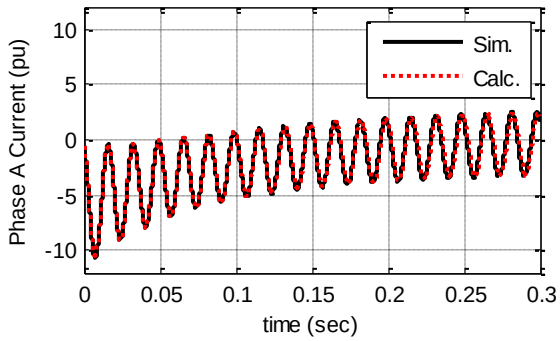


**Fig. 3.6: Comparison of simulated short-circuit current and closed-form solution (calculated current) for a SLG fault.**

As discussed in the previous chapter, the voltage-behind-transient-reactance model of an induction machine is proportional to the rotor flux linkage, and is given by

$$\vec{v}' = j\omega_s \frac{L_m}{L_r} \vec{\lambda}_r \,. \tag{3.4}$$

The solution of (3.3) for the rotor flux linkage also gives the instantaneous solution for the voltage behind transient reactance in (3.4). The solution of the rotor flux linkage contains some negative-sequence component if the stator voltages are unbalanced because negative-sequence currents flow in the stator and rotor [69]. Therefore, the negative-sequence rotor flux produces a negative-sequence voltage behind transient reactance. Further, because the positive-sequence rotor flux depends on the initial conditions of the flux linkages prior to the fault, the positive-sequence voltage behind transient reactance varies depending on these initial conditions. Since the flux linkages in

steady state are periodic, the range of initial conditions varies over a cycle of the fundamental frequency. Therefore, it can be concluded that the positive-sequence voltage behind transient reactance depends on the voltage waveform angle $\delta$ at which the fault occurs. It is assumed that the machine operates under balanced, steady-state conditions prior to the fault; thus, the initial conditions for the negative-sequence rotor flux are zero. Hence, the negative-sequence voltage behind transient reactance does not depend on the fault angle $\delta$. An improved sequence-network circuit accounting for these factors is shown in Fig. 3.7 for the example of a SLG fault at the machine terminals. Details on how to calculate these parameters for an example system are given in Appendix B.

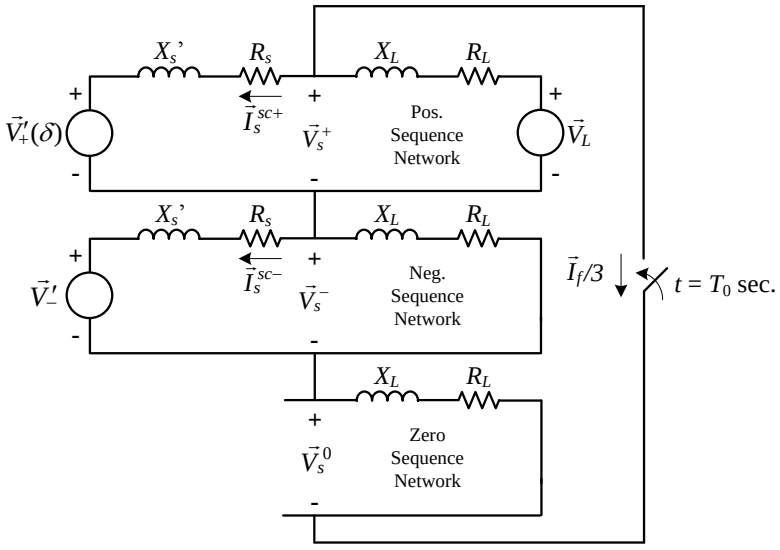


**Fig. 3.7: Improved sequence-network model of induction machine for unbalanced fault.**

An example calculation for a SLG fault at the machine terminals is performed to compare the calculation results from the conventional sequence-network model discussed in the previous section and the improved sequence-network model described in this section. The details of these calculations are provided in Appendix B, and are not reproduced here. A comparison of these two calculation methods is shown in Table 3.3.

The two calculation methods are compared using the closed-form solution of (3.3) at $t = T_0$ as a reference, where $T_0$ is the time of the fault. Comparing the phase current magnitudes calculated using the conventional and improved sequence-network circuits, the improved sequence-network circuit shows less than 1% error in each phase calculation, while the conventional method shows over 16% error in one of the phases. Thus, the improved sequence-network circuit provides a much better estimate of the short-circuit currents.

**Table 3.3: Comparison of conventional and improved sequence-network calculations.**

| | Ref. Current from Sol. of (3.3) | | Conv. Seq. Net. Calc. $\vec{V}'_+ = 0.952 \text{ /\_ } 9.01°$, $\vec{V}'_- = 0$ | | | Improved Seq. Net. Calc. $\vec{V}'_+ = 0.947 \text{ /\_ } 7.20°$, $\vec{V}'_- = 0.010 \text{ /\_ } 93.32°$ | | |
|---|---|---|---|---|---|---|---|---|
| | Mag. | Ang. | Mag. | Ang. | %Err | Mag. | Ang. | %Err |
| $\vec{I}_a$ | 3.92 | 103.4 | 3.95 | 105.3 | **0.68** | 3.91 | 103.5 | **0.29** |
| $\vec{I}_b$ | 1.33 | -85.0 | 1.11 | -81.0 | **16.30** | 1.32 | -85.0 | **0.60** |
| $\vec{I}_c$ | 2.61 | -72.3 | 2.84 | -72.3 | **8.87** | 2.61 | -72.2 | **0.11** |

## 3.5. Experimental Waveforms vs. PSCAD Simulations

Experimental validation of the transient models used for simulation is important to ensure the simulation results accurately represent the transient behavior of a WTG. Also, since transient simulations will be used in later sections to validate the developed sequence-network models, it is important to ensure that the sequence-network circuits are not validated against an incorrect model. In this section, experimental short-circuit tests performed on the lab-scale induction machine shown in Fig. 3.8 are described. To compare the experimental results with simulation results, the parameters of an equivalent circuit of the induction machine must be derived from various experimental tests [8] [70]. These equivalent-circuit parameters are then used as inputs into the induction machine model in the PSCAD component library. The experimental tests used to obtain the induction machine equivalent-circuit parameters are described in this section.

Additionally, experimental short-circuit waveforms and PSCAD simulation waveforms are compared. Magnetic saturation has been shown to affect the transient currents in induction machines [71] [72], and is therefore considered in this experimental analysis for the induction machine short-circuit currents.

### *3.5.1. Machine Parameter Identification: No-Load Test*

The traditional method for identifying the magnetizing reactance of an induction machine is the no-load test [8], in which the machine is run with rated voltage applied to the stator terminals and no mechanical load on the rotor shaft. The speed of the machine under these conditions is approximately synchronous speed, making the slip $s$ approximately zero. Thus, from the steady-state equivalent circuit of the induction machine shown in Fig. 3.9, the rotor circuit is assumed to be open. In a squirrel-cage induction machine, this technique is the only way to "open" the rotor circuit to strictly isolate the stator and magnetizing branches from the rotor in the circuit of Fig. 3.9. The DC stator resistance can be measured directly.

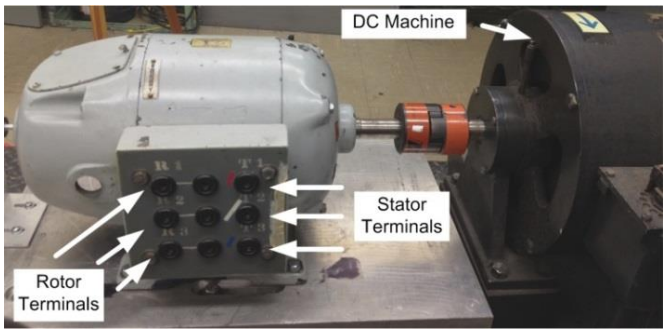


**Fig. 3.8: Photo of experimental wound-rotor induction machine used for testing.**

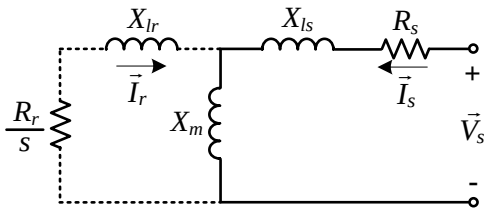


**Fig. 3.9: Steady-state equivalent circuit of induction machine.**

In a wound-rotor induction machine (WRIM), the stator *and* rotor resistances can be measured directly. The no-load test can be performed by manually opening the rotor circuit windings, which does not require the machine to rotate to perform the test. By measuring the stator voltage and current under this test, an approximation of the reactance $X_{ls} + X_m$ can be found.

The results of the no-load test performed on the WRIM shown in Fig. 3.8 for a range of stator voltage levels are shown in Fig. 3.10. The plotted data points are the per-unit values of the stator voltage and current over the range of stator voltage test points. These data points represent the positive-sequence, fundamental-frequency voltages and currents, and are obtained by collecting 60 cycles of steady-state, sinusoidal voltage and current waveforms, performing a discrete-fourier transform on the three-phase waveform data to obtain the fundamental-frequency phasors, and then calculating the positive-sequence phasors. The calibration method of the voltage and current sensors used to obtain these measurements is described in Appendix D, as well as an analysis of the measurement uncertainty in the current and voltage measurements. From the uncertainty analysis, it is found that the uncertainty in the current measurements is roughly ± 0.39 A (0.02 pu) over the range of 0 – 1 per unit current and the uncertainty in the voltage measurements is roughly ± 1.51 V (0.01 pu) over the range of 0 – 1 per unit voltage with a confidence level of approximately 95%.

A range of voltage levels were considered to determine if saturation occurs within the operating voltage range of the machine and to determine the shape of the saturation

curve. As shown in the curve of Fig. 3.10, the machine begins saturating at approximately 70% of rated voltage. The calculated curve shown in Fig. 3.10 is the calculated V-I characteristics of the machine for this test using the estimated values of the unsaturated machine parameters (given in Appendix A). Thus, under normal operating conditions, the machine will be in the non-linear, saturated region of the curve. Therefore, to accurately model this machine, the non-linear saturation characteristics of the magnetic core must be considered.

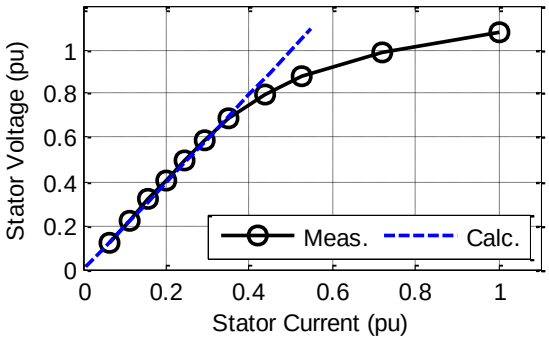


**Fig. 3.10: No-load saturation curve of induction machine.**

### *3.5.2. Machine Parameter Identification: Blocked-Rotor Test*

The blocked-rotor test is a method for determining the leakage reactances $X_{ls}$ and $X_{lr}$ of the stator and rotor windings. This test is performed by prohibiting the rotor from turning by physically forcing the rotor to stay in a rested position while applying reduced voltage to the stator windings. The rotor windings are short circuited in this test. Because the machine rotational speed is zero, the slip $s$ in Fig. 3.9 is one. It is assumed in this test that the magnetizing reactance $X_m$ is significantly larger than the winding leakage reactances; thus, all of the current flowing in the stator flows into the rotor circuit of Fig. 3.9. By measuring the stator voltage and current from this test, an approximation of the reactance $X_{ls} + X_{lr}$ can be found. As a crude approximation, it is typically assumed that

the per-unit value of $X_{ls}$ and $X_{lr}$ are equal. The ac resistances of the stator and rotor windings are estimated from the measured voltages and currents using a resistance gain factor *a*, calculated by

$$a = \frac{\text{real}\left(\vec{V}_s / \vec{I}_s\right)}{R_s^{dc} + R_r^{dc}}. \tag{3.5}$$

where $\vec{V}_s$ is the measured stator voltage phasor during the blocked-rotor test, $\vec{I}_s$ is the measured stator current phasor during the blocked-rotor test, and $R_s^{dc}$ and $R_r^{dc}$ are the measured dc winding resistances of the stator and rotor, respectively. The ac winding resistances are estimated by multiplying their corresponding dc resistance by this gain factor *a*. The numerical values of these parameters are given in Appendix A.

The results of the blocked-rotor test are plotted in Fig. 3.11. The calculated V-I characteristics of this machine using the estimated machine parameters are shown in the calculated curve in Fig. 3.11. In this case, the calculated approximation of the V-I characteristics shows good agreement at all current levels up to 1 pu. Therefore, the leakage reactances do not appear to saturate in this operating region of the induction machine. The machine parameters found from this test are given in Appendix A.

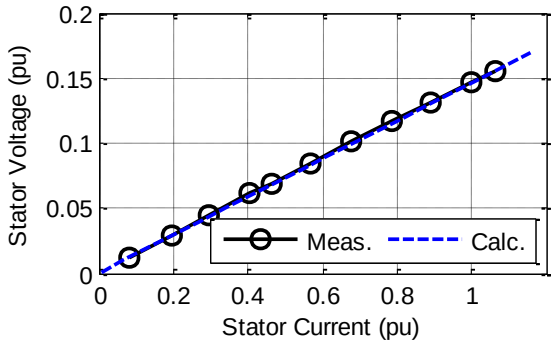


**Fig. 3.11: Blocked-rotor test result curve.**

### *3.5.3. Measured vs. Simulated Short-Circuit Currents*

Experimental short-circuit tests were carried out on the WRIM shown in Fig. 3.8, and are described in [73]. The circuit used to apply faults to the WRIM is shown in Fig. 3.12. The circuit consists of three switches in series with the machine and another three switches in parallel with the machine. Each switching device is a triac with a 600 V blocking voltage capability and a 400 A surge current capability. A photo of these switches and their controls is shown in Fig. 3.13. The switches are turned on by applying a 5 kHz, 10% duty cycle PWM signal to the triac gate. In normal operation, the series switches' gating signals are permanently turned on and the shunt switches gating signals are permanently turned off. To apply the fault, the series switches' gating signals are first turned off (thus inserting the 1.2 Ω resistors in series with the machine), and after 10 milliseconds, the shunt switches' gating signals are turned on, thus short-circuiting the machine terminals. A 10 millisecond delay is inserted to ensure the series devices are not conducting when the shunt switches are turned on. The short circuit is applied for 150 milliseconds and then removed by first turning off the shunt switches' gating signals, then waiting 10 milliseconds, and then turning the series switches' gating signals on.

The circuit shown in Fig. 3.12 represents the application of a balanced three-phase short circuit to the machine terminals. However, this circuit can easily be reconfigured to apply unbalanced faults to the machine terminals. To apply a phase A to neutral fault, the shunt connections in phases B and C can be manually disconnected.

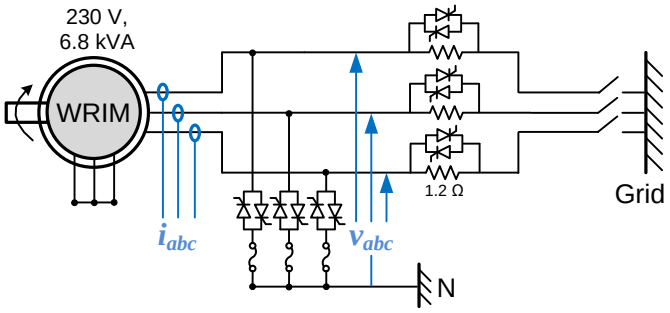


**Fig. 3.12: Induction machine circuit for applying fault.**

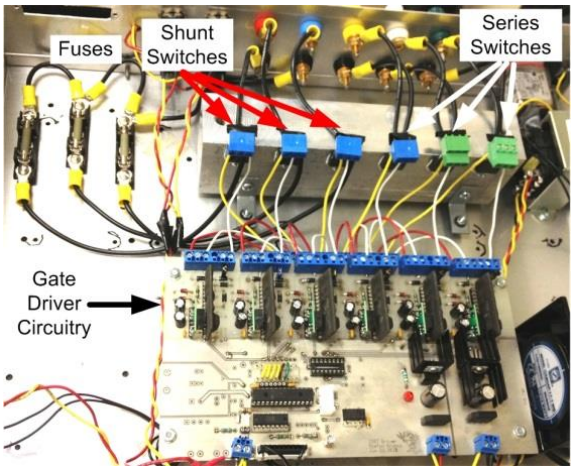


**Fig. 3.13: Photo of control circuitry for applying a fault to the induction machine.**

Transient simulations were run in PSCAD that replicate the experimental setup shown in Fig. 3.12. The machine parameters found from the blocked-rotor and no-load test were used in the WRIM model in the PSCAD component library. The measured data points of the no-load saturation curve shown in Fig. 3.10 were directly input into the WRIM model to ensure that the mutual-flux saturation characteristics of the machine were incorporated into the model.

Both the experimental tests and simulations were carried out with the machine running at no load and rotor windings short circuited. The point-on-wave (angle $\delta$) at which the fault occurs significantly affects the short-circuit current waveforms of the induction machine. In the experimental tests, the fault was applied at a random point-on-

wave. However, in the simulation results, the fault was intentionally applied at the same point-on-wave as seen in the experimental results. The resulting simulation waveforms for a three-phase short circuit are shown in the left column of Fig. 3.14. The measured waveforms are shown in the right column of Fig. 3.14. The stator voltage waveforms match closely in both the simulation and measured results in Fig. 3.14. However, the measured stator currents after the short-circuit show a much higher magnitude in the first cycle following the fault and they decay more rapidly than the simulation results. Additionally, the measured current is much higher in magnitude in the first cycle after the fault is removed (after $t$ = 0.15 sec. in Fig. 3.14). A comparison of the measured and simulation waveforms for the case of a phase-A-to-neutral fault are shown in Fig. 3.15. In this case, much better agreement occurs between the measured waveforms and simulations waveforms during the fault. However, after the fault is removed, the measured current magnitude is significantly higher than the simulated current.

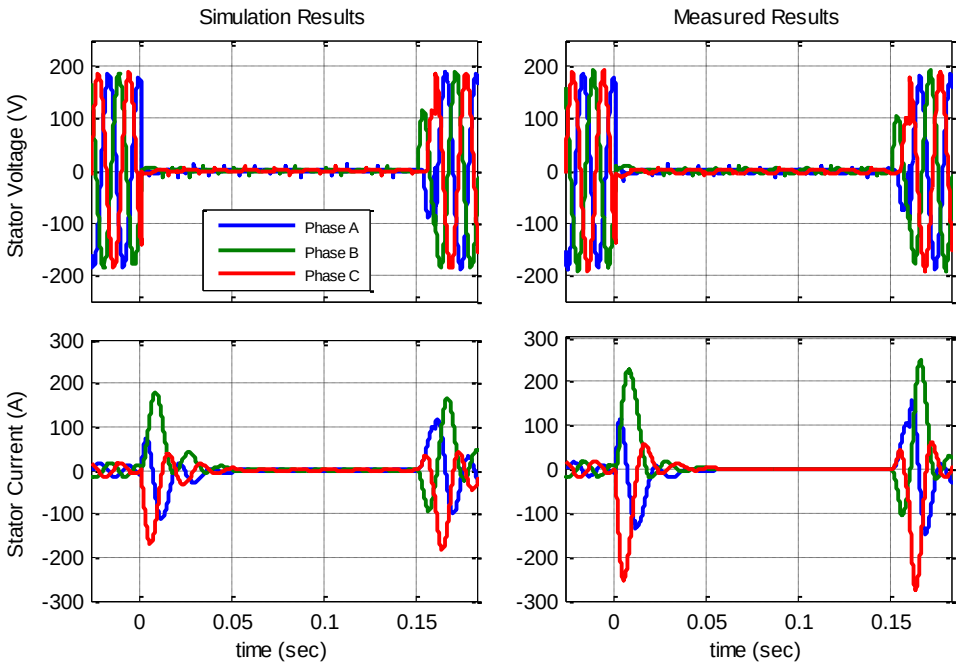


**Fig. 3.14: Experimental and simulation results for a three-phase fault on the induction machine.**

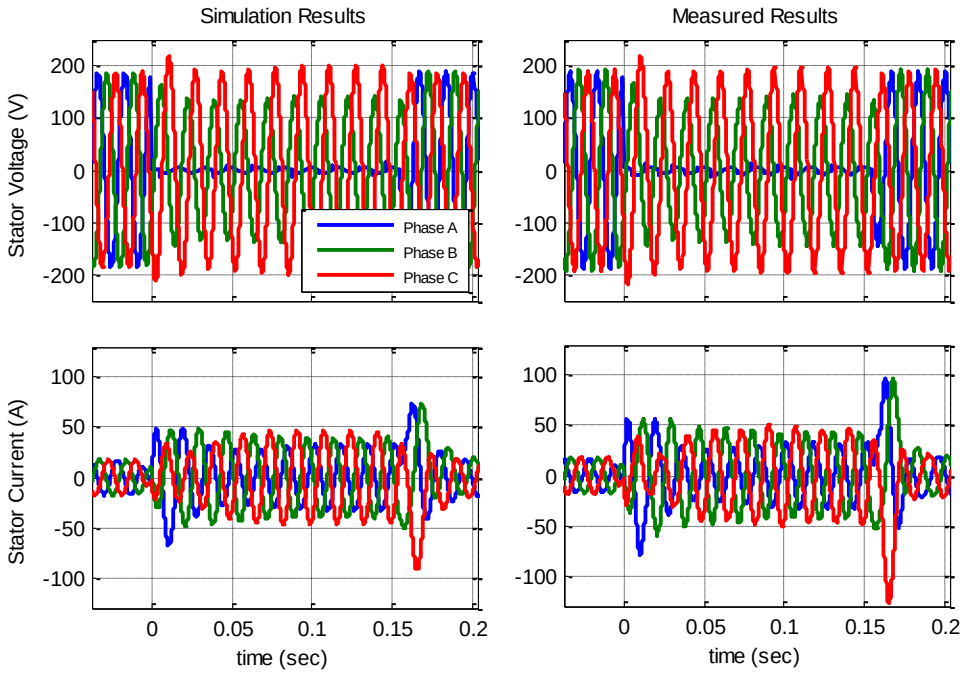


**Fig. 3.15: Experimental and simulation results for a phase-A-to-neutral fault on the induction machine.**

### *3.5.4. Effects of Leakage Saturation*

The discrepancy in the current magnitudes between the measured and simulation results, as shown in Fig. 3.14, is possibly due to leakage-flux saturation. This behavior has been described in terms of the startup of induction machines [72], and contributes to higher startup current magnitudes than might be expected using machine parameters found from steady-state tests. This behavior occurs due to portions of the leakage flux that pass through magnetic material, such as the stator and rotor teeth. These portions of the magnetic material can saturate when high currents flow through the machine windings. A logical inference is that the same phenomenon that occurs during startup can occur after a three-phase fault, since roughly the same magnitude of current flows through the machine windings briefly after the fault occurs. This behavior can be

explained by recognizing that the short-circuit current in an induction machine is primarily limited by the machine's stator transient reactance, given by

$$X_s' = X_{ls} + \frac{X_{lr} X_m}{X_{lr} + X_m} \approx X_{ls} + X_{lr}\,, \tag{3.6}$$

where it is assumed that $X_{lr} + X_m \approx X_m$. Thus, the leakage reactances primarily limit the short-circuit current from an induction machine. To test this theory, the same three-phase short-circuit test described in the previous section was repeated, except the machine was run at 40% of rated voltage. Running the machine at reduced voltage results in a lower flux; thus, the electro-motive force (emf) that drives the short-circuit current is reduced. Thus, performing this test at reduced voltage reduces the magnitude of the short-circuit currents. The leakage flux is less likely to saturate the magnetic material if the magnitude of the current is reduced. The results of this test are shown in Fig. 3.16. The transient simulation results for this test are shown in the left column, and the experimental results are shown in the right column. As expected, the magnitude of the short-circuit current after the fault is significantly reduced from the current magnitude seen in Fig. 3.14 with the machine running at rated voltage. However, the experimental results again show higher current magnitude in the first peak after the fault occurs, similar to the results in Fig. 3.14. Therefore, it is inconclusive based on these results whether leakage saturation causes the discrepancy in the results, since the magnitude of the current in the first peak (roughly 92 A in phase A of the experimental results) is roughly 3.8 times the machine rated current. Therefore, leakage-flux saturation can still occur during this test because of the relatively high magnitude of the currents.

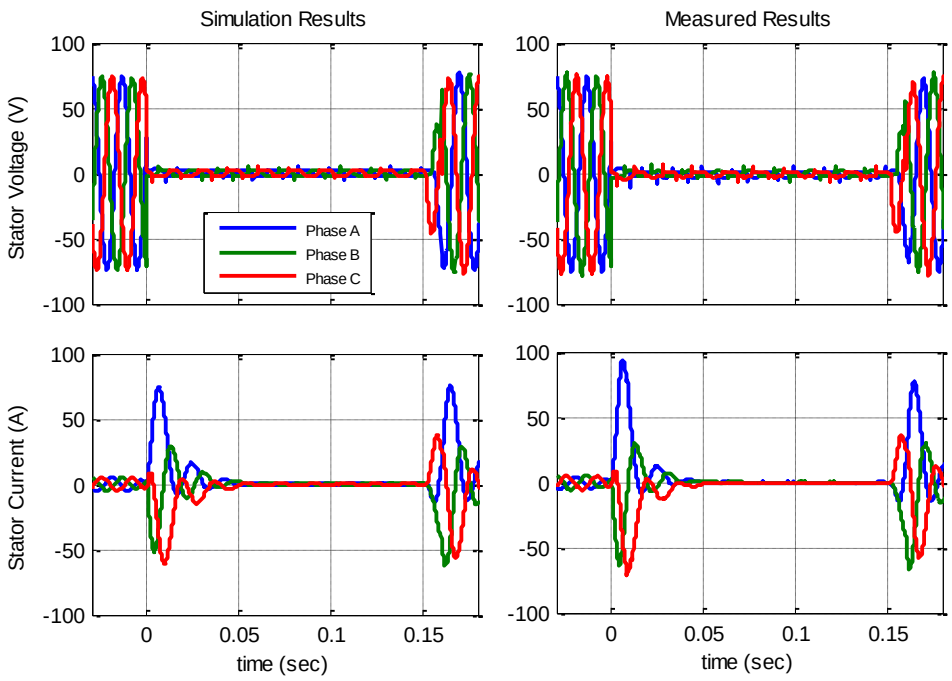


**Fig. 3.16: Experimental and simulation results for a three-phase short-circuit test at reduced voltage.**

Additional simulations were run for the case of a three-phase fault, except the value of the stator and rotor leakage reactances were reduced, which is a rough approximation to the effects of leakage-flux saturation. Simulation results for the case of a 0%, 20% and 40% reduction in the value of the stator and rotor leakage reactances are shown in Fig. 3.17, along with the experimental results for the phase C current shown in Fig. 3.14. All other parameters are left unchanged in the simulation model. The results indicate that a reduction in the value of the leakage reactances causes a higher short-circuit current magnitude. The case of a 40% reduction in the leakage reactance shows the best agreement to the measured results. Thus, the results in Fig. 3.17 indicate that modeling the induction machine with leakage reactances lower than the values determined from the blocked-rotor test give better agreement to the actual short-circuit currents from the induction machine. Because leakage-flux saturation can cause an effective reduction in the leakage inductance of the machine windings, this may be the

cause of the discrepancy between the measured and transient simulation results seen in Fig. 3.14 and Fig. 3.16.

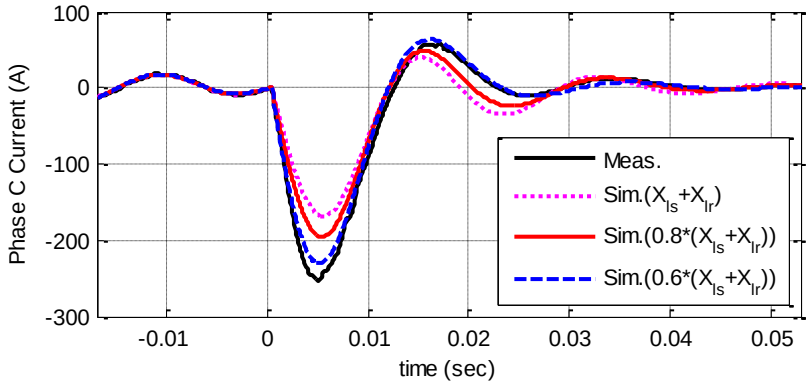


**Fig. 3.17: Comparison of measured short-circuit currents to simulated currents with a reduction in the winding leakage reactances.**

Leakage-saturation characteristics are difficult to obtain experimentally since this requires performing the blocked-rotor tests at much higher currents than rated current. Performing this test at higher current can cause the windings to overheat and possibly be damaged. Additionally, locking the rotor in place becomes more problematic since a very rigid mechanical structure is needed to counteract the higher machine torques produced. However, current and voltage measurements from the startup transient may be sufficient to get a reasonable saturated value of the stator and rotor leakage reactances [73]. The leakage-flux saturation in an induction machine is a very complex issue, and is best analyzed using finite-element analysis software. However, understanding these effects in great detail is beyond the scope of this work.

## 3.6. Single-Machine Infinite-Bus Studies

Transient simulation results are presented in this section of a single utility-scale Type 1 WTG within a realistic transmission-connected system. The network used for these studies is shown in Fig. 3.18. The network consists of a Type 1 WTG, WTG step-

up transformer, collector cable, substation transformer, and transmission system. The parameter values of the various components shown in Fig. 3.18 are given in Appendix C. The transmission lines and collector cable are represented as *RL* circuits. Additionally, power-factor correction capacitors (PFCC) are included at the terminals of the WTG. For these studies, the WTG is assumed to be producing rated power output, and the PFCC are chosen such that the WTG produces unity power factor at its terminals. Faults on one of the parallel transmission lines are considered in this study of the single-machine system. Transient simulation results for both balanced and unbalanced faults are provided and compared with sequence-network calculation results on this network.

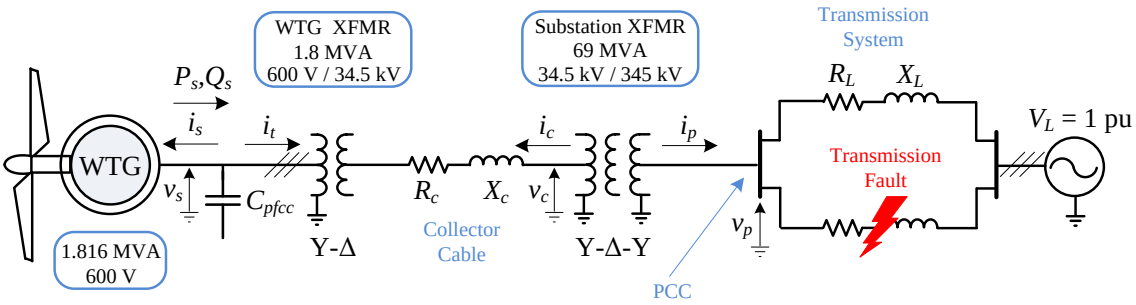


**Fig. 3.18: Single-machine infinite bus network.**

The case of a three-phase fault on one of the transmission lines of the system in Fig. 3.18 is represented by the transient sequence-network circuit shown in Fig. 3.19. Only positive-sequence current flows in the network since the system remains balanced for a three-phase fault. The parameters *k* and *m* in Fig. 3.19 together determine the length of the transmission line and the location of the fault along this transmission line. For this case, *k* is chosen to be 0.2 and *m* is chosen to be 0.8. The circuit in Fig. 3.19 is used to calculate the currents and voltages in the network immediately after the fault occurs ($t = 0^+$). For this reason, the Type 1 WTG is represented as a voltage source behind its transient reactance, since the flux in the machine immediately after the fault does not change from its pre-fault value. The steady-state sequence-network circuit for this fault

is shown in Fig. 3.20. This circuit is used to calculate the voltages and currents in the network during the fault after the initial flux transients have died away. Thus, the induction machine is represented using the conventional steady-state equivalent circuit (assuming the slip *s* has not changed from the pre-fault value).

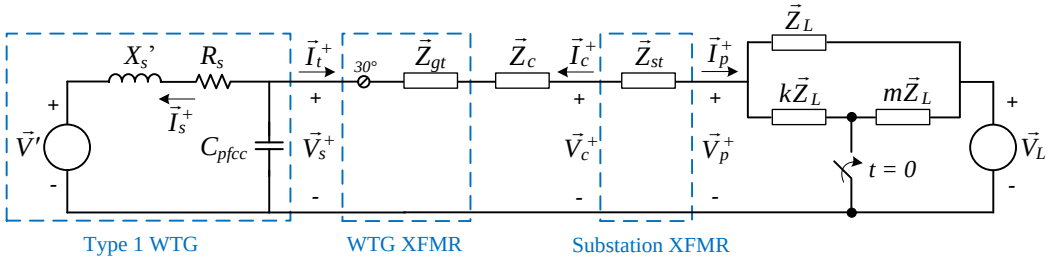


**Fig. 3.19: Transient sequence-network circuit of the single-machine network for a three-phase fault on the transmission system.**

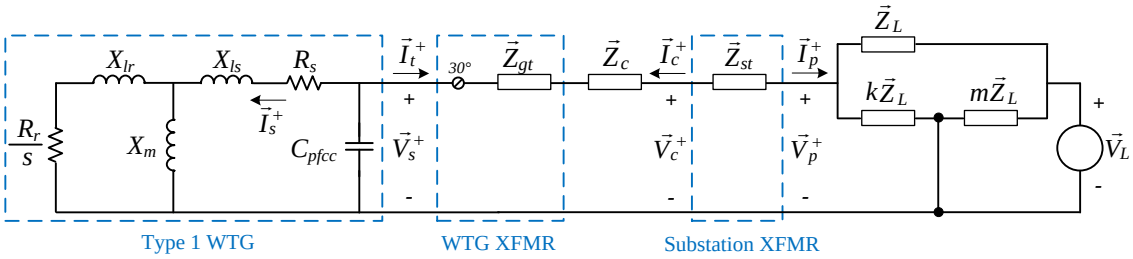


**Fig. 3.20: Steady-state sequence-network circuit of the single-machine network for a three-phase fault on the transmission system.**

Transient waveforms of the voltage and currents in this network from the PSCAD simulation results for this fault are shown in Fig. 3.21(a). At $t$ = 0, roughly an 80% drop in voltage can be seen on both the collector cable voltage $v_c$ and the point of common coupling (PCC) voltage $v_p$. A large increase in both the collector cable current $i_c$ and the total wind plant current $i_p$ can be seen after the fault occurs. A high frequency resonance component can be seen in the current waveforms, which is due to the resonance induced by the PFCC at the terminals of the WTG. The positive-sequence components of each of these voltage and current waveforms (labeled as simulated values) are shown in Fig.

3.21(b), and are calculated from the cosine filter algorithm discussed in chapter 2 and in [63]. Also shown in Fig. 3.21(b) are the calculated values of the positive-sequence voltages and currents using the circuits of Fig. 3.18, Fig. 3.19, and Fig. 3.20. The voltage behind transient reactance $\vec{V}'$ in Fig. 3.19 is calculated using the following procedure:

1. Perform a load-flow calculation on the network of Fig. 3.18 assuming a real and reactive power $P_s$ and $Q_s$ generated by the WTG. Designate the stator terminal voltage $\vec{V}_s$ as a bus.
2. From the load-flow calculation results, use $\vec{V}_s$, $P_s$, and $Q_s$ to calculate the stator current phasor of the WTG using

$$\vec{I}_s = -\left( \frac{P_s + jQ_s}{\vec{V}_s} \right)^* , \tag{3.7}$$

   where $P_s$ and $Q_s$ are per-phase quantities and the negative sign is present due to the direction of current chosen, as shown in Fig. 3.18.
3. Calculate $\vec{V}'$ using (2.21).

The load-flow calculation can be performed using any conventional technique, such as manually building the $Y_{bus}$ matrix and using a Gaussian iteration algorithm to solve for each of the bus voltages [7]. To find the remaining voltage and current phasors in Fig. 3.19, the steady-state solver in Matlab's SimPowerSystems (SPS) toolbox is used. The calculations are performed by building the per-phase sequence-network circuit shown in Fig. 3.19 in SPS using the library components for resistors, inductors, and ideal voltage sources. The calculated magnitude and angle of $\vec{V}'$ from the steps above are manually inserted into the ideal voltage source parameters in the circuit of Fig. 3.19. The pre-fault (before $t$ = 0) calculations are performed with the switch in Fig. 3.19 open. The post-fault calculations (after $t$ = 0) are performed in the same way, except the switch in the circuit of Fig. 3.19 is closed. The post-fault steady-state values are found in the same way, except the circuit of Fig. 3.20 is used assuming some pre-fault slip $s$. Performing

the calculations in this way gives three sets of phasor quantities for each of the voltages and currents shown in Fig. 3.18. The three phasors for each quantity (voltage or current) represents its value (magnitude and phase angle) at specific points in time (before the fault, immediately after the fault, and steady-state after the fault). To calculate how the magnitude of these phasors vary with time *after* the fault, (3.2) is used. Note that this equation is given for current, but a similar equation is used for the voltages. The components of this equation labeled with a '*t*' subscript represent the calculated values using the circuit of Fig. 3.19. The components of this equation labeled with a '*ss*' subscript represent the calculated phasor using the circuit of Fig. 3.20. The time constant of decay in (3.2) is the machine's rotor transient time constant, but is modified in these calculations to account for the added impedance between the machine and the fault. The time constant of decay is given by

$$T_r' = \frac{L_r'}{R_r}, \tag{3.8}$$

where $R_r$ is the rotor winding resistance and the rotor transient inductance $L_r$' is modified from (2.26) to be

$$L_r' = L_{lr} + \frac{L_m(L_{ls} + L_{gt}' + L_c' + L_{st}')}{L_m + L_{ls} + L_{gt}' + L_c' + L_{st}'}, \tag{3.9}$$

where $L_{gt}$', $L_c$', and $L_{st}$' are the WTG transformer leakage inductance, collector cable inductance, and substation transformer leakage inductance referred to the low-voltage side of the WTG transformer. Calculating the voltages and currents in this way gives the calculated curves shown in Fig. 3.21(b). The calculated values of the positive-sequence voltages give good agreement to the simulated values. The calculated values of the currents also show good agreement to the simulated values, except that as the currents approach steady state (near 0.15 seconds), the calculated values of the current are slightly less than the simulated values. This discrepancy is due to the assumption in the

calculations that the slip does not change during the fault, while in the simulations the rotational speed of the machine does increase, causing the slip to increase.

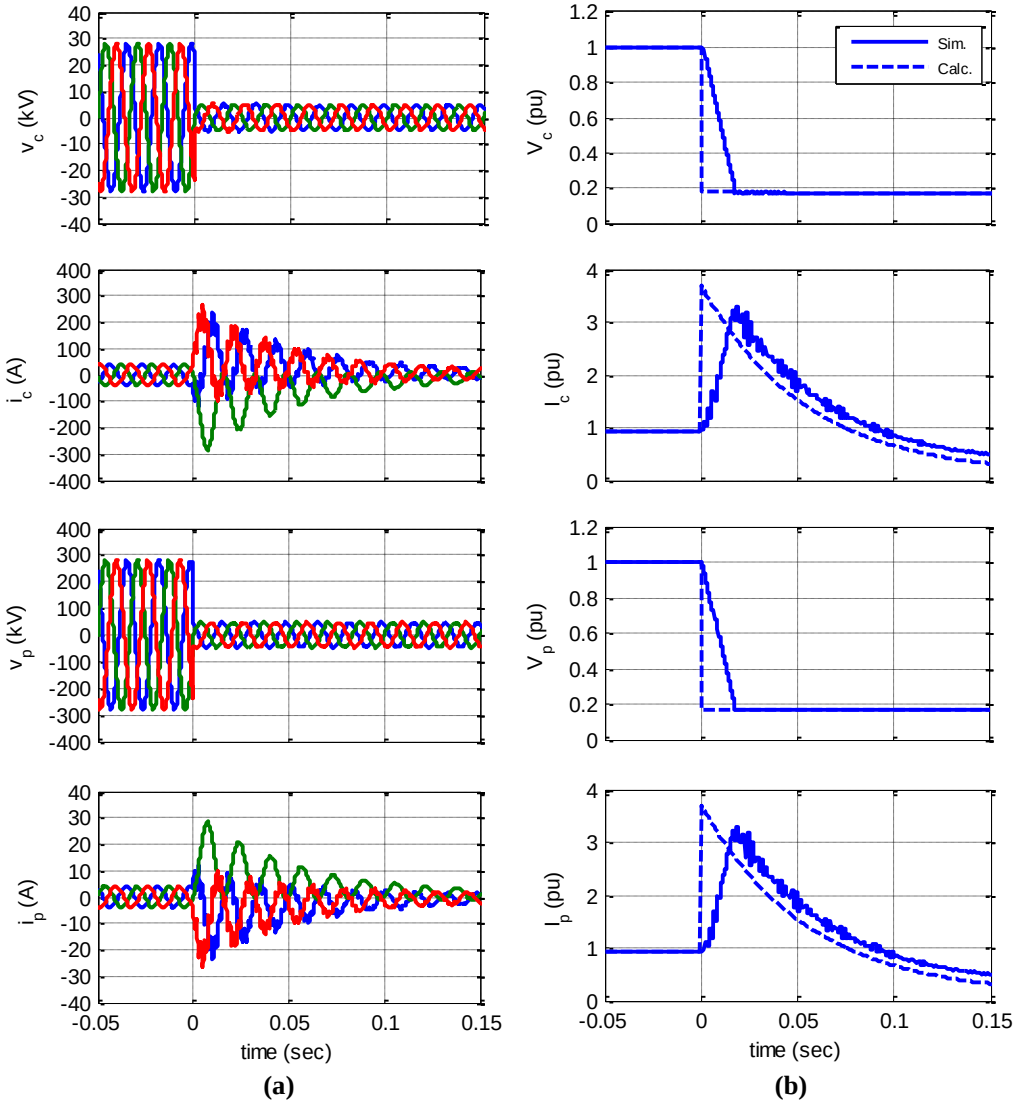


**Fig. 3.21: (a) Transient simulation results of the voltages and currents for a three-phase fault on the transmission system and (b) comparison of the calculated and simulated positive-sequence components of these voltages and currents.**

The transient sequence-network circuit for a phase-A-to-ground fault at the same location in the network of Fig. 3.18 is shown in Fig. 3.22. In this case, positive-, negative-, and zero-sequence currents flow in the network. The sequence circuits used to

represent the Type 1 WTG are the same as shown in Fig. 2.8(b). The steady-state sequence-network circuit for this fault is shown in Fig. 3.23. The sequence circuits used to represent the Type 1 WTG in this circuit are the same as shown in Fig. 2.8(a).

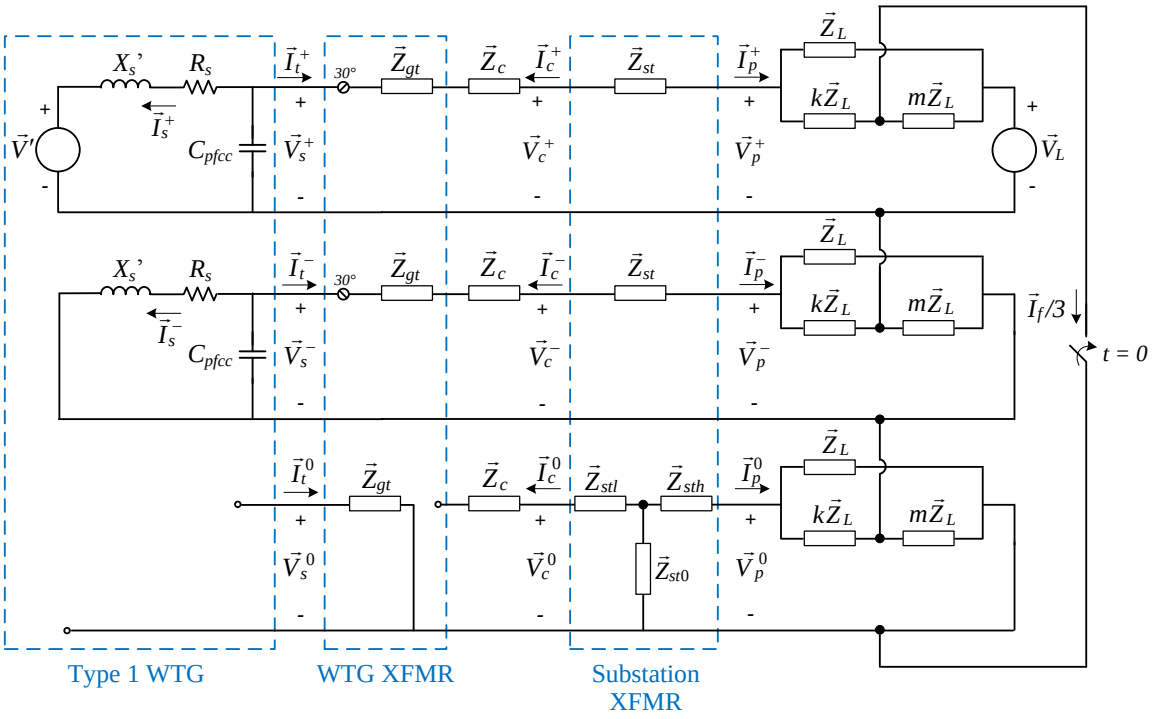


**Fig. 3.22: Transient sequence-network circuit for a single-phase fault on the single machine system.**

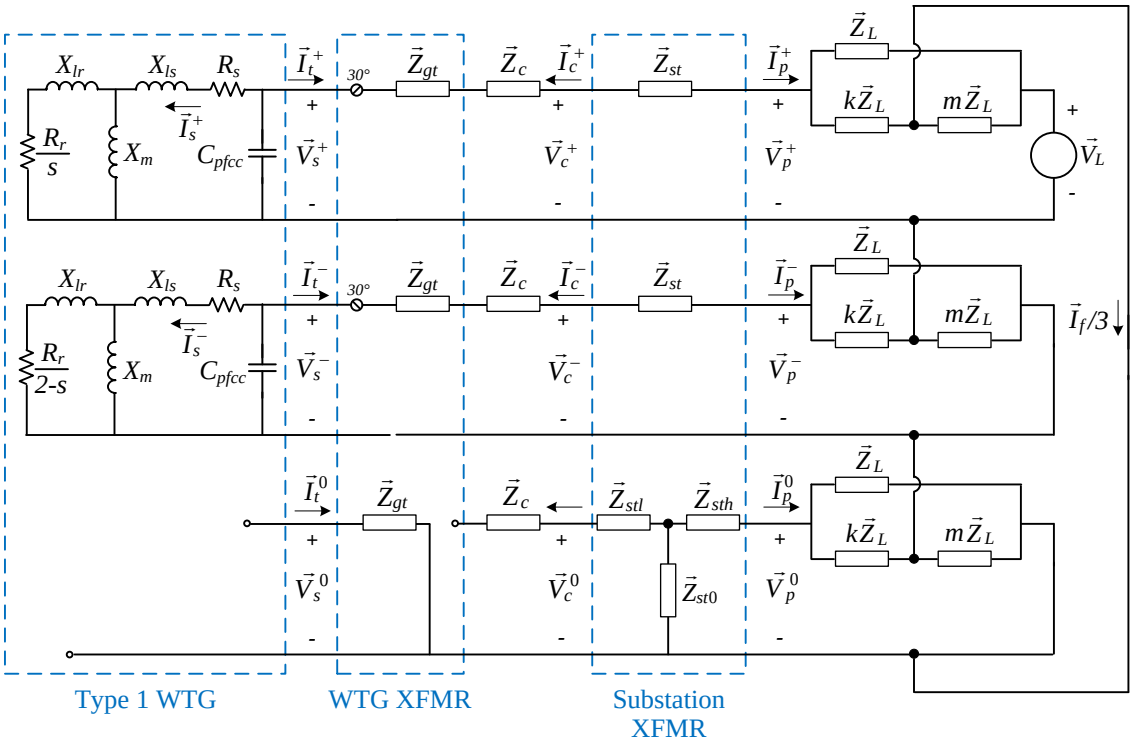


**Fig. 3.23: Steady-state sequence-network circuit for a single-phase fault on the single machine system.**

The transient waveforms of the voltages and currents from the PSCAD simulations for this fault are shown in Fig. 3.24(a). The sequence components of these voltages and currents found from the cosine filter algorithm are shown in Fig. 3.24(b) (denoted by the solid lines). After the fault, the collector current $\vec{I}_c$ does not contain any zero-sequence component, while the plant current $\vec{I}_p$ contains a large amount of zero-sequence current. This agrees with the sequence-network circuit in Fig. 3.22 since the collector circuit is open in the zero sequence due to the winding configuration of the WTG transformer. The calculated sequence components of the voltages and currents are also shown in Fig. 3.24(b) (denoted by the dashed lines). These curves were calculated following the same procedure discussed previously for the three-phase fault case. However, in this case, the circuit of Fig. 3.22 is used to calculate the voltages and currents immediately after the fault and the circuit of Fig. 3.23 is used to calculate the

steady-state voltages and currents after the fault. The calculated and simulated values show good agreement in this case.

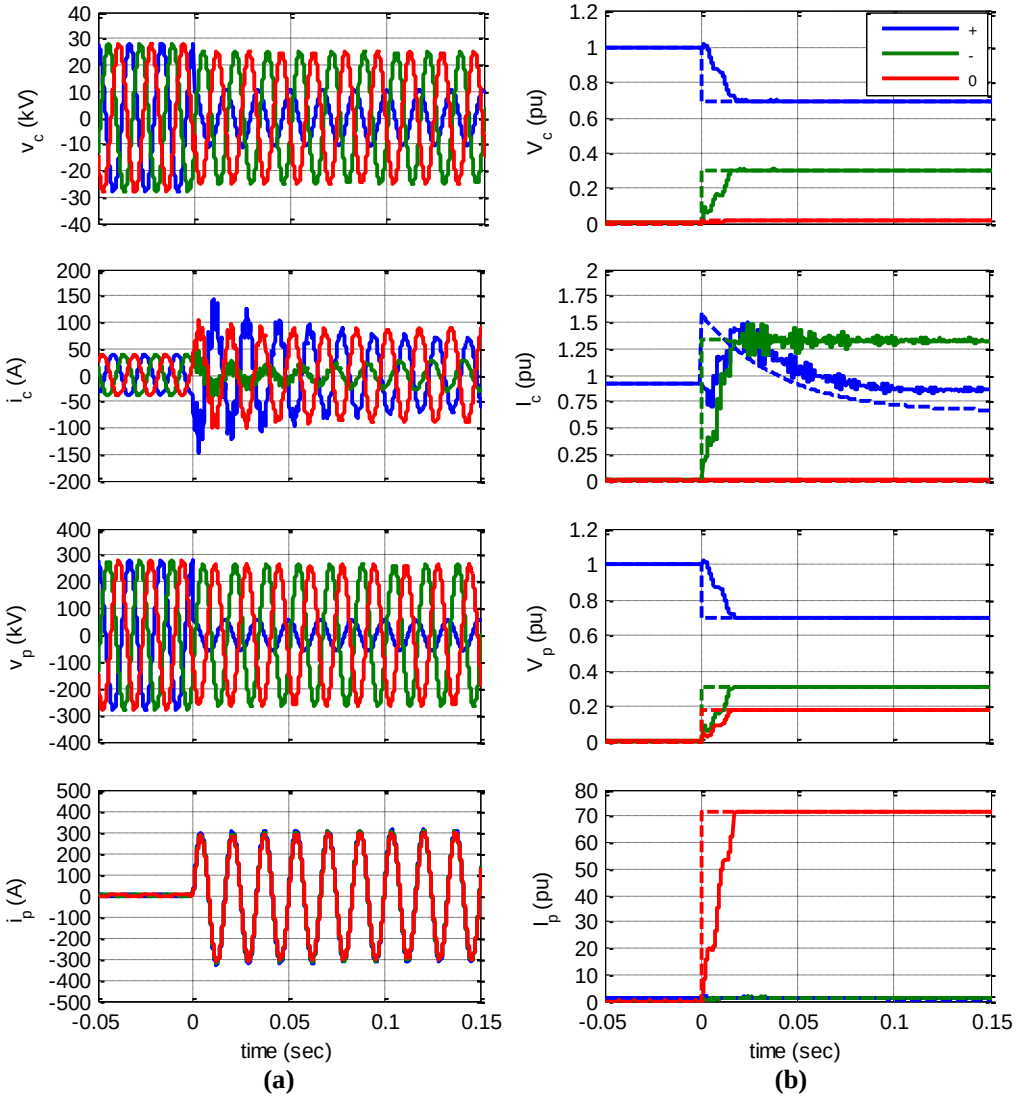


**Fig. 3.24: (a) Transient simulation results of the voltages and currents for a single-phase fault on the transmission system and (b) comparison of the calculated and simulated sequence components of these voltages and currents (solid = simulated, dashed = calculated).**

## 3.7. Multi-Machine Studies with a Type 1 Wind Farm

Short-circuit studies on the small Type 1 wind farm shown in Fig. 3.25 are described in this section. This network consists of two collector feeders, the first of

which contains four WTGs (of equal rating) at the end of the feeder. The second collector feeder contains three WTGs at the end of the feeder. The two collector-feeder cables are assumed to be of equal length. Additionally, it is assumed that the WTGs on each feeder are equally spaced apart (in other words, the cable impedance in between the WTGs is equal). All of the cables are represented as π-equivalent circuits, with parameters given in Appendix C. The same parameters are used for each of the WTGs, and they are all assumed to be generating rated power for these studies. Each of the WTGs has PFCCs at its terminals. The PFCCs for each WTG are of equal capacitance. The substation transformer is connected in wye-delta-wye configuration, and the PCC is assumed to be at the substation transform high-voltage winding. The transmission system parameters are given in Appendix C. Faults on both the collector system and on the transmission system are analyzed in this section.

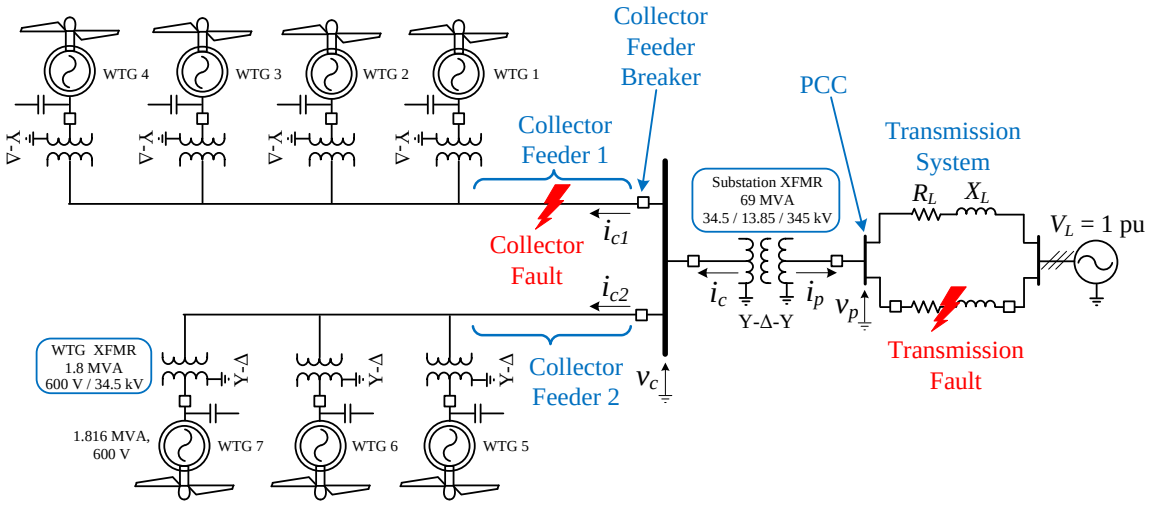


**Fig. 3.25: Multi-machine Type 1 wind farm used for short-circuit studies.**

Transient simulation results for a phase-A-to-ground fault on collector cable one are shown in Fig. 3.26(a). The sequence components of these voltages and currents from the cosine filter algorithm are shown in Fig. 3.26(b) (denoted by the solid lines). The collector bus voltage $v_c$ clearly indicates that the phase A voltage drops after the fault.

The total collector system currents $i_c$ show very high magnitude in phase A (blue line). In terms of the sequence components, the collector system currents contain nearly 12 per unit magnitude in the positive-, negative-, and zero-sequence values. The current injected by the second collector cable $i_{c2}$ is much smaller in magnitude than the total collector current, indicating that the transmission system is supplying most of the short-circuit current. Because of this particular winding configuration for the substation transformer, the transmission system "sees" very little zero-sequence current, as indicated by the plots of $\vec{I}_p$.

The sequence-network circuit for the system shown in Fig. 3.25 is much too complicated to draw succinctly here. However, the sequence-network circuit was built in Matlab's SimPowerSystem (SPS) software, similar to the single-machine network discussed in the previous sub-section. The steady-state solver in the SPS toolbox was used to calculate the phasor quantities of the voltages and currents for both the transient and steady-state sequence-network circuits. The sequence-network circuits used for each of the seven WTGs shown in Fig. 3.25 are displayed in Fig. 2.8. These voltages $\vec{V}'$ for each of the WTGs are calculated using the same procedure described in the previous section, except each of the seven WTG stator terminals is used as a bus in the load-flow calculation. Thus, the sequence-network circuit for this network contains eight voltages sources, including seven for each of the seven WTGs and one for the infinite bus voltage source. Following the same procedure described in the previous sub-section for the single-machine system, the pre-fault and post-fault phasor calculation results for the case of a phase A-to-ground fault on the collector system of the network in Fig. 3.25 are also plotted in Fig. 3.26(b). Good agreement can be seen between the simulated sequence components and the calculated values, indicating that representing the Type 1 WTG with these simplified circuits gives a good estimate of the short-circuit behavior.

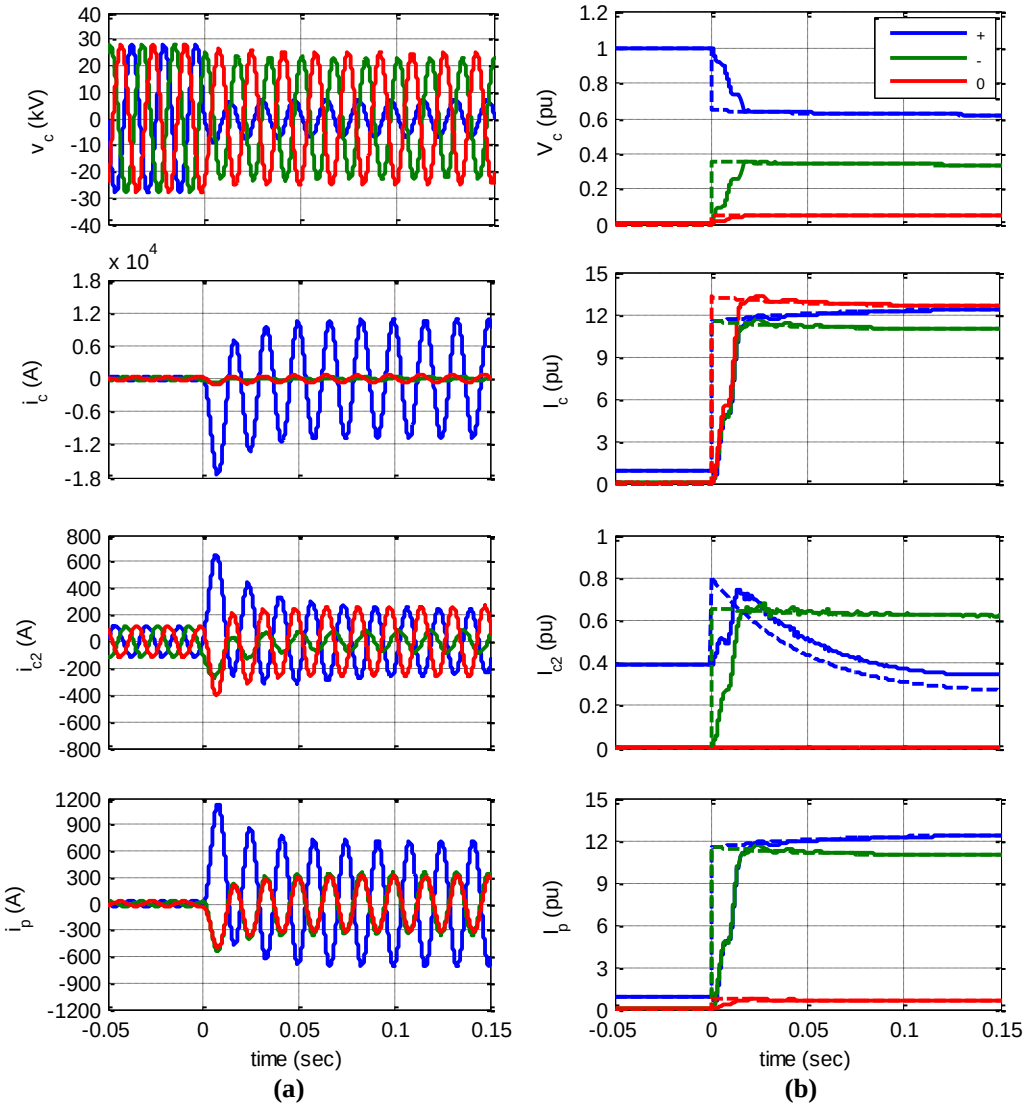


**Fig. 3.26: (a) Transient simulation results of the voltages and currents for a single-phase fault on the collector system of the multi-machine system and (b) comparison of the calculated and simulated sequence components of these voltages and currents (solid = simulated, dashed = calculated).**

Simulation results for the case of a phase-B-and-C-to-ground fault on the transmission system are shown in Fig. 3.27(a) and the corresponding sequence components are shown in Fig. 3.27(b). In this case, a negligible amount of zero-sequence current flows within the wind farm collector system, as seen in the plot of $\vec{I}_c$. However, the wind plant does inject both positive- and negative-sequence current into the fault in the transmission system. From the plot of $\vec{I}_p$, mostly zero-sequence current flows at the

plant interconnection point on the substation transformer due to the low-impedance ground path provided by this transformer. Calculation results of the sequence components of these voltages and currents are also shown in Fig. 3.27(b). These calculations were performed in the same way described for the previous case. Good agreement between the calculated and simulated sequence components can be seen.

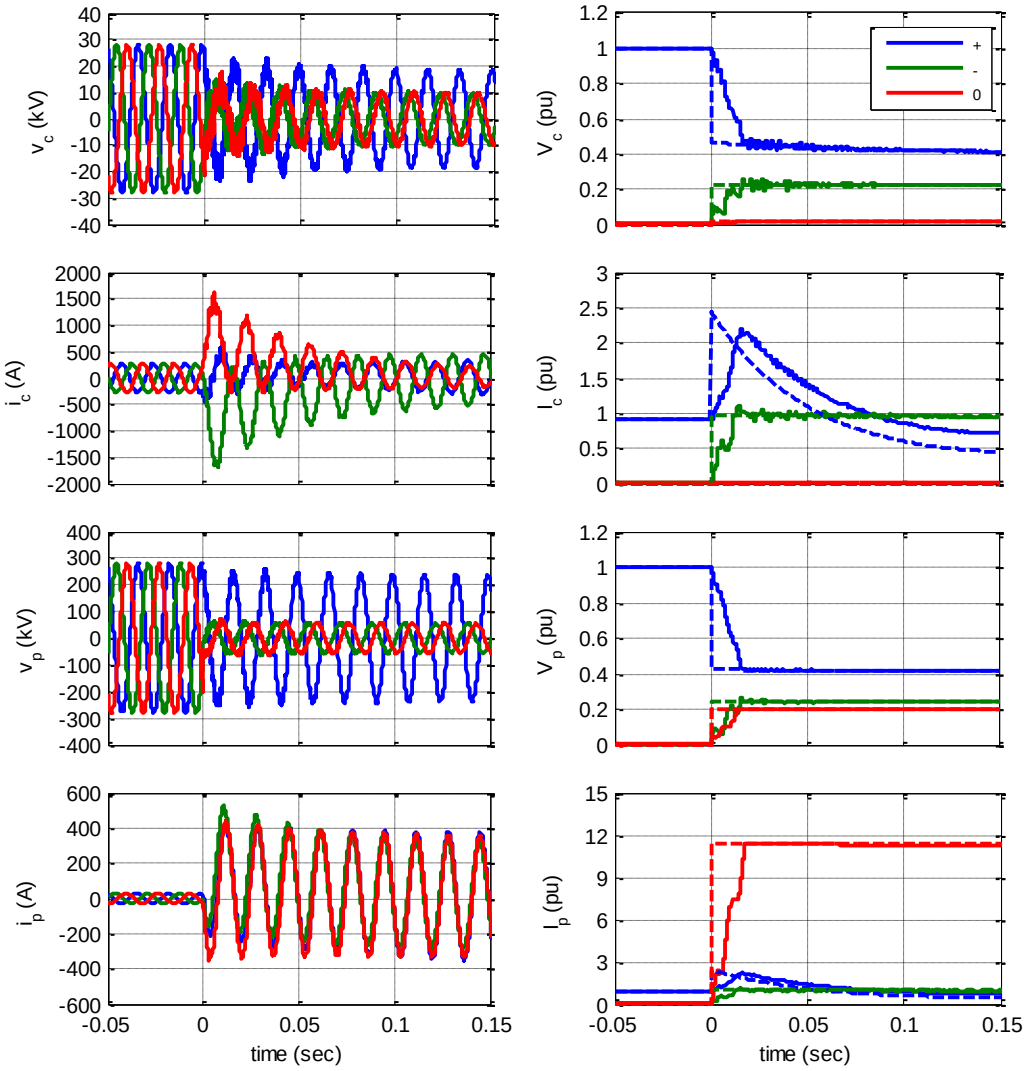


**Fig. 3.27: (a) Transient simulation results of the voltages and currents for a two-phase-to-ground fault on the transmission system of the multi-machine system and (b) comparison of the calculated and simulated sequence components of these voltages and currents (solid = simulated, dashed = calculated).**

## 3.8. Multi-Machine Studies with a Type 2 Wind Farm

The Type 2 WTG is analyzed in this section using the same network as the Type 1 wind farm shown in Fig. 3.25. All network parameters are identical to the values used for the Type 1 WTG studies discussed in the previous section. Additionally, all of the induction machine parameters used for the Type 2 WTG are identical to the parameters of the Type 1 WTG, with the exception of the rotor resistance. The Type 2 WTGs in this study are assumed to be operating at their highest slip rating (-10% slip), and an external rotor resistance is inserted into the rotor circuit which gives rated electric power output at the stator terminals at this operating slip, where the rated power output of the Type 2 is the same as the Type 1 discussed in the previous section. This external rotor resistance was found to be 0.0923 per unit, which is roughly 10 times the rotor winding resistance.

Simulation results for the case of a three-phase fault on the transmission system on the Type 2 wind farm are shown in Fig. 3.28(a). The voltage at the PCC and collector system ($v_p$ and $v_c$) drops to roughly 20% of the rated value during this fault. The total collector current $i_c$ and total plant current $i_p$ sharply increase after the fault, but the AC component of the current is quickly damped after the fault occurs due to the high value of rotor resistance. The short-circuit currents appear almost entirely as DC components for a three-phase fault. This behavior is reflected in the sequence components of the short-circuit currents (shown in Fig. 3.28(b), denoted by a solid line), where the positive-sequence current in both $\vec{I}_p$ and $\vec{I}_c$ briefly increases for one cycle after the fault, but quickly drops to roughly 0.2 per unit roughly two cycles after the fault.

Sequence-network calculations are performed on the Type 2 wind farm in the same way described in the previous section for the Type 1 wind farm. The same value of transient reactance is used for the Type 2 WTG as the Type 1 WTG, and the voltage behind transient reactance is calculated in the same way. The calculated results for this case are also shown in Fig. 3.28(b) (denoted by a dashed line). The time constant of

decay of for the Type 2 WTG is different than the Type 1 WTG because of the higher rotor resistance. This time constant of decay is given by

$$T_r' = \frac{L_r'}{R_r + R_{r,ext}}, \tag{3.10}$$

where $R_r$ is the rotor winding resistance and $R_{r,ext}$ is the external rotor resistance. The rotor transient inductance $L_r$' is the same as calculated in (3.9). While the calculated and simulated positive-sequence voltages show good agreement, significant difference between the calculated and simulated positive-sequence currents can be seen in Fig. 3.28(b). This discrepancy is primarily due to the error from the sampling and cosine filter algorithm used to obtain the phasor quantities from the simulation results. Because the AC component in the current decays so rapidly with a Type 2 WTG, the algorithm cannot accurately determine this phasor's magnitude. However, after roughly two cycles, good agreement between the calculated and simulated positive-sequence currents can be seen. This is because the current waveforms have reached a quasi-steady state after only two cycles. This rapid decay in the currents is the key difference between the Type 1 and Type 2 WTG.

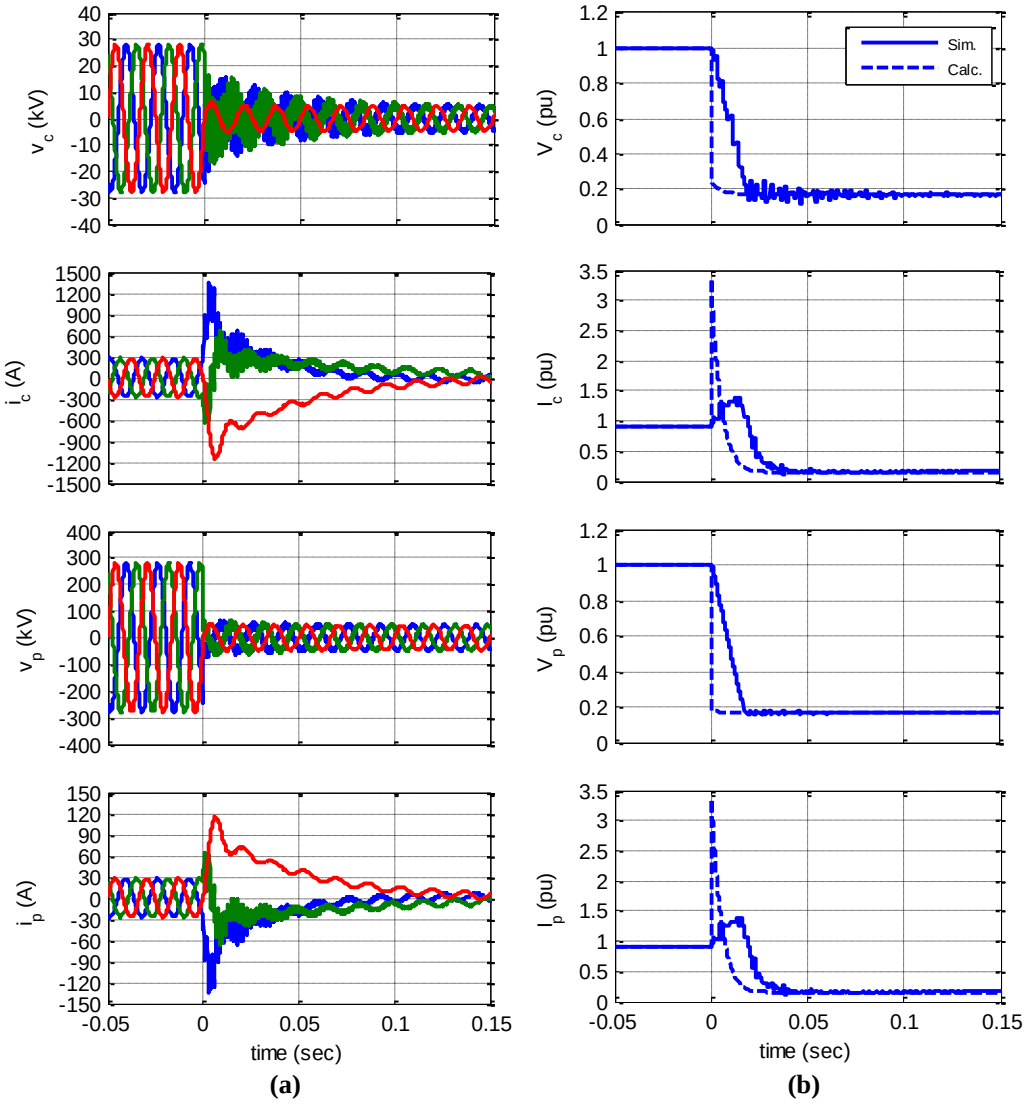


**Fig. 3.28: (a) Transient simulation results of the voltages and currents for a three-phase fault on the transmission system of the multi-machine system and (b) comparison of the calculated and simulated positive-sequence components of these voltages and currents (solid = simulated, dashed = calculated).**

Simulation results for the case of a line-to-line fault (phase B to C) on the transmission system in the network of Fig. 3.25 are shown in Fig. 3.29(a) and the corresponding sequence components are shown in Fig. 3.29(b) (denoted by the solid line). In this case, no zero-sequence current flows in the network since there is no ground path in a phase-to-phase fault. From the results in Fig. 3.29(b), it can be seen that large negative-sequence currents flow in both the collector system and at the PCC. However, the positive-sequence currents decrease rapidly due to the high rotor resistance.

The sequence-network calculations for this type of fault are also shown in Fig. 3.29(b) (denoted by the dashed line). Good agreement can be seen between the calculated and simulated voltages and currents, particularly two cycles after the fault occurrence. However, it is difficult to conclude that this model is accurate for the first two cycles after the fault, since the sampling and cosine filter estimation of the phasor magnitudes is highly unreliable for such a fast transient.

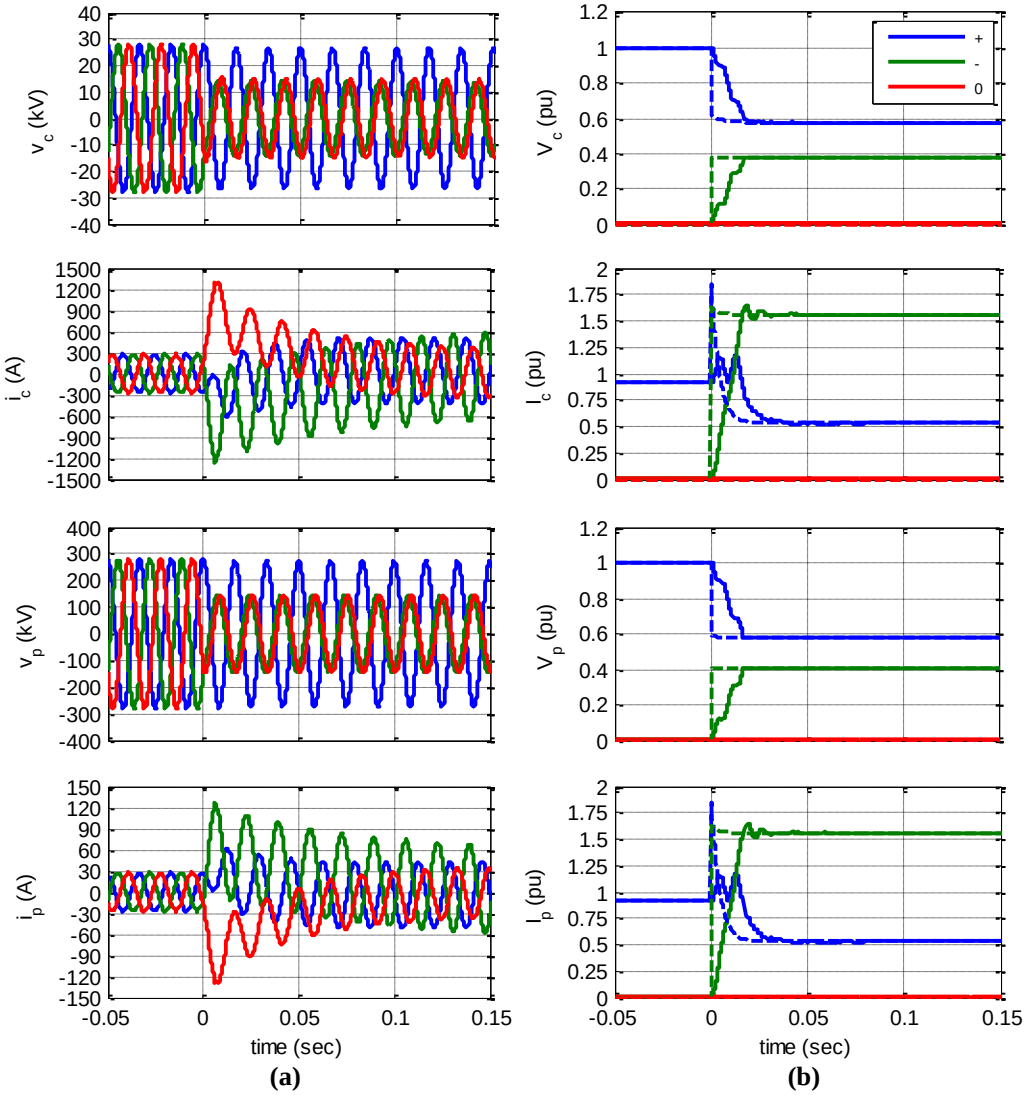


**Fig. 3.29: (a) Transient simulation results of the voltages and currents for a line-to-line fault on the transmission system of the multi-machine system and (b) comparison of the calculated and simulated sequence components of these voltages and currents (solid = simulated, dashed = calculated).**

## 3.9. Conclusions

The work presented in this chapter shows that the conventional sequence-network model of induction machines gives a good approximation to the short-circuit currents of Type 1 WTGs. An improved sequence-network model of the induction machine was proposed in this chapter that can be used if a high degree of accuracy in the short-circuit calculation is required. This improved sequence-network model accounts for the negative-sequence voltage induced in the machine during unbalanced faults, which is otherwise assumed to be zero in the conventional sequence-network circuit. Transient simulations were compared with experimental results on a lab-scale Type 1 WTG, and found to show good agreement during unbalanced faults, but show significant discrepancy in the peak short-circuit current magnitude for a balanced three-phase fault. Leakage-flux saturation is believed to be the cause of this discrepancy. It is unclear whether these same effects would be present in utility-scale induction machines used in Type 1 WTGs, as the overall design characteristics of the magnetic core can be significantly different. In worst-case short-circuit calculations, these effects may need to be considered. However, faults further away from the machine terminals result in lower fault current magnitudes, which reduce the impact of any leakage-saturation effects.

Transient simulation results described in this chapter on realistic utility-scale Type 1 WTG networks show good agreement to sequence-network calculations performed using the conventional sequence-network model. Therefore, this indicates that the previously developed models for Type 1 WTGs are a good representation of the short-circuit-current characteristics of these types of WTGs. Calculations on a realistic Type 2 WTG network using the same sequence-network model for the Type 2 WTG as the Type 1 WTG indicate that the decay of the current must be accounted for in Type 2 WTG networks. However, the same sequence-network circuits can be used for the short-circuit calculations.

The short-circuit behavior of Type 1 and Type 2 WTGs resembles that of a conventional synchronous generator, since these types of WTGs can be represented as a voltage source behind a reactance. However, modern WTGs consist mostly of Type 3 and Type 4 WTGs, which are discussed in the next two chapters. These types of WTGs do not behave like a conventional synchronous generator during short circuits; thus, a new type of short-circuit model must be developed for these WTGs.

# CHAPTER 4: TYPE 3 WIND-TURBINE GENERATOR

## 4.1. Introduction

The Type 3 wind-turbine generator (WTG) is different from the Type 1 and Type 2 WTGs by the power-electronic converter connected to the rotor windings of the wound-rotor induction machine (WRIM), as shown in Fig. 4.1. The ability to control the rotor currents in the Type 3 WTG presents many operational benefits over the Type 1 and 2 WTGs, including higher energy production and a decrease in torsional stress on the drive train due to wind gusts. However, the Type 3 WTG has a much more complicated short-circuit behavior than the Type 1 and 2 WTGs due to this power-electronic converter. The control of this power-electronic converter strongly dictates the short-circuit behavior of the Type 3 WTG; thus, a simplified short-circuit model of this type of WTG must account for these controls. Another complication in analyzing the short-circuit behavior of the Type 3 WTG is that it can change topology during the fault because of the AC crowbar protection. In this case, the Type 3 WTG transitions from a controlled topology (AC crowbar off) to an uncontrolled topology (AC crowbar on), and the short-circuit currents are determined by the physics of the WRIM.

The controls of the grid-side converter (GSC) and rotor-side converter (RSC) in Fig. 4.1 are described in detail in this chapter, along with a design methodology used to tune the controller parameters. A sequence-network circuit of the Type 3 WTG is proposed in this chapter based on simplifying assumptions regarding the GSC and RSC controls. The control limitations of the RSC due to the voltages induced on the rotor windings are also discussed in detail. Experimental results of a lab-scale Type 3 WTG during short-circuit tests are described and compared with equivalent PSCAD transient simulations. Similarly, transient simulations of realistic WTG networks are compared

with calculation results using the proposed sequence-network circuits, and shown to give good results.

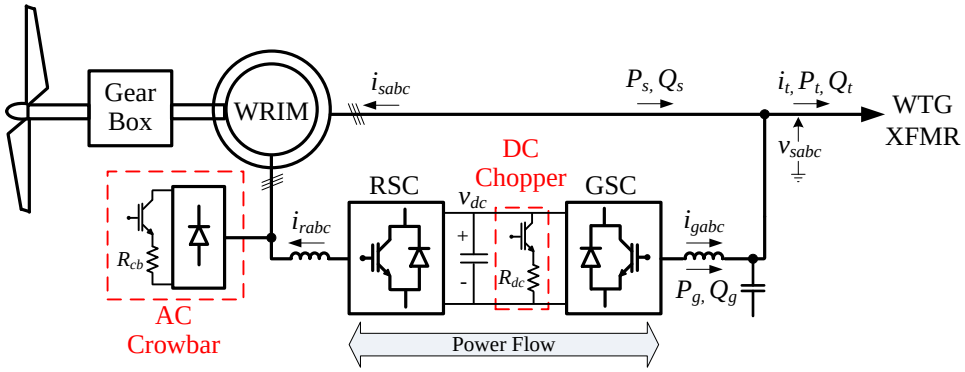


**Fig. 4.1: Circuit diagram of Type 3 WTG.**

## 4.2. GSC and RSC Controller Design

The short-circuit behavior of the Type 3 WTG is highly dependent on the controls of the GSC and RSC, as discussed in Chapter 2. Therefore, the methodology for designing the proportional-integral (PI) controllers used in the Type 3 WTG is described in this section. The same control topology for the GSC and RSC discussed in Chapter 2 (see Fig. 2.13 and Fig. 2.14) is used here. Approximate linear transfer functions for the various electrical and mechanical systems of the Type 3 WTG are developed, and linear control theory is used to tune the various PI controllers in the GSC and RSC. The proposed sequence-network model of the Type 3 WTG (discussed in the next section) is developed based on simplifying assumptions regarding the developed controls.

The following key assumptions are made in the design of the PI controller parameters:

1. The switching transients and harmonics are negligible (only the fundamental component is considered).
2. The DC-link voltage limitations are negligible.

3. Sampling and control delays are negligible.
4. The feed-forward compensation terms provide perfect decoupling of the d- and q-axis current controls.
5. The grid voltage is fixed at its nominal magnitude (1 per unit).

These assumptions are used to develop linearized models of the system dynamics for the design of the PI controller parameters. However, in the hardware and transient simulation results discussed in later sections, the nonlinearities of the actual system affect the results.

### *4.2.1. GSC Inner Current-Loop Controllers*

The simplified representation of the GSC shown in Fig. 4.2 is used to develop the dynamic equations of the GSC currents. Both the GSC voltages $v_{gabc}$ and the stator terminal voltage $v_{sabc}$ are represented as ideal fundamental-frequency, three-phase voltage sources. The inner current-control loops used to control the d- and q-axis components of the GSC current are shown in Fig. 4.3. The dynamic equations of the GSC currents in *abc* coordinates are given by

$$v_{gabc} = R_g i_{gabc} + L_{gf}\, p i_{gabc} + v_{sabc}\,, \tag{4.1}$$

where $i_{gabc}$ is the three-phase GSC output current. $R_g$ represents the resistance of the phase conductors and the parasitic resistance of the GSC filter inductors, and is typically

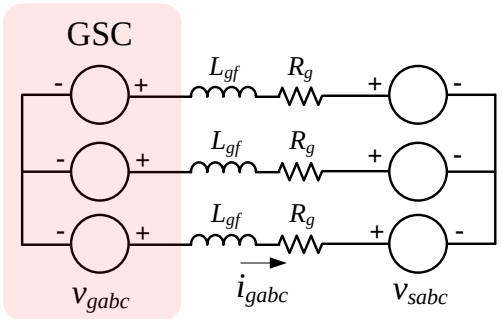


**Fig. 4.2: Simplified three-phase circuit of GSC.**

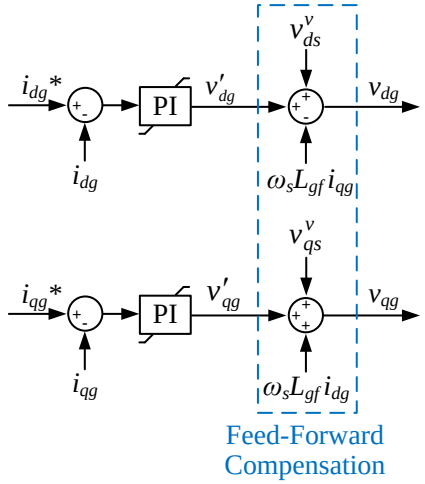


**Fig. 4.3: GSC inner-current control loops.**

a small resistance. $L_{gf}$ is the GSC filter inductance that is designed to reduce the switching ripple of AC output currents of the GSC. Referring the *abc* quantities to a synchronously rotating reference frame oriented with stator voltage, the GSC current dynamic equations in *dq* notation are given by [41] [42]

$$\begin{aligned} v_{dg} &= R_g i_{dg} - \omega_s L_{gf} i_{qg} + L_{gf}\, p i_{dg} + v^v_{ds} \\ v_{qg} &= R_g i_{qg} + \omega_s L_{gf} i_{dg} + L_{gf}\, p i_{qg} + v^v_{qs} \end{aligned}, \tag{4.2}$$

where the '*v*' superscript in the *dq* stator voltages indicates that these voltages were transformed using a reference frame oriented with the stator voltage (as opposed to the RSC controls, which use *dq* stator voltages transformed using a reference frame oriented with the stator flux). The *dq* equations in (4.2) are cross coupled, and can be decoupled by introducing fictitious voltages $v_{dg}$' and $v_{qg}$', given by

$$\begin{aligned} v'_{dg} &= v_{dg} + \omega_s L_{gf} i_{qg} - v^v_{ds} \\ v'_{qg} &= v_{qg} - \omega_s L_{gf} i_{dg} - v^v_{qs} \end{aligned}. \tag{4.3}$$

Solving for $v_{dg}$ and $v_{qg}$ in (4.3) and inserting into (4.2), the dynamic equations of the GSC currents become

$$\begin{aligned} v'_{dg} &= R_g i_{dg} + L_{gf}\, p i_{dg} \\ v'_{qg} &= R_g i_{qg} + L_{gf}\, p i_{qg} \end{aligned}. \tag{4.4}$$

Thus, the GSC *dq* current equations are now decoupled, which allows for decoupled control of each of these *dq* currents. The feed-forward compensation terms in Fig. 4.3 provide this decoupling in the practical implementation of the control loops.

Taking the Laplace transform of the d-axis equation in (4.4) and rearranging terms, the transfer function of the d-axis GSC current is given by

$$\frac{I_{dg}}{V'_{dg}} = \frac{1/L_{gf}}{s + R_g / L_{gf}}. \tag{4.5}$$

A similar relationship exists for the q-axis GSC current and voltage. Thus, from (4.5), the relationship between the d-axis current and the fictitious d-axis voltage $V_{dg}$' is represented by a first-order transfer function. For the control topology shown in Fig. 4.3, a PI controller with negative feedback is used, and this fictitious voltage $V_{dg}$' is given by

$$V'_{dg} = (I^*_{dg} - I_{dg})\left(K_{pg} + \frac{K_{ig}}{s}\right) = (I^*_{dg} - I_{dg})\left(\frac{K_{pg}(s + K_{ig}/K_{pg})}{s}\right), \tag{4.6}$$

where $K_{pg}$ is the proportional gain of the inner current loop PI controller, $K_{ig}$ is the integral gain, and $I_{dg}$* is the d-axis current command supplied from the DC-link voltage controller. Thus, assuming perfect decoupling of the d- and q-axis currents, the control diagram of Fig. 4.3 can be simplified and represented in block-diagram form as shown in Fig. 4.4. The total open-loop transfer function of the d-axis inner current loop is found by multiplying the result of (4.5) and (4.6), given by

$$GH_o(s) = \frac{I_{dg}}{I^*_{dg} - I_{dg}} = \frac{K_{pg}/L_{gf}(s + K_{ig}/K_{pg})}{s(s + R_g/L_{gf})}. \tag{4.7}$$

It can be shown that the corresponding closed-loop transfer function of the d-axis inner current loop is given by

$$GH_c(s) = \frac{I_{dg}}{I^*_{dg}} = \frac{GH_o}{1 + GH_o} = \frac{K_{pg}/L_{gf}(s + K_{ig}/K_{pg})}{s^2 + s(R_g + K_{pg})/L_{gf} + K_{ig}/L_{gf}}. \tag{4.8}$$

The numerical values of the parameters in (4.8) are given in Appendix A.

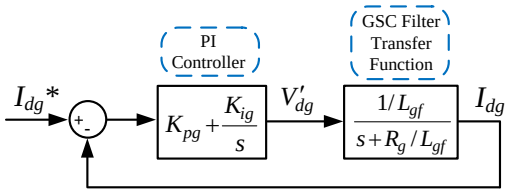


**Fig. 4.4: Block diagram of GSC inner current-control loop.**

Any linear control design technique, such as Bode design or root-locus design, can be used to choose the proper value of $K_{pg}$ and $K_{ig}$ to achieve the desired closed-loop control dynamics. In this work, the controller parameters are tuned by first arbitrarily choosing a value of $K_{pg}$ and $K_{ig}$ (such as one), and then using the Bode plot of the closed-loop transfer function of (4.8) to iteratively adjust $K_{pg}$ until the desired closed-loop control bandwidth is achieved. The closed-loop control bandwidth is defined here as the -3 dB frequency of the closed-loop transfer function in (4.8). The desired closed-loop bandwidth is chosen to be roughly one tenth of the GSC PWM switching frequency. For utility-scale WTGs, it is assumed that their switching frequencies are 2-4 kHz; thus, the closed-loop control bandwidths of the inner-current loops are designed to be roughly 200 Hz. Once the desired bandwidth is achieved, the value of $K_{ig}$ is adjusted until roughly 10% overshoot is seen in the step response of the closed-loop transfer function. This control design procedure is carried out in Matlab using the built-in "bode" and "step" functions. The resulting Bode magnitude plot of the closed-loop system is shown in Fig. 4.5 and the step response of the closed-loop system is shown in Fig. 4.6. Note that the control bandwidth has some dependence on the integral gain $K_{ig}$, but these effects are rather insignificant when compared to the dependence on $K_{pg}$. Because the transfer function of the q-axis current is identical to that of the d-axis, the same controller parameter values used for the d-axis current loop can be used for the q-axis current loop to achieve the same control response.

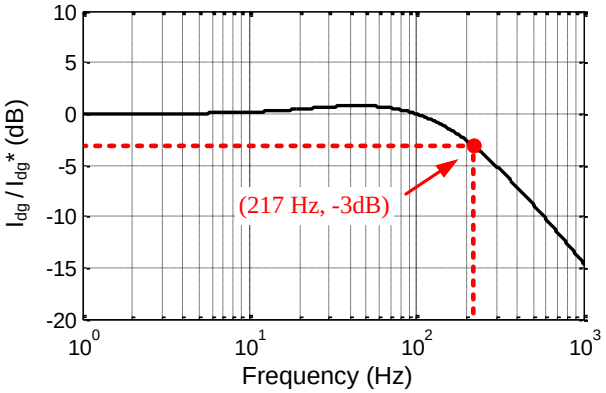


**Fig. 4.5: Bode plot of GSC closed-loop current control system.**

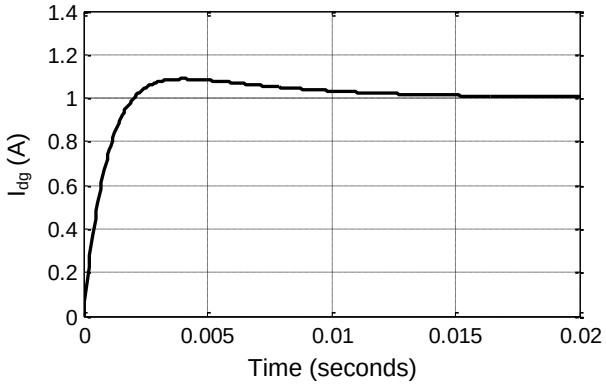


**Fig. 4.6: Step response of GSC closed-loop current control system.**

## *4.2.2. DC-Link Voltage Controller*

The DC-link circuit is shown in Fig. 4.7, and the typical DC-link control loop is shown in Fig. 4.8(a). The differential equation describing the DC-link capacitor dynamics is given by

$$i_{ro} - i_{go} = C\frac{dv_{dc}}{dt}, \tag{4.9}$$

where $i_{ro}$ and $i_{go}$ are the DC currents from the RSC and GSC, respectively, $C$ is the DC-link capacitance, and $v_{dc}$ is the DC-link voltage. The real power transferred from the DC link to the GSC AC output can be written as [41] [42]

$$P_g = v_{dc} i_{go} = \frac{3}{2}(v_{ds}^v i_{dg} + v_{qs}^v i_{qg}) = \frac{3}{2} v_{ds}^v i_{dg}\,, \tag{4.10}$$

where the losses of the GSC are neglected and it is assumed that $v_{qs}{}^v$ is zero due to the orientation of stator voltage reference frame. Equation (4.10) relates the DC-link power to the AC real power output of the GSC. Assuming that the stator voltage is fixed, the real power generated (or consumed) by the GSC can be controlled by $i_{dg}$. The relationship between $i_{dg}$ and the DC-link voltage is found by combining (4.9) and (4.10), and is given by

$$P_g = v_{dc} i_{go} = v_{dc}\left(i_{ro} - C\frac{dv_{dc}}{dt}\right) = P_r - \frac{1}{2} C \frac{dv_{dc}^2}{dt} = \frac{3}{2} v_{ds}^v i_{dg}\,, \tag{4.11}$$

where $P_r = v_{dc} i_{ro}$. Equation (4.11) contains a $v_{dc}{}^2$ term, making the relationship between the DC-link voltage and $i_{dg}$ nonlinear. This is highly undesirable, as it prevents the use of linear control theory to tune the PI controllers of the DC-link voltage controller. However, by introducing a fictitious DC-link voltage of $v_{dc}' = v_{dc}{}^2$, (4.11) can be rewritten as

$$C\frac{dv_{dc}'}{dt} = 2P_r - 3v_{ds}^v i_{dg}\,. \tag{4.12}$$

This linearization of the relationship between $v_{dc}$ and $i_{dg}$ is achieved in the practical implementation of the control using the alternative control loop for the DC-link voltage shown in Fig. 4.8(b). This alternative is required since the dynamic equation of (4.12) is now in terms of $v_{dc}'$, not $v_{dc}$. Thus, using this mathematical "trick", the actual parameter being controlled is the *square* of the DC-link voltage. This technique has the advantage that the PI controllers can be designed using linear control theory. However, a similar control response can be achieved using the control loop shown in Fig. 4.8(a), except there are no straightforward ways of analytically determining the PI controller parameters.

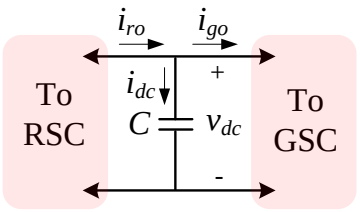


**Fig. 4.7: DC-link circuit.**

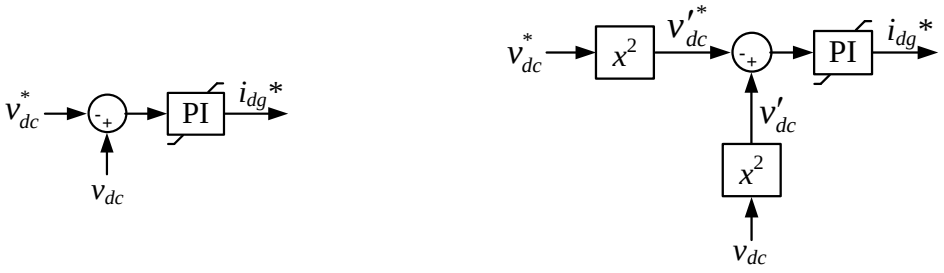


**Fig. 4.8: Two options for DC-link voltage control loop.**

The DC-link voltage control loop in block-diagram form is shown in Fig. 4.9. The PI controller for the DC-link voltage is tuned with the assumption that the rotor power $P_r$ does not change. For this assumption, only a change in $i_{dg}$ results in a change in the DC-link voltage. Thus, the $P_r$ term is neglected in (4.12). Taking the Laplace transform of (4.12), a transfer function between $i_{dg}$ and this fictitious DC-link voltage can be found, and is given by

$$\frac{V_{dc}'}{I_{dg}} = -\frac{3v_{ds}^v}{Cs}. \tag{4.13}$$

The DC-link PI controller output is the reference d-axis current for the GSC inner current-control loop, and is given by

$$I_{dg}^* = (V_{dc}' - V_{dc}'^*)\left(K_{pv} + \frac{K_{iv}}{s}\right) = -(V_{dc}'^* - V_{dc}')\left(\frac{K_{pv}(s + K_{iv}/K_{pv})}{s}\right). \tag{4.14}$$

The dynamics of the inner current-control loops are assumed to be much faster than the dynamics of the DC-link voltage outer-control loop; thus, it is assumed that $I_{dg}^* = I_{dg}$. The total open-loop transfer function of the DC-link voltage control loop can be found by inserting (4.14) into (4.13), given by

$$\frac{V'_{dc}}{(V'^{*}_{dc} - V'_{dc})} = \frac{3v^{v}_{ds} K_{pv} (s + K_{iv} / K_{pv})}{Cs^2}. \tag{4.15}$$

The corresponding closed-loop transfer function is given by

$$\frac{V'_{dc}}{V'^{*}_{dc}} = \frac{3v^{v}_{ds} K_{pv} / C (s + K_{iv} / K_{pv})}{s^2 + s3v^{v}_{ds} K_{pv} / C + 3v^{v}_{ds} K_{iv} / C}. \tag{4.16}$$

The numerical values of these parameters are given in Appendix A.

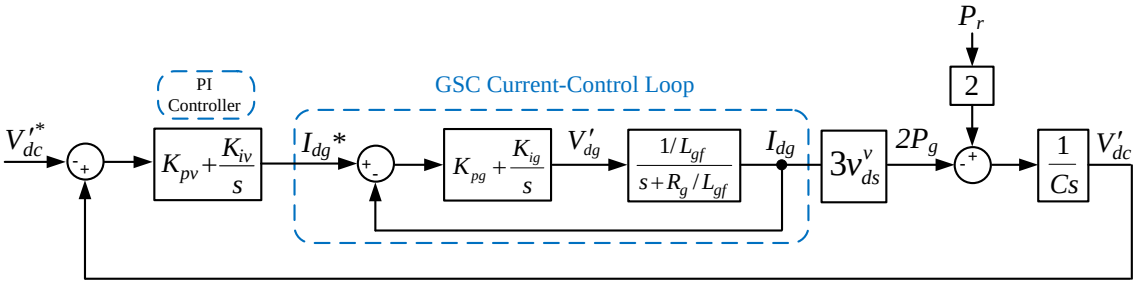


**Fig. 4.9: Block diagram of DC-link voltage-control loop.**

From the closed-loop transfer function of (4.16), the PI controller gains can be tuned in the same way described in the previous sub-section for the GSC current-loop controllers. However, note that the closed-loop dynamics of DC-link voltage controller depend on the stator voltage $v_{ds}^{v}$. In the design of this controller, it is assumed that this voltage is fixed at the rated value. However, in practice, this voltage can vary by ± 5% in normal operating conditions. The transfer function in (4.16) represents a linearized model of the system around the operating point of nominal stator voltage. In practice, however, the dynamics and control response of this system change depending on the operating conditions. However, for ± 5% changes in the stator voltage magnitude, these changes in the dynamics are not significant.

For this work, it is assumed that the closed-loop bandwidth of the DC-link voltage control is limited to one tenth of the inner current-loop bandwidth. Choosing a high bandwidth for this control has the benefit of "tight" control of the DC-link voltage. However, there are a few disadvantages to choosing a high bandwidth controller. In the presence of stator voltage unbalance (whether caused by an unbalanced fault or just normal system unbalance), 120 Hz oscillations appear in the DC-link voltage. These oscillations appear in the DC-link voltage feedback, and can potentially cause the controller to inject a 120 Hz reference d-axis current command, which results in distorted currents being injected into the grid. Oscillations in the DC-link voltage at other frequencies can occur due to ripple in the power from the RSC, which cause machine transients affecting the RSC to couple over to the GSC. To minimize these effects, the controller proportional gain $K_{pv}$ is chosen such that the Bode plot of the *open-loop* transfer function of (4.15) has roughly -30 dB gain at 60 Hz so that these ripple components in the DC-link voltage cause minimal distortion in the currents injected by the GSC. The integral gain $K_{iv}$ is chosen by iteratively adjusting its value until the *closed-loop* step response has roughly 10% overshoot. Designing the PI controller gains $K_{pv}$ and $K_{iv}$ in this way, an inspection of the Bode plot of the *closed-loop* transfer function given in (4.16) yields a 2-3 Hz closed-loop control bandwidth, as shown in Fig. 4.10. The step response of the closed-loop system of (4.16) is shown in Fig. 4.11. Note that the numerical value of DC-link voltage plotted in Fig. 4.11 is not a realistic value, as the DC-link voltage can never be zero volts. However, because the closed-loop transfer function in (4.16) is a linear system, the same step response can be expected for any initial value of DC-link voltage and magnitude of step change. Thus, the plot of Fig. 4.11 gives a qualitative step response of the closed-loop system.

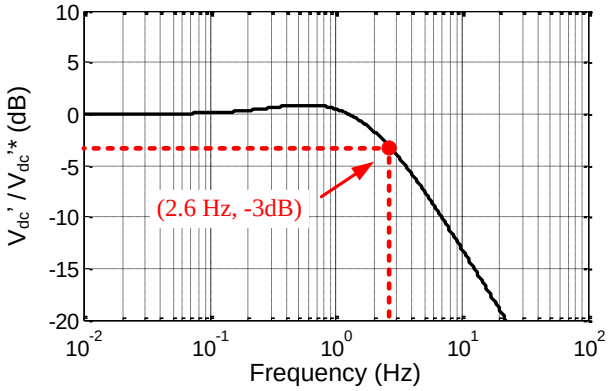


**Fig. 4.10: Bode plot of closed-loop DC-link voltage controller.**

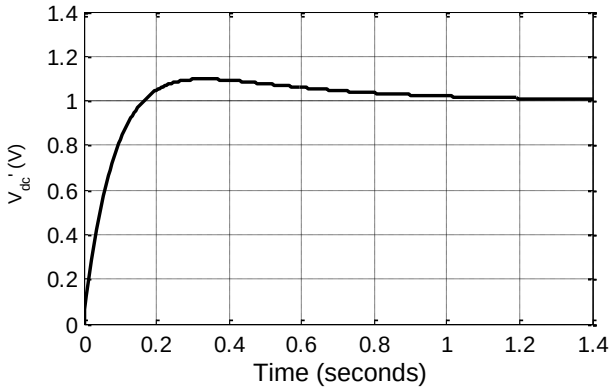


**Fig. 4.11: Step response of closed-loop DC-link voltage controller.**

### *4.2.3. RSC Inner Current-Loop Controllers*

Shown in Fig. 4.12 is a simplified circuit diagram of the RSC and its connection to the wound-rotor induction generator (WRIG) rotor windings. The inductance $L_{rf}$ is a filter inductance used to decrease the switching ripple in the rotor AC currents. This inductance is only needed if the rotor leakage inductance is not large enough to limit the switching ripple in the current to an acceptable level. The resistance $R_{rf}$ represents the conductor resistance and the parasitic resistance of the filter inductance. The control of the rotor currents is achieved using the control loops shown in Fig. 4.13. The differential

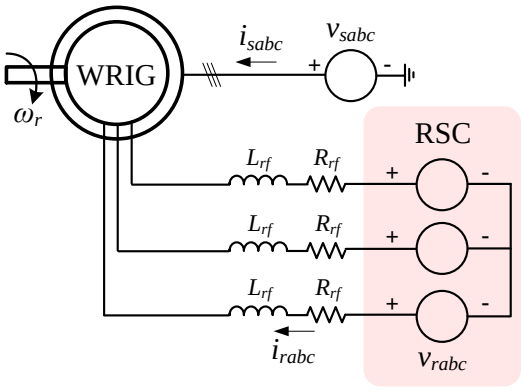


**Fig. 4.12: Simplified three-phase circuit of RSC.**

equations describing the induction machine electrical characteristics (as seen in (2.12)) in a synchronous reference frame oriented with the stator flux are given by

$$\begin{aligned} v_{ds}^{s} &= R_s i_{ds} - \omega_s \lambda_{qs} + p\lambda_{ds} \quad & v_{dr} &= R_r i_{dr} - (\omega_s - \omega_r)\lambda_{qr} + p\lambda_{dr} \\ v_{qs}^{s} &= R_s i_{qs} + \omega_s \lambda_{ds} + p\lambda_{qs} \quad & v_{qr} &= R_r i_{qr} + (\omega_s - \omega_r)\lambda_{dr} + p\lambda_{qr} \end{aligned}, \tag{4.17}$$

where the '*s*' superscript denotes that the *dq* stator voltages are oriented with the stator flux and the flux linkages in (4.17) are given by

$$\begin{aligned} \lambda_{ds} &= L_s i_{ds} + L_m i_{dr} \quad & \lambda_{dr} &= L_r i_{dr} + L_m i_{ds} \\ \lambda_{qs} &= L_s i_{qs} + L_m i_{qr} \quad & \lambda_{qr} &= L_r i_{qr} + L_m i_{qs} \end{aligned}. \tag{4.18}$$

The filter inductance $L_{rf}$ is lumped in with the rotor leakage inductance; thus, $L_r = L_{lr} + L_{rf} + L_m$. The resistance $R_{rf}$ is lumped in with the rotor winding resistance in (4.17) in a similar way. The rotor flux linkages in (4.18) can be rewritten as a function of the stator flux linkages by first solving for $i_{ds}$ and $i_{qs}$ in the stator flux linkage equations, and then substituting these values into the rotor flux linkage equations, given by

$$\begin{aligned} \lambda_{dr} &= L_r' i_{dr} + \frac{L_m}{L_s}\lambda_{ds} \\ \lambda_{qr} &= L_r' i_{qr} + \frac{L_m}{L_s}\lambda_{qs} \end{aligned}, \tag{4.19}$$

where $L_r$' is defined in (2.26). Taking the rotor voltage equations in (4.17) and replacing the flux linkages using the equations in (4.19), the rotor voltage equations become

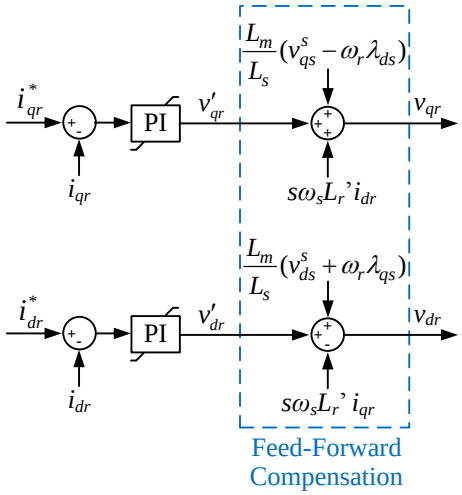


**Fig. 4.13: RSC inner current control loops.**

$$\begin{aligned} v_{dr} &= R_r i_{dr} - s\omega_s \frac{L_m}{L_s} \lambda_{qs} - s\omega_s L_r' i_{qr} + \frac{L_m}{L_s} p\lambda_{ds} + L_r' p i_{dr} \\ v_{qr} &= R_r i_{qr} + s\omega_s \frac{L_m}{L_s} \lambda_{ds} + s\omega_s L_r' i_{dr} + \frac{L_m}{L_s} p\lambda_{qs} + L_r' p i_{qr} \end{aligned} . \tag{4.20}$$

Solving for $p\lambda_{ds}$ and $p\lambda_{qs}$ in (4.17) and inserting the result into (4.20), the rotor voltage equations become

$$\begin{aligned} v_{dr} &= R_r i_{dr} + \omega_r \frac{L_m}{L_s} \lambda_{qs} - s\omega_s L_r' i_{qr} + \frac{L_m}{L_s} v_{ds}^s + L_r' p i_{dr} \\ v_{qr} &= R_r i_{qr} - \omega_r \frac{L_m}{L_s} \lambda_{ds} + s\omega_s L_r' i_{dr} + \frac{L_m}{L_s} v_{qs}^s + L_r' p i_{qr} \end{aligned} , \tag{4.21}$$

where the stator resistance $R_s$ has been neglected. The d- and q-axis rotor voltage equations in (4.21) are cross coupled, and can be decoupled by introducing artificial d- and q-axis voltages $v_{dr}$' and $v_{qr}$', given by

$$\begin{aligned} v'_{dr} &= v_{dr} - \omega_r \frac{L_m}{L_s} \lambda_{qs} + s\omega_s L_r' i_{qr} - \frac{L_m}{L_s} v_{ds}^s \\ v'_{qr} &= v_{qr} + \omega_r \frac{L_m}{L_s} \lambda_{ds} - s\omega_s L_r' i_{dr} - \frac{L_m}{L_s} v_{qs}^s \end{aligned} . \tag{4.22}$$

Solving for $v_{dr}$ and $v_{qr}$ in (4.22) and inserting the result into (4.21), the rotor voltage equations become

$$\begin{aligned} v'_{dr} &= R_r i_{dr} + L'_r p i_{dr} \\ v'_{qr} &= R_r i_{qr} + L'_r p i_{qr} \end{aligned} . \tag{4.23}$$

Thus, the d- and q-axis rotor equations are decoupled by substituting these artificial d- and q-axis voltages $v_{dr}$' and $v_{qr}$' into the machine dynamic equations. This decoupling is realized in the practical implementation of the controls by using the feed-forward compensation terms shown in the control loops in Fig. 4.13. The instantaneous stator-flux linkages in the feed-forward compensation terms are estimated using the equations given in Appendix E.

The rotor voltage dynamic equations in (4.23) are of the same form as the GSC dynamic equations given in (4.4). Therefore, a closed-loop transfer function using a PI controller for the inner RSC current loop can be derived in the same way for the RSC as was done for the GSC in (4.5) - (4.8). A block diagram of this closed-loop system is shown in Fig. 4.14. The PI controller gains for the RSC inner current loop can also be tuned in the same way as described for the GSC PI controllers. Similar to the GSC, the d- and q-axis transfer functions for the rotor current are identical; thus, identical control parameters are used for both the d- and q-axis rotor current loops. The controller gains of the RSC current controller are tuned to give roughly the same closed-loop control bandwidth and step response as the GSC current controller. The Bode plot and step response of this closed-loop system are shown in Fig. 4.15 and Fig. 4.16, where the numerical values of the parameters of this system are given in Appendix A.

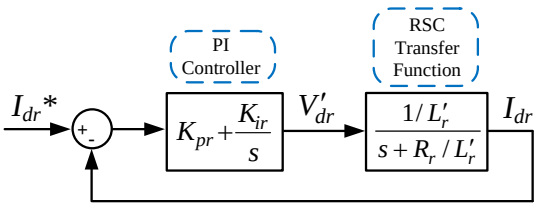


**Fig. 4.14: Block diagram of RSC current-control loop.**

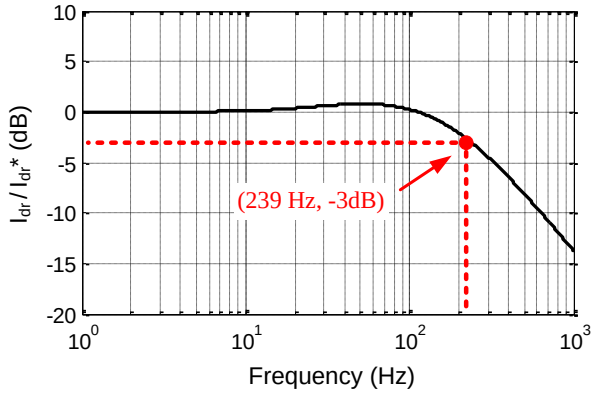


**Fig. 4.15: Bode plot of closed-loop RSC current controller.**

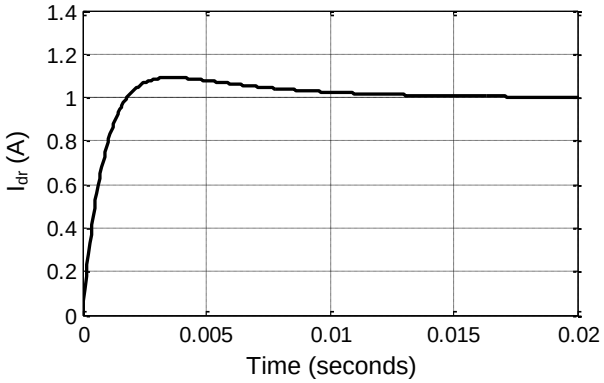


**Fig. 4.16: Step response of closed-loop RSC current controller.**

### *4.2.4. Rotor-Speed Controller*

Assuming the WTG rotor behaves as a single-mass mechanical system, the differential equation defining the mechanical rotor dynamics (as seen in (2.18)) is given by

$$Jp\omega_r = T_e - F\omega_r - T_m, \tag{4.24}$$

where $T_m$ is the mechanical torque supplied by the wind turbine. The electric torque can be written in terms of the machine flux linkages as [74]

$$T_e = \frac{3}{2}\frac{poles}{2}(i_{qs}\lambda_{ds} - i_{ds}\lambda_{qs}) = -\frac{3}{2}\frac{poles}{2}\frac{L_m}{L_s} i_{qr}\lambda_{ds}, \tag{4.25}$$

where it is assumed that $\lambda_{qs}$ is zero due to the stator-flux-oriented reference frame, which also makes $i_{qs} = -i_{qr}\,(L_m/L_s)$ from (4.18). If the stator voltage magnitude is assumed constant, then $\lambda_{ds}$ is constant. Thus, equation (4.25) indicates that the electric torque can be controlled by $i_{qr}$ in a stator-flux-oriented synchronous reference frame. To design a closed-loop controller for the rotor speed, a detailed model of the wind turbine torque-speed characteristics must be used. However, because the rotational dynamics of the wind turbine are much slower than the electrical dynamics, a detailed model of the wind turbine is of little interest in this work. Therefore, for this analysis, the mechanical torque from the wind turbine is assumed to be independent of speed ($T_m$ = constant). The rotor dynamic equation of (4.24) can be written as

$$p\omega_r = -K_\omega i_{qr} - F\omega_r / J - T_m / J\ , \tag{4.26}$$

where the gain $K_\omega$ is given by

$$K_\omega = \frac{3}{2}\frac{1}{J}\frac{poles}{2}\frac{L_m}{L_s}\frac{v_{qs}^s}{\omega_s}, \tag{4.27}$$

where $\lambda_{ds} \approx v_{qs}^s/\omega_s$ in steady-state, assuming the stator resistance is negligible (see (4.17)). Assuming the mechanical torque does not change for small changes in rotor speed, it is assumed that this term in (4.26) does not affect the *change* in the rotor speed; thus, this term is neglected in (4.26). Taking the Laplace transform of (4.26) and rearranging terms, the transfer function of the rotor speed is given by

$$\frac{\omega_r}{I_{qr}} = \frac{-K_\omega}{s + F/J}\,. \tag{4.28}$$

The block diagram of the rotor speed control system is shown in Fig. 4.17. The $I_{qr}$ reference is supplied by the rotor speed PI controller as shown in Fig. 4.17, and (in the Laplace domain) is given by

$$I_{qr}^* = (\omega_r - \omega_r^*)\left(K_{p\omega} + \frac{K_{i\omega}}{s}\right) = -(\omega_r^* - \omega_r)\left(\frac{K_{p\omega}(s + K_{i\omega}/K_{p\omega})}{s}\right). \tag{4.29}$$

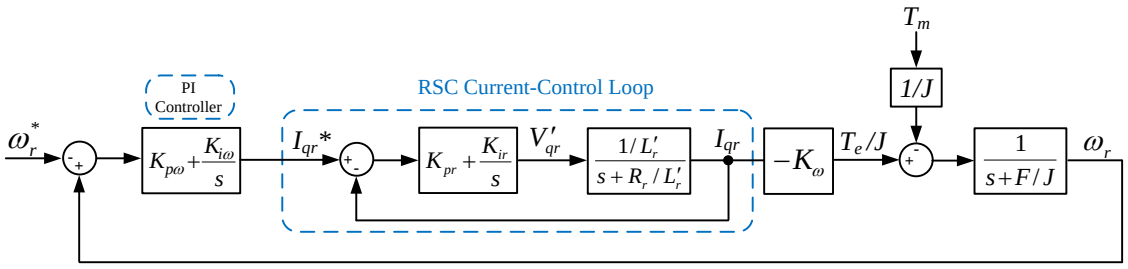


**Fig. 4.17: Block diagram of rotor speed controller.**

The dynamics of the inner-current control loop are assumed to be much faster than that of the outer-speed control loops; thus, it is assumed that $I_{qr}* = I_{qr}$. With this assumption, the open-loop transfer function of the speed control loop is found by combining (4.28) and (4.29) to give

$$\frac{\omega_r}{\omega_r^* - \omega_r} = \frac{K_\omega K_{p\omega}(s + K_{i\omega}/K_{p\omega})}{s(s + F/J)}. \tag{4.30}$$

It can be shown that the corresponding closed-loop transfer function is given by

$$\frac{\omega_r}{\omega_r^*} = \frac{K_\omega K_{p\omega}(s + K_{i\omega}/K_{p\omega})}{s^2 + s(K_\omega K_{p\omega} + F/J) + K_\omega K_{i\omega}}, \tag{4.31}$$

where the numerical values of the parameters in (4.31) are given in Appendix A. The PI controller gains for the speed-control loop can be set by choosing a value of $K_{p\omega}$ that gives the desired closed-loop control bandwidth and a value of $K_{i\omega}$ that gives the desired step response. Similar to the DC-link voltage controller, the upper limit to the control bandwidth of the speed controller is assumed to be one tenth of the RSC inner current loop bandwidth. However, there is little benefit for choosing a high controller bandwidth for the speed loop since high performance speed control is unnecessary in this application. A significant disadvantage to choosing a high control bandwidth for the speed controller is that abrupt changes in the electric torque result, which can wear on the WTG drive train over time. A low control bandwidth also has the advantage of "smoothing" the power generated by the WTG during wind gusts, which can further reduce strain on the WTG drive train. For this work, the proportional gain of the speed

controller is set to give roughly a 0.1 Hz closed-loop bandwidth and the integral gain is set to give roughly 10% overshoot in the step response. A Bode plot of the closed-loop speed control system is shown in Fig. 4.18 and the step response of this closed-loop system for a step change in the reference speed is shown in Fig. 4.19.

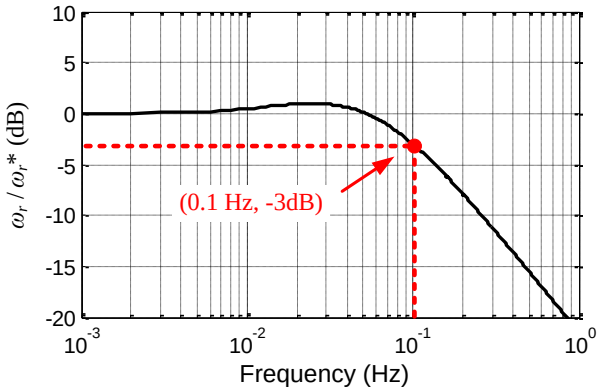


**Fig. 4.18: Bode plot of closed-loop rotor speed controller.**

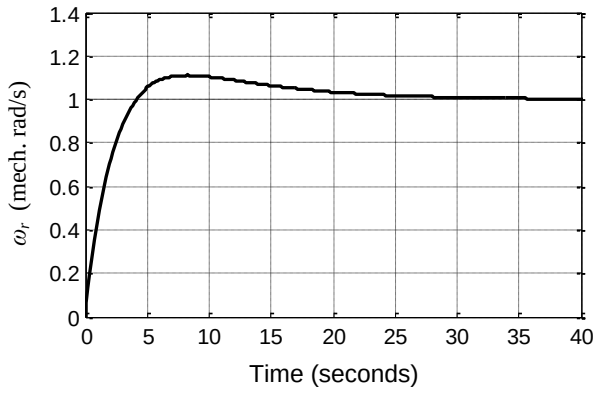


**Fig. 4.19: Step response of speed controller.**

A two-mass model of the WTG rotor [41] [75] [76] is the most accurate representation, since Type 3 WTGs are often connected to the wind-turbine rotor through a gearbox. A two-mass model of the WTG rotor is often used to study sub-synchronous resonance phenomenon and other low-frequency power system oscillations. However, these low-frequency dynamics are neglected in this work since the dynamics of interest in

short-circuit studies are much faster. However, these low-frequency dynamics may need to be considered in the design of the RSC speed controller since the control parameters may affect the damping of these oscillations. However, this type of analysis is beyond the scope of this work.

### *4.2.5. Reactive-Power Controllers*

The reactive power generated at the terminals of the Type 3 WTG is given by

$$Q_s = \frac{3}{2}(v_{ds}^s i_{qs} - v_{qs}^s i_{ds}) \approx -\frac{3}{2} v_{qs}^s i_{ds}, \tag{4.32}$$

where $v_{ds}^s \approx 0$ in a synchronous reference frame oriented with the d-axis stator flux. The q-axis stator voltage is assumed to be constant for this analysis. The d-axis stator current can be found by inserting the d-axis stator-flux linkage equation in (4.18) into the q-axis stator voltage equation in (4.17), and solving for the d-axis stator current, given by

$$i_{ds} = \frac{v_{qs}^s}{\omega_s L_s} - \frac{L_m}{L_s} i_{dr}, \tag{4.33}$$

where the stator resistance has been neglected. Substituting this equation into (4.32) gives the reactive power produced at the stator terminals to be

$$Q_s \approx \frac{3}{2} v_{qs}^s \left( \frac{L_m}{L_s} i_{dr} - \frac{v_{qs}^s}{\omega_s L_s} \right) = \frac{3}{2} v_{qs}^s \frac{L_m}{L_s} i_{dr} - \frac{3}{2} \frac{(v_{qs}^s)^2}{\omega_s L_s}. \tag{4.34}$$

The second term in (4.34) stays relatively constant, except for variations in the stator voltage of ± 5% in normal operating conditions; thus, as a rough approximation, this term is assumed to remain constant in this analysis. The first term is the controllable quantity, in which the d-axis rotor current can be used to control the stator reactive power. Therefore, the second term in (4.34) is neglected since it does not affect the change in $Q_s$ for fixed grid voltage conditions. The transfer function relating the change in $i_{dr}$ to the change in $Q_s$ is given by

$$\frac{Q_s}{I_{dr}} = \frac{3}{2} v_{qs}^s \frac{L_m}{L_s} = K_{qs}. \tag{4.35}$$

Using a PI controller for the stator reactive power controller gives the block diagram of the stator reactive power control loop shown in Fig. 4.20. The open-loop transfer function of the stator reactive power control loop is given by

$$\frac{Q_s}{Q_s^* - Q_s} = \frac{K_{qs} K_{pq} (s + K_{iq} / K_{pq})}{s}, \tag{4.36}$$

where $K_{pq}$ is the proportional gain and $K_{iq}$ is the integral gain of the PI controller. It can be shown that the closed-loop transfer function of the stator reactive power controller is given by

$$\frac{Q_s}{Q_s^*} = \frac{K_{qs} K_{pq}}{(1 + K_{qs} K_{pq})} \frac{(s + K_{iq} / K_{pq})}{s + K_{qs} K_{iq} / (1 + K_{qs} K_{pq})}. \tag{4.37}$$

The PI controller proportional gain is chosen to be very low since this system has differentiator properties (high gain at high frequencies) with a high value of proportional gain. Therefore, the PI controller behaves more like a pure integral controller with an open-loop transfer function given by

$$\frac{Q_s}{Q_s^* - Q_s} = \frac{K_{qs} K_{iq}}{s}, \tag{4.38}$$

with a corresponding closed-loop transfer function given by

$$\frac{Q_s}{Q_s^*} \approx \frac{K_{qs} K_{iq}}{s + K_{qs} K_{iq}}. \tag{4.39}$$

Thus, the closed-loop system behaves as a first-order system and $K_{iq}$ completely determines the control bandwidth of the system. $K_{iq}$ is designed so that the open-loop system of (4.36) has at least -30 dB gain at 60 Hz so that this controller attenuates both 120 Hz and 60 Hz signals in the feedback caused by negative-sequence voltages and DC offsets in the stator currents during transients. The resulting closed-loop control bandwidth of this system is roughly 2 Hz, as shown by the Bode plot of this closed-loop system shown in Fig. 4.21. The step response of the closed-loop system for a unit step

change in the reactive power command is shown in Fig. 4.22. The numerical values of the parameters in (4.37) are given in Appendix A.

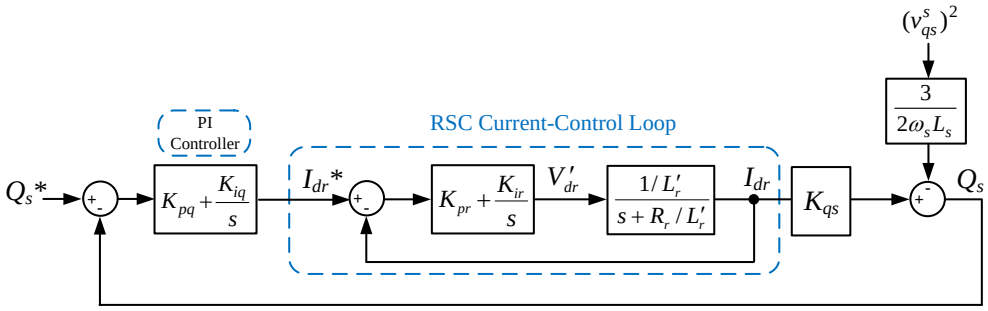


**Fig. 4.20: Block diagram of the stator reactive power control loop.**

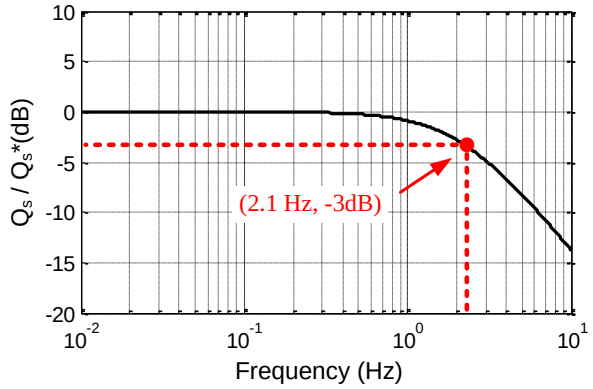


**Fig. 4.21: Bode plot of closed-loop stator reactive-power controller.**

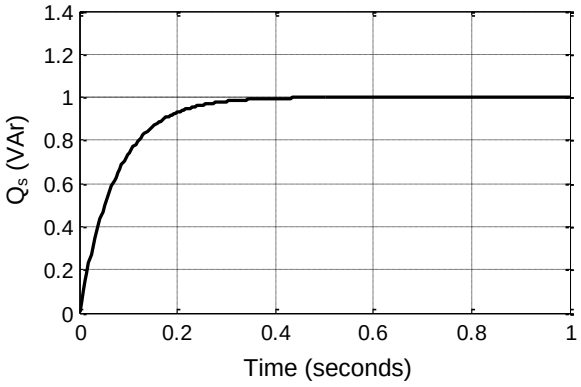


**Fig. 4.22: Step response of closed-loop stator reactive-power controller.**

The reactive power controller for the GSC can be designed in the same way as the stator reactive power controller. The reactive power produced by the GSC is given by

$$Q_g = \frac{3}{2}(v_{qs}^v i_{dg} - v_{ds}^v i_{qg}) \approx -\frac{3}{2} v_{ds}^v i_{qg}\,, \tag{4.40}$$

where $v_{qs}{}^v$ is approximately zero in a reference frame oriented with the d-axis stator voltage. Thus, the GSC reactive power can be controlled through $i_{qg}$. Because the reactive power from the GSC is (negatively) proportional to the stator voltage, a controller can be designed in the same way as described for the stator reactive power controller, except the polarity of the summation junction for the error signal is reversed. Therefore, the GSC reactive power can be controlled in two ways, using either a PI controller with output feedback, as shown in Fig. 4.23, or a constant $I_{qg}$* reference (zero for unity power factor, for example) can be injected into the GSC current controller (thus the reactive power PI controller is disabled). For this work, the GSC reactive power controller is not considered, and a constant reference value of $I_{qg}$* = 0 is used to always inject currents at unity power factor.

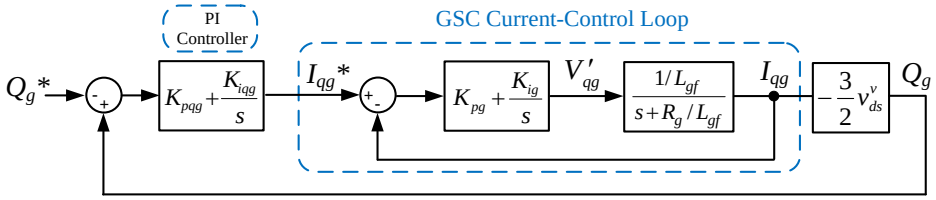


**Fig. 4.23: Block diagram of GSC reactive-power control loop.**

## *4.2.6. Effects of Mutual-Flux Saturation on Controls*

The magnetic core of induction machines is often designed to operate slightly in the saturated region at rated operating conditions. This ensures complete use of the magnetic material and saves on system cost. However, the non-linear effects of operating in magnetic saturation are often not considered in the control and dynamics of the Type 3 WTG. Mutual-flux saturation in induction machines is briefly discussed in this section,

in addition to its effects on the Type 3 WTG controls. The effects of mutual-flux saturation on the short-circuit behavior of Type 3 WTGs is discussed in later sections.

The mutual-flux saturation characteristics of the lab-scale WRIM have already been discussed in Section 3.5.1, and are based on the no-load test results shown in Fig. 3.10. These no-load test results are shown again in Fig. 4.24. These results indicate that the magnetic core starts saturating at roughly 70% voltage (35% no-load current). The mutual flux in the core can be estimated from the steady-state voltage equations of the WRIM stator for no-load conditions, given by

$$\vec{V}_s = R_s \vec{I}_s + j\omega_s \vec{\Lambda}_s \,. \tag{4.41}$$

The stator flux linkage in terms of its leakage and mutual-flux components are given by

$$\vec{\Lambda}_s = \vec{\Lambda}_{ls} + \vec{\Lambda}_m = L_{ls}\vec{I}_s + L_m(\vec{I}_s + \vec{I}_r) \,. \tag{4.42}$$

By inserting the flux linkage equation in (4.42) into the stator voltage equation in (4.41), the mutual-flux linkage can be written as

$$\vec{\Lambda}_m = \frac{\vec{V}_s - R_s\vec{I}_s - j\omega_s L_{ls}\vec{I}_s}{j\omega_s} \,. \tag{4.43}$$

The mutual inductance of the induction machine can be calculated from the mutual-flux linkage equation in (4.42), given by

$$L_m = \left| \frac{\vec{\Lambda}_m}{\vec{I}_s + \vec{I}_r} \right| = \left| \frac{\vec{\Lambda}_m}{\vec{I}_s} \right| , \tag{4.44}$$

where $\vec{I}_r$ = 0 since the rotor windings are open circuited during the no-load test. Thus, from (4.43) and (4.44), an estimate of the mutual inductance for no-load test conditions can be found if the stator voltage and current are known. Using the measured voltage and currents from the no-load test, the mutual inductance at each data point is calculated and shown in Fig. 4.24 (green curve). The results indicate that the mutual inductance is highly non-linear over this operating range of the machine. Additionally, small changes

in the amount of flux result in significant changes in the mutual inductance when the machine is operating in the saturated region.

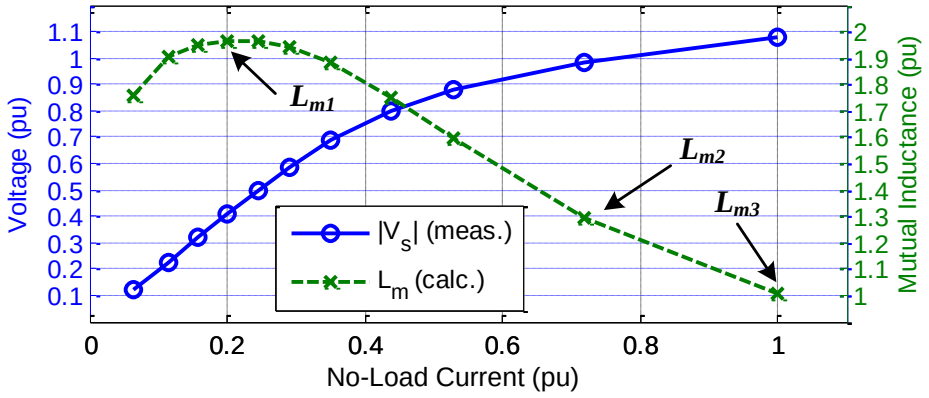


**Fig. 4.24. No-load saturation characteristics of wound-rotor induction machine.**

Equation (4.34) indicates that the reactive power produced at the stator terminals of the Type 3 WTG depends on the mutual inductance of the WRIM and the stator voltage. The non-linear relationship between the stator voltage and the mutual inductance of the WRIM caused by saturation results in a non-linear relationship between the d-axis rotor current and the stator reactive power. It follows from (4.35), therefore, that the value of $i_{dr}$ required to output a given $Q_s$* depends on the mutual-flux linkage in the core and the stator voltage magnitude. However, because closed-loop control of the stator reactive power is often used (as shown in Fig. 4.20), the reactive power can be controlled with zero steady-state error despite the saturation effects. Thus, the stator reactive power control loop automatically compensates for the non-linear saturation effects. However, mutual-flux saturation has been shown to limit the amount of reactive power that can be generated by the Type 3 WTG when operated in the over excited (positive $Q_s$) region [77].

Mutual-flux saturation also affects the feed-forward compensation terms shown in the RSC control diagram of Fig. 4.13. $L_m$ is used explicitly in the feed-forward term calculations; thus, the assumption that this term is constant results in imperfect

decoupling of the d- and q-axis rotor current controls. However, because the term $L_m/L_s = L_m/(L_{ls}+L_m) \approx 1$, this term is not significantly affected by the variations in $L_m$ since $L_m >> L_{ls}$, even in saturation.

As discussed in this section, mutual-flux saturation does not have a significant impact on the *steady-state* control of the Type 3 WTG. However, mutual-flux saturation *does* have a large impact on the short-circuit currents contributed by the Type 3 WTG, and these effects are discussed in later sections.

## 4.3. Proposed Sequence-Network Model of the Type 3 WTG

The sequence-network model of the Type 3 WTG is developed based upon simplifying assumptions of the RSC and GSC controls described in the previous section. The per-phase, positive-sequence, steady-state equivalent circuit is derived, and this circuit serves as a basis for the positive-sequence circuit for short-circuit calculations. Two sets of sequence-network circuits are described for two distinct cases of operation of the Type 3 WTG: one for the case in which the RSC maintains control of the rotor currents and one for the case in which the AC crowbar turns on immediately after the fault (thus control of the rotor currents is lost).

### *4.3.1. Steady-State Equivalent Circuit*

The steady-state equivalent circuit of the Type 3 WTG can be derived by examining the RSC and GSC controls shown in Fig. 2.13 and Fig. 2.14. It is assumed that the controls are in the linear modulation region of the PWM scheme, and that the inner current loops in the RSC and GSC track the reference currents with zero steady-state error. Additionally, these inner current loops have relatively high bandwidths, making these controllers "appear" as a controlled current source to the interconnecting network. Thus, the positive-sequence equivalent circuit of the Type 3 WTG is displayed in Fig. 4.25. $\vec{I}_r$ is a current-source phasor representing the d- and q-axis current

commands shown in Fig. 2.14 for the RSC. Similarly, $\vec{I}_g$ is a current-source phasor representing the d- and q-axis current commands by the GSC. $\vec{V}_L$, $X_L$, and $R_L$ represent the equivalent circuit of the network to which the Type 3 WTG is connected. The currents injected by the RSC and GSC ($\vec{I}_r$ and $\vec{I}_g$) in Fig. 4.25 depend on the terminal voltage $\vec{V}_s$ and the real and reactive power output of the stator and the GSC. The currents and voltages in the steady-state circuit shown in Fig. 4.25 can be found using the following steps:

1. Initialize the total Type 3 WTG real and reactive power output $P_t$ and $Q_t$ and the infinite-bus voltage source $\vec{V}_L$ (usually set to 1 per unit with an angle of 0°).
2. Calculate the terminal voltage $\vec{V}_s$ by solving the load-flow equations of the external network.
3. Determine the stator power $P_s$ and $Q_s$ and the GSC power $P_g$ and $Q_g$ from $P_t$ and $Q_t$ and from the WTG manufacturer's curves or approximate equations.
4. Calculate $\vec{I}_g$ and $\vec{I}_s$ from $P_g$, $Q_g$, $P_s$, $Q_s$, and $\vec{V}_s$.
5. Calculate $\vec{I}_r$ from $\vec{I}_s$ and $\vec{V}_s$.

Step 2 can be completed using any conventional load-flow solution technique, such as Euler or Gaussian solvers, etc. The load-flow equations are set up in the conventional way with the Type 3 WTG terminal voltage as a bus with real and reactive power input as $P_t$ and $Q_t$.

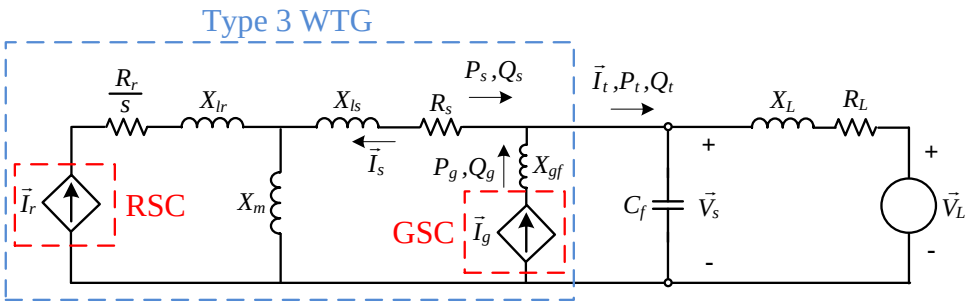


**Fig. 4.25: Steady-state equivalent circuit of the Type 3 WTG.**

Step 3 requires a curve or equation supplied by the wind-turbine manufacturer that gives the proportion of the output real power from the stator and GSC for a given total output power and terminal voltage magnitude. A similar curve is required for the reactive power. A rough approximation to the real-power curves is shown in Fig. 4.26. The stator output power in Fig. 4.26 (dashed red line) is calculated using

$$P_s = P_t(1-s)\,, \tag{4.45}$$

where $s$ is the slip. Similarly, the GSC power output in Fig. 4.26 (dotted blue line) is calculated using

$$P_g = -P_t s\,. \tag{4.46}$$

These equations are based on steady-state induction machine theory [8] and do not account for the machine and converter losses. $P_t$ is assumed to be directly proportional to the rotor speed, as shown by the solid black line in Fig. 4.26. However, this is a rough approximation since this curve is determined by the maximum (real) power point tracking characteristics of the wind turbine. Using a set of curves similar to Fig. 4.26, the real-power output of the stator and GSC can be determined for any given real-power output $P_t$ of the Type 3 WTG. Detailed calculations can be performed from realistic curves similar to those shown in Fig. 4.26 that are supplied by the wind-turbine manufacturer. Since the reactive power is a purely controllable quantity, it can be set to any desired value within

the capabilities of the DFIG. However, the proportion of the reactive power that is supplied from the stator and GSC must be known.

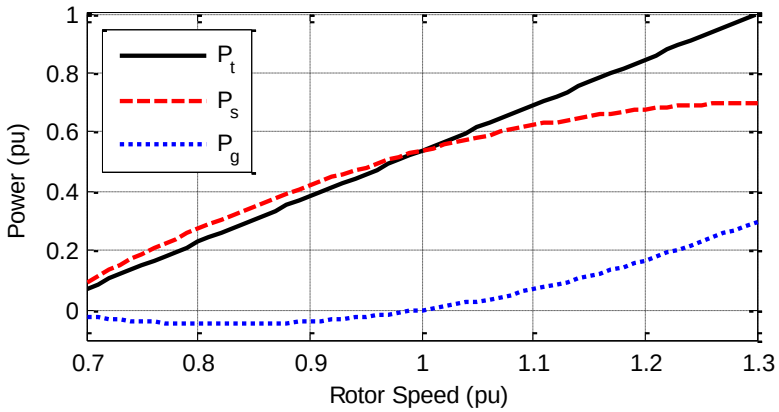


**Fig. 4.26. Approximation of the steady-state real-power output of the Type 3 WTG.**

In Step 4, the GSC current can be found by

$$\vec{I}_g = \left( \frac{P_g + jQ_g}{\vec{V}_s} \right)^*, \tag{4.47}$$

where * represents the complex conjugate and $P_g$ and $Q_g$ are the per-phase real and reactive power from the GSC. Similarly, the stator current is given by

$$\vec{I}_s = -\left( \frac{P_s + jQ_s}{\vec{V}_s} \right)^*. \tag{4.48}$$

The minus sign in (4.48) is due to the direction of the stator current chosen in Fig. 4.25.

In Step 5, it can be shown from conventional circuit theory that the RSC current can be calculated from $\vec{I}_s$ and $\vec{V}_s$, given by

$$\vec{I}_r = \left[ \frac{\vec{V}_s}{R_s + j(X_{ls} + X_m)} - \vec{I}_s \right] \frac{R_s + jX_{ls}}{\vec{Z}_{req}}, \tag{4.49}$$

where $\vec{Z}_{req}$ is given by

$$\vec{Z}_{req} = \frac{jX_m(R_s + jX_{ls})}{R_s + j(X_{ls} + X_m)}. \tag{4.50}$$

To demonstrate this procedure, an example calculation is performed using the network shown in Fig. 4.27. The network to which the Type 3 WTG is connected is represented as an ideal voltage source in series with an impedance of 0.01 + *j*0.02 per unit. The per-phase equivalent circuit of this network is identical to that in Fig. 4.25. The filter capacitance is neglected in this example to simplify the calculations.

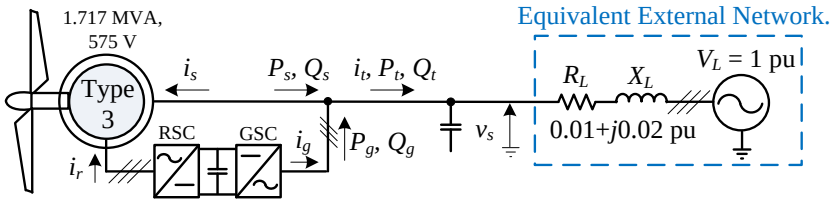


**Fig. 4.27: Single-machine infinite bus network for steady-state calculations.**

The equivalent-circuit elements in Fig. 4.25 are calculated following the procedure described previously and using the Type 3 WTG parameters given in Appendix A:

1. *Initialize the total Type 3 WTG real and reactive power output $P_t$ and $Q_t$ and the infinite-bus voltage source $\vec{V}_L$ (usually set to 1 per unit with an angle of 0°).*

   The infinite-bus voltage source $\vec{V}_L$ is set to 1 per unit at an angle of zero degrees. Assume the Type 3 WTG is generating 0.75 per unit real power $P_t$ and that the Type 3 WTG is operating at 0.95 power factor (overexcited). Thus,

   $$Q_t = P_t \tan(\theta) = P_t \tan(\cos^{-1}(0.95)) = 0.75 * 0.3287 = +0.2465 \text{ per unit.} \tag{4.51}$$

   where $\theta$ is the power-factor angle.

2. *Calculate the terminal voltage $\vec{V}_s$ by solving the load-flow equations of the external network.*

Details of the load-flow calculation are not given here, as numerous references are available that describe how to perform these calculations (see [7] for further reading). The final solution of the stator voltage is $\vec{V}_s = 1.0122\angle 0.7096°$.

3. *Determine the stator power $P_s$ and $Q_s$ and the GSC power $P_g$ and $Q_g$ from $P_t$ and $Q_t$ and from the WTG manufacturer's curves or approximate equations.*

   Assuming the Type 3 WTG generates real power according to the curve shown in Fig. 4.26, the corresponding rotor speed at 0.75 per unit real-power output ($P_t$) is approximately 1.15 per unit. The corresponding real-power output from the stator ($P_s$) and GSC ($P_g$) (according to the curves of Fig. 4.26) at this rotor speed is approximately 0.65 per unit and 0.1 per unit, respectively. Assuming that all of the reactive power generated by the Type 3 WTG comes from the stator, and that the GSC operates at unity power factor ($Q_g = 0$), then $Q_s = Q_t = 0.2465$ per unit.

4. *Calculate $\vec{I}_g$ and $\vec{I}_s$ from $P_g$, $Q_g$, $P_s$, $Q_s$, and $\vec{V}_s$.*

   From (4.47),

$$\vec{I}_g = \left( \frac{P_g + jQ_g}{\vec{V}_s} \right)^* = \left( \frac{0.1 + j0}{1.0122\angle 0.7096°} \right)^* = 0.0988\angle 0.7096°, \tag{4.52}$$

   and from (4.48)

$$\vec{I}_s = -\left( \frac{P_s + jQ_s}{\vec{V}_s} \right)^* = -\left( \frac{0.65 + j0.2465}{1.0122\angle 0.7096°} \right)^* = 0.6868\angle 159.94°. \tag{4.53}$$

5. *Calculate $\vec{I}_r$ from $\vec{I}_s$ and $\vec{V}_s$.*

   From (4.52),

$$\vec{Z}_{req} = \frac{jX_m(R_s + jX_{ls})}{R_s + j(X_{ls} + X_m)} = \frac{j2.9913*(0.0073 + j0.1766)}{0.0073 + j(0.1766 + 2.9913)} = 0.1669\angle 87.77°. \tag{4.54}$$

   where the various parameter values are listed in Appendix A. Thus, from (4.49),

$$\begin{aligned}\vec{I}_r &= \left[\frac{\vec{V}_s}{R_s + j(X_{ls} + X_m)} - \vec{I}_s\right]\frac{R_s + jX_{ls}}{\vec{Z}_{req}} \\ &= \left[\frac{1.0122\angle 0.7096°}{0.0073 + j(0.1766 + 2.9913)} - 0.6868\angle 159.94°\right]\frac{0.0073 + j0.1766}{0.1669\angle 87.77°}. \\ &= 0.9051\angle -40.63°\end{aligned} \tag{4.55}$$

The procedure described in this section for calculating the steady-state parameters of the Type 3 WTG defines the pre-fault conditions of the system. As shown in the next sub-section, the pre-fault conditions directly affect the short-circuit currents injected by the Type 3 WTG using the type of controls discussed in the previous section.

### *4.3.2. Sequence-Network Circuits*

The sequence-network circuit of the Type 3 WTG is derived with the following assumptions:

1. The rotor speed, stator reactive power, DC-link voltage, and GSC reactive power control loops of the RSC and GSC have low enough bandwidths such that their control response during a short circuit can be neglected. In other words, the output of these controls does not change from the pre-fault value.
2. The inner current-control loops of the RSC and GSC have infinitely fast dynamics such that they always track their reference signals with zero error.

Assumption 1 implies that the reference currents supplied by these outer control loops do not change during the short-circuit transient. However, this does not mean that the rotor speed, stator reactive power, DC-link voltage, and GSC reactive power do not change during the short circuit, but only that their *controls do not respond to these changes* in the short time frame of interest. Assumption 2 follows from assumption 1, implying that pre-fault reference current outputs by these outer control loops are tracked perfectly by the inner current-control loops.

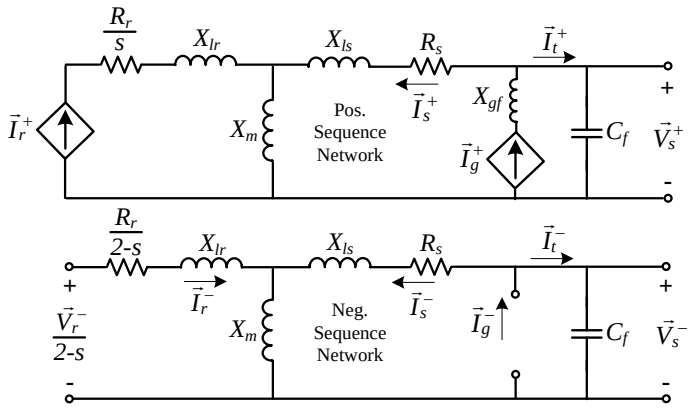


**Fig. 4.28: Proposed sequence-network circuits of the Type 3 WTG for uninterrupted control of the RSC.**

For these assumptions, the positive-sequence circuit of the Type 3 WTG is shown in Fig. 4.28 for the particular case in which there is no AC crowbar interruption after the fault. Note that this circuit is identical to the steady-state equivalent circuit of the Type 3 WTG shown in Fig. 4.25. The current sources in Fig. 4.28 are assumed to be the same values as calculated for the pre-fault, steady-state calculations described in the previous sub-section. These current sources are assumed to remain unchanged because of the assumptions described above.

During unbalanced faults, 120 Hz ripple appears in the reactive power feedback and the DC-link voltage feedback due to the presence of negative-sequence voltage and/or currents. Therefore, some amount of 120 Hz ripple appears in the reference currents supplied by these controllers due to the proportional component in the PI controller. However, the control bandwidths of these controllers are assumed to be small enough such that the proportional gains in these controllers pass through a negligibly small amount of this 120 Hz ripple component. With these assumptions, only DC current references are supplied to the inner current-loop controls. These DC current references represent positive-sequence values in a synchronous reference frame. Thus, with the assumption that the inner current-loop controllers track their reference values with zero error, the RSC and GSC only allow positive sequence currents to flow. However, the

feed-forward compensation terms in the RSC and GSC inner current loops *do* feed forward 120 Hz signals into the voltage commands sent to the converter's PWM algorithm. Thus, the controls block negative-sequence currents from flowing by synthesizing a negative-sequence voltage which counteracts the negative-sequence voltages on the stator (or the negative-sequence voltages induced on the rotor for the RSC). This behavior is reflected in the negative-sequence circuit shown in Fig. 4.28. For this negative-sequence circuit, the GSC and RSC portions are represented as open circuits since it is assumed that their controls only allow positive-sequence currents to flow. Therefore, the only path for negative-sequence currents to flow is through the machine's magnetizing reactance and through the filter capacitance.

In the case that that the AC crowbar protection circuit does activate after the fault, the Type 3 WTG resembles a Type 1 or Type 2 WTG since the rotor windings are short circuited. Control of the rotor current is completely lost while the AC crowbar protection is activated. However, the GSC maintains control of the DC-link voltage and GSC currents, even in the case of AC crowbar activation. Thus, assuming the AC crowbar activates instantly after the fault, the transient sequence-network circuits of the Type 3 WTG are shown in Fig. 4.29(a). Note that these circuits are identical to the transient sequence-network circuits of the Type 1 WTG, with the exception of the parallel branch for the GSC. The voltage $\vec{V}'$ in the positive-sequence circuit can be calculated in the same way as for the Type 1 WTG. Because of the added crowbar resistance in the rotor windings, the currents decay much faster than the Type 1 WTG. Therefore, the crowbar resistance should be included in the time constant of decay for calculations of the current magnitude in the few cycles after the fault occurs. The current source $\vec{I}_g^+$ for the GSC is calculated in the same way described previously based on the pre-fault conditions. The sequence-network circuits for the Type 3 WTG after the initial transients have died away and assuming the AC crowbar is activated are shown in Fig. 4.29(b). Note that these

circuits are identical to the steady-state sequence-network circuits of the Type 1 WTG, with the exception of the crowbar resistance in the rotor and the GSC current source. In many cases, the AC crowbar is only activated for a 2-3 cycles; thus, in this case, the Type 3 WTG will not likely reach a quasi-steady state with the AC crowbar activated and the circuit of Fig. 4.29(b) is of little use.

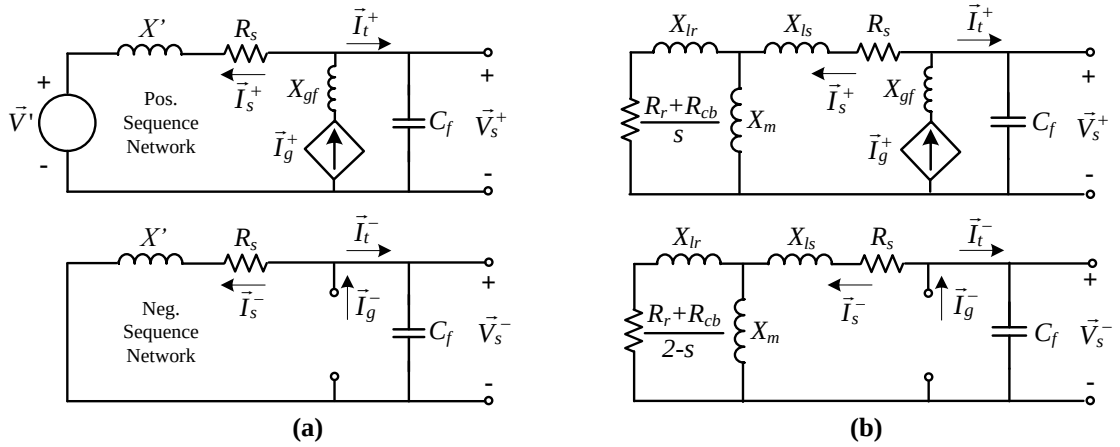


**Fig. 4.29: Proposed sequence-network circuits of the Type 3 WTG with crowbar protection (a) immediately after fault and (b) in steady-state after the fault.**

## 4.4. Effects of RSC Voltage Limitations

The DC-link voltage of the Type 3 WTG is typically designed to be as low as possible to minimize the cost of the power electronics in the RSC and GSC. Under normal conditions, the DC-link voltage required to operate a Type 3 WTG (assuming the maximum slip is 0.3) is either one-third of the WRIM's rated rotor voltage (L-L, peak value) or the GSC AC voltage level (L-L, peak value), whichever is greater. However, the actual DC-link voltage is designed to be slightly higher than this for various design margins and so that the WTG can continuously operate during over voltage conditions [78]. The sequence-network model of the Type 3 WTG proposed in the previous section is based upon the assumption that the RSC current controllers track the reference d- and

q-axis currents with zero steady-state error. However, both unbalanced voltages on the stator and voltages induced on the rotor during faults are sometimes higher than the RSC rated voltage, and the DC link voltage cannot always compensate for these over voltages. Therefore, the control capabilities of the RSC are limited by the DC-link voltage rating, and these limitations are discussed in detail in this section.

### *4.4.1. Transient Over Voltages*

To understand the overvoltage phenomenon which occurs on the rotor windings of the Type 3 WTG during short-circuit transients, the wound-rotor induction machine is analyzed under the hypothetical scenario in which the stator windings are connected to a voltage source and the rotor windings are open circuited while the machine's rotor rotates at a constant speed $\omega_r$. Analyzing the machine behavior in this way allows for a simplified way of understanding how transients occurring on the stator of the induction machine affect the rotor windings through the electromagnetic coupling of the stator and rotor windings.

The wound-rotor induction machine dynamic equations in a rotor reference frame are given by

$$\begin{aligned} \vec{v}_s &= R_s\vec{i}_s + j\omega_r\vec{\lambda}_s + p\vec{\lambda}_s \\ \vec{v}_r &= p\vec{\lambda}_r \end{aligned}, \tag{4.56}$$

where $\vec{i}_r = 0$ since the rotor windings are assumed to be open. The flux-linkage equations are given by

$$\vec{\lambda}_s = L_s\vec{i}_s \quad \vec{\lambda}_r = L_m\vec{i}_s \,. \tag{4.57}$$

Solving for the stator current in the stator flux-linkage equation in (4.57) and inserting into the stator voltage equation in (4.56) gives

$$\vec{v}_s = \left(\frac{R_s}{L_s} + j\omega_r\right)\vec{\lambda}_s + p\vec{\lambda}_s \,. \tag{4.58}$$

By solving the linear first-order differential equation of (4.58) to get a closed-form solution of the stator flux linkage, a solution of the rotor voltage can be found. Details of these calculations are given in Appendix G, but the induced rotor voltage is of the form

$$\vec{v}_{r,induced} = \vec{V}_{0r} e^{-(R_s/L_s)t} e^{-j\omega_r t} + \vec{V}_{1r} e^{js\omega_s t}. \tag{4.59}$$

The first term represents the transient component and depends on the initial conditions at which the fault occurs. This component decays with a time constant of $L_s/R_s$. The frequency of this component depends on the rotor speed. The second term in (4.59) represents the steady-state component of the rotor voltage after the transients have died away. A space vector diagram of the induced rotor voltage is shown in Fig. 4.30. The DC-link voltage of a Type 3 WTG determines the radius of the maximum RSC voltage $\vec{v}_{RSC,\max}$, and the voltage induced on the rotor during normal conditions is less than the RSC voltage rating. However, following a disturbance on the stator, the induced rotor voltage can exceed the rated voltage temporarily until the transient component dies away. Because of the transient component of the induced voltage $\vec{V}_{0r}$, the induced rotor voltage moves into and out of the control region of the RSC during the transient because of the rotation of $\vec{V}_{0r}$. In a typical utility-scale Type 3 WTG, these transient over voltages can take many cycles to decay, resulting in a temporary loss of rotor current control.

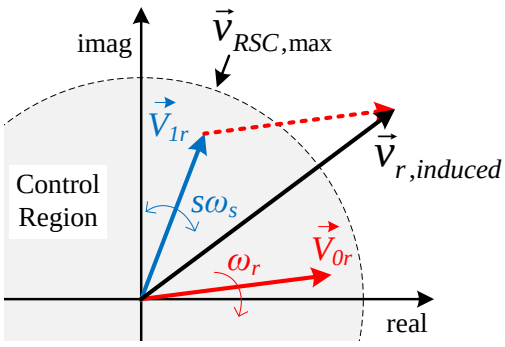


**Fig. 4.30: Space vector of rotor voltage during transients.**

### *4.4.2. Overvoltages Due to Stator Voltage Unbalance*

The stator voltage of the Type 3 WTG in a reference frame rotating with the rotor speed can be written in space-vector notation as

$$\vec{v}_s = \vec{V}_1 e^{js\omega_s t} + \vec{V}_2 e^{-j(2-s)\omega_s t}, \tag{4.60}$$

where $\vec{V}_1$ represents the positive-sequence component of the stator voltage and $\vec{V}_2$ represents the negative-sequence component. Assuming the machine is in steady state, the stator current can also be written in the same form as (4.60). By substituting the flux linkage equations in (4.57) into the stator voltage equation of the Type 3 WTG in (4.56), the stator voltages can be rewritten as

$$\begin{aligned} \vec{V}_1 e^{js\omega_s t} + \vec{V}_2 e^{-j(2-s)\omega_s t} &= \vec{I}_1 (R_s + j\omega_r L_s + pL_s) e^{js\omega_s t} \\ &\quad + \vec{I}_2 (R_s + j\omega_r L_s + pL_s) e^{-j(2-s)\omega_s t} \end{aligned}. \tag{4.61}$$

Substituting the derivative terms in (4.61) with $js\omega_s$ for the positive sequence and $-j(2-s)\omega_s$ for the negative sequence, the stator voltage equation is given by

$$\begin{aligned} \vec{V}_1 e^{js\omega_s t} + \vec{V}_2 e^{-j(2-s)\omega_s t} &= \vec{I}_1 (R_s + j\omega_r L_s + js\omega_s L_s) e^{js\omega_s t} \\ &\quad + \vec{I}_2 (R_s + j\omega_r L_s - j(2-s)\omega_s L_s) e^{-j(2-s)\omega_s t} \end{aligned}. \tag{4.62}$$

Solving for the stator current in (4.62) and recognizing that $\omega_r + s\omega_s = \omega_s$ and that $\omega_r - (2\text{-}s)\omega_s = -\omega_s$ gives

$$\vec{i}_s = \vec{I}_1 e^{js\omega_s t} + \vec{I}_2 e^{-j(2-s)\omega_s t} = \frac{\vec{V}_1}{R_s + jX_s} e^{js\omega_s t} + \frac{\vec{V}_2}{R_s - jX_s} e^{-j(2-s)\omega_s t}. \tag{4.63}$$

The induced rotor voltage is given by

$$\begin{aligned} \vec{v}_{r,induced} = L_m p\vec{i}_s &= js\omega_s L_m \frac{\vec{V}_1}{R_s + jX_s} e^{js\omega_s t} - j(2-s)\omega_s L_m \frac{\vec{V}_2}{R_s - jX_s} e^{-j(2-s)\omega_s t} \\ &= \vec{V}_{1r} e^{js\omega_s t} + \vec{V}_{2r} e^{-j(2-s)\omega_s t} \end{aligned}. \tag{4.64}$$

Under normal, balanced operating conditions ($\vec{V}_2 = 0$), the rotor voltage consists of only the first term in (4.64). However, under unbalanced conditions ($\vec{V}_2 \neq 0$), a voltage is induced on the rotor at a frequency of $(2\text{-}s)\omega_s$. A space-vector diagram of the induced

rotor voltage during stator voltage unbalance is shown in Fig. 4.31. This diagram is similar to the diagram for transient over voltages shown in Fig. 4.30. However, the induced rotor voltage $\vec{V}_{2r}$ due to the negative-sequence stator voltage rotates at a higher frequency. The negative-sequence stator voltage can induce rotor voltages which are outside the control region of the RSC, similar to the over voltages caused by transients. However, the over voltages caused by unbalance do not decay and these high voltages remain until the unbalance conditions are removed. During normal grid operating conditions, some amount of unbalance between the phases is common. However, this unbalance is typically quite small and the voltages induced on the rotor because of these small negative-sequence voltages are not large enough to exceed the RSC voltage ratings. However, during *unbalanced faults*, the negative-sequence voltages are much higher, and can induce voltages large enough to exceed the RSC voltage ratings. Thus, control of the rotor currents can be lost in a Type 3 WTG during significant stator voltage unbalance because the RSC cannot compensate for these large voltages induced on the rotor.

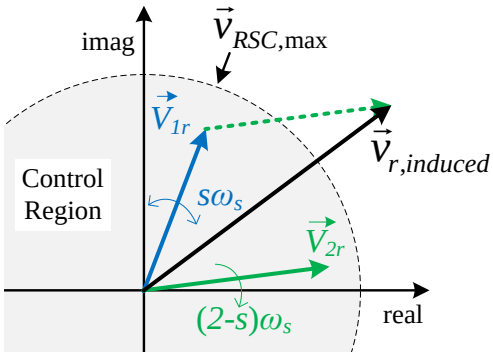


**Fig. 4.31: Space vector of induced rotor voltages during stator voltage unbalance.**

After a balanced three-phase fault, temporary transient voltages are induced in the rotor windings of a Type 3 WTG, as described in the previous sub-section. The magnitudes of these transient voltages depend on the "severity" of the fault (how large of a change in voltage) and the "point-on-wave" at which the fault occurs. However, after

an unbalanced fault, both temporary transient voltages *and* negative-sequence voltages (frequency of $(2\text{-}s)\omega_s$) are induced in the rotor windings of the Type 3 WTG. Therefore, unbalanced faults can result in more severe over voltages in the rotor windings of the Type 3 WTG than balanced faults. After either a balanced or unbalanced fault, over voltages can result in large currents flowing in the RSC, which can potentially trigger the AC crowbar or other protection circuitry to turn on, thereby losing control of the RSC current and therefore the rotor currents.

## 4.5. Experimental Results vs. Transient Simulations

### *4.5.1. Experimental Testbed*

A circuit diagram of the Type 3 WTG testbed is shown in Fig. 4.32. A 115 Vdc, 7.5 hp, separately-excited DC motor is used as the prime mover. The field and armature voltage of this DC motor are manually adjusted in this testbed to obtain the desired rotational speed of the rotor shaft. Thus, no closed-loop control of the DC motor is implemented in this testbed. The wound-rotor induction machine (WRIM) is a 6.8 kVA, 230 V, 60 Hz, three-phase, four-pole machine.

The GSC and RSC are controlled as shown in Fig. 2.13 and Fig. 2.14, respectively, and these controls are implemented on a digital signal processor (DSP), which produces the gating signals for the insulated-gate bipolar transistor (IGBT) modules in the RSC and GSC. The PI controller gains in this experimental testbed are chosen using the same techniques described in Section 4.2. Using the various parameters of this system (given in Appendix A), closed-loop transfer functions can be found, and the proportional and integral gains can be chosen to achieve the desired control bandwidth and step response. The switching frequency of the RSC and GSC of this experimental setup is 10 kHz, which is higher than typical utility-scale WTG. Thus, the inner current-control loops of the RSC and GSC can have a higher bandwidth. These closed-loop bandwidths are designed to be roughly 600-700 Hz. The PI controllers for

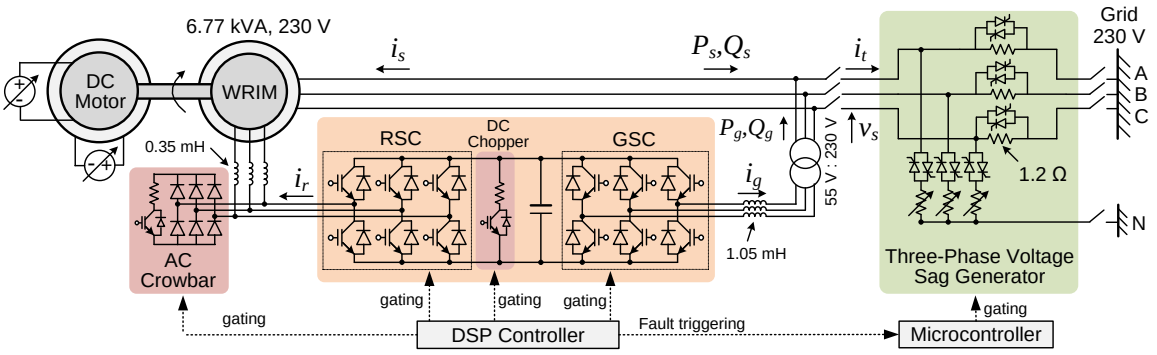


**Fig. 4.32. Circuit diagram of Type 3 WTG testbed.**

the outer control loops (DC-link voltage, rotor speed, and stator reactive power) were designed to have roughly the same closed-loop bandwidth as described in Section 4.2. The GSC reactive power control loop is disabled, and a zero q-axis GSC current reference is applied to this controller. The space-vector modulation algorithm used to generate the duty cycles of the gating signals [79] is also implemented on this DSP. Additionally, the AC crowbar logic, DC chopper logic (described in Appendix H), and fault-triggering signals are implemented on the DSP.

The switching devices in the voltage-sag generator shown in Fig. 4.32 are triacs, whose gating signals are supplied using a microcontroller. To turn these switching devices on, a 5 kHz, 10% duty cycle pulse-width modulation (PWM) signal is applied to the gate of the device. The voltage-sag generator consists of three series switches and three shunt switches that are separately controlled to apply a fault at the WTG terminals. The series switches are in parallel with 1.2 ohm current-limiting resistors that are inserted into the system during the fault. The shunt switches are in series with variable stages of resistor banks to vary the level of the voltage during the fault. The DSP controller supplies the fault triggering signal to the microcontroller. A fault is applied to the generator terminals according to the following sequence of events:

1. In normal operating conditions, the series switches' gating signals are enabled (thus bypassing the series 1.2 ohm current-limiting resistors) and the shunt switches' gating signals are disabled.

2. After a grid-fault trigger signal is received from the DSP, the series switches' gating signals are disabled (thus inserting the 1.2 ohm current-limiting resistors into the circuit).
3. 10 milliseconds after series switches' gating signals are disabled, the shunt switches' gating signals are enabled (thus short-circuiting the Type 3 WTG terminals).
4. 150 milliseconds after the shunt switches' gating signals are enabled, these gating signals are disabled (thus removing the fault).
5. 10 milliseconds after the shunt switches' gating signals are disabled, the series switches' gating signals are enabled (thus restoring the system to normal operating conditions).

A time delay of 10 milliseconds is inserted in between the enable/disable signals of the series and shunt switches, since the switching devices of the voltage-sag generator are triacs, which may take up to one-half cycle to stop conducting after it's gating signals are disabled. A photo of the experimental hardware in this testbed is shown in Fig. 4.33. Detailed circuit diagrams of this hardware testbed have been provided in [80].

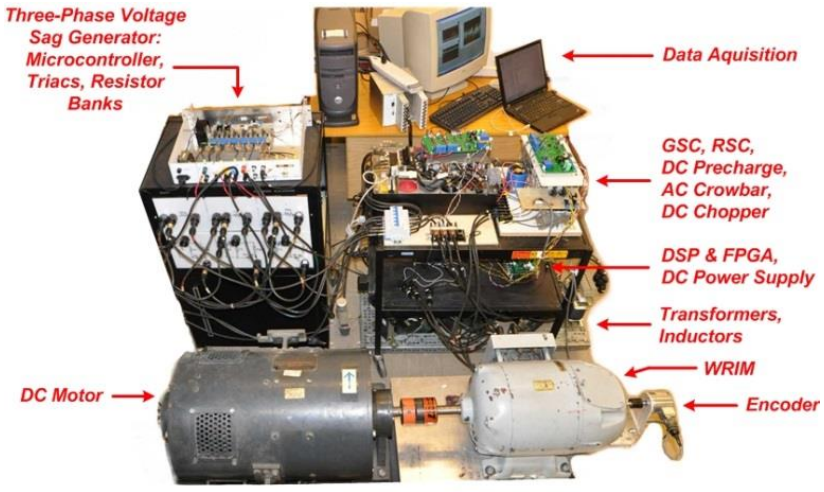


**Fig. 4.33. Photo of Type 3 WTG experimental testbed.**

### *4.5.2. Simulation and Measurement Comparison: Three-phase Fault*

The experimental circuit shown in Fig. 4.32 was replicated in PSCAD transient-simulation software, and simulations were run identical to the experimental tests. Care was taken so that the initial conditions of the simulation results matched the initial conditions of the experimental results, and all of the same PI controller gains used in the experimental tests were also used in the simulations. A switching-level model of the RSC and GSC was assembled using the library PSCAD components, and the space-vector modulation algorithm [79] was implemented with custom user-written code in Fortran. Additionally, custom control designs were built within PSCAD to match the controls used in the hardware testbed. A three-phase fault was applied to the terminals of the machine using a shunt resistance of 1.2 ohm, resulting in roughly a 50% voltage drop at the terminals of the machine. A comparison of the measured quantities and the corresponding simulated values are shown in Fig. 4.34. Shown in the left column are the various voltages, currents, and power outputs of the Type 3 WTG for the measured results. The corresponding simulated values are shown in the right column. Good agreement can be seen between the measured and simulated results, indicating that the custom-made PSCAD model of the Type 3 WTG closely resembles an actual Type 3 WTG short-circuit behavior during a balanced fault.

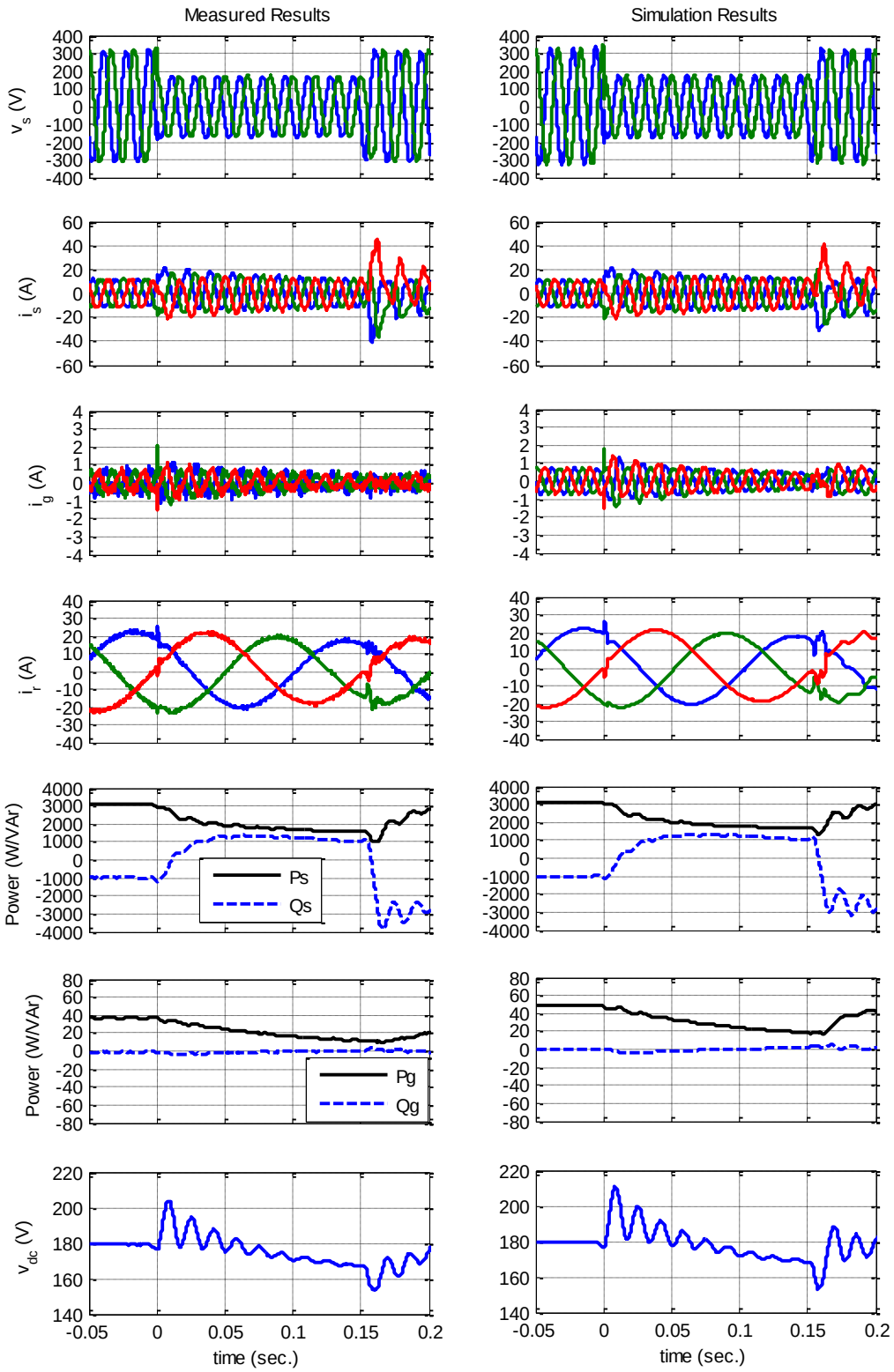


**Fig. 4.34: Comparison of experimental and transient simulation results for a three-phase fault on a Type 3 WTG ($\omega_r$* = 1.1 pu).**

### *4.5.3. Simulation and Measurement Comparison: Single Phase Fault*

Transient simulations were run in PSCAD in the same way described in the previous sub-section, except the fault was only applied to phase A. This was achieved by manually disconnecting the cables in the shunt fault connection in phases B and C. A 1.2 ohm resistor was used as the phase A shunt fault resistance. A comparison of the transient simulation results and the measured results for this test are shown in Fig. 4.35. Good agreement can be seen between the measured and simulation results, indicating that the custom-built PSCAD model of the Type 3 WTG closely resembles the behavior of an actual Type 3 WTG during unbalanced faults.

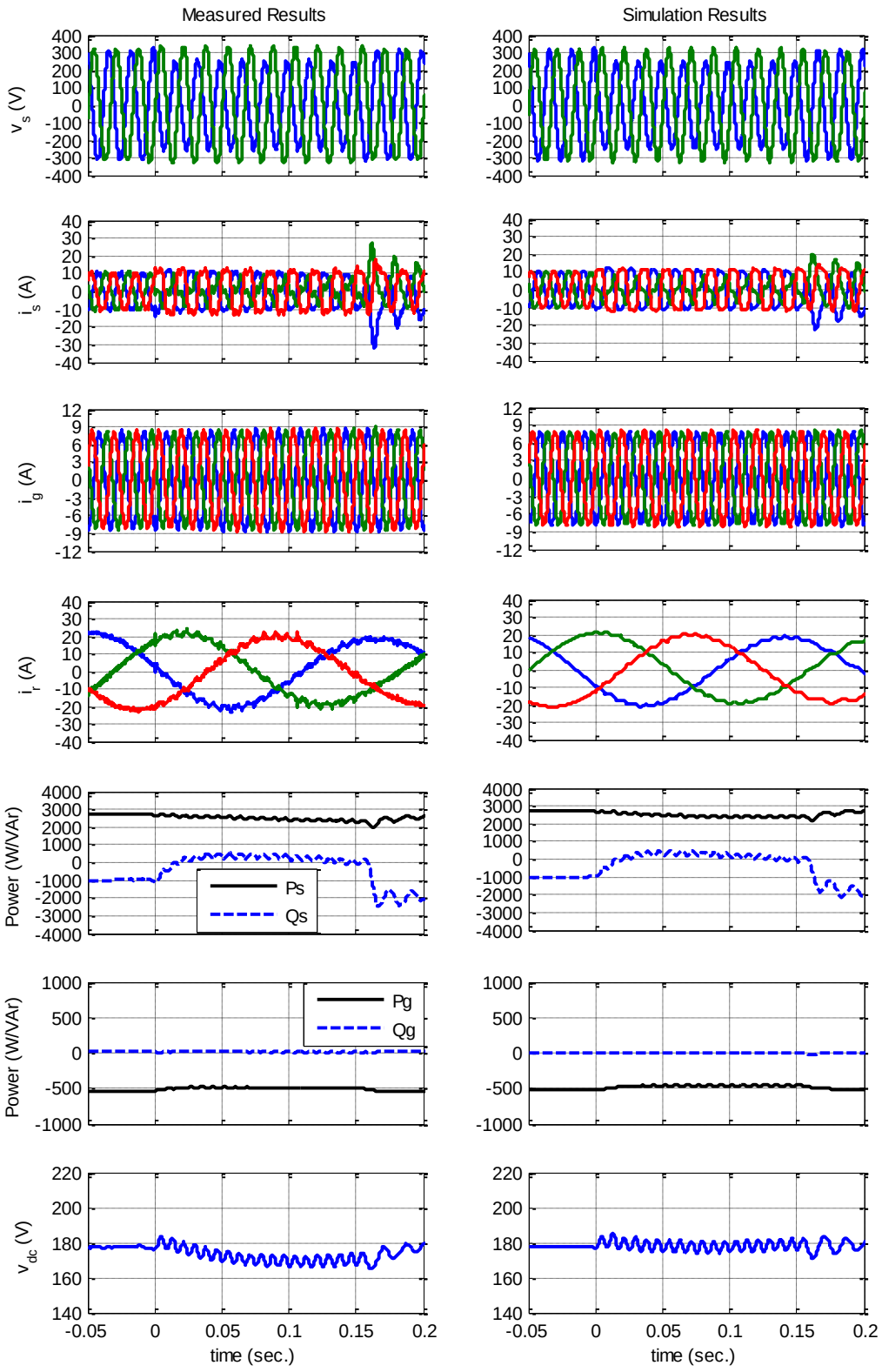


**Fig. 4.35: Comparison of experimental and transient simulation results for a single-phase fault on a Type 3 WTG ($\omega_r$* = 0.92 pu).**

## 4.6. Experimental Results vs. Sequence-Network Calculations

### *4.6.1. Three-Phase Fault Case*

In this section, experimental results are compared with approximate phasor calculations using the theory described in Section 4.3. The measured results in Fig. 4.34 are used for comparison. The per-unit, pre-fault stator and GSC power output are given in Table 4.1, in addition to the pre-fault GSC and stator current phasors calculated using (4.47) and (4.48). In this case, the stator voltage is taken to be 1 pu at an angle of zero degrees. The RSC current phasor depends on the magnetizing reactance, as shown in (4.49). As discussed in Section 4.2.6, significant variation in the magnetizing reactance occurs for different mutual-flux levels due to magnetic saturation. For this reason, the RSC current phasor is calculated using three different values of the magnetizing reactance along the curve shown in Fig. 4.24. The results of these calculations are shown in Table 4.2. These results indicate that the pre-fault rotor current depends strongly on the level of saturation in the induction machine prior to the fault. From the rotor current waveforms shown in Fig. 4.34, the peak rotor current prior to the fault is roughly 22 A, which corresponds to 0.92 pu. This value is roughly half way between the rotor-current magnitudes calculated using $X_{m2}$ and $X_{m3}$ in Table 4.2. Thus, for the particular operating point shown in Fig. 4.34, the actual magnetizing reactance is at a point somewhere between $L_{m2}$ and $L_{m3}$ along the curve of Fig. 4.24.

**Table 4.1: Pre-fault conditions for three-phase fault on experimental testbed (all parameters in per unit).**

| $P_s$ | $Q_s$ | $P_g$ | $Q_g$ | $\vec{V}_s$ | | $\vec{I}_s$ | | $\vec{I}_g$ | |
|---|---|---|---|---|---|---|---|---|---|
| | | | | Mag. | Ang. | Mag. | Ang. | Mag. | Ang. |
| 0.46 | -0.15 | -0.01 | 0.00 | 1.00 | 0.0° | 0.48 | -162.1° | 0.01 | 0.0° |

**Table 4.2: Calculated pre-fault rotor current considering saturation effects.**

| | Case 1 ($X_m = X_{m1}$) | | Case 2 ($X_m = X_{m2}$) | | Case 3 ($X_m = X_{m3}$) | |
|---|---|---|---|---|---|---|
| | Mag. | Ang. | Mag. | Ang. | Mag. | Ang. |
| $\vec{I}_r$ | 0.60 | -37.42° | 0.79 | -52.29° | 0.98 | -59.86° |

The circuit used to calculate the phasor values of the short-circuit currents from the testbed Type 3 WTG is shown in Fig. 4.36. $R_g$ is the current-limiting resistor inserted into the circuit during the fault and $R_f$ is the fault resistor (for this test, $R_f = R_g = 1.2\ \Omega$ = 0.15 per unit on machine's base power). The calculated value of $\vec{I}_g$ in Table 4.1 and the calculated value of $\vec{I}_r$ for Case 3 in Table 4.2 are used in this circuit. The series switch $S_g$ in parallel with $R_g$ is closed during normal operation, while the shunt switch $S_f$ in series with $R_f$ is open during normal operation. After the fault, the series switch is open and the shunt switch is closed. As mentioned in Section 4.5.1, a 10 millisecond delay occurs in between the opening of $S_g$ and the closing of $S_f$. However, in the calculation results, this time delay is neglected. As discussed in Section 4.3, the current sources $\vec{I}_g$ and $\vec{I}_r$ are assumed to remain unchanged after the fault occurs. However, the other currents and voltages in the networks are assumed to *change instantaneously* after the fault. Thus, the short-circuit currents flowing in the network of Fig. 4.36 can be found using the principal of superposition and conventional circuit analysis techniques. Performing this type of analysis gives the stator-current phasor after the fault to be

$$\vec{I}_s = \vec{V}_s\left(\frac{1-\vec{Z}_{seq}}{\vec{Z}_m}\right) + \vec{I}_g\left(\frac{\vec{Z}_{geq}}{\vec{Z}_m + \vec{Z}_{geq}}\right) - \vec{I}_r\left(\frac{\vec{Z}_{req}}{R_s + jX_{ls} + \vec{Z}_{geq}}\right), \qquad (4.65)$$

where the various impedances are defined in Appendix F. Equation (4.65) indicates that each of the sources in Fig. 4.36 contributes to the stator short-circuit current. The total current $\vec{I}_t$ from the Type 3 WTG is given as the phasor sum of the GSC current and stator current ($\vec{I}_t = \vec{I}_g - \vec{I}_s$).

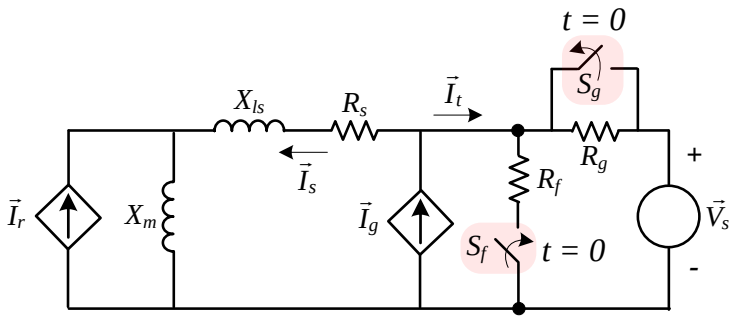


**Fig. 4.36: Equivalent circuit for short-circuit calculations on testbed Type 3 WTG.**

To compare the instantaneous measured waveforms shown in Fig. 4.34 with the short-circuit calculations on the equivalent circuit shown in Fig. 4.36, the positive-sequence currents are extracted from the measured data using the cosine filter and phasor estimation algorithm described in Section 2.9.5. The measured total current from the Type 3 WTG is shown in Fig. 4.37(a), and the extracted positive-sequence current magnitude of this current is shown in in Fig. 4.37(b). The actual turn on/off times of the shunt ($S_f$) and series ($S_g$) switches are shown in Fig. 4.37. A small decrease in the instantaneous current magnitudes can be seen after $S_g$ opens, but these changes are barely noticeable in Fig. 4.37(a). However, after $S_f$ closes, an increase in the currents can clearly be seen. For this test, the AC crowbar protection did not activate; thus, the RSC maintained control of the rotor currents for the duration of the fault. The positive-sequence current in Fig. 4.37(b) rises after the fault (after $S_f$ closes), and slowly decreases in magnitude as time progresses. This slow decrease in the current magnitude is due to the response of the RSC reactive power control loop. The drop in the terminal voltage of after the fault requires a decrease in $i_{dr}$*. As $i_{dr}$ decreases, $L_m$ increases due to the mutual-flux saturation characteristics, which requires a further decrease in $i_{dr}$* to maintain a given reactive power output $Q_s$* (see (4.35)).

Also shown in Fig. 4.37(b) are the calculated currents from the equivalent circuit shown in Fig. 4.36. The pre-fault currents for both the measured results and the

calculations show good agreement. For the short-circuit calculations (after $t = 0$ in Fig. 4.37), the RSC and GSC current-source phasors are assumed to remain unchanged from their pre-fault values. However, the other currents (and voltages) in the network are assumed to change instantaneously; thus, in the calculation results, an instantaneous change in the calculated currents can be seen at $t = 0$.

Three different calculations are performed using the three labeled values of $L_m$ in the curve of Fig. 4.24. The level of mutual-flux saturation in the Type 3 WTG after the fault causes significant variation in the calculated magnitude of the short-circuit currents. An important consideration is to determine the appropriate value of $X_m$ to use in the short-circuit calculations, since there is so much variation in this parameter over the operating range of the machine. Using the largest value of the measured $L_m$ ($L_{m1}$ in Fig. 4.24) is a reasonable option, since the mutual-flux linkage in the WRIM decreases significantly when the voltage drops after a fault (see (4.43)). Using the largest value of $L_m$ also gives the most conservative estimate of the short-circuit-current magnitude, as shown by the results in Fig. 4.37(b). However, using any single value for $X_m$ for these types of calculations will inevitably result in some error, since this value depends on the level of voltage drop at the machine terminals after the fault. Additionally, there is some error in the calculations shown in Fig. 4.37(b) due to the control response of the RSC reactive power controller. In these calculations, the rotor currents are assumed to remain constant after the fault and the slow decrease seen in the measured current is not accounted for in the calculations. For the first three to four cycles after the fault, this decrease in the short-circuit current from the Type 3 WTG is quite small. Transmission level protective relays often operate within this time frame; thus, this control response may be of little significance in this particular application.

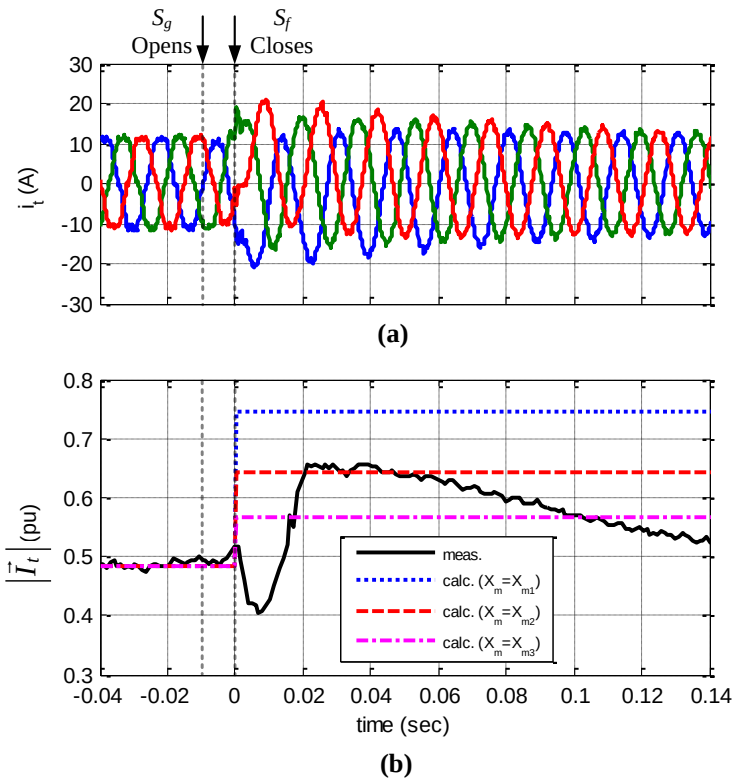


**Fig. 4.37: (a) Instantaneous currents from the Type 3 WTG and (b) comparison of measured and calculated positive-sequence currents.**

## *4.6.2. Single-Phase Fault Case*

In this section, experimental results for a phase-A-to-neutral fault are compared to sequence-network calculations in the same way as described in the previous sub-section. The pre-fault conditions for this test are shown in Table 4.3. The calculated rotor current for these initial conditions is shown in Table 4.4 for three different levels of mutual-flux saturation.

**Table 4.3: Pre-fault conditions for single-phase fault on experimental testbed (all parameters in per unit).**

| $P_s$ | $Q_s$ | $P_g$ | $Q_g$ | $\vec{V}_s^+$ | | $\vec{I}_s^+$ | | $\vec{I}_g^+$ | |
|---|---|---|---|---|---|---|---|---|---|
| | | | | Mag. | Ang. | Mag. | Ang. | Mag. | Ang. |
| 0.42 | -0.15 | 0.00 | 0.00 | 1.00 | 0.0° | 0.44 | -160.6° | 0.00 | 0.0° |

**Table 4.4: Calculated pre-fault rotor current considering saturation effects (current in per unit).**

| | Case 1 ($X_m = X_{m1}$) | | Case 2 ($X_m = X_{m2}$) | | Case 3 ($X_m = X_{m3}$) | |
|---|---|---|---|---|---|---|
| | Mag. | Ang. | Mag. | Ang. | Mag. | Ang. |
| $\vec{I}_r^+$ | 0.57 | -39.73° | 0.77 | -54.55° | 0.96 | -61.87° |

Short-circuit calculations for the case of a phase A-to-neutral fault are performed using the circuit of Fig. 4.38. The positive-sequence GSC current used in this circuit is given in Table 4.3 and the positive-sequence RSC current calculated for Case 3 in Table 4.4 is used. The zero-sequence circuit of the Type 3 WTG is open circuited.

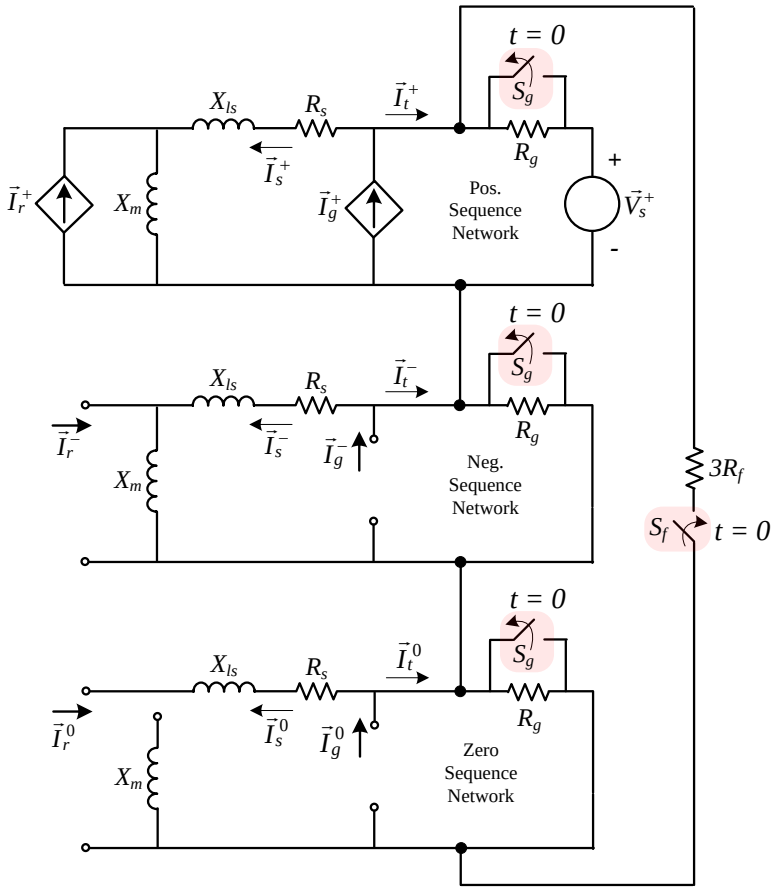


**Fig. 4.38: Sequence-network circuit for a phase-A-to-neutral fault in experimental setup.**

The sequence-network calculations using the circuit of Fig. 4.38 are compared to the measured waveforms for a phase-A-to-neutral fault shown in Fig. 4.39(a). The

positive- and negative-sequence currents are extracted from the instantaneous waveforms using a cosine filter and phasor estimation algorithm. These values are shown by the solid lines shown in Fig. 4.39(b). The calculated sequence currents from the Type 3 WTG are calculated by

$$\begin{aligned} \vec{I}_t^{+} &= \vec{I}_g^{+} - \vec{I}_s^{+} = \vec{I}_g^{+} - f_1(V_s^{+}, \vec{I}_g^{+}, \vec{I}_r^{+}) \\ \vec{I}_t^{-} &= -\vec{I}_s^{-} = -f_2(V_s^{+}, \vec{I}_g^{+}, \vec{I}_r^{+}) \\ I_t^{0} &= 0 \end{aligned} \quad . \tag{4.66}$$

The sequence components of the stator current in (4.66) are determined by the algebraic functions $f_1$ and $f_2$ of the three different voltage/current sources in Fig. 4.38. These functions are complicated functions of all the impedances in the network of Fig. 4.38, and cannot be written concisely here. Custom Matlab code was written to solve for the currents and voltages in this network to obtain the calculation results shown in Fig. 4.39(b). The calculations results shown in Fig. 4.39(b) are for the same cases of $L_m$ described in the previous sub-section. Unlike the case of a three-phase fault, the lowest value of $L_m$ ($L_m = L_{m3}$ in Fig. 4.24) gives the best agreement to the measured results. This result is expected, however, because the mutual-flux levels in the machine do not change significantly during a phase-A-to-neutral fault since the remaining un-faulted phases maintain flux in the machine. Thus, the iron core of the machine can remain saturated after an unbalanced fault because of the un-faulted phases.

The results in this section indicate that mutual-flux saturation significantly impacts the magnitude of the short-circuit currents contributed by the Type 3 WTG. To accurately capture the effects of mutual-flux saturation in the short-circuit calculations would require a detailed model of the saturation characteristics of the machine, which is highly undesirable in short-circuit studies, since these calculations have traditionally been based on simplified, linear circuits of the system. Therefore, it is recommended that the unsaturated value of the magnetizing reactance be used in these calculations because this value gives a conservative estimate of the short-circuit currents for balanced, three-phase

faults. However, using any single value of the magnetizing reactance in these calculations inevitably results in some calculation error, as indicated by the results in this section.

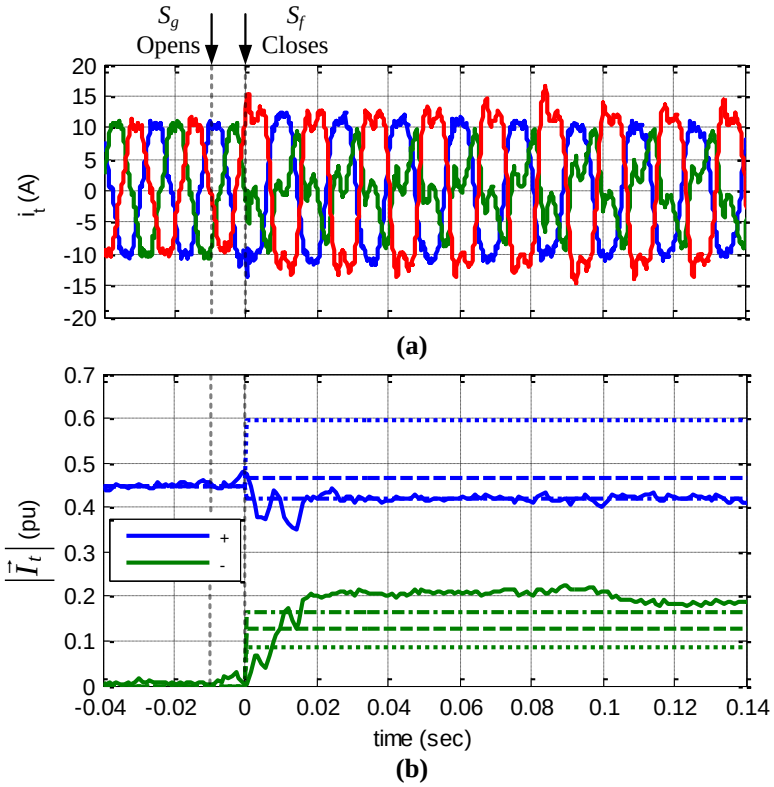


**Fig. 4.39: (a) Instantaneous current after a phase A to neutral fault and (b) comparison of measured and calculated sequence currents (measured: solid, calculated: dotted -> $X_m = X_{m1}$, dashed -> $X_m = X_{m2}$, dot/dash -> $X_m = X_{m3}$).**

## 4.7. Single Machine Infinite Bus Studies

The network shown in Fig. 4.40 is used as a test case to compare the proposed sequence-network circuit model of the Type 3 WTG to transient simulation results. The parameters of the Type 3 WTG in Fig. 4.40 are given in Appendix A, and the transformer, cable, and transmission line parameters used in the network of Fig. 4.40 are given in Appendix C. Transient simulations of this network are run in PSCAD using switching-level models of the RSC and GSC and the controls are implemented as shown

in Fig. 2.14 and Fig. 2.13. The reactive power reference for the RSC is set to zero and the q-axis current command in the GSC controls is also set to zero (the GSC reactive power control is disabled). The wind turbine is represented as a constant mechanical torque, and the rotor speed reference in the RSC controls is set to 1.2 pu.

Simulation results of the voltages and currents in the Type 3 WTG for both a three-phase fault and a single-phase fault are shown in Fig. 4.41. The length of the faulted line and the location of the fault along this line were intentionally chosen such that the Type 3 WTG does not crowbar for either of the cases shown in Fig. 4.41. For both cases, neither the RSC currents nor the GSC currents change significantly after the fault, which agrees with the assumptions about their control responses discussed in Section 4.3.2.

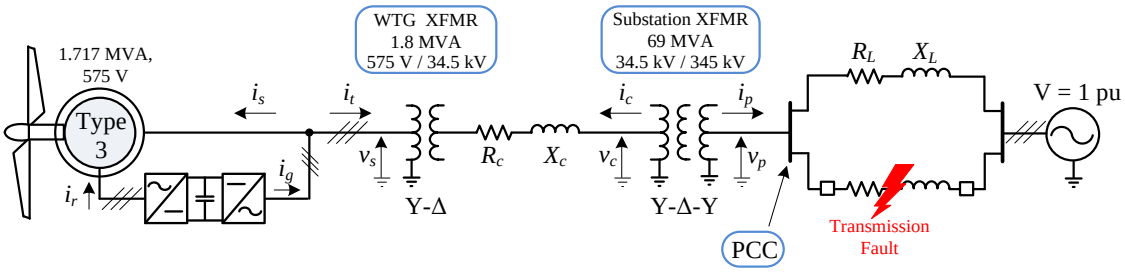


**Fig. 4.40. Single-machine network for analyzing the short-circuit behavior of a Type 3 WTG.**

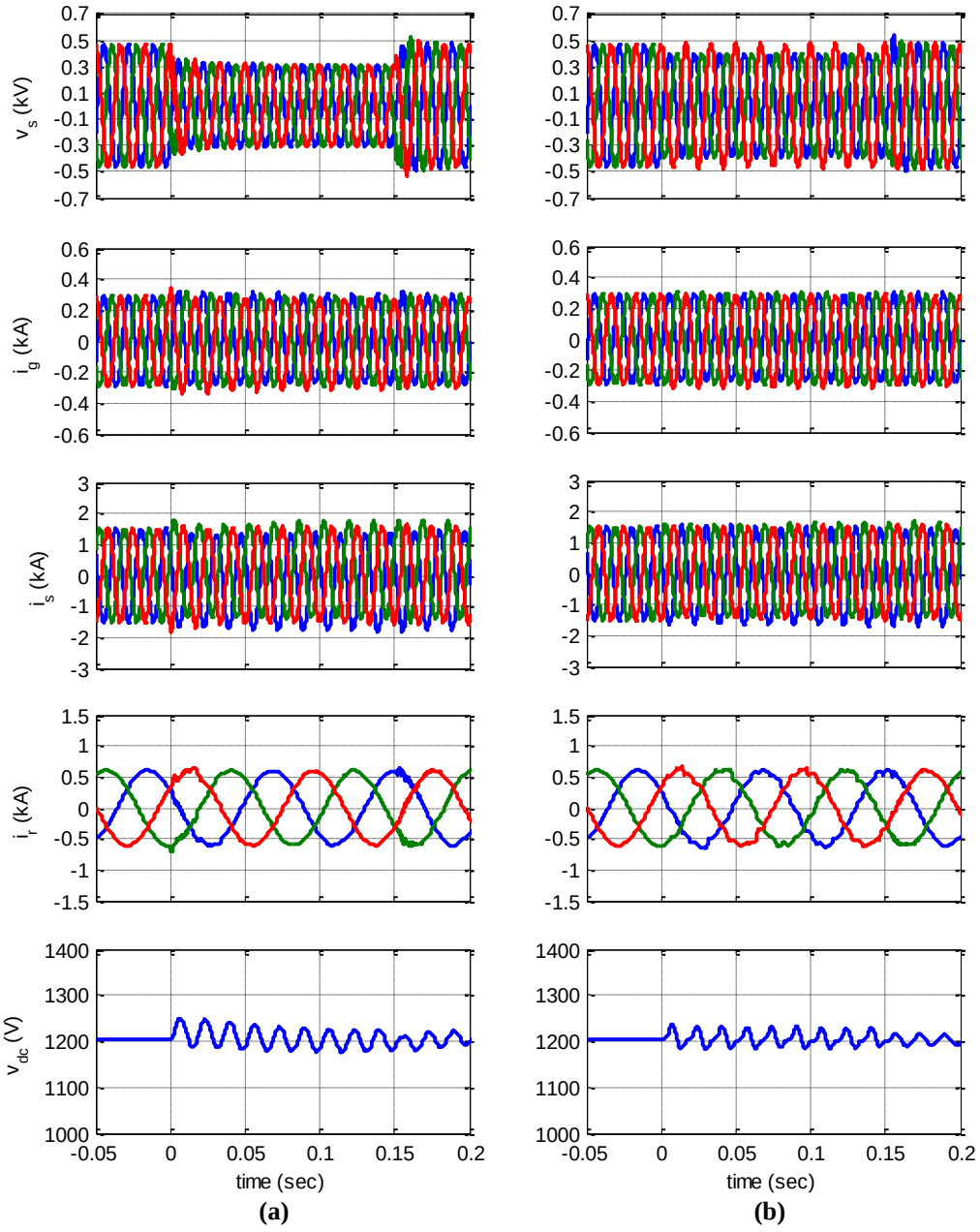


**Fig. 4.41: Simulation results for a (a) three-phase fault and (b) single-phase fault.**

The sequence-network circuit for calculating the short-circuit currents for a three-phase fault in the network of Fig. 4.40 is shown in Fig. 4.42. For this case, $k = 2$ and $m = 0.2$. The current sources $\vec{I}_g$ and $\vec{I}_r$ in Fig. 4.42 are calculated using the steps described in Section 4.3.1, except the pre-fault power outputs of the stator and GSC are taken directly from the transient simulation results. These parameters are listed in Table 4.5

(note: the 30° phase shift caused by the wind-turbine generator transformer is not reflected in the tabulated values).

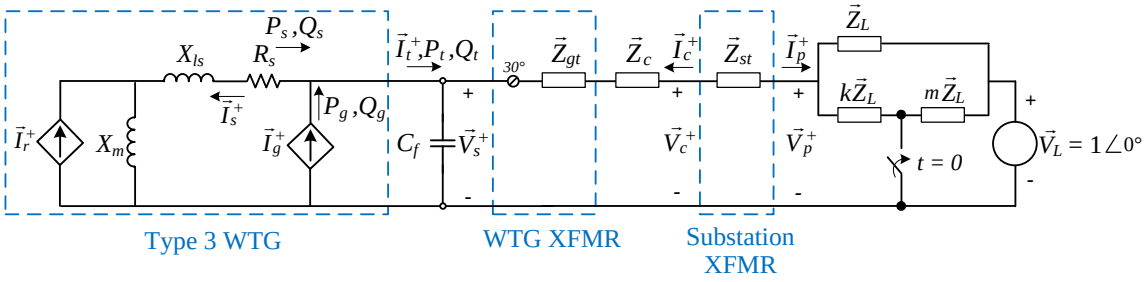


**Fig. 4.42: Sequence-network circuit for a three-phase fault for no crowbar operation.**

**Table 4.5: Pre-fault conditions of Type 3 WTG and parameters for short-circuit calculations (all parameters in per unit)**

| $P_s$ | $Q_s$ | $P_g$ | $Q_g$ | $\vec{V}_s$ | | $\vec{I}_r$ | | $\vec{I}_g$ | | $\vec{I}_s$ | |
|---|---|---|---|---|---|---|---|---|---|---|---|
| | | | | Mag. | Ang. | Mag. | Ang. | Mag. | Ang. | Mag. | Ang. |
| 0.64 | 0 | 0.12 | 0 | 1.01 | 2.58° | 0.75 | -24.24° | 0.12 | 2.58° | 0.63 | -177.42° |

To compare the PSCAD transient simulation results to the short-circuit calculations, the sequence currents are extracted from the instantaneous simulation waveforms of the network shown in Fig. 4.40 using a 16 sample-per-cycle cosine filter and phasor calculation algorithm discussed in Section 2.9.5. The transient simulation waveforms of the point-of-common-coupling (PCC) voltage $v_p$, the total plant current $i_p$, the collector cable current $i_c$, and the collector cable voltage $v_c$ are shown in Fig. 4.43(a). These simulation waveforms are from the same simulation case shown of the Type 3 WTG parameters displayed in Fig. 4.41(a). The positive-sequence components extracted from these instantaneous waveforms are shown in Fig. 4.43(b). Also shown in Fig. 4.43(b) are the calculated positive-sequence currents and voltages found from calculations on the network of Fig. 4.42. These short-circuit calculations were performed using the steady-state solver in Matlab's SimPowerSystems (SPS) software by

assembling the sequence-network circuit shown in Fig. 4.42 using the library components in this software. The calculated values before $t = 0$ in Fig. 4.43(b) reflect the calculated values of these parameters before the switch closes in Fig. 4.42. The calculated values after $t = 0$ reflect the calculated values after the switch closes. As described in Section 4.3.2, the RSC and GSC current sources are assumed to remain unchanged after the fault. However, the other currents and voltages in the network are assumed to change instantaneously after the fault in the calculations. Good agreement can be seen between the calculated positive-sequence currents and the positive-sequence currents from the simulation results in Fig. 4.43(b), and very little change in these currents occurs after the fault. The positive-sequence voltages drop to roughly 70% after fault, and good agreement between the calculated voltages and simulated voltages can be seen, with the exception of the first cycle after the fault, in which some difference can be seen between the calculated and simulated values. This difference is a result of the cosine filter and phasor estimation algorithm used to calculate the sequence components from the instantaneous waveforms. As discussed in Section 2.9.5, this algorithm makes calculations based on the most recently sampled data point (of the voltages/currents) and sampled data points from the previous cycle. Thus, after a sudden disturbance, it takes one full cycle for this algorithm to clear the previous data from its "memory".

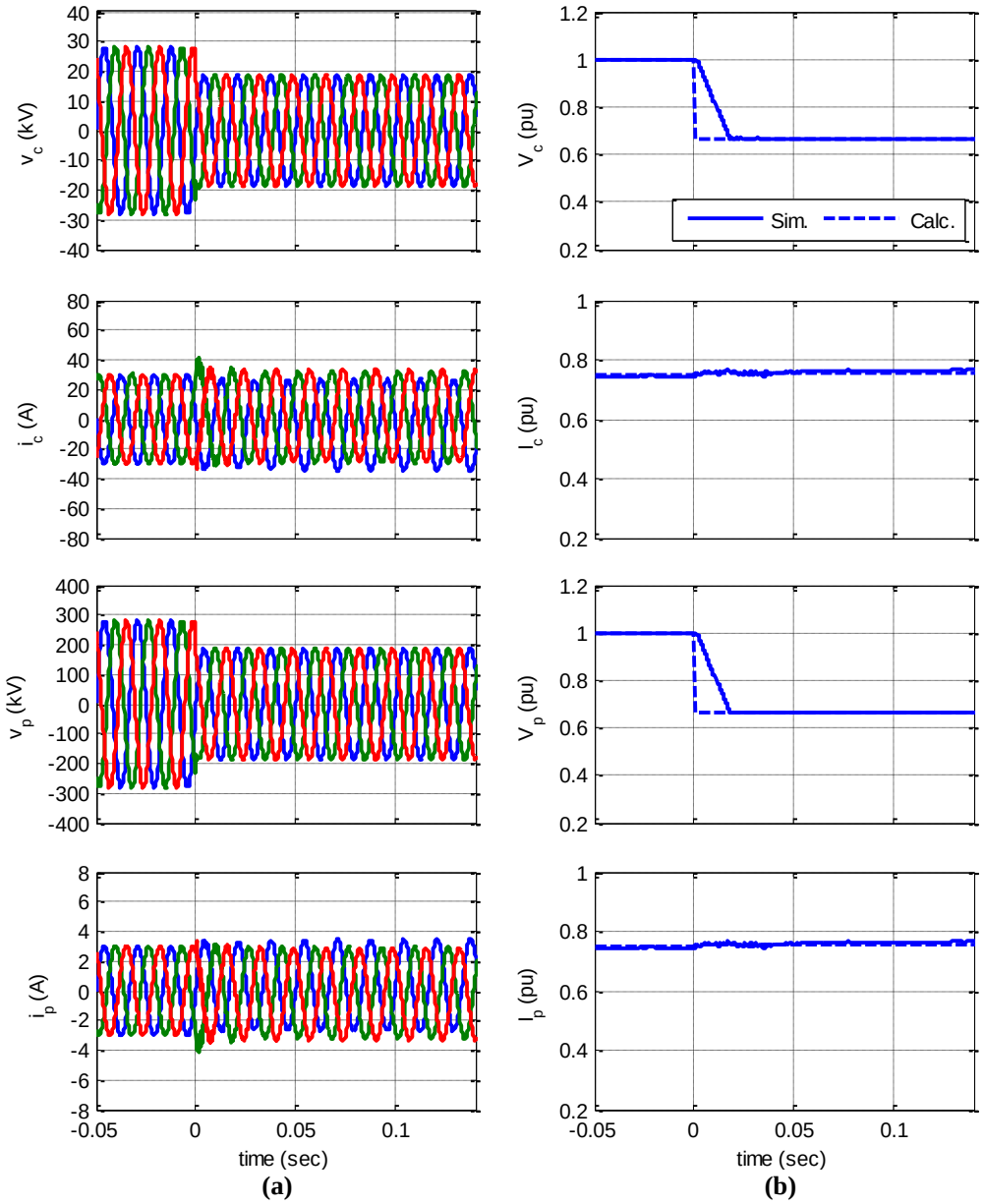


**Fig. 4.43: (a) Instantaneous waveforms of SMIB network voltages and currents for a three-phase fault and (b) comparison of simulated and calculated positive-sequence components of these voltages and currents.**

The sequence-network circuit used to calculate the short-circuit currents in the network of Fig. 4.40 for a single-phase fault is shown in Fig. 4.44. The values of $\vec{I}_r^+$ and $\vec{I}_g^+$ in this circuit are the same as those given in Table 4.5. As discussed in Section 4.3.2, the RSC and GSC in the negative-sequence circuit of the Type 3 WTG are represented as

open circuits. Additionally, the zero-sequence circuit of the Type 3 WTG is open circuited because it is assumed that the WRIM's neutral point is ungrounded.

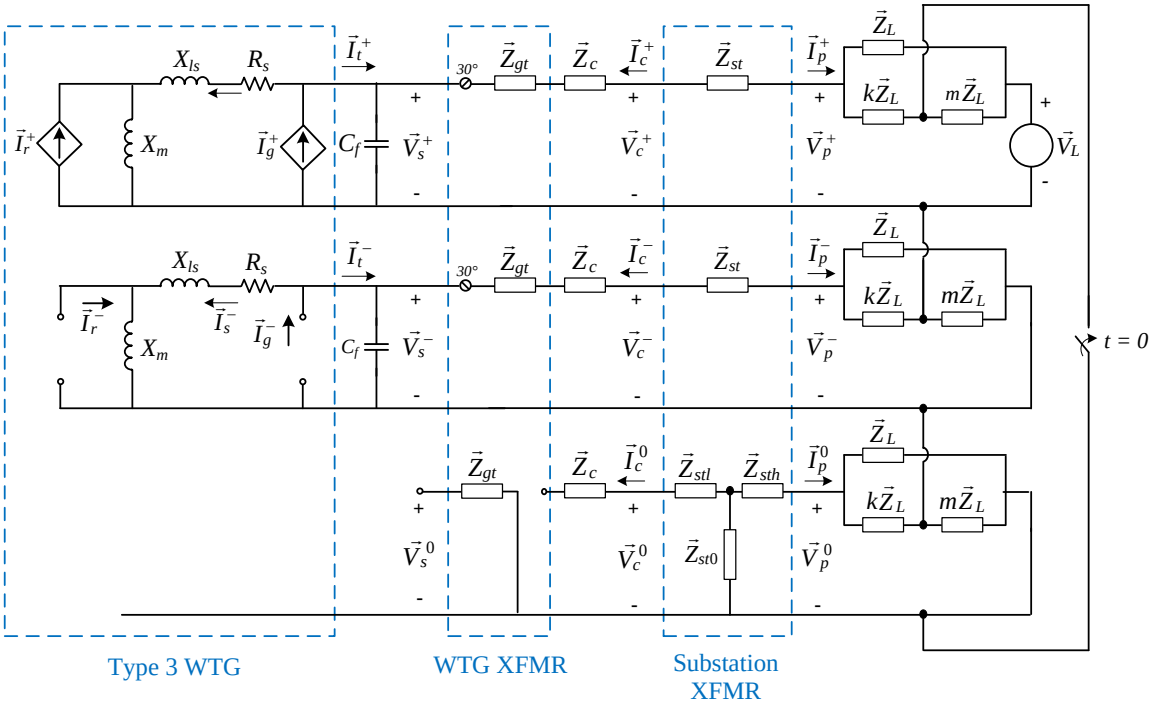


**Fig. 4.44: Sequence-network circuit for calculating the short-circuit currents in the SMIB system for a single-phase fault on the transmission system.**

The simulation results for a single-phase fault in the system of Fig. 4.40 are compared to the calculation results in the same way described above for the three-phase fault case. The simulated voltages and currents for this case are shown in Fig. 4.45(a) and the sequence components of these voltages and currents are shown in Fig. 4.45(b). Also shown in Fig. 4.45(b) are the calculated sequence components of the voltages and currents from the circuit of Fig. 4.44. Good agreement between the calculated results and the simulation results can be seen.

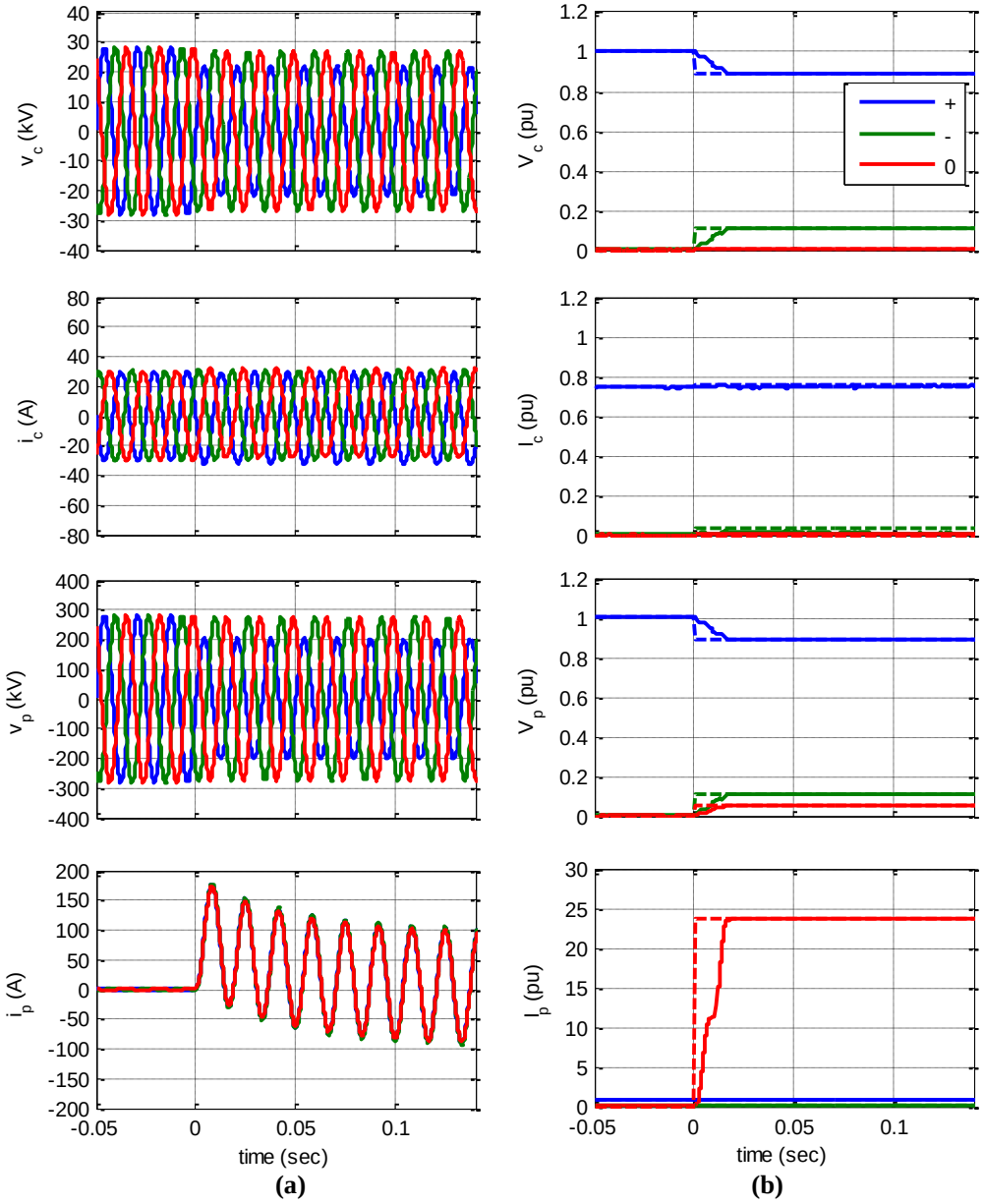


**Fig. 4.45: (a) Instantaneous simulation waveforms of SMIB system for a single-phase fault and (b) comparison of calculation and simulated sequence currents (solid = simulated, dashed = calculated).**

As another case, a three-phase fault is applied at a point along the transmission line closer to the wind-turbine generator (for this case, $k$ = 0.2 and $m$ = 2). For a fault at this location, the AC crowbar circuit is activated immediately after the fault. The transient simulation results for this case are shown in Fig. 4.46(a). The AC crowbar remains activated for roughly two cycles, and then the RSC regains control of the rotor

currents. As shown in the collector and PCC currents ($i_c$ and $i_p$ in Fig. 4.46(a)), the currents sharply increase during the AC crowbar activation. After two cycles, the current magnitude decreases. Calculation of the short-circuit currents for this case is much more complicated due to the change in topology of the Type 3 WTG during the fault. Further, it is not known exactly for what type of fault or the location of the fault at which the AC crowbar will activate. Therefore, for this case, two sets of calculations are performed. The first calculation assumes the AC crowbar does not activate. In this case, the calculations are done in exactly the same way described previously for the results shown in Fig. 4.43(b). For the second case, it is assumed that the AC crowbar activates immediately after the fault, and remains activated for the duration of the fault. The sequence-network circuits used for this case are the positive-sequence circuits shown in Fig. 4.29, and are calculated in the same way described in Chapter 3 for the Type 1 and Type 2 WTG. For this case, the short-circuit currents decay according to the same time constant given in (3.10), except the crowbar resistance is used in place of the external resistance of the Type 2 WTG. The results of these calculations are shown in Fig. 4.46(b), along with the positive-sequence components of the voltages and currents from the simulation results. The calculated positive-sequence components assuming the AC crowbar does not activate are shown by the blue-dashed line, and the calculated positive-sequence components assuming the AC crowbar does activate are shown by the red-dotted line. For the first two cycles, neither of the calculated results gives a good approximation to the currents calculated from the cosine filter algorithm in the simulation results. This is due to the rapidly decaying stator currents caused by the crowbar resistance. However, the calculated currents for the case of crowbar activation do capture the rapid decay of these currents. After the crowbar is removed (roughly after 0.03 seconds), the calculated currents assuming no crowbar activation give a better approximation to the simulated currents. However, using any one of these circuits for the calculations does not capture the complete behavior of the Type 3 WTG for this case, but

may provide some indication of the upper and lower limits of the currents in the time after the fault.

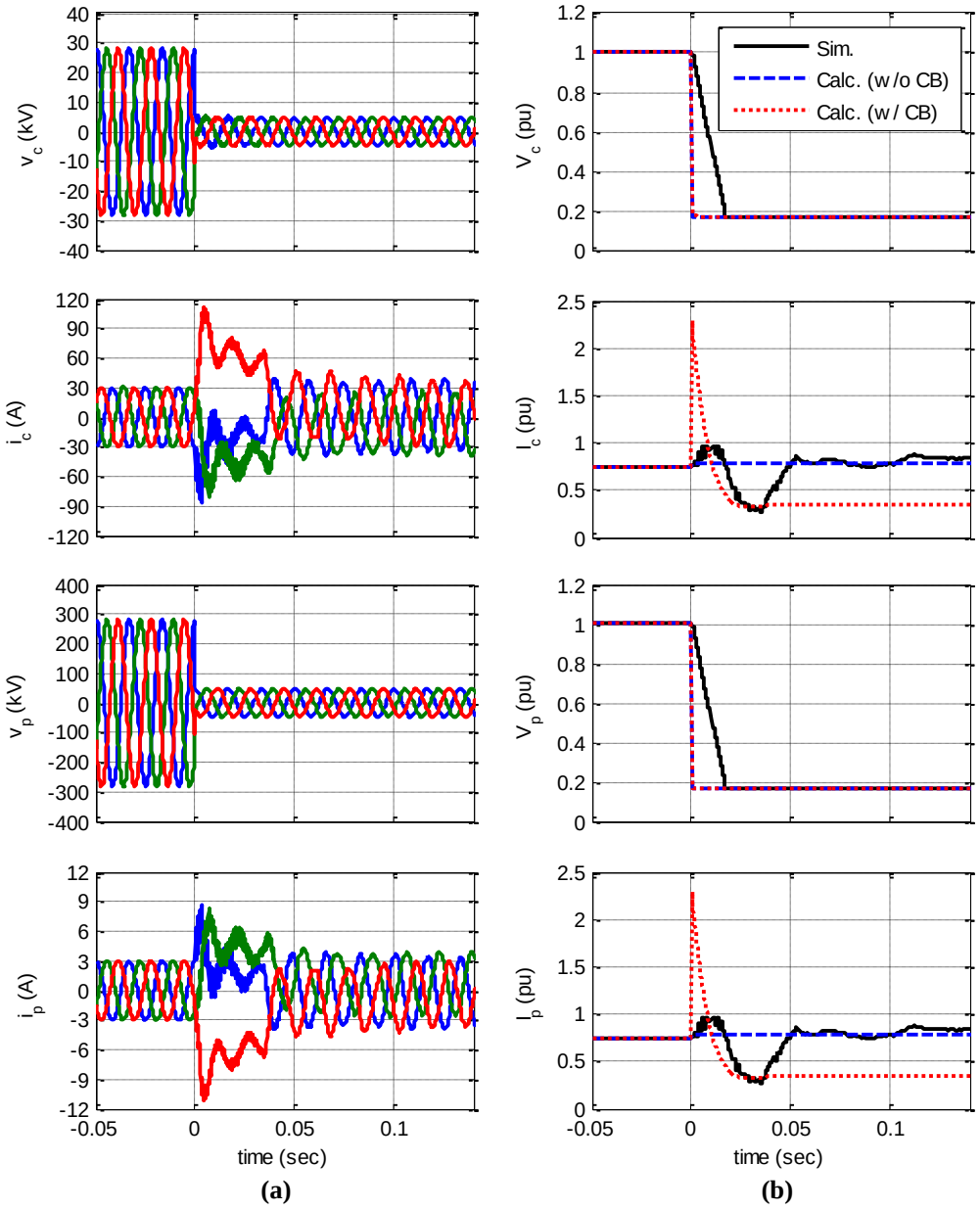


**Fig. 4.46: (a) Transient simulation results of various system voltage and currents for the case of a three-phase fault and AC crowbar activation and (b) comparison of the calculated and simulated positive-sequence components of these voltages and currents.**

## 4.8. System Studies of Multi-Machine Type 3 Wind Farm

The network shown in Fig. 4.47 is used to study the short-circuit behavior of a small Type 3 wind farm. This network is identical to the network used to study the Type 1 and Type 2 wind farms shown in Fig. 3.25, except that the WTGs in this system are the Type 3 WTGs with parameters given in Appendix A and the low-voltage winding of the WTG step-up transformer is set to 575 V (the rated voltage of the Type 3 WTG stator). The various other system parameters in the network of Fig. 4.47 are given in Appendix C. Unlike the single-machine infinite bus (SMIB) studies discussed in the previous section, the Type 3 WTGs are represented as an "averaged" model within the network shown in Fig. 4.47. Using a switching-level model for the Type 3 WTG within the network of Fig. 4.47 requires excessively long simulation time; however, using the averaged model, the RSC and GSC of each WTG are represented as current-controlled voltage sources, which permits the use of a larger simulation time step. Details of this averaged model are given in Appendix I, and transient simulation results comparing the averaged model to the switching-level model show that the two models have good agreement. For these studies, it is assumed that all seven WTGs are producing the same real and reactive power prior to the fault.

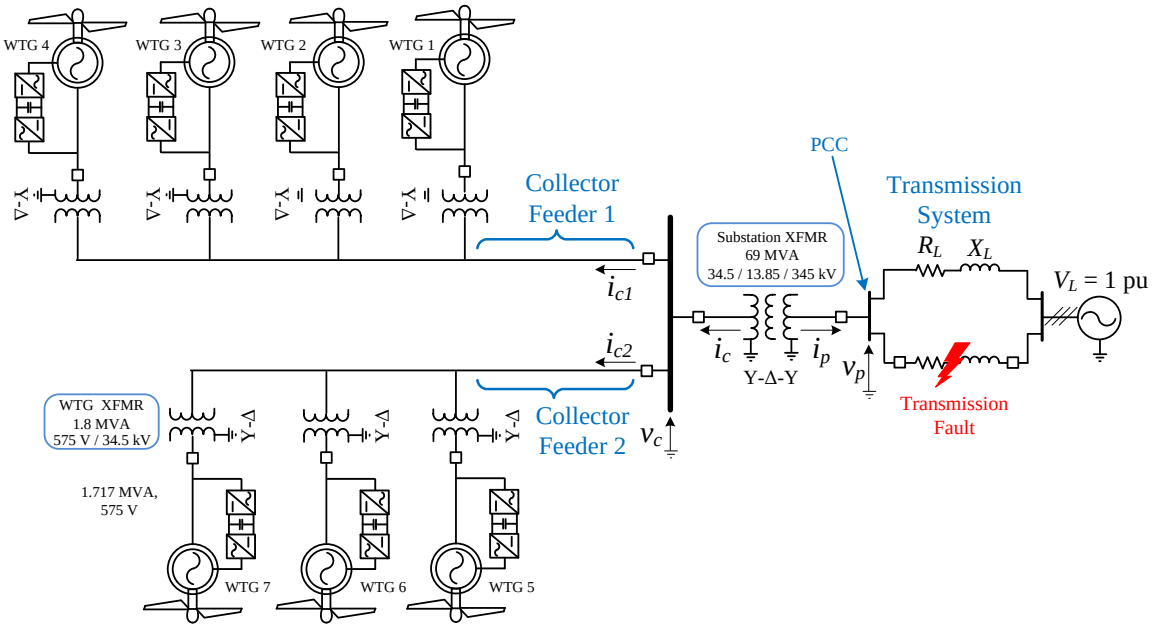


**Fig. 4.47: Multi-machine network used for system studies of Type 3 WTG wind farm.**

Simulation results for a three-phase fault on the transmission system in the network of Fig. 4.47 are shown in Fig. 4.48(a). A fault at this particular location results in approximately a 32% drop in the voltage on the wind plant collector system $v_c$. This fault location was intentionally chosen such that the crowbar protection does not activate on any of the Type 3 WTGs within the network.

Sequence-network calculations are performed for this network in the same way described in the previous section for the SMIB system. However, the sequence-network circuit for this network is much too complicated to draw succinctly here. However, each WTG within the network is represented in the same way shown in Fig. 4.25. Thus, a total of 14 current sources are used within the sequence-network circuit for this network, one for each of the GSCs and RSCs for all seven WTGs. The magnitude and phase angle of each current source is calculated in the same way already described in Section 4.3.1, where the pre-fault terminal voltage of each WTG is found from a load-flow solution on the network using the assumed real and reactive power output of each WTG. The results of these calculations for a three-phase fault on the transmission system are shown in Fig.

4.48(b) in addition to the positive-sequence voltages and currents from the simulation results. Each of the calculated values of the voltages and currents match closely to the simulation values, indicating the sequence-network model of the wind farm gives good results.

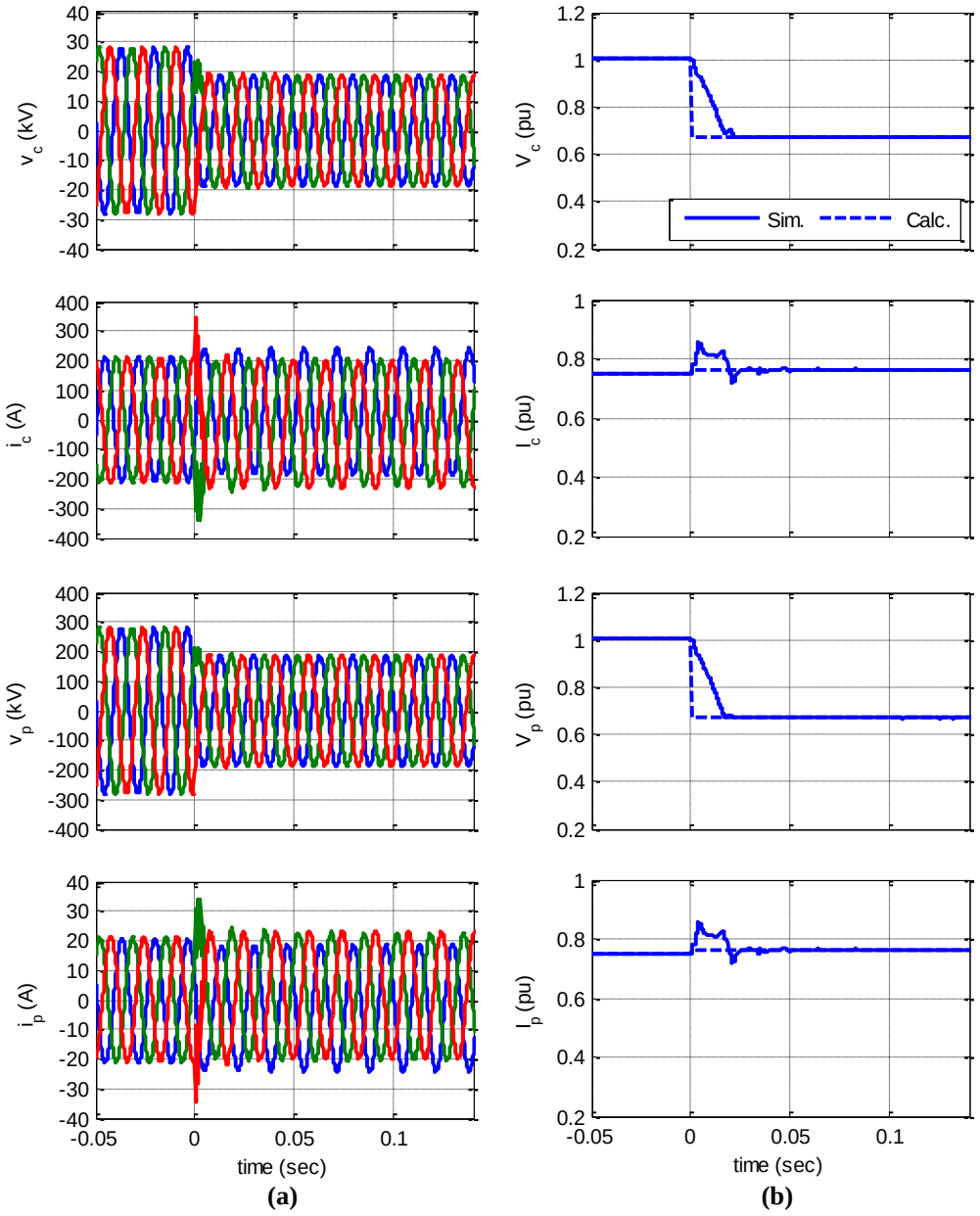


**Fig. 4.48: (a) Simulation results for a three-phase fault on the transmission system and (b) comparison of the calculated and simulated positive-sequence voltages and currents in the network.**

Simulation results for the case of a phase-B-and-C-to-ground fault in the transmission system in the network of Fig. 4.47 are shown in Fig. 4.49(a). The calculated sequence components of the voltages and currents are shown in Fig. 4.49(b), as well as the sequence components of the voltages and currents from the simulation results. Good agreement between the simulated sequence components and the calculated sequence components can be seen, indicating that the sequence-network models developed for the WTG provide good results.

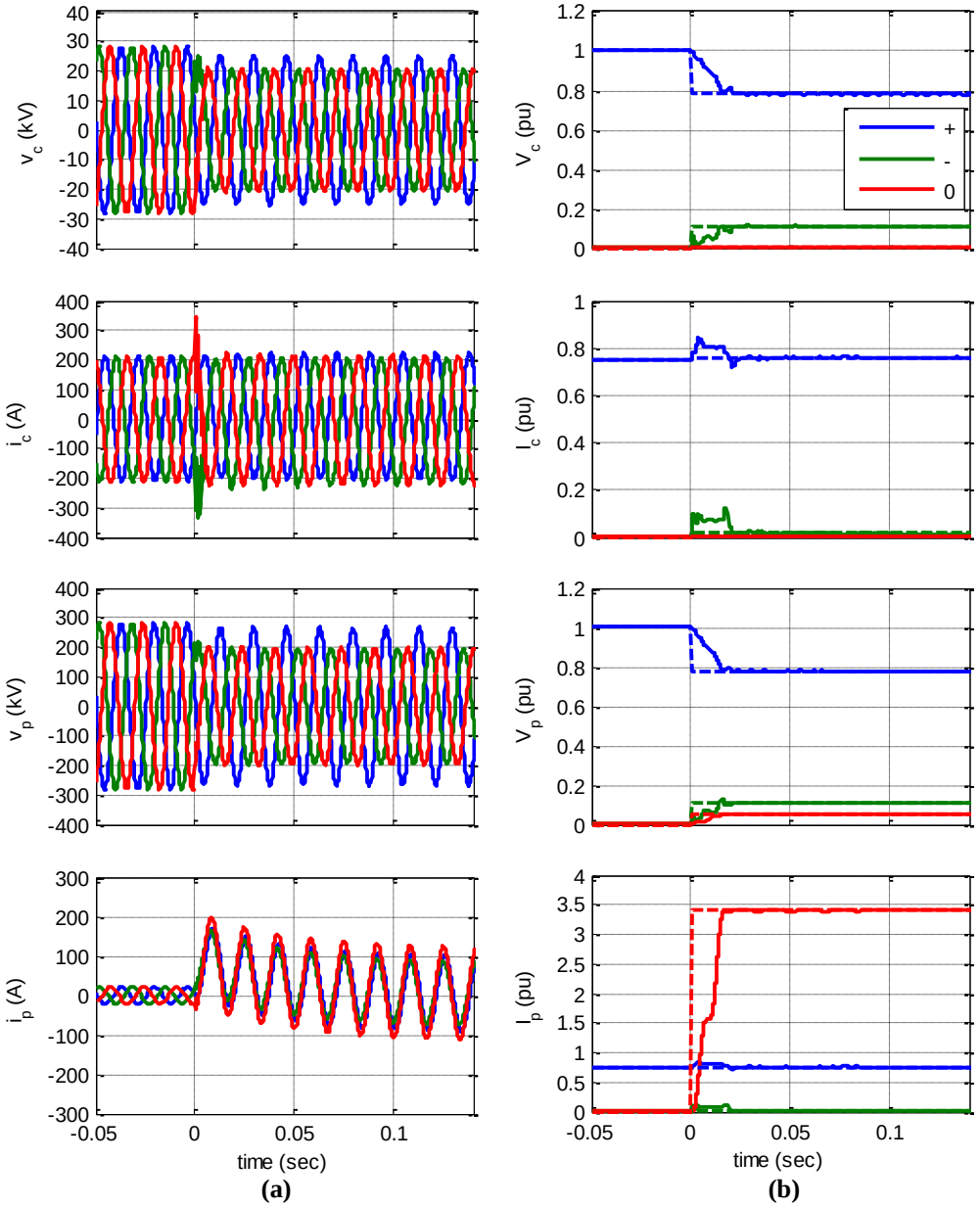


**Fig. 4.49: (a) Simulation results for a phase-B-and-C-to-ground fault on the transmission system and (b) comparison of calculated and simulated sequence quantities (solid = simulated, dashed = calculated).**

## 4.9. Conclusions

The sequence-network circuit derived in this chapter for the Type 3 WTG gives an approximation of the fundamental-frequency behavior of a Type 3 wind farm during short-circuit faults. This model provides a similar "template" equivalent circuit used for

other types of generators since the equivalent-circuit parameters are based solely on the pre-fault conditions of the system. This is similar to the concept of the constant flux linkage model used in synchronous machines and induction machines that justify the use of a constant voltage source behind a reactance. However, the models are quite different because of the use of *current sources* within the proposed sequence-network model as opposed to a *voltage source* within conventional short-circuit model. Additionally, the use of a voltage source in the conventional model is justified based on the physics of the generator. However, the model developed for the Type 3 WTG is justified based on simplifying assumptions of the controls. Therefore, the approach for determining the parameters of the sequence-network circuits for both Type 3 WTGs and conventional generators are the same; however, their behavior during faults is fundamentally different. The proposed sequence-network circuit of the Type 3 WTG described in this chapter encompasses these fundamental differences. Another key difference that separates the Type 3 WTG short-circuit behavior from the other types of WTGs is the AC crowbar protection. The crowbar activation occurs for particularly "severe" faults, in which the fault is close enough to the wind plant to cause a large reduction in the voltage. In this case, the short-circuit behavior is difficult to capture with one simplified circuit. It is recommended that both cases (crowbar activation and no crowbar activation) should be considered in fault studies using both sets of sequence-network circuits to capture the two possible operating modes of the WTG.

# CHAPTER 5: TYPE 4 WIND-TURBINE GENERATOR

## 5.1. Introduction

Unlike wind-turbine generator (WTG) Types 1-3, the AC generator of the Type 4 WTG does not directly interface to the grid, as displayed by the circuit diagram of the Type 4 WTG shown in Fig. 5.1. Therefore, the wind plant collector system "sees" only the grid-side converter (GSC) of the Type 4 WTG that is interfaced to the system. The controls of the GSC have the greatest impact on the short-circuit characteristics of the Type 4 WTG. Therefore, the Type 4 WTG can be understood to have a "programmed" response to short-circuit transients that is determined by the control system designer. This is in contrast to Type 1 and Type 2 WTGs, whose response is determined strictly by the physical characteristics of the generator itself. While the Type 3 WTG also has a controlled response to short-circuit transients, this controlled response only takes place if the fault is remote from the wind plant such that the Type 3 WTG can maintain control of its rotor-side converter. However, the Type 4 WTG has a controlled response, regardless of the location or type of fault. For this reason, the short-circuit behavior of the Type 4 WTG is much less complex than the Type 3 WTG.

In this chapter, the controls used for the GSC and machine-side converter (MSC) of the Type 4 WTG are described. A sequence-network model of the Type 4 WTG is proposed based on simplifying assumptions of the GSC controls. Calculations on a realistic wind-turbine generator network under different types of faults are performed using the proposed sequence-network model, and these calculations are compared to transient simulations of this network performed in PSCAD simulation software. Additionally, experimental short-circuit tests and results are provided for a lab-scale Type 4 WTG and compared with transient simulations as a means for validating the PSCAD model of the Type 4 WTG.

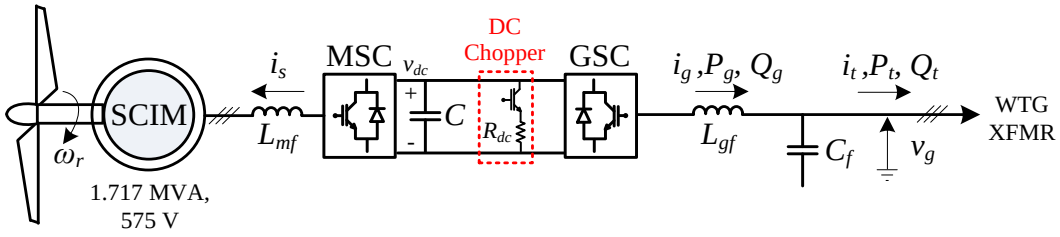


**Fig. 5.1: Circuit diagram of Type 4 WTG.**

## 5.2. GSC and MSC Control Design

The GSC of the Type 4 WTG is of most interest in short-circuit studies since this converter interfaces directly to the interconnecting network. The controls of the GSC, as shown by the block diagram in Fig. 5.2, completely determine the short-circuit current contributed by the Type 4 WTG. Therefore, the control design used in this work is discussed in detail in this section. The controls of the machine-side converter (MSC) are not particularly important to the short-circuit behavior of the Type 4 WTG, but the controls used for this converter are discussed in this section for completeness. The assumptions used in the design of these controllers are the same as those used for the design of the controllers for the Type 3 WTG discussed in Section 4.2.

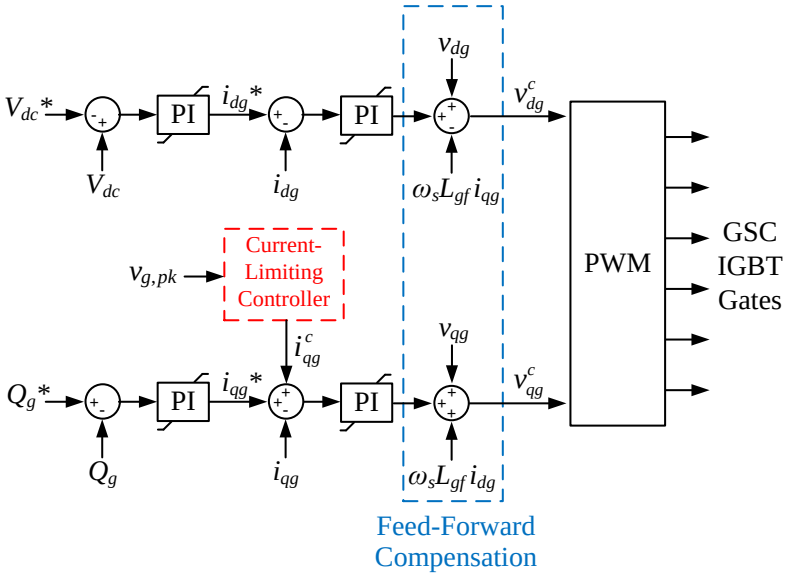


**Fig. 5.2: Block diagram of GSC controls.**

### *5.2.1. GSC Control Design*

Under normal operating conditions (not faulted conditions), the GSC of the Type 4 WTG is controlled in the same way as the GSC of the Type 3 WTG. These control objectives are to control the GSC AC currents, the DC-link voltage, and the GSC reactive power output with zero steady-state error. Alternatively, the terminal voltage of the Type 4 WTG can be controlled instead of the GSC reactive power if the Type 4 WTG is connected to a "weak" system, in which the voltage of the system fluctuates significantly based on operating conditions. However, using voltage control is less efficient than reactive power control, since the conductor currents are higher when the WTG is not operating at unity power factor ($Q_g$ = 0). The four (or three, if a constant reactive current reference is used instead of a closed-loop GSC reactive power controller) PI controllers of the Type 4 WTG GSC can be tuned in the same way described for the Type 3 WTG GSC. However, during fault conditions, Type 4 WTGs switch into "current-limiting" control, in which the GSC injects a manufacturer-specified current magnitude (typically up to 1.1 to 1.4 pu) with strictly a positive-sequence component [49] [50]. This current-

limiting control can be implemented using the GSC current-control loops shown in Fig. 5.3. This current controller is identical to the Type 3 WTG GSC current controller, except an additional q-axis compensation current $i_{qg}^{c}$ is added to the reference q-axis current. This compensation component is determined by the current-limiting controller shown in Fig. 5.3. Under normal operating conditions, $i_{qg}^{c}$ is zero, and the peak instantaneous current injected by the GSC is given by

$$i_{g,pk} = \sqrt{(i_{dg}^{*})^2 + (i_{qg}^{*})^2} \ . \tag{5.1}$$

During low-voltage conditions, the value $i_{qg}^{c}$ is determined such that the GSC injects a pre-determined current-limiting magnitude of $I_{gmax}$ (peak instantaneous value). Thus, in low-voltage conditions, the peak value of the GSC instantaneous current is given by

$$i_{g,pk} = I_{g\max} = \sqrt{(i_{dg}^{*})^2 + (i_{qg}^{*} + i_{qg}^{c})^2} \ . \tag{5.2}$$

Using this relationship, the value of the q-axis current ($i_{qg}^{*} + i_{qg}^{c}$) to be injected is found by solving for this term in (5.2), given by

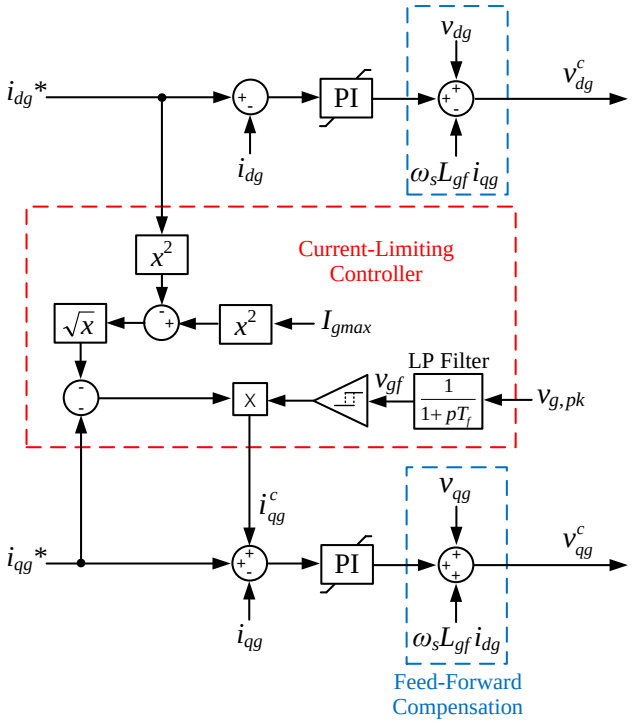


**Fig. 5.3: Block diagram of GSC current controller.**

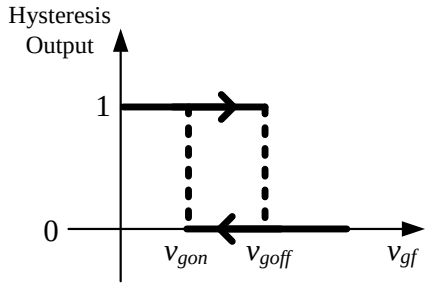


**Fig. 5.4: GSC hysteresis buffer output logic.**

$$\pm (i_{qg}^{c} + i_{qg}^{*}) = \sqrt{I_{g\max}^{2} - (i_{dg}^{*})^{2}} \; . \tag{5.3}$$

Using either the + or – in (5.3) to calculate the value of $i_{qg}^{c}$ will result in the GSC injecting a current with magnitude $I_{gmax}$. However, it is desirable to inject a value of $i_{qg}^{c}$ that produces positive reactive power to help support the grid voltage. Thus, according to (4.40), a negative value of q-axis GSC current corresponds to injecting a positive reactive power. Thus, in (5.3), the minus sign is chosen, and the compensating current is given by

$$i_{qg}^{c} = -\sqrt{I_{g\max}^{2} - (i_{dg}^{*})^{2}} - i_{qg}^{*} \, . \tag{5.4}$$

This relationship is identical to the calculation of the compensating current in the current-limiting controller shown in Fig. 5.3.

A hysteresis buffer outputs the control logic that turns on the q-axis compensation current. The hysteresis buffer logic appears in Fig. 5.4. The hysteresis buffer output is determined based on a low-pass (LP) filtered signal $v_{gf}$ of the peak instantaneous terminal voltage, given by

$$v_{g,pk} = \sqrt{v_{dg}^{2} + v_{qg}^{2}} \; . \tag{5.5}$$

The hysteresis buffer helps to prevent any "chopping" behavior of the current-limiting control around a threshold voltage. Additionally, the hysteresis buffer can help prevent this chopping behavior that may occur due to a 120 Hz oscillation in the terminal voltage magnitude during unbalanced faults. The low-pass filter in Fig. 5.3 is designed to

attenuate the 120 Hz component in the measured peak voltage. However, setting the cutoff frequency of this filter too low may limit the detection time of the low-voltage condition due to the slow step response of the filter. Thus, the time constant $T_f$ of this filter is chosen to give a cutoff frequency of 20 Hz ($T_f = 1/(2\pi 20)$). The Bode magnitude plot of this filter is shown in Fig. 5.5. The gain of this filter at 120 Hz is approximately -15 dB; thus, significant attenuation of the 120 Hz ripple is achieved. The step response of this filter for a unit-step increase in $v_{g,pk}$ is shown in Fig. 5.6. The output of this filter reaches roughly 90% output one cycle after the step change in the input. Thus, for most faults, this filter will enable the current-limiting controller within one cycle of the fault occurrence.

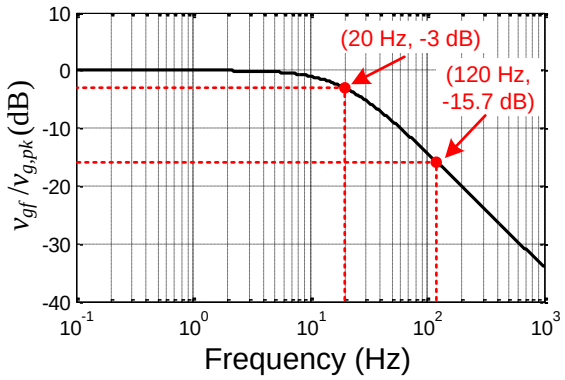


**Fig. 5.5: Bode plot of the low-pass filter for current-limiting controller.**

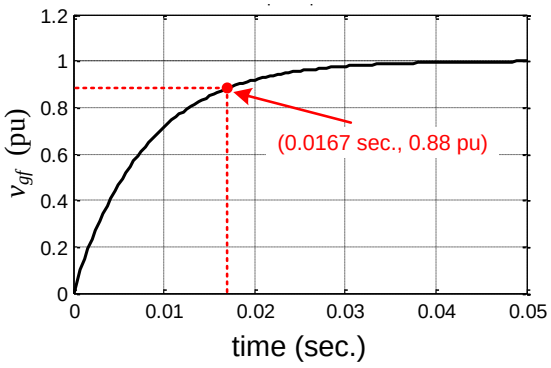


**Fig. 5.6: Step response of the low-pass filter used in current-limiting controller for a unit step change in the peak instantaneous voltage.**

The exact turn-on/turn-off times of the current-limiting controller depend on three parameters: the filter time constant, the turn-on/turn-off voltages $v_{gon}$ and $v_{goff}$ of the hysteresis buffer, and the magnitude of the change in voltage caused by the fault. For example, assume that the GSC is designed so that the current-limiting controller turns on for a 10% drop in voltage from the nominal value. Thus, the voltages $v_{gon}$ and $v_{goff}$ of the hysteresis buffer could be chosen as 0.89 and 0.91 per unit, respectively, to prevent "chopping" around the threshold of 0.9 per-unit voltage. As a simplifying assumption, a fault that causes a 50% drop in the GSC terminal voltage can be understood as a 0.5 per-unit (negative) step change in $v_{g,pk}$. The output of the current-limiting filter for this scenario is shown in Fig. 5.7, with the assumption that the pre-fault voltage peak is at 1 per unit (note, a filter time constant that gives a cutoff frequency of 20 Hz is assumed in the results). From Fig. 5.7, the current-limiting controller will turn on when the filtered peak voltage goes below 0.89 per unit, which is approximately 2 milliseconds after the drop in voltage. The increase in voltage after the fault is cleared can be considered a positive step change in the voltage magnitude of 0.5 per unit (0.5 to 1.0 per unit). The filter output for this scenario is shown in Fig. 5.8. Thus, the current-limiting controller turns off after the filtered peak voltage exceeds 0.91 per unit, which is approximately 14 milliseconds after the voltage recovers. Thus, the turn-off time of the current-limiting controller is much longer than the turn-on time, but is still less than one cycle. However, note that the turn-on/turn-off times change depending on the amount of voltage drop at the GSC terminals. In other words, if the voltage drop is larger than 50%, the turn-on time is smaller, but the turn-off time is larger (and vice versa). This type of analysis only provides an approximation of the turn-on/turn-off times of the current-limiting controller, since the actual terminal voltages of the GSC do not change instantaneously before and after a fault.

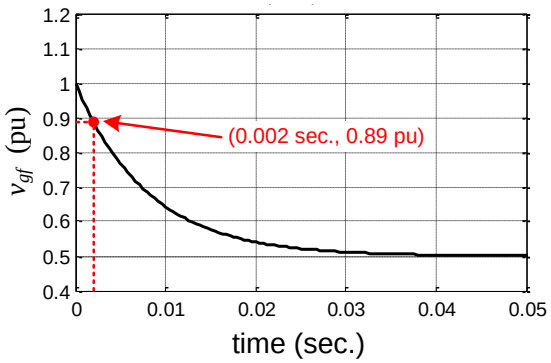


**Fig. 5.7: Approximation of turn-on time of the current-limiting controller for a 50% drop in the GSC terminal voltage.**

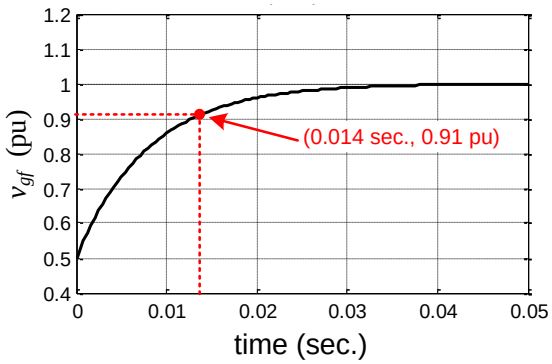


**Fig. 5.8: Approximation of turn-off time of the current-limiting controller after the recovery of the GSC terminal voltage from a 50% drop in voltage.**

The value of $I_{gmax}$ for a particular Type 4 WTG depends on current rating of the insulated-gate bipolar transistor (IGBT) switching devices in the GSC. The value of $I_{gmax}$ is determined by the amount of current that the GSC can safely output without damaging these devices. Another consideration for the choice of $v_{gon}$ and $v_{goff}$ in the current-limiting controller is the power rating of the GSC. For the example discussed in the previous paragraph, the (per-unit) apparent power during current-limiting control can be as high $v_{goff} * I_{gmax}$. Thus, if $I_{gmax}$ is chosen to be 1.2 per unit, then the apparent power can be as high as 0.91*1.2 = 1.09 per unit. Designing the GSC with these parameters can result in temporary overloads of the GSC beyond its power rating. The GSC may be capable of operating in overloaded conditions temporarily; otherwise, either the value of

$I_{gmax}$ must be reduced or the value of $v_{gon}$ and $v_{goff}$ must be reduced to avoid these overloads. The numerical values of these parameters are given in Appendix A.

The closed-loop transfer functions of the GSC current controllers are identical to the Type 3 WTG GSC transfer functions discussed in Section 4.2.1. Thus, the proportional-integral (PI) controller gains of the GSC current controllers shown in Fig. 5.3 can be designed in the same way as for the Type 3 WTG GSC current controllers. However, the value of the filter inductance is not the same for the Type 4 WTG; thus, the controller gains are not the same. The numerical values of the Type 4 GSC parameters and current-controller gains are given in Appendix A.

The DC-link voltage PI controller for the GSC of the Type 4 WTG can be tuned in the same way described in Section 4.2.2 for this controller in the Type 3 WTG. The closed-loop transfer function of this controller in the Type 3 and Type 4 WTG are identical. Therefore, this control design is not repeated here, but the values of the PI controller gains are given in Appendix A.

### *5.2.2. MSC Control Design*

The generator for the Type 4 WTG in this work is a squirrel-cage induction machine (SCIM). An indirect field-oriented vector control scheme [74], with block diagram shown in Fig. 5.9, is used in the MSC to control the stator currents, rotor speed, and machine flux. A brief description of these controls is given in this section.

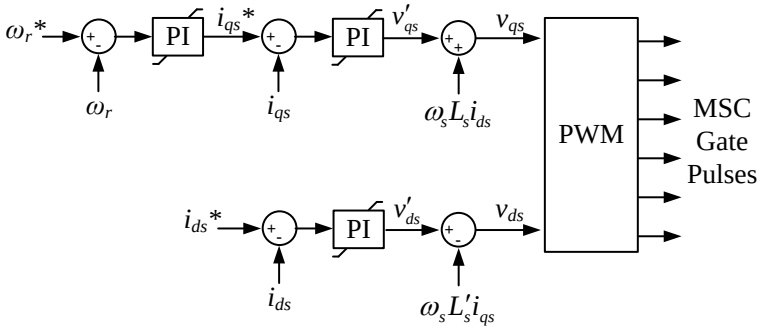


**Fig. 5.9: Machine-side converter control block diagram.**

The stator and rotor voltage equations of the induction machine given in (2.12) in a synchronous reference frame oriented with the rotor-flux linkage are given by

$$\begin{aligned} v_{ds} &= R_s i_{ds} - \omega_s \lambda_{qs} + p\lambda_{ds} \quad & 0 &= R_r i_{dr} + p\lambda_{dr} \\ v_{qs} &= R_s i_{qs} + \omega_s \lambda_{ds} + p\lambda_{qs} \quad & 0 &= R_r i_{qr} + s\omega_s \lambda_{dr} \end{aligned}, \tag{5.6}$$

where the rotor voltages are zero in a squirrel-cage induction machine and the q-axis rotor flux linkage is zero due to the orientation of the reference frame. The flux linkages in (5.6) are given by

$$\begin{aligned} \lambda_{ds} &= L_s i_{ds} + L_m i_{dr} \quad & \lambda_{dr} &= L_r i_{dr} + L_m i_{ds} \\ \lambda_{qs} &= L_s i_{qs} + L_m i_{qr} \quad & 0 &= L_r i_{qr} + L_m i_{qs} \end{aligned}. \tag{5.7}$$

Solving for the rotor currents in the rotor-flux linkage equations in (5.7) gives

$$\begin{aligned} i_{dr} &= \frac{\lambda_{dr} - L_m i_{ds}}{L_r} \\ i_{qr} &= -\frac{L_m}{L_r} i_{qs} \end{aligned}. \tag{5.8}$$

The stator voltage equations in (5.6) can be rewritten by substituting in the stator-flux linkage equations in (5.7) and the rotor current equations in (5.8), given by

$$
\begin{aligned}
v_{ds} &= R_s i_{ds} - \omega_s \left( L_s i_{qs} - \frac{L_m^2}{L_r} i_{qs} \right) + p \left( L_s i_{ds} + \frac{L_m}{L_r} \lambda_{dr} - \frac{L_m^2}{L_r} i_{ds} \right) \\
&= (R_s + pL_s') i_{ds} - \omega_s L_s' i_{qs} + \frac{L_m}{L_r} p\lambda_{dr} \\
v_{qs} &= R_s i_{qs} + \omega_s \left( L_s i_{ds} + \frac{L_m}{L_r} \lambda_{dr} - \frac{L_m^2}{L_r} i_{ds} \right) + p \left( L_s i_{qs} - \frac{L_m^2}{L_r} i_{qs} \right) \\
&= (R_s + pL_s') i_{qs} + \omega_s L_s' i_{ds} + \omega_s \frac{L_m}{L_r} \lambda_{dr}
\end{aligned}
\quad . \tag{5.9}
$$

From (5.6), the d-axis rotor-flux linkage is given by

$$
p\lambda_{dr} = -R_r i_{dr} = -\frac{R_r}{L_r} \lambda_{dr} + R_r \frac{L_m}{L_r} i_{ds} \, . \tag{5.10}
$$

The d-axis stator current can be written in terms of the d-axis rotor-flux linkage by rearranging terms, to yield

$$
i_{ds} = \frac{1}{L_m} \left( \frac{L_r}{R_r} p + 1 \right) \lambda_{dr} \, . \tag{5.11}
$$

Equation (5.11) indicates that the rotor-flux linkage can be controlled by controlling $i_{ds}$. In conventional field-oriented control terminology, $i_{ds}$ is known as the "flux-producing" component of the stator current. For this work, $\lambda_{dr}$ is kept constant (making $p$ = 0) by controlling $i_{ds}$ to be constant; thus, $\lambda_{dr} = L_m i_{ds}^*$ and $p\lambda_{dr}$ = 0, where $i_{ds}$* is the constant d-axis stator current reference. Therefore, the voltage equations in (5.9) become

$$
\begin{aligned}
v_{ds} &= (R_s + pL_s') i_{ds} - \omega_s L_s' i_{qs} \\
v_{qs} &= (R_s + pL_s') i_{qs} + \omega_s L_s i_{ds}
\end{aligned}
\quad , \tag{5.12}
$$

where $L_s$' is the stator transient inductance, given by

$$
L_s' = L_s - \frac{L_m^2}{L_r} \, . \tag{5.13}
$$

Similar to the technique used in the previous chapter for the Type 3 WTG controllers, fictitious voltages are introduced to decouple the d- and q-axis stator current controls, given by

$$\begin{aligned} v'_{ds} &= v_{ds} + \omega_s L'_s i_{qs} \\ v'_{qs} &= v_{qs} - \omega_s L_s i_{ds} \end{aligned}. \tag{5.14}$$

Solving for the d- and q-axis stator voltages in (5.14) and substituting into (5.12) gives

$$\begin{aligned} v'_{ds} &= (R_s + pL'_s) i_{ds} \\ v'_{qs} &= (R_s + pL'_s) i_{qs} \end{aligned}. \tag{5.15}$$

These equations are of the same form as in (4.4) for the GSC currents of the Type 3 WTG. Thus, the PI controller gains for the d- and q-axis stator currents can be tuned in the same way described in Section 4.2.1. Because the transfer functions of the d- and q-axis components of the stator current are identical, the same controller gains are used in both the d- and q-axis current PI controllers. A block diagram of the d-axis stator current control loop is shown in Fig. 5.10. An identical control loop is used for the q-axis stator current. The numerical values of the machine parameters and controller gains are given in Appendix A.

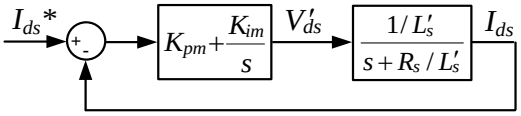


**Fig. 5.10: Block diagram of MSC inner current-control loop.**

## *5.2.3. Rotor Speed Control Design*

The electric torque of the induction machine can be written in terms of the rotor flux linkages as

$$T_e = \frac{3}{2}\frac{poles}{2}\frac{L_m}{L_r}(i_{qs}\lambda_{dr} - i_{ds}\lambda_{qr}) = \frac{3}{2}\frac{poles}{2}\frac{L_m}{L_r} i_{qs}\lambda_{dr}, \tag{5.16}$$

where $\lambda_{qr}$ is zero due to the orientation of the reference frame. As mentioned in the previous sub-section, the d-axis rotor flux is controlled to be constant ($\lambda_{dr} = L_m i_{ds}^*$). Thus,

the electric torque is approximately proportional to the q-axis stator current. The rotor speed of the Type 4 WTG is given by

$$p\omega_r + \frac{F}{J}\omega_r = \frac{1}{J}(T_e - T_m). \tag{5.17}$$

Substituting the electric torque equation in (5.16) into (5.17) gives

$$p\omega_r + \frac{F}{J}\omega_r = \frac{1}{J}\left(\frac{3}{2}\frac{poles}{2}\frac{L_m^2}{L_r} i_{ds}^* i_{qs} - T_m\right) = K_\omega i_{qs} - \frac{1}{J}T_m, \tag{5.18}$$

where

$$K_\omega = \frac{1}{J}\frac{3}{2}\frac{poles}{2}\frac{L_m^2}{L_r} i_{ds}^*. \tag{5.19}$$

In conventional induction machine field-oriented control terminology, the q-axis stator current is known as the "torque-producing" component of the stator current. Note that this is a similar situation as described in Section 4.2.4 for the electric torque of the Type 3 WTG, where the electric torque in that case could be controlled through the q-axis rotor current. Nonetheless, the rotor speed PI controller for the Type 4 WTG can be tuned in the same way as the rotor speed controller for the Type 3 WTG, and this control design is not repeated here. The block diagram of the speed-control loop is shown in Fig. 5.11, and the various system parameters and controller gains are given in Appendix A.

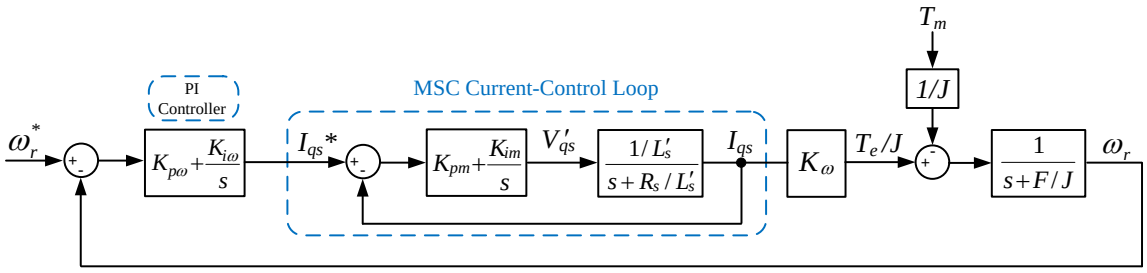


**Fig. 5.11: Block diagram of speed control loop in MSC.**

## 5.3. Proposed Sequence-Network Model of Type 4 WTG

The sequence-network model of the Type 4 WTG is developed by making simplifying assumptions about the controls of the GSC. The generator and MSC are assumed to be completely decoupled from the grid; thus, these components are assumed to have no impact on the short-circuit behavior of the Type 4 WTG.

### *5.3.1. Steady-State Equivalent Circuit*

The proposed steady-state equivalent circuit of the Type 4 WTG is shown in Fig. 5.12. The controlled current source $\vec{I}_g$ is a current phasor representing the commanded d- and q-axis components of the GSC controls. It is assumed that the GSC current controllers track their reference values with zero steady-state error. The reference values of the d- and q-axis GSC currents $i_{dg}$* and $i_{qg}$* are determined from the DC-link voltage and GSC reactive power controllers, respectively, as shown in Fig. 5.2. The currents commanded by these outer-loop controls determine the real and reactive power output of the Type 4 WTG. Thus, in steady state, the current $\vec{I}_g$ is completely determined by the real and reactive power output of the Type 4 WTG. The inductance $L_{gf}$ is the filter inductance of the GSC and the capacitor $C_f$ is the filter capacitance of the GSC. The voltage source $\vec{V}_L$ and the impedance $R_L + jX_L$ are a Thevenin-equivalent representation of the network to which the Type 4 WTG is connected. The current source $\vec{I}_g$ in Fig. 5.12 can be calculated using the following steps:

1. Initialize the power output of the Type 4 WTG $P_g$ and $Q_g$.
2. Obtain the terminal voltage phasor $\vec{V}_g$ by solving the load-flow equations on the external network with the Type 4 WTG terminals as a bus.
3. Calculate the current $\vec{I}_g$ from the voltage $\vec{V}_g$ and the power outputs $P_g$ and $Q_g$ by

$$\vec{I}_g = \left( \frac{P_g + jQ_g}{\vec{V}_g} \right)^*, \tag{5.20}$$

where * represents the complex conjugate.

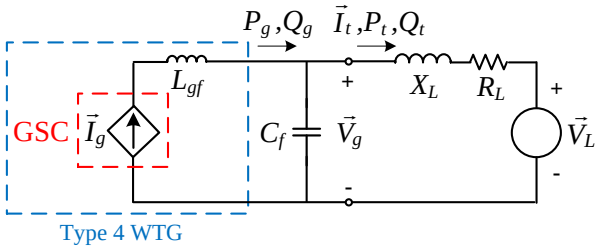


**Fig. 5.12: Steady-state equivalent circuit of Type 4 WTG.**

To demonstrate the calculation steps above, an example calculation is performed to determine the steady-state voltage and phasor quantities in Fig. 5.12. The impedance $R_L + jX_L$ is assumed to be 0.01 + *j*0.02 per unit and the voltage source $\vec{V}_L$ is assumed to be 1 per unit with an angle of zero degrees. To simplify the calculations, the filter capacitance $C_f$ is neglected in the calculations:

1. *Initialize the power output of the Type 4 WTG $P_g$ and $Q_g$.*

   Assume the Type 4 WTG is generating 0.75 per unit real power and is operating at a power factor of 0.95 (overexcited). Thus, the reactive power generated by the Type 4 WTG is given by

   $$Q_g = P_g \tan\theta = 0.75 * \tan(\cos^{-1}(0.95)) = +0.2465 \text{ per unit.} \tag{5.21}$$

2. *Obtain the terminal voltage phasor $\vec{V}_g$ by solving the load-flow equations on the external network with the Type 4 WTG terminals as a bus.*

   Details of the load-flow calculation are not provided here, as many references are available that provide details on how to perform these calculations (see [7] for further reading). The GSC terminal voltage phasor is calculated to be $\vec{V}_g = 1.0122 \angle 0.7096°$.

3. *Calculate the current $\vec{I}_g$ from the voltage $\vec{V}_g$ and the power outputs $P_g$ and $Q_g$.*

From (5.20), the GSC current phasor is given by

$$\vec{I}_g = \left( \frac{P_g + jQ_g}{\vec{V}_g} \right)^* = \left( \frac{0.75 + j0.2465}{1.0122 \angle 0.7096^\circ} \right)^* = 0.7800 \angle -17.48^\circ . \quad (5.22)$$

The steady-state equivalent circuit in Fig. 5.12 gives the pre-fault operating conditions of the Type 4 WTG. From the GSC current phasor $\vec{I}_g$ calculated for steady-state conditions, the short-circuit currents can be estimated, as described in the following sub-sections.

### *5.3.2. Sequence-Network Circuits*

The sequence-network circuit of the Type 4 WTG is derived based on the controls of the GSC described in Section 5.2.1. Similar to the GSC of the Type 3 WTG, it is assumed that the control response of the DC-link voltage controller is negligibly small in the time frame of interest during a short circuit. Thus, it is assumed that the d-axis component of the GSC current does not change from its pre-fault value. However, because of the current-limiting controller, the q-axis component of the GSC changes quickly after a drop in the terminal voltage. Controlling the GSC in the way described in Section 5.2.1 results in a q-axis current which forces the total GSC to be the pre-determined current-limiting magnitude of the GSC ($I_{gmax}$). Therefore, for any type of fault that results in a voltage drop at the WTG terminals below some pre-set voltage threshold ($v_{gon}$ in Fig. 5.4), the total current injected by the GSC will have a peak-current magnitude equal to $I_{gmax}$. However, the proportion of the d- and q-axis (real and reactive) components of the current depends on the pre-fault conditions. Thus, the GSC current *after* the fault can be calculated using (5.3), and is given by

$$\vec{I}_g^{\,a} = \text{Real}(\vec{I}_g^{\,a}) + j\text{Imag}(\vec{I}_g^{\,a}) = \text{Real}(\vec{I}_g^{\,b}) - j\sqrt{\left(\frac{I_{g\max}}{\sqrt{2}}\right)^2 - \left(\text{Real}(\vec{I}_g^{\,b})\right)^2}\,, \qquad (5.23)$$

where the '*b*' and '*a*' superscripts denote the before-fault and after-fault quantities, respectively. The relationship between (5.3) and (5.23) is that the d-axis component of the GSC current in (5.3) corresponds to the "Real" component of the GSC current phasor in (5.23). A similar relationship exists for the q-axis component and imaginary ("Imag") component of the GSC current phasor. Thus, (5.23) reflects the assumption that the d-axis component (or real component) of the GSC does not change after the fault, but the q-axis component changes *instantaneously* after the fault according to (5.3). Equation (5.23) indicates that the post-fault GSC current can be calculated strictly from the known pre-fault conditions and a known maximum current injection determined by the WTG manufacturer. The GSC current-limiting control is not enabled immediately after the voltage drop occurs due to the low-pass filter and hysteresis buffer shown in Fig. 5.3. For this reason, the current calculated using (5.23) is not immediately injected after the fault. The amount of time between the instant of the fault and the enabling of the current-limiting control is dependent on the time constant of the low-pass filter, the magnitude of the change in voltage, and the turn-on voltage threshold $v_{gon}$. However, in this work, these parameters are chosen in such a way that the current-limiting controller is enabled within one cycle after the fault occurs; thus, for simplicity, it is assumed that this short time is negligible and that this current is injected instantaneously after the fault.

The GSC current-controllers are assumed to track their reference currents with zero error. Because the reference currents are assumed to be strictly DC values, these current controllers allow only positive-sequence currents to flow in the GSC (since DC quantities in a synchronous reference frame correspond to the positive-sequence quantities). Therefore, the negative-sequence currents in the GSC are zero. However, if shunt filter capacitors are used at the output of the GSC, some negative-sequence currents may flow through these capacitors. Additionally, no zero-sequence currents flow in the

Type 4 WTG since it is assumed that the converter is a three-wire system. Thus, the sequence-network circuits of the Type 4 WTG are shown in Fig. 5.13.

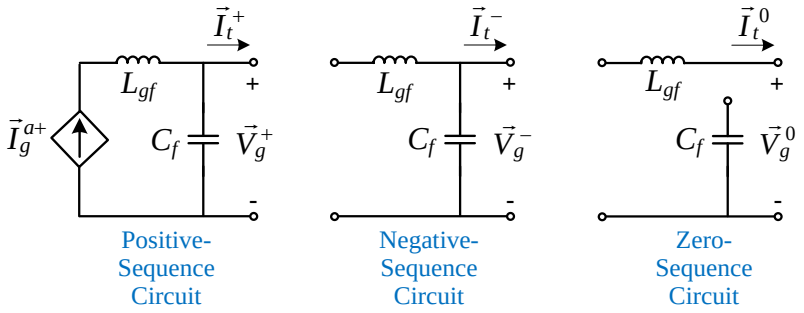


**Fig. 5.13: Sequence-network circuits of a Type 4 WTG.**

## 5.4. Experimental Results vs. Transient Simulations

Short-circuit tests were carried out on the experimental setup shown in Fig. 5.14. Note that this is the same equipment shown in Fig. 4.33 used in the study of the Type 3 WTG. However, the equipment has been reconfigured as a Type 4 WTG according to the circuit diagram shown in Fig. 5.15. The rotor windings of the wound-rotor induction generator (WRIG) have been short circuited so that this machine behaves like a squirrel-cage induction machine. Conventional indirect field-oriented vector control is used in the machine-side converter (MSC) controls, as described in Section 5.2.2. Vector control is also used in the grid-side converter, as described in Section 5.2.1. For both the MSC and GSC, a space-vector pulse-width modulation (PWM) algorithm is implemented to determine the IGBT gate turn on/off signals.

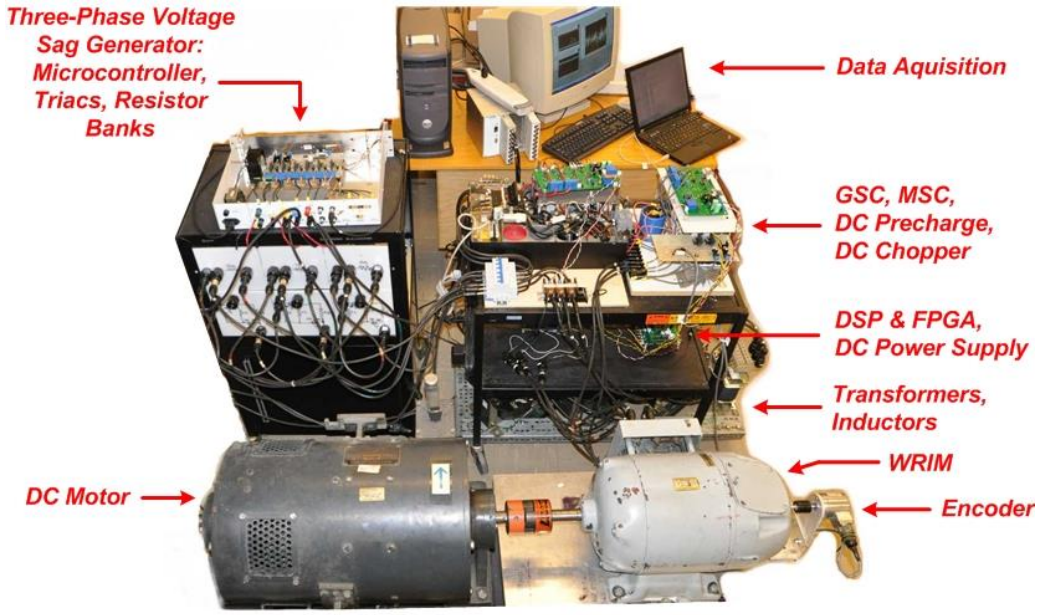


**Fig. 5.14: Photo of experimental testbed of Type 4 wind turbine generator.**

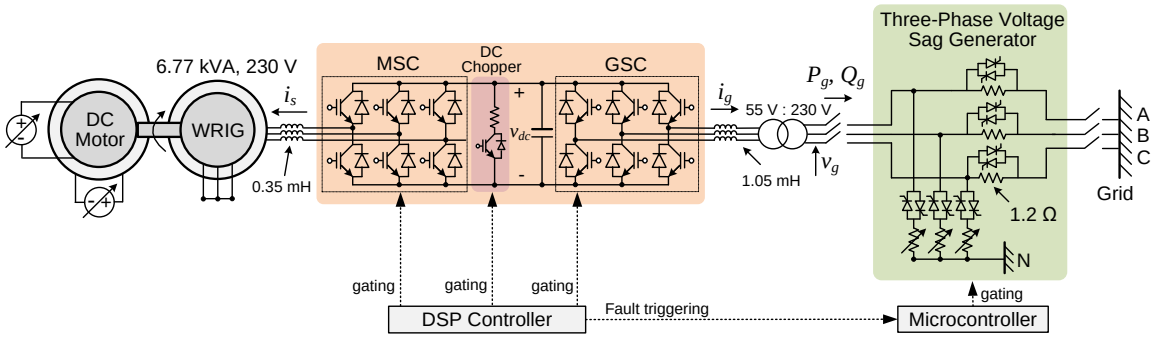


**Fig. 5.15: Circuit diagram of Type 4 WTG experimental testbed.**

The experimental setup shown in Fig. 5.15 is replicated in PSCAD simulation software to compare the transient simulation results to the experimental results from the short-circuit tests. This comparison is used to validate the PSCAD transient simulation model of the Type 4 WTG. Identification of the circuit parameters of the wound-rotor induction generator (WRIG) in Fig. 5.15 was described in Chapter 3, and these machine parameters are given in Appendix A. For this experimental testbed, the current-limiting

value $I_{gmax}$ is set to 35 A peak, and the turn-on and turn-off voltages of the current-limiting control are 0.9 and 0.95 per unit, respectively.

### *5.4.1. Three-Phase Short-Circuit Case*

Experimental short-circuit tests were carried out on the system shown in Fig. 5.15 using a resistance of 0.5 ohm in the shunt resistors of the three-phase voltage sag generator, resulting in a voltage drop of roughly 70% at the terminals of the Type 4 WTG. The experimental results for a three-phase fault are shown in left column of Fig. 5.16. Immediately after the GSC voltage ($v_g$) drops, the GSC transitions to the current-limiting control and begins injecting 35 A (peak) of current from the GSC ($i_g$). This additional current injected after the voltage drop mostly consists of reactive current, as shown by the large change in the q-axis GSC current shown in Fig. 5.16. There is very little change in the real component (d-axis) of the GSC current. Because of the large drop in the voltage magnitude, the real power output of the GSC decreases. However, because of the large increase in the reactive current injected, an increase in the reactive power produced can be seen. The DC-link voltage sharply increases after the fault because of the power imbalance between the MSC and the GSC. During this time, the DC chopper is continuously operating, which dissipates the excess power coming from the MSC while the voltage is low on the GSC. Notice, however, that the currents in the stator of the WRIG remain completely unchanged before and after the fault. Therefore, the induction machine does not "see" the fault on the grid side. The simulation results for the same test are shown in the right column of Fig. 5.16. Good agreement between the simulation results and the experimental results can be seen for each of the plotted quantities, indicating that the PSCAD model gives a good representation of the behavior of an actual Type 4 WTG.

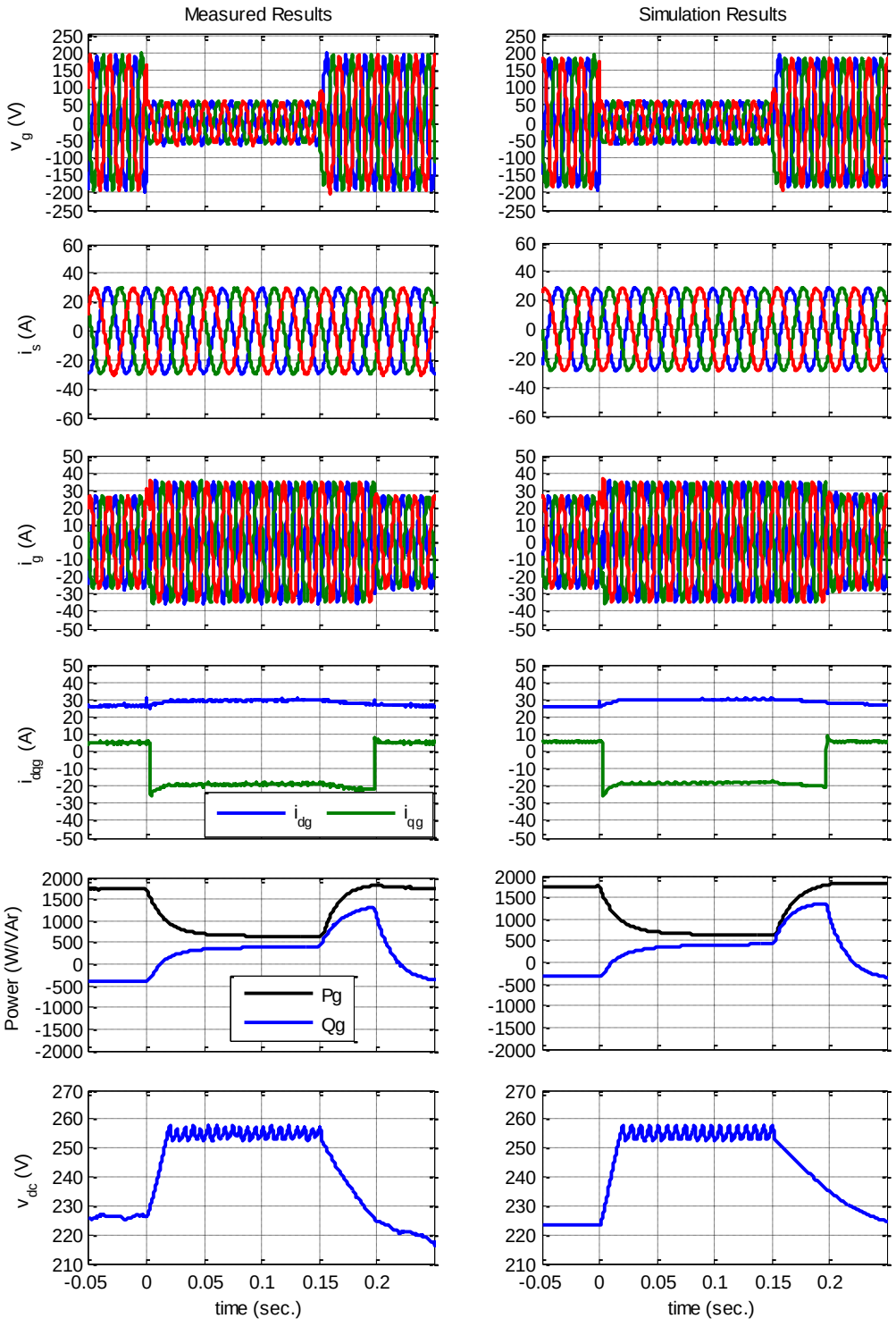


**Fig. 5.16: Comparison of experimental and simulation results for a three-phase fault.**

### *5.4.2. Single-Phase Fault Case*

Experimental tests and simulations were carried out in the same way described in the previous sub-section, except a phase-A-to-neutral fault was applied to the terminals of the machine using the voltage-sag generator shown in Fig. 5.15. A phase-A-to-neutral fault was applied by controlling the switches in the voltage-sag generator in the same way as for the three-phase fault, except the shunt connections in phases B and C were manually removed. The experimental results for this test are shown in the left column of Fig. 5.17. After the GSC voltage drops, the GSC current immediately transitions to current-limiting control. These currents injected are strictly positive sequence, despite the clear unbalance (negative sequence) in the GSC voltages. While the sequence components of the GSC currents are not shown explicitly in Fig. 5.17, the conclusion can be drawn that there are no negative-sequence currents since GSC currents appear balanced and symmetrical and the d- and q-axis currents have no (or a negligible amount) of 120 Hz component. However, a 120 Hz ripple component can clearly be seen the real and reactive power from the GSC as well as the DC-link voltage. The simulation results for this test are shown in the right column of Fig. 5.17. Again, good agreement can be seen between the experimental and simulation results for each of the plotted quantities, indicating that the PSCAD model of the Type 4 WTG provides a good representation of a realistic Type 4 WTG.

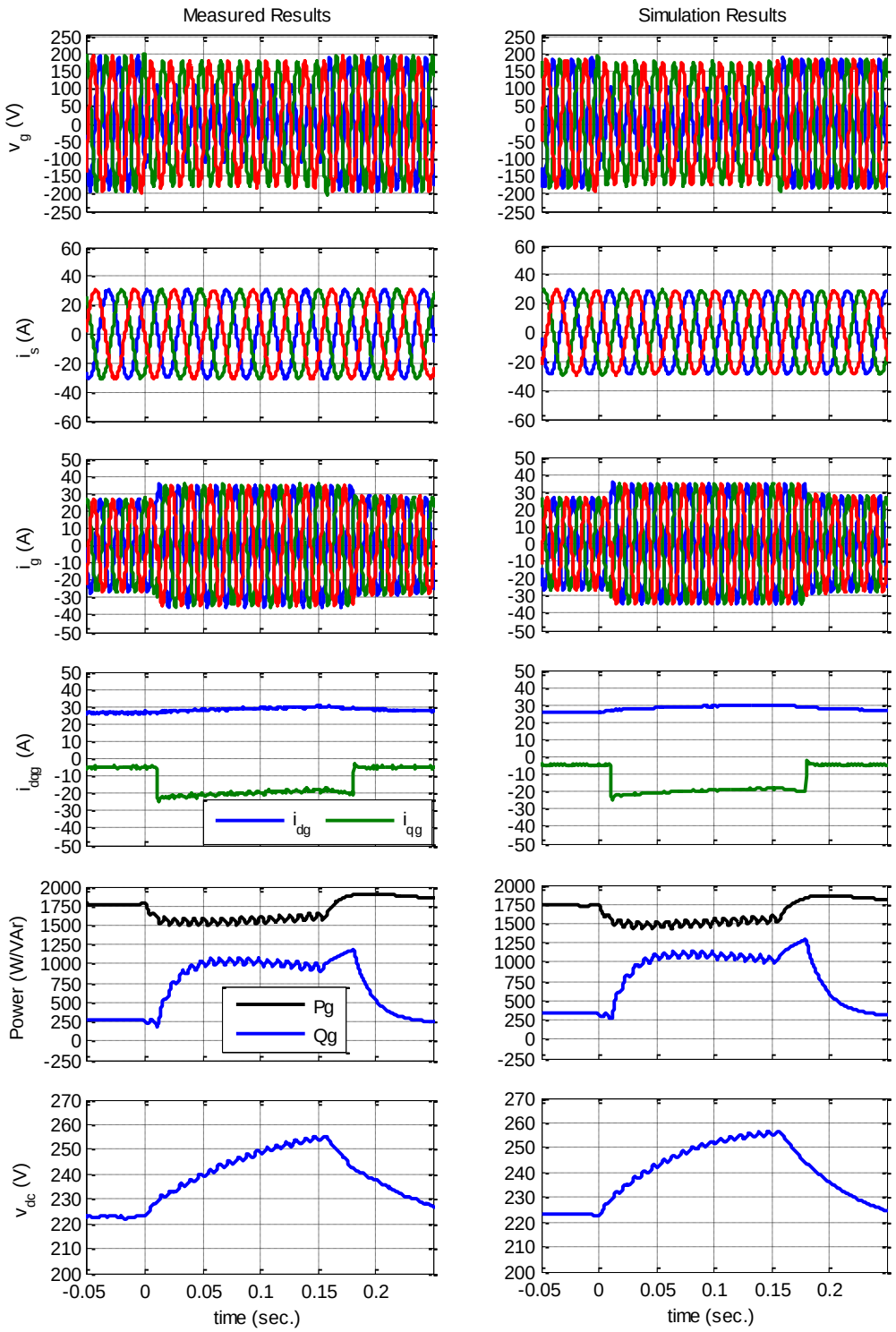


**Fig. 5.17: Comparison of experimental and simulation results for a single-phase fault.**

## 5.5. Single-Machine Infinite Bus Studies

The network shown in Fig. 5.18 is used to study the short-circuit behavior of a single utility-scale Type 4 WTG. This network is identical to the single-machine infinite bus (SMIB) network used to study the Type 3 WTG short-circuit behavior. A squirrel-cage induction generator (IG) is used as the generator, with machine parameters given in Appendix A. A switching-level model of the MSC and GSC is implemented in the PSCAD simulation of this network. The MSC and GSC are controlled as described in Section 5.2. The maximum current injected by the GSC during voltage dips is set to 1.2 per unit, and the current-limiting control is set to turn on when the magnitude of the positive-sequence voltage drops below 0.9 per unit. The current-limiting controller is turned off when the terminal voltage magnitude is above 0.95 per unit. These settings correspond to the hysteresis buffer settings shown in Fig. 5.4. Under normal operating conditions, the GSC is controlled to inject currents at unity power factor (the $i_{qg}$ reference is set to zero). The various parameters of this system are listed in Appendix C.

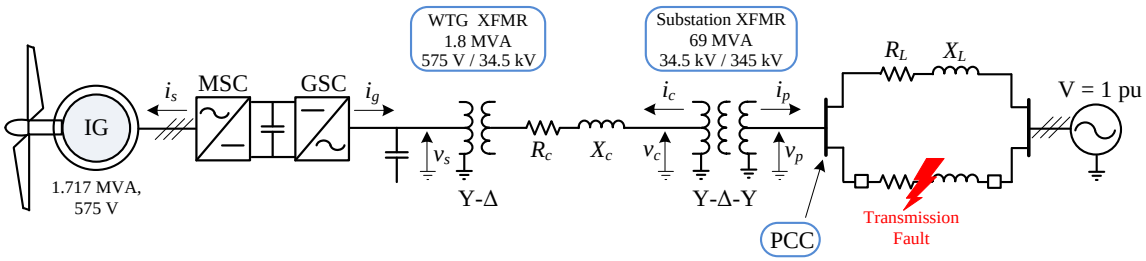


**Fig. 5.18: Single-machine infinite bus network for simulating the Type 4 WTG.**

Transient simulation results are shown in Fig. 5.19 for a three-phase fault (left column) and phase-A-to-ground fault (right column) on the transmission system of the network shown in Fig. 5.18. In each case, the GSC current $i_g$ increases to 1.2 per unit (2,926 A peak) almost instantly after the fault occurs. Additionally, the "shape" of the GSC current waveforms is nearly identical for the two types of faults, which is expected

since the GSC injects only positive-sequence currents, even for unbalanced faults. The d-axis component of the GSC increases slightly after the fault because of the abrupt increase in the DC-link voltage. However, the largest change is in the q-axis component of the GSC current because of the current-limiting controller. As expected, the stator current of the IG appears unchanged during the fault since the MSC is relatively unaffected by grid faults. The voltage drop on the GSC causes a sudden decrease in the real power output of the GSC (thus causing the DC-link voltage to sharply increase). The DC-chopper circuit activates when the DC-link voltage exceeds 1500 V, which prevents the DC-link voltage from exceeding this value. The reactive power rises in each case because of the current-limiting controller injecting a large reactive (q-axis) current.

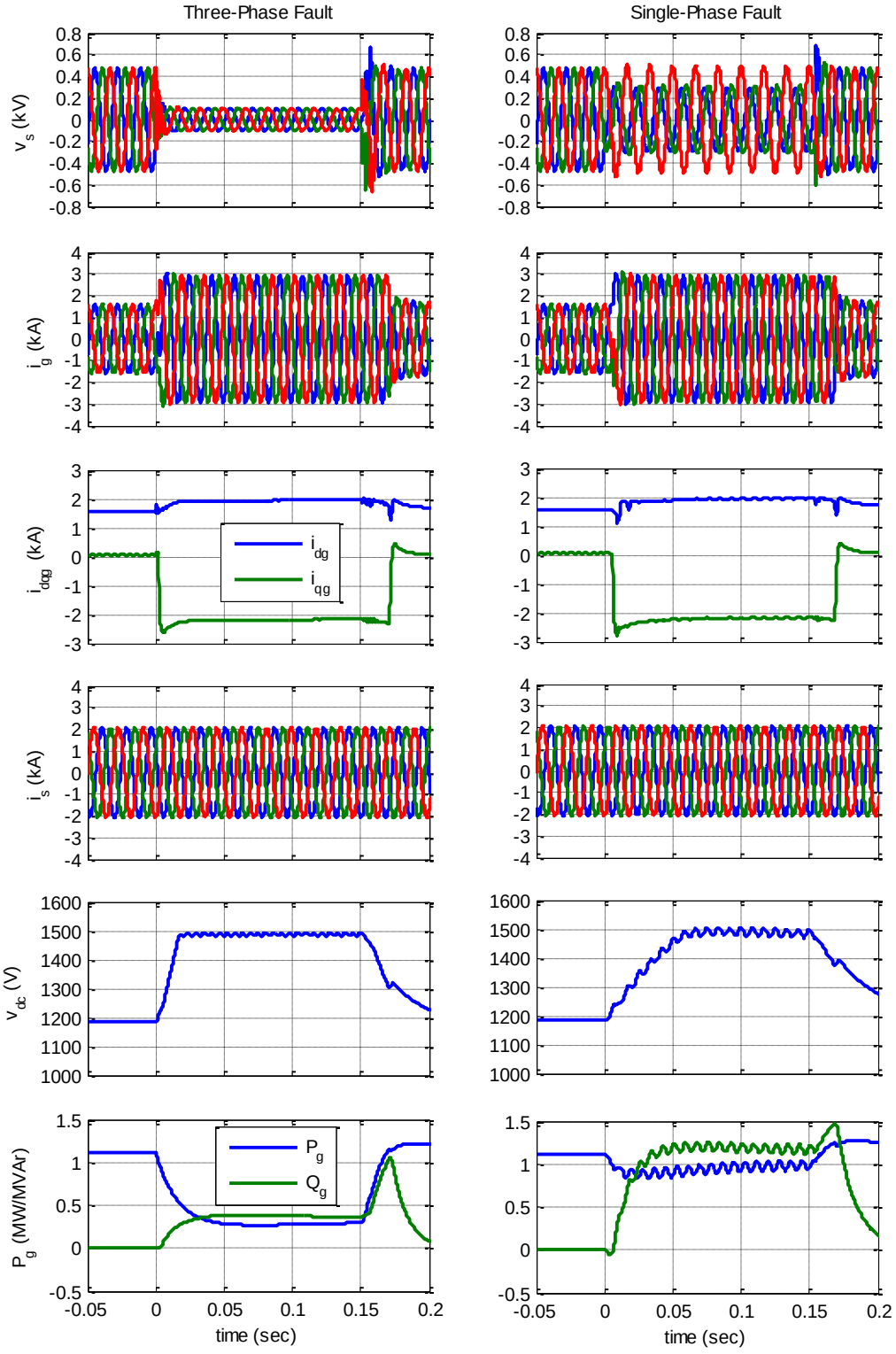


**Fig. 5.19: Simulation results for a three-phase and single-phase fault on the transmission system of the SMIB network.**

The sequence-network circuit for a three-phase fault on the transmission system of the network shown in Fig. 5.18 is given in Fig. 5.20. The value of $k$ and $m$ for this case are 0.2 and 2, respectively. Note that the equivalent circuit used for the Type 4 WTG in this circuit is the same as the positive-sequence circuit shown in Fig. 5.13. The phasor value of the GSC current source is calculated following the steps described in Section 5.3. The short-circuit currents in this network can be estimated by using conventional circuit analysis that entails the use of the superposition principle.

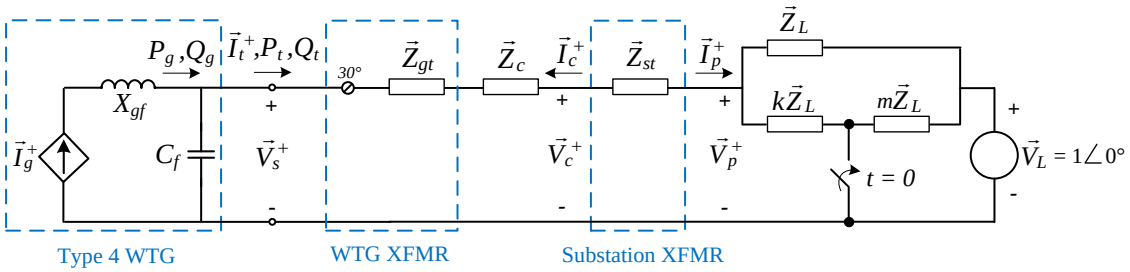


**Fig. 5.20: Sequence-network circuit for a three-phase fault on the transmission system.**

Simulation results for the collector voltage $v_c$, collector cable current $i_c$, point-of-common-coupling (PCC) voltage $v_p$, and total plant current $i_p$ are shown in Fig. 5.21(a). These results correspond to the same simulation from which the results in the left column of Fig. 5.19 are taken. The corresponding positive-sequence components of the voltages and currents shown in Fig. 5.21(a) are shown in Fig. 5.21(b). Also shown in Fig. 5.21(b) are the calculation results found from circuit analysis on the circuit shown in Fig. 5.20. These calculations are not done by hand, but are calculated using the steady-state solver in Matlab's SimPowerSystems (SPS) toolbox by building the circuit in Fig. 5.20 manually using the library components within the software. The calculated values shown in Fig. 5.21(b) before $t = 0$ correspond to the use of $\vec{I}_g^+ = \vec{I}_g^{b+}$, calculated from the steady-state calculation steps described in Section 5.3.1. However, a different value of $\vec{I}_g^+$ is used in the post-fault (after $t = 0$) calculation due to the current-limiting control.

After the fault, $\vec{I}_g^{+} = \vec{I}_g^{a+}$, which is calculated using (5.23). In the calculations, the GSC current source is assumed to change instantaneously from $\vec{I}_g^{b+}$ to $\vec{I}_g^{a+}$ instantaneously after the fault occurs. The results indicate that the calculated results give good agreement to the simulated components of the currents and voltages, within two cycles after fault. The error in the calculation for the first two cycles is due to the calculation delay of cosine-filter algorithm and the slight delay caused by the current-limiting controller low-pass filter.

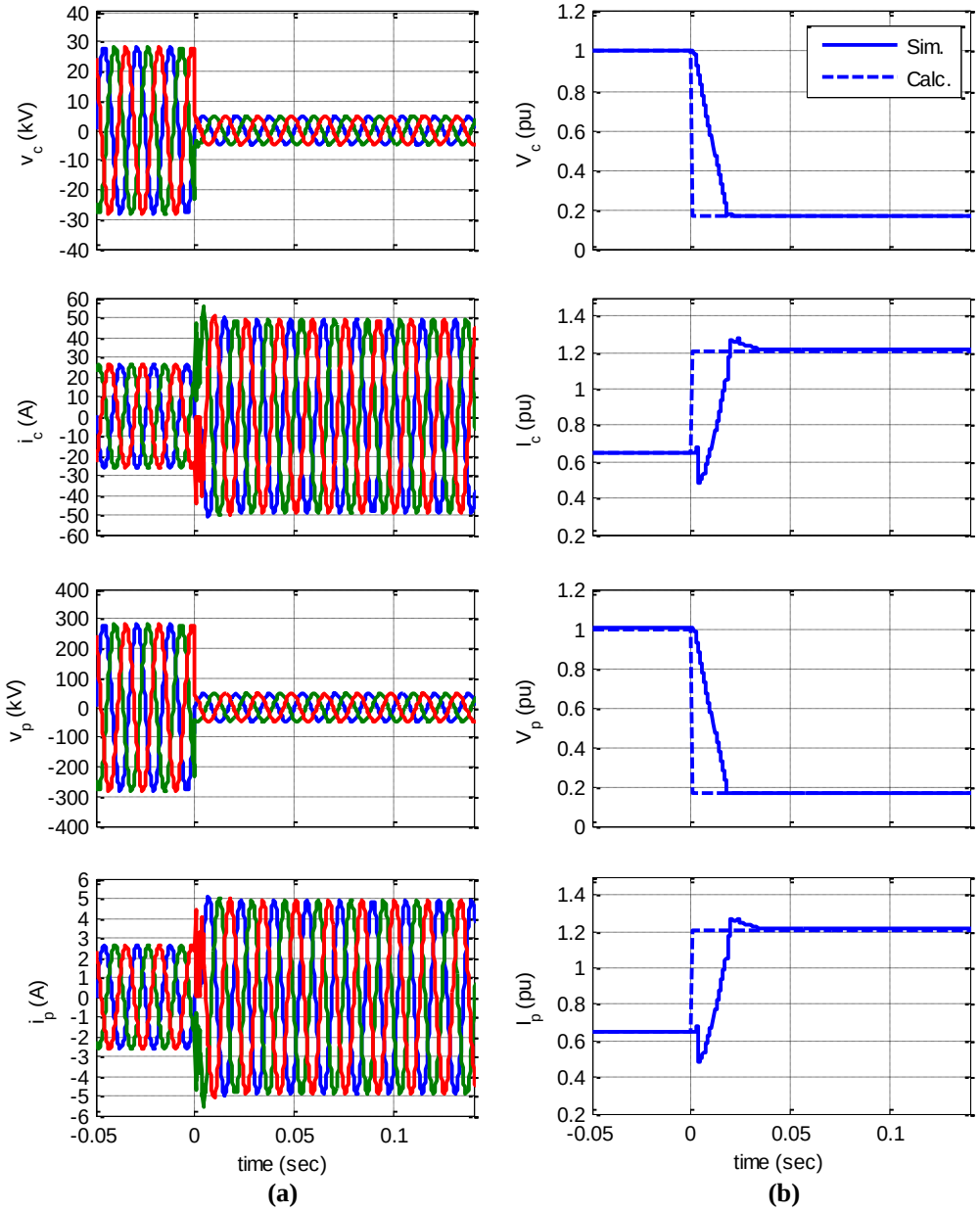


**Fig. 5.21: (a) Simulation results of network voltages and currents for a three-phase fault and (b) comparison of calculated and simulated positive-sequence components of these voltages and currents.**

The sequence-network circuit for a phase-A-to-ground fault on the transmission system of the network shown in Fig. 5.18 is shown in Fig. 5.22. The sequence-network circuits used for the Type 4 WTG are the same as shown in Fig. 5.13. The current-source phasor quantities used for the GSC current before the fault (before $t$ = 0) and after the

fault (after $t = 0$) are calculated the same way as those for the three-phase fault discussed in the previous paragraph.

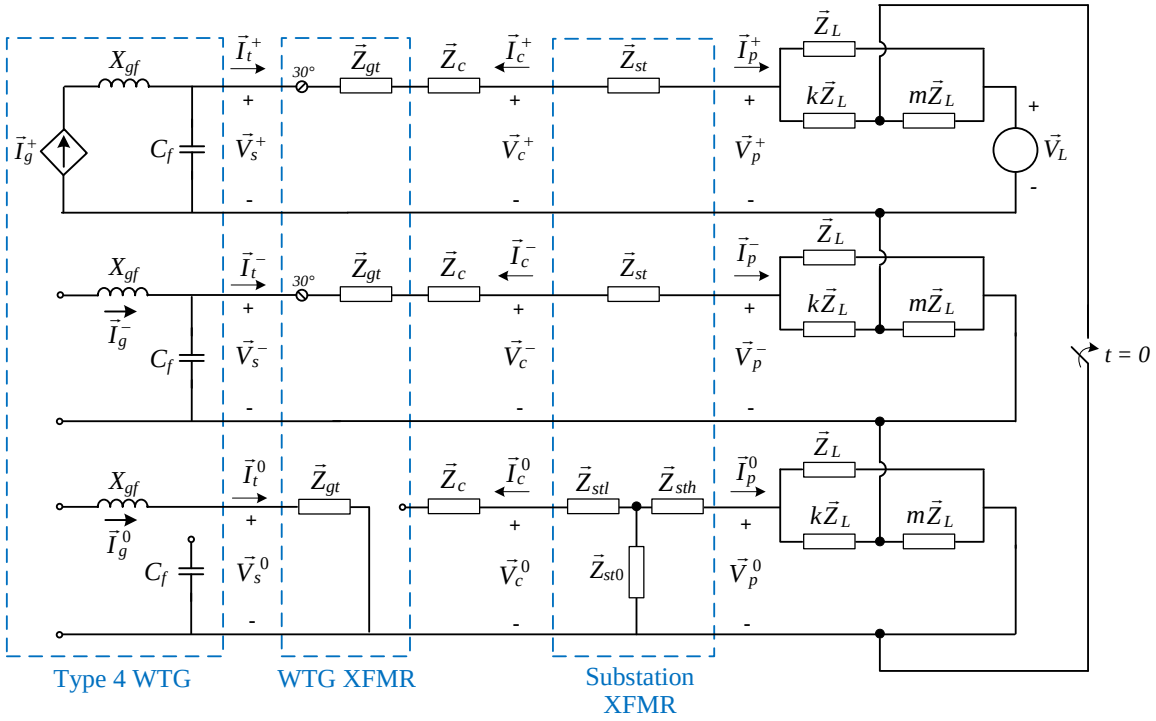


**Fig. 5.22: Sequence-network circuit for single-phase fault on the transmission system.**

Transient simulation results for the network voltages and currents for a phase-A-to-ground fault are shown in Fig. 5.23(a). The corresponding sequence components of these voltages and currents are shown in Fig. 5.23(b). Additionally, the calculated sequence-components of the voltages and currents (found from building the circuit of Fig. 5.22 in SPS software and using the built-in steady-state solver) are also shown in Fig. 5.23(b). Good agreement between the calculated sequence components and the simulated sequence components can be seen, particularly two cycles after the fault occurrence. The error for the first two cycles is due to the same reasons discussed previously for the three-phase fault case. Thus, the proposed sequence-network circuit of

the Type 4 WTG appears to give good estimates of the short-circuit currents in the network.

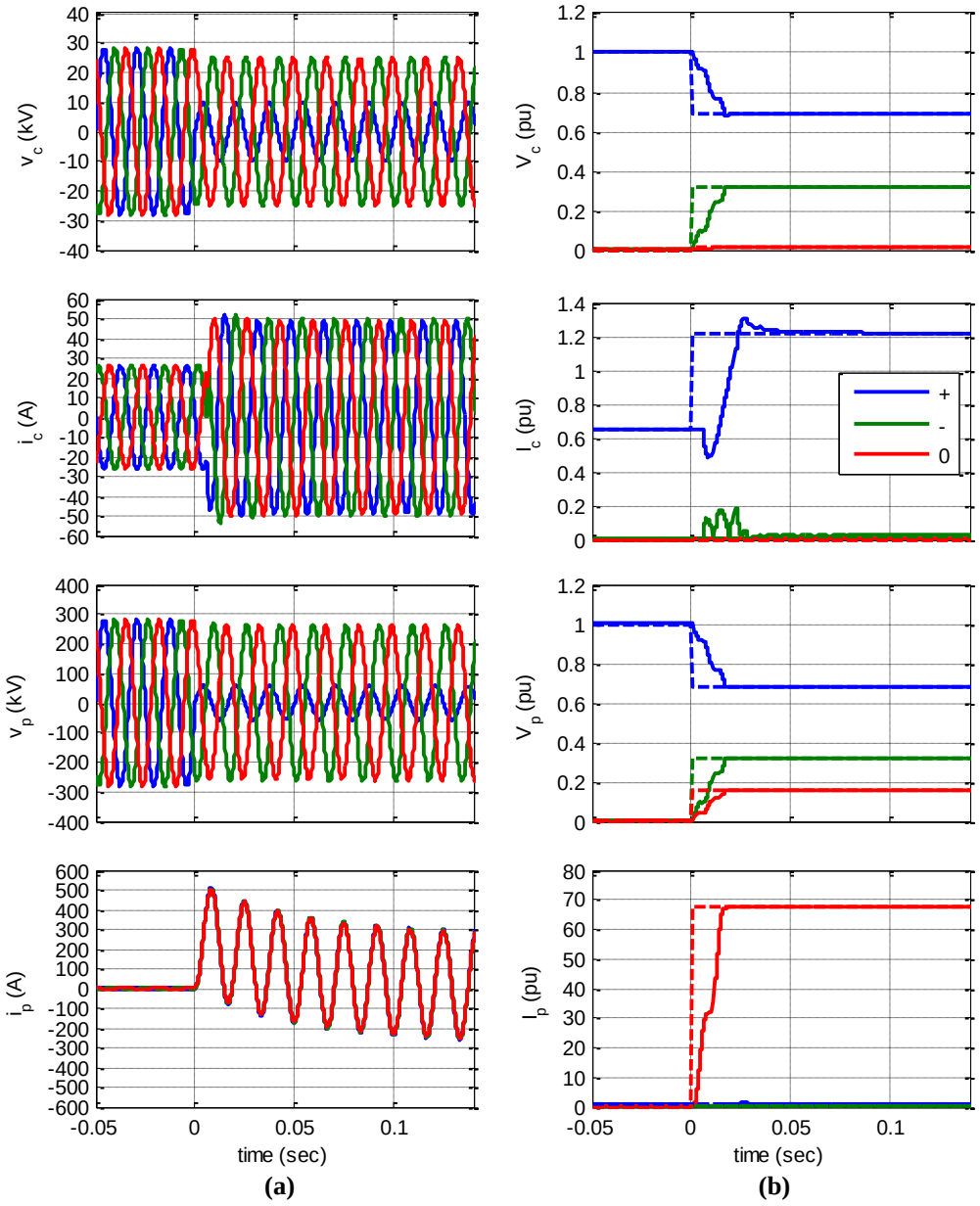


**Fig. 5.23: (a) Simulation results of network voltages and currents for a single-phase fault and (b) comparison of the simulated and calculated sequence components of these voltages and currents (solid = simulated, dashed = calculated).**

## 5.6. Multi-Machine Network Studies

The network shown in Fig. 5.24 is used to study the short-circuit behavior of a small Type 4 wind farm. This network is identical to the network used to study the Type 1 and Type 2 wind farms shown in Fig. 3.25, except that the WTGs in this system are Type 4 WTGs with parameters given in Appendix A and the low-voltage winding of the WTG step-up transformer is set to 575 V (the rated voltage of the Type 4 WTG GSC). Unlike the single-machine infinite bus (SMIB) studies discussed in the previous section, the Type 4 WTGs are represented as an "averaged" model within the network shown in Fig. 5.24. Using a switching-level model for the Type 4 WTG within the network of Fig. 5.24 requires excessively long simulation time; however, using the averaged model, the MSC and GSC of each WTG are represented as current-controlled voltage sources, which permits the use of a larger simulation time step. Details of this averaged model are given in Appendix I, and transient simulation results comparing the averaged model to the switching-level model show that the two models have good agreement. For these studies, it is assumed that all seven WTGs are producing the same real and reactive power prior to the fault. Additionally, the underground collector cables are represented as $\pi$-equivalent circuits in this network to account for the distributed capacitance of the underground cables. The various parameters of this system are given in Appendix C.

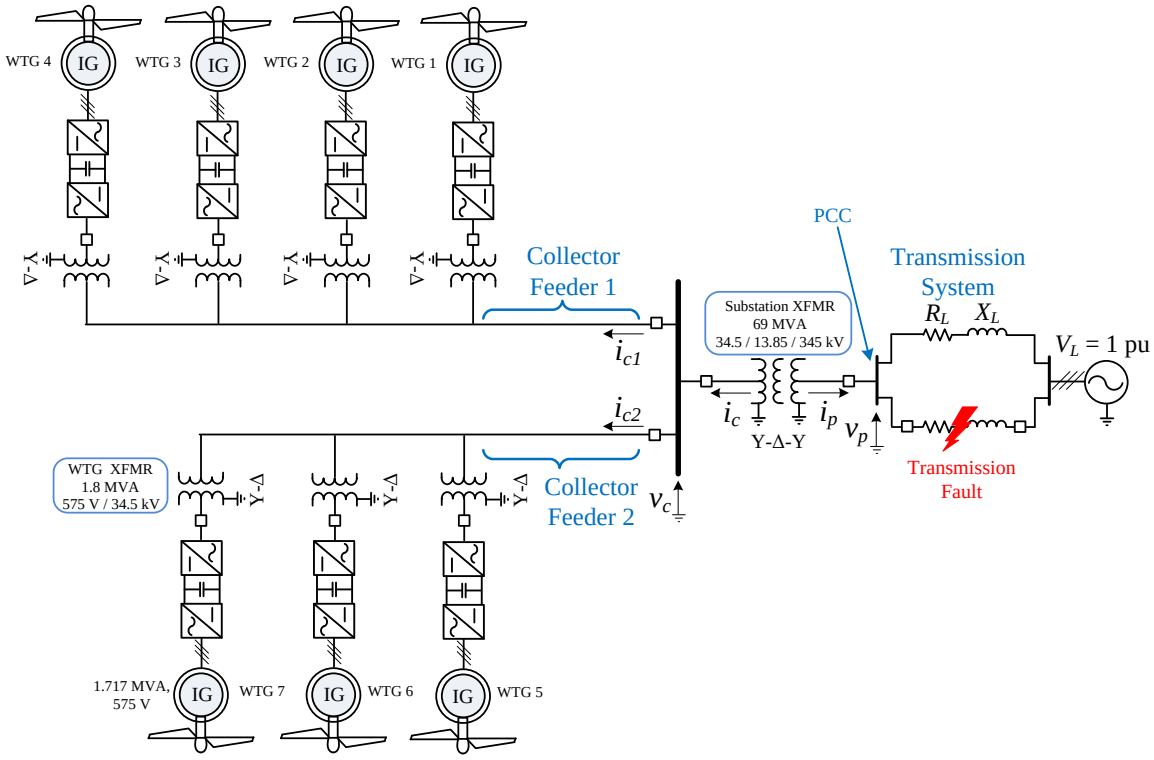


**Fig. 5.24: Type 4 wind farm with seven WTGs.**

Simulation results for a three-phase fault on the transmission system in the network of Fig. 5.24 are shown in Fig. 5.25(a). A fault at this particular location results in approximately a 80% drop in the voltage on the wind plant collector system $v_c$. From the plots of the collector current ic and total plant current ip, a high-frequency resonant component can be seen in the waveforms after the fault, but is quickly damped. This high-frequency component appears to be caused by the capacitance of the underground cables, and causes a brief but significant increase in the instantaneous current magnitude.

Sequence-network calculations are performed for this network in the same way described in the previous section for the SMIB system. However, the sequence-network circuit for this network is much too complicated to show here. The GSC of each WTG within the network is represented in the same way as the sequence-network circuits shown in Fig. 5.13. Thus, a total of seven current sources are used within the sequence-network circuit for this network, one for each of the GSCs for all seven WTGs. The

magnitude and phase angle of each current source is calculated in the same way already described in Section 5.3.2, where the pre-fault terminal voltage of each WTG is found from a load-flow solution on the network using the assumed real and reactive power output of each WTG. However, similar to the calculations described in the previous section, a different value of the GSC current phasor is used for the pre- and post-fault calculations due to the current-limiting controller. The results of these calculations for a three-phase fault on the transmission system are shown in Fig. 5.25(b) in addition to the positive-sequence voltages and currents from the simulation results. Each of the calculated values of the voltages and currents match closely to the simulation values, indicating the sequence-network model of the wind farm gives good results.

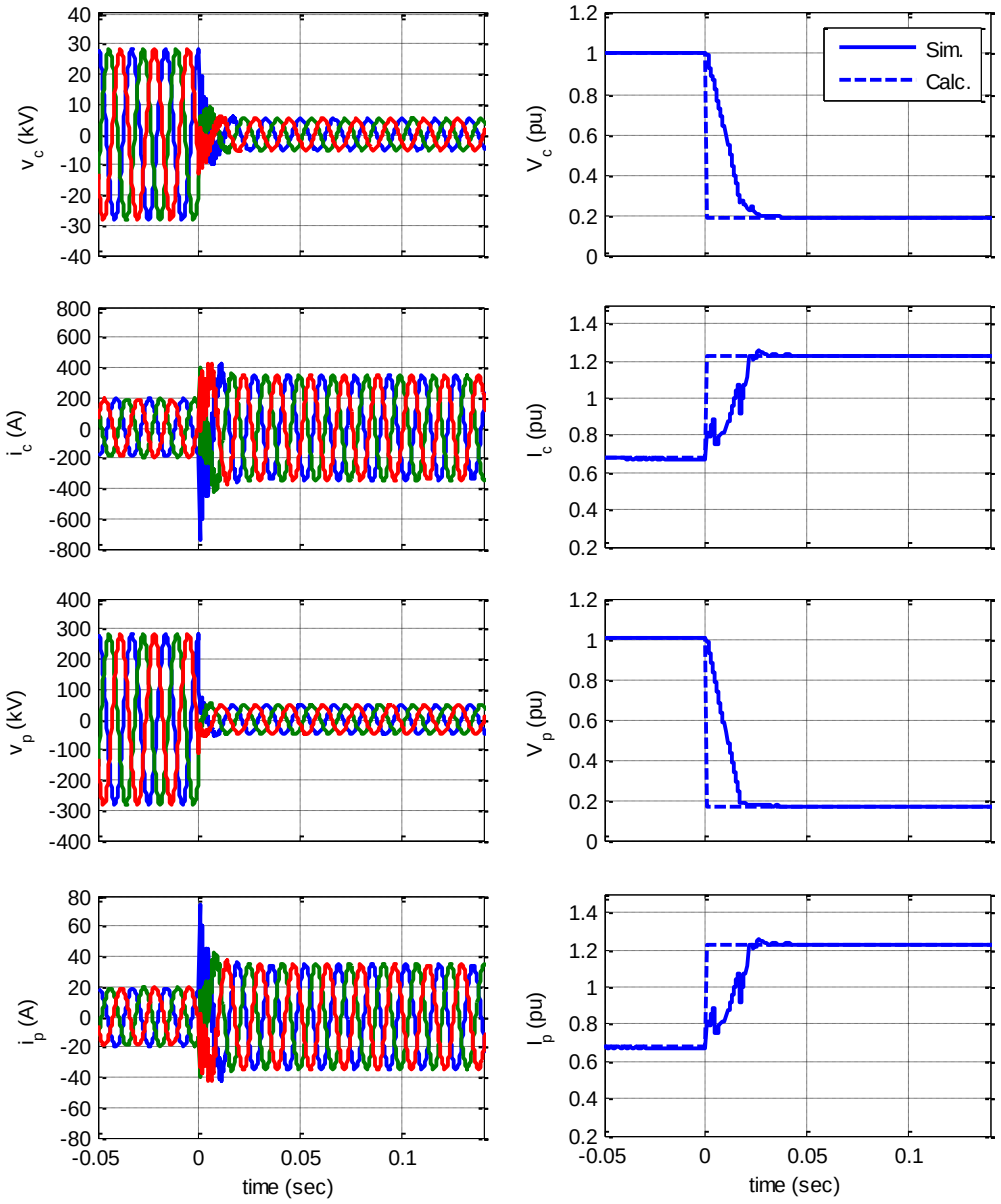


**Fig. 5.25: (a) Transient simulation results of network voltages and currents for a three-phase fault and (b) comparison of simulated and calculated positive-sequence components of these voltages and currents.**

Simulation results for the case of a phase-B-and-C-to-ground fault in the transmission system in the network of Fig. 5.24 are shown in Fig. 5.26(a). The calculated sequence components of the voltages and currents are shown in Fig. 5.26(b), as well as the sequence components of the voltages and currents from the simulation results. Good

agreement between the simulated sequence components and the calculated sequence components can be seen, indicating that the sequence-network models developed for the WTG provide good results.

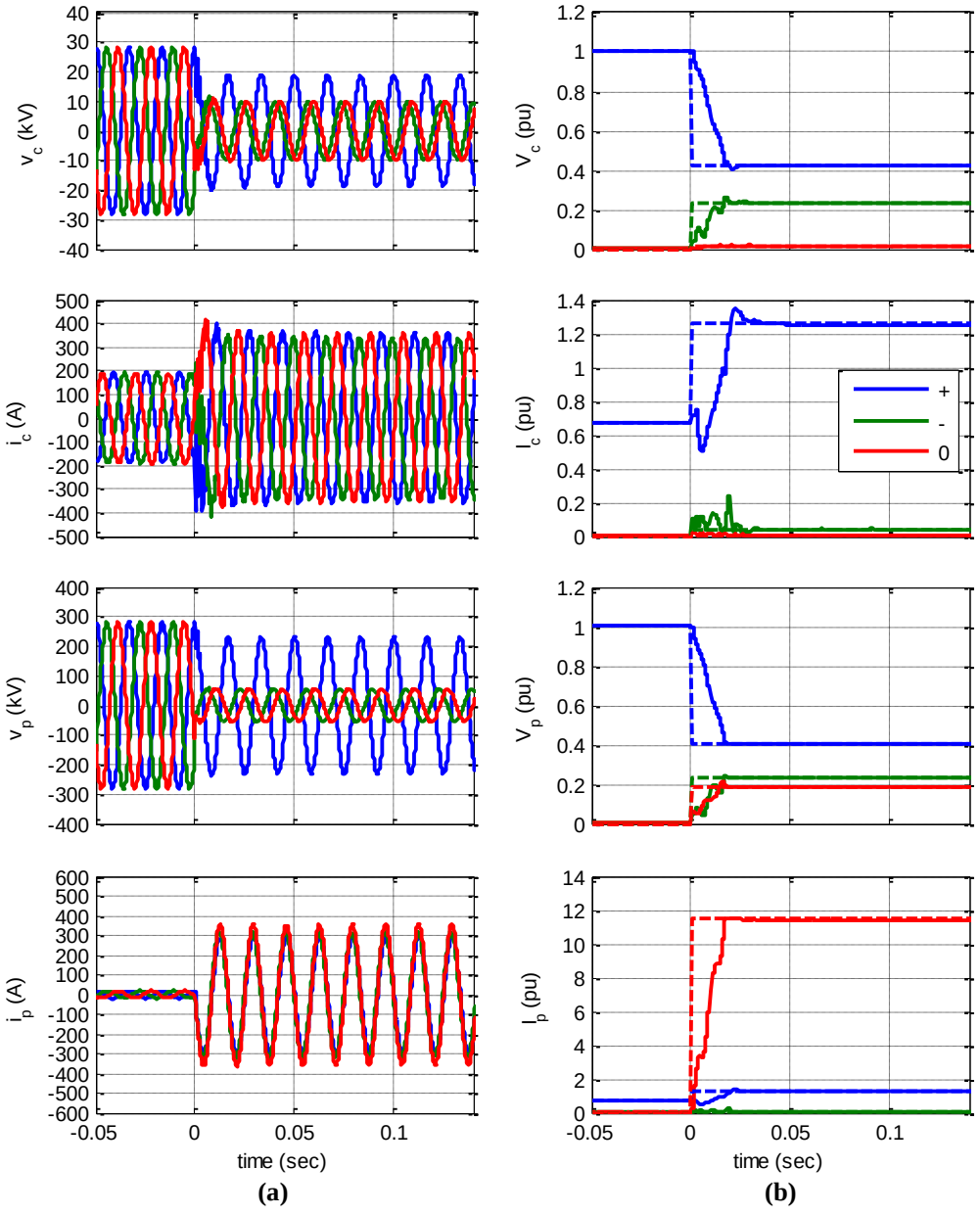


**Fig. 5.26: (a) Transient simulation results of network voltages and currents for a two-phase-to-ground fault and (b) comparison of simulated and calculated sequence components of these voltages and currents (solid = simulated, dashed = calculated).**

## 5.7. Conclusion

The Type 4 WTG is one of the most common types of wind-turbine generators installed in today's wind farms. The Type 4 WTG provides many of the same advantages as the Type 3 WTG, such as variable speed operation, dynamic reactive power compensation, and higher energy yield. A typical control topology of the Type 4 WTG was described in this chapter and implemented in both transient simulation and an experimental hardware testbed. A sequence-network circuit was proposed for the Type 4 WTG based on simplifying assumptions about these controls, and shown to give good agreement in sample calculations to corresponding transient simulation results. It should be noted, however, that the sequence-network circuit described in this chapter for the Type 4 WTG is not completely general since other control structures can be used with this type of WTG. In particular, there is much freedom for the control designer to choose how the reactive (q-axis) component of the GSC current is controlled during the fault. However, the current-source model presented in this chapter provides a template for calculations with other types of controls.

# CHAPTER 6: CONCLUSIONS, CONTRIBUTIONS, AND RECOMMENDATIONS FOR FUTURE WORK

## 6.1. Conclusions

The emergence of wind power as a viable and substantial source of electric power presents new problems in ensuring the reliability of the power grid. Among the many factors affecting this reliability, power system protection is a key component in mitigating equipment damage, minimizing system outages due to faults, and preventing injury to maintenance personnel and customers. Short-circuit studies provide protection system designers with estimates of the voltages and currents in a power system during faults so that protection equipment can be designed to operate reliably. Therefore, it is pertinent that the models used in these short-circuit studies give accurate results to ensure that the protective devices are not improperly designed. Because the short-circuit response of some types of wind plants are fundamentally different than conventional power plants, existing models for estimating short-circuit currents are not always sufficient to represent wind power plants. Further, short-circuit models that capture these fundamental differences do not currently exist. In this dissertation, short-circuit models for the four types of wind-turbine generators (WTGs) are proposed based on: thorough analysis of the wind turbine dynamic equations, analysis of the control topology, experimental tests, transient simulations, and sequence-network analysis.

For the purpose of short-circuit calculations, conventional power plants with synchronous generators are modeled as a voltage source with a series impedance. This type of model is a result of the *theory of constant flux linkages*, in which the machine flux linkages, which cannot change instantaneously following a disturbance, produce an

electro-motive force which produces large short-circuit currents. These flux linkages decay according to internal time constants of the machine, which also causes the machine short-circuit currents to decay. It has been shown in previous work that the Type 1 and Type 2 WTGs behave according to the same physical principles; thus, these types of WTGs can be represented as a voltage source in series with an impedance, much like conventional power plants.

The Type 3 WTG has the most complex short-circuit behavior of the four types of WTGs, since it can change topology during the fault because of the crowbar protection circuitry. In the absence of a crowbar protection initiation, the controls of the power electronic converters dominate the response of the Type 3 WTG. In this case, the fast-acting current controllers in the rotor-side converter (RSC) and grid-side converter (GSC) "appear" as current sources to the interconnecting system during the fault. Thus, the short-circuit model for this case consists of two current sources, one for each of the power electronics converters, and various machine parameters. The total fault current from the Type 3 WTG is the sum of the GSC current and the stator current, which can be determined from steady-state sequence-network analysis on the faulted power network. Unlike the RSC and GSC currents, which are assumed to remain unchanged from the pre-fault values after the fault occurrence, the stator current is assumed to change instantaneously after the fault. In the case that the crowbar protection *does* initiate, the Type 3 WTG resembles a Type 1 or Type 2 WTG since the rotor windings are short circuited. Thus, using any one short-circuit model of the Type 3 WTG (either current-source or voltage-source model) does not provide a complete picture of the dynamics of these types of WTGs. However, using both of these models in conjunction can provide upper and lower bounds to the short-circuit currents expected from the system.

The Type 4 WTG is the only type of WTG that does not have an AC machine directly connected to the power grid. For this reason, it is the controls of the grid-side converter that determine the short-circuit behavior of the Type 4 WTG. The fast-acting

current controllers of the grid-side converter make this type of WTG "appear" as a current source during faulted conditions. The amount of current injected by the Type 4 WTG is completely determined by these controls; thus, the Type 4 WTG has a "programmed" response to short-circuits, whereas in Type 1 and Type 2 WTGs, the short-circuit currents are strictly determined by physics. For this reason, there are no transient time constants required to represent the Type 4 WTG, as is the case for conventional power plants. The controlled current source used to represent the Type 4 WTG is determined in a similar manner as the current sources for the Type 3 WTG; however, while the current-source phasors in the Type 3 WTG are assumed to remain unchanged from their pre-fault values after a fault, the current-source phasor for the Type 4 WTG is assumed to change instantaneously after a fault because of the current-limiting controller.

## 6.2. Summary of Contributions

The contributions of this work are summarized below:

- A closed-form solution of the instantaneous short-circuit currents from a Type 1 WTG was developed assuming the machine rotational speed does not change during a fault. From this closed-form solution, an improved sequence-network model of Type 1 WTGs was derived which is more accurate than the conventional model.
- The effects of leakage-flux saturation on the short-circuit currents contributed by Type 1 WTGs was described based on experimental tests on a lab-scale Type 1 WTG. This work revealed that the short-circuit currents from a Type 1 WTG can be significantly higher in the presence of leakage saturation than would otherwise be expected when assuming a linear characteristic of the leakage fluxes.
- A simplified, fundamental-frequency short-circuit model of the Type 3 WTG was developed based upon simplifying assumptions about the controls of this type of

WTG. This model represents the WTG as two controlled current sources connected to the machine steady-state equivalent circuit. This circuit was validated with transient simulations and experimental tests for particular cases where the crowbar protection circuitry does not turn on.

- The effects of mutual-flux saturation on the Type 3 WTG controls and short-circuit behavior was evaluated. A methodology of accounting for this saturation within the proposed sequence-network model of the Type 3 WTG was developed and validated by experimental short-circuit tests.
- A short-circuit model of the Type 4 WTG was developed and validated with transient simulation results.

Portions of the research presented in this dissertation have been included in conference panel presentations, IEEE working group documents, conference papers, and journal papers. A joint working group between the IEEE Power & Energy Society Transmission and Distribution Committee, Electric Machines Committee, and Power System Relaying Committee was established in July 2008 and has prepared a report entitled "Fault Current Contribution from Wind Plants." Portions of this research have been included in that report. A list of the published papers and presentations contributed as a part of this research is given below.

Conference Presentations

**D. F. Howard**, J. Restrepo, T. Smith, M. Starke, J. Dang, and R. G. Harley, "Calculation of Fault Current Contribution of Type I Wind Turbine-Generators," presented at the Wind Plant Short-Circuit Contribution Panel Session, IEEE PES General Meeting, July 26, 2011, Detroit, MI.

**D. F. Howard**, T. Smith, M. Starke, and R. G. Harley, "Calculation of Fault Current Contribution of Type I Wind Turbine-Generators," presented at the Power System Relaying Committee Meeting, Sept. 13, 2011, Minneapolis, MN.

**D. F. Howard**, T. Smith, M. Starke, and R. G. Harley, "Short Circuit Analysis of Induction Machines – Wind Application," presented at the Wind Plant Short-Circuit Contribution Panel Session, IEEE PES Transmission & Distribution Conference & Exposition, May 10, 2012, Orlando, FL.

**D. F. Howard**, T. G. Habetler, and R. G. Harley, "Experimental Study on the Short-Circuit Contribution of Induction Machines," presented at the International Electric Machines and Drives Conference, Chicago, IL, May 15, 2013.

Conference Publications

**D. F. Howard**, J. Restrepo, T. Smith, M. Starke, J. Dang, and R. G. Harley, "Calculation of Fault Current Contribution of Type I Wind Turbine-Generators," in *Proc. 2011 IEEE Power & Energy Society General Meeting*, July 24-28, 2011, Detroit, MI.

**D. F. Howard**, T. M. Smith, M. Starke, and R. G. Harley, "Short Circuit Analysis of Induction Machines – Wind Power Application," in *Proc. 2012 IEEE Transmission & Distribution Conference & Exposition*, May 7-10, 2012, Orlando, FL.

**D. F. Howard**, T. G. Habetler, and R. G. Harley, "Experimental Study on the Short-Circuit Contribution of Induction Machines," in *Proc. 2013 IEEE International Electric Machines and Drives Conference*, May 12-15, 2013, Chicago, IL.

Journal Publications

**D. F. Howard**, T. G. Habetler, and R. G. Harley, "Improved Sequence Network Model of Wind Turbine Generators for Short-Circuit Studies," *IEEE Trans. Energy Conversion*, vol. 27, pp. 968-977, Dec. 2012.

J. Liang, **D. F. Howard**, J. Restrepo, and R. G. Harley, "Feed-Forward Transient Compensation Control for DFIG Wind Turbines during both Balanced and Unbalanced Grid Disturbances," *IEEE Transactions on Industry Applications, vol. 49, pp. 1452-1463, Mar. 2013.*

**D. F. Howard**, J. Liang, and R. G. Harley, "Short-Circuit Modeling of DFIGs with Uninterrupted Control," *IEEE Journal of Emerging and Selected Topics in Power Electronics: Special Issue on Wind Energy* (Under Review). Submitted July 2013.

## 6.3. Future Work

### *6.3.1. Control Topology Effect on Sequence-Network Models*

The sequence-network model proposed for the Type 3 WTG is developed based upon simplifying assumptions of the particular type of control described in this dissertation. However, variations on this control topology may require changes to the sequence-network model developed in this dissertation. In particular, there is much freedom in how the reactive current from the grid-side converter is controlled in the event of a voltage sag caused by a short-circuit fault. Controlling the reactive current in a different way than described in this dissertation will require a different technique for calculating the current phasor representing the grid-side converter within the sequence-network circuit of the Type 3 WTG.

Similar to the Type 3 WTG, variations in the control of the Type 4 WTG grid-side converter are possible. Under the current-limiting control topology of the grid-side converter described in this dissertation, the amount of reactive current injected by the GSC is the difference between the maximum current rating of the converter and the actual current commanded by the DC-link voltage controller. However, any amount of reactive current (within the rating of the converter) can be injected by the converter during the fault. Similarly, the total current injected could be controlled in a different way to output more active power during the fault. In either case, the way of calculating the current source phasor quantity must be changed.

### *6.3.2. Incorporation into Existing Protection and Short-Circuit Software*

Further work is required to implement the sequence-network circuits into existing software used by protection engineers for performing short-circuit studies. However, because the models currently used in these software packages are based upon IEEE standards, a current-source model may not be available for application in this software.

In this dissertation, the phasor calculations were performed using Matlab's SimPowerSystems toolbox, which has a built-in steady-state solver. However, the sequence-network circuits must be manually built using the library components of capacitors, resistors, inductors, voltage sources, and current sources. To study different types of faults, the connections between the sequence-network circuits must be manually changed in the software. A better solution is the formation of a matrix-based solution to the set of algebraic equations.

### *6.3.3. Study of Temporary Over Voltages in Wind Plant Collector System*

For faults occurring within the wind plant collector system, temporary over voltages can occur after the collector feeder breaker (see Fig. 3.25) trips due to the interaction between the WTGs on that feeder and the distributed capacitance of the underground cables internal to the wind plant. The WTGs can continue to "feed" the fault for many cycles after the feeder breaker trips. To mitigate this problem, grounding transformers are often installed on the WTG side of the collector feeder circuit breaker (see Fig. 3.25) to provide grounding of the collector system when the feeder is isolated from the rest of the power system. However, there is some uncertainty in the proper approach to designing these grounding transformers to mitigate these over voltages without significantly increasing the cost of the system.

### *6.3.4. Protection Considerations with Short Time Constants of Decay*

The short time constants of decay in Type 2 WTGs and Type 3 WTGs under crowbar protection cause a rapid decay in the alternating components in the short-circuit currents contributed by these types of WTGs. In the case of a three-phase fault, there may be no zero crossings in the fault current contributed by these WTGs for several cycles, which may be difficult for circuit breakers to interrupt. It is unclear at this time whether this is an issue that needs to be addressed. Additionally, some relay elements

may not “see” the large increase in the fault currents from these WTGs since the alternating components decay quickly.

# APPENDICES

# APPENDIX A: WIND-TURBINE GENERATOR PARAMETERS

**Table A.1: Lab-scale Type 1 wind-turbine generator parameters.**

| | | | | | |
|---|---|---|---|---|---|
| Power (3 phase) | - | 6,772.3 | VA | 3 | pu |
| Voltage (L-L) | $V_s$ | 230 | V | 1.7321 | pu |
| Stator dc Resistance (Measured)* | $R_s^{dc}$ | 0.1672 ± 0.0101 | ohm | 0.0214 | pu |
| Stator ac Resistance (Estimated) | $R_s$ | 0.2178 | ohm | 0.0279 | pu |
| Stator Leakage Reactance | $X_{ls}$ | 0.5319 | ohm | 0.0681 | pu |
| Unsat. Mag. Reactance | $X_m^u$ | 15.21 | ohm | 1.9470 | pu |
| Sat. Mag. Reactance (at 1 pu $V_s$) | $X_m^s$ | 10.09 | ohm | 1.2921 | pu |
| Rotor dc Resistance (Measured)* | $R_r^{dc}$ | 0.1587 ± 0.0121 | ohm | 0.0203 | pu |
| Rotor ac Resistance (Estimated) | $R_r$ | 0.2068 | ohm | 0.0265 | pu |
| Rotor Leakage Reactance | $X_{lr}$ | 0.5319 | ohm | 0.0681 | pu |
| Resistance gain factor | $a$ | 1.3030 | - | - | - |
| Stator/Rotor Turns Ratio | - | 1 | - | - | - |
| Poles | - | 4 | - | - | - |

* The resistance measurements are based on the mean of 30 different measurements, 10 for each phase winding. The confidence interval is based on two standard deviations of these 30 measurements from the calculated mean, giving roughly a 95% confidence level.

**Table A.2: Utility-scale Type 1 and Type 2 wind-turbine generator parameters.**

| **Quantity** | **Sym.** | **Actual Value** | | **Per-Unit Value** | |
|---|---|---|---|---|---|
| Power | - | 1.816 | MVA | 3 | pu |
| Voltage | $V_s$ | 600 | V | 1.7321 | pu |
| Stator Resistance | $R_s$ | 0.0008 | ohm | 0.0040 | pu |
| Stator Leakage Reactance | $X_{ls}$ | 0.0173 | ohm | 0.0873 | pu |
| Magnetizing Reactance | $X_m$ | 0.7783 | ohm | 3.9261 | pu |
| Rotor Resistance | $R_r$ | 0.002 | ohm | 0.0101 | pu |
| Rotor Leakage Reactance | $X_{lr}$ | 0.0143 | ohm | 0.0721 | pu |
| Stator/Rotor Turns Ratio | - | 1 | - | - | - |
| Inertia | $J$ | 1,120.1 | $kg*m^2$ | 4.87 | sec |
| Poles | - | 6 | - | - | - |
| Power Factor Correction Capacitor | $C_{pfcc}$ | 5165 | μF | - | - |

**Table A.3: Lab-scale Type 3 wind-turbine generator parameters.**

| **Wound-Rotor Induction Machine Parameters** | | | | | |
|---|---|---|---|---|---|
| Power (3 phase) | - | 6,772.3 | VA | 3 | pu |
| Voltage (L-L) | $V_s$ | 230 | V | 1.7321 | pu |
| Stator ac Resistance (Estimated) | $R_s$ | 0.2178 | ohm | 0.0279 | pu |
| Stator Leakage Reactance | $X_{ls}$ | 0.5319 | ohm | 0.0681 | pu |
| Unsat. Mag. Reactance | $X_m{}^u$ | 15.21 | ohm | 1.9470 | pu |
| Sat. Mag. Reactance (at 1 pu $V_s$) | $X_m{}^s$ | 10.09 | ohm | 1.2921 | pu |
| Rotor ac Resistance (Estimated) | $R_r$ | 0.2068 | ohm | 0.0265 | pu |
| Rotor Leakage Reactance | $X_{lr}$ | 0.5319 | ohm | 0.0681 | pu |
| Stator/Rotor Turns Ratio | - | 1 | - | - | - |
| Inertia | $J$ | 0.3145 | kg*m$^2$ | 0.825 | sec. |
| Poles | - | 4 | - | - | - |
| **GSC Parameters** | | | | | |
| Filter Capacitance | $C_f$ | N/A | - | - | - |
| DC-Link Capacitance | $C$ | 2300 | μF | - | - |
| Parasitic Filter Resistance | $R_g$ | 0.001 | ohm | 0.0022 | pu |
| Filter Inductance | $L_{gf}$ | 1.05 | mH | 0.8829 | pu |
| DC-Link Voltage | $V_{dc}$ | 180 | V (dc) | - | - |
| DC-Link Voltage Controller Prop. Gain | $K_{pv}$ | 0.00012 | - | - | - |
| DC-Link Voltage Controller Integral Gain | $K_{iv}$ | 6.667e-5 | - | - | - |
| GSC Current Controller Prop. Gain | $K_{pg}$ | 5 | - | - | - |
| GSC Current Controller Integral Gain | $K_{ig}$ | 2000 | - | - | - |
| Nominal d-axis Stator Voltage | $v_{ds}{}^v$ | 44.99 | V | - | - |
| DC-Chopper Resistance | $R_{dc}$ | 12 | ohm | - | - |
| DC-Chopper Turn-on/Turn-off Voltage | $v_{dcon}$<br>$v_{dcoff}$ | 220<br>210 | V(dc) | - | - |
| **RSC Parameters** | | | | | |
| Parasitic Filter Resistance | $R_{rf}$ | 0.001 | ohm | 0.0022 | pu |
| Filter Inductance | $L_{rf}$ | 0.35 | mH | 0.2943 | pu |
| Rotor Speed Controller Prop. Gain | $K_{p\omega}$ | 0.002 | - | - | - |
| Rotor Speed Controller Integral Gain | $K_{i\omega}$ | 0.5 | - | - | - |
| Stator Reactive Power Prop. Gain | $K_{pq}$ | 1e-5 | - | - | - |
| Stator Reactive Power Prop. Gain | $K_{iq}$ | 0.02 | - | - | - |
| RSC Current Controller Prop. Gain | $K_{pr}$ | 15 | - | - | - |
| RSC Current Controller Integral Gain | $K_{ir}$ | 5000 | - | - | - |
| Nominal q-axis Stator Voltage | $v_{qs}{}^s$ | 187.79 | V | 1 | pu |
| AC Crowbar Resistance | $R_{cb}$ | 2 | ohm | 0.2560 | pu |
| AC Crowbar Threshold Current | $I_{cb}$ | 40 | A (pk) | 1.6638 | pu |
| **GSC Transformer** | | | | | |
| Per-Phase Power Rating | - | 3 | kVA | | |
| Primary Winding Voltage Rating | - | 480 | V | | |
| Secondary Winding Voltage Rating | - | 115 | V | | |
| Turns Ratio | - | 0.2396 | - | | |
| Pos. Sequence Leakage Inductance (Referred to LV Winding) | - | 0.23 | mH | 0.1934 | pu |

**Table A.4: Utility-scale Type 3 WTG parameters.**

| **Wound-Rotor Induction Machine Parameters** | | | | | |
|---|---|---|---|---|---|
| **Quantity** | **Sym.** | **Actual Value** | | **Per-Unit Value** | |
| Power | - | 1.717 | MVA | 3 | pu |
| Voltage | $V_s$ | 575 | V | 1.7321 | pu |
| Stator Resistance | $R_s$ | 0.0014 | ohm | 0.0073 | pu |
| Stator Leakage Reactance | $X_{ls}$ | 0.0340 | ohm | 0.1766 | pu |
| Magnetizing Reactance | $X_m$ | 0.5760 | ohm | 2.9913 | pu |
| Rotor Resistance | $R_r$ | 0.0010 | ohm | 0.0052 | pu |
| Rotor Leakage Reactance | $X_{lr}$ | 0.0310 | ohm | 0.1610 | pu |
| Stator/Rotor Turns Ratio | - | 0.3353 | - | - | - |
| Inertia | $J$ | 989.45 | kg*m$^2$ | 4.55 | sec |
| Poles | - | 6 | - | - | - |
| **GSC Parameters** | | | | | |
| Filter Capacitance | $C_f$ | 500 | μF | 27.5508 | pu |
| DC-Link Capacitance | $C$ | 30,000 | μF | - | - |
| Parasitic Filter Resistance | $R_g$ | 0.002 | ohm | 0.0104 | pu |
| Filter Inductance | $L_{gf}$ | 1.00 | mH | 1.9578 | pu |
| DC-Link Voltage | $V_{dc}$ | 1,200 | V (dc) | - | - |
| DC-Link Voltage Controller Prop. Gain | $K_{pv}$ | 0.0003 | - | - | - |
| DC-Link Voltage Controller Integral Gain | $K_{iv}$ | 6.667e-4 | - | - | - |
| GSC Current Controller Prop. Gain | $K_{pg}$ | 1.2 | - | - | - |
| GSC Current Controller Integral Gain | $K_{ig}$ | 200 | - | - | - |
| Nominal d-axis Stator Voltage | $v_{ds}{}^v$ | 469.49 | V (pk) | 1 | pu |
| DC-Chopper Resistance | $R_{dc}$ | 10 | ohm | - | - |
| DC-Chopper Turn-on/Turn-off Voltage | $v_{dcon}$<br>$v_{dcoff}$ | 1,500<br>1,475 | V (dc) | - | - |
| **RSC Parameters** | | | | | |
| Parasitic Filter Resistance | $R_{rf}$ | 0.002 | ohm | 0.0104 | pu |
| Filter Inductance | $L_{rf}$ | 0.2 | mH | 0.3916 | pu |
| Rotor Speed Controller Prop. Gain | $K_{p\omega}$ | 100 | - | - | - |
| Rotor Speed Controller Integral Gain | $K_{i\omega}$ | 10 | - | - | - |
| Stator Reactive Power Prop. Gain | $K_{pq}$ | 1e-6 | - | - | - |
| Stator Reactive Power Prop. Gain | $K_{iq}$ | 0.02 | - | - | - |
| RSC Current Controller Prop. Gain | $K_{pr}$ | 0.25 | - | - | - |
| RSC Current Controller Integral Gain | $K_{ir}$ | 50 | - | - | - |
| Nominal q-axis Stator Voltage | $v_{qs}{}^s$ | 469.49 | V | - | - |
| AC Crowbar Resistance | $R_{cb}$ | 0.5 | ohm | 0.2919 | pu |
| AC Crowbar Threshold Current | $I_{cb}$ | 1,100 | A (pk) | 1.3457 | pu |

**Table A.5: Lab-scale Type 4 WTG parameters.**

| **Wound-Rotor Induction Machine Parameters** | | | | | |
|---|---|---|---|---|---|
| **Quantity** | **Sym.** | **Actual Value** | | **Per-Unit Value** | |
| Power | $P$ | 6,772.3 | VA | 3 | pu |
| Voltage | $V_s$ | 230 | V | 1.7321 | pu |
| Stator Resistance | $R_s$ | 0.2178 | ohm | 0.0279 | pu |
| Stator Leakage Reactance | $X_{ls}$ | 0.5319 | ohm | 0.0681 | pu |
| Magnetizing Reactance | $X_m$ | 10.09 | ohm | 1.2921 | pu |
| Rotor Resistance | $R_r$ | 0.2068 | ohm | 0.0265 | pu |
| Rotor Leakage Reactance | $X_{lr}$ | 0.5319 | ohm | 0.0681 | pu |
| Stator/Rotor Turns Ratio | - | 1 | - | - | - |
| Inertia | $J$ | 0.3145 | $kg*m^2$ | 0.825 | sec. |
| Poles | - | 4 | - | - | - |
| **GSC Parameters** | | | | | |
| Filter Capacitance | $C_f$ | N/A | μF | - | - |
| DC-Link Capacitance | $C$ | 2300 | μF | - | - |
| Parasitic Filter Resistance | $R_g$ | 0.001 | ohm | 0.0022 | pu |
| Filter Inductance | $L_{gf}$ | 1.05 | mH | 0.8829 | pu |
| DC-Link Voltage | $V_{dc}$ | 225 | V (dc) | - | - |
| DC-Link Voltage Controller Prop. Gain | $K_{pv}$ | 0.0002 | - | - | - |
| DC-Link Voltage Controller Integral Gain | $K_{iv}$ | 3.33e-4 | - | - | - |
| GSC Current Controller Prop. Gain | $K_{pg}$ | 4.0 | - | - | - |
| GSC Current Controller Integral Gain | $K_{ig}$ | 2000 | - | - | - |
| Nominal d-axis GSC voltage | $v_{dg}$ | 44.99 | V | | |
| Maximum GSC Current Output | $I_{gmax}$ | 35 | A (peak) | 0.4933 | pu |
| Low-Pass Filter Time Constant | $T_f$ | 7.958e-3 | seconds | - | - |
| Current-Limiting Turn-On Voltage | $v_{gon}$ | 169.0 | V (peak) | 0.9 | pu |
| Current-Limiting Turn-Off Voltage | $v_{goff}$ | 178.4 | V (peak) | 0.95 | pu |
| DC-Chopper Resistance | $R_{dc}$ | 10 | Ohm | - | - |
| DC-Chopper Turn-on/Turn-off Voltage | $v_{dcon}$<br>$v_{dcoff}$ | 260<br>250 | V (dc) | - | - |
| **GSC Transformer** | | | | | |
| Per-Phase Power Rating | - | 3 | kVA | | |
| Primary Winding Voltage Rating | - | 480 | V | | |
| Secondary Winding Voltage Rating | - | 115 | V | | |
| Turns Ratio | - | 0.2396 | - | | |
| Pos. Sequence Leakage Inductance (Referred to LV Winding) | | 0.23 | mH | 0.1934 | pu |
| **MSC Parameters** | | | | | |
| Parasitic Filter Resistance | $R_{mf}$ | 0.001 | ohm | - | - |
| Filter Inductance | $L_{mf}$ | 0.35 | mH | - | - |
| Rotor Speed Controller Prop. Gain | $K_{p\omega}$ | 0.01 | - | - | - |
| Rotor Speed Controller Integral Gain | $K_{i\omega}$ | 0.5 | - | - | - |
| d-axis stator current reference | $i_{ds}$* | 15 | A | 0.8824 | pu |
| MSC Current Controller Prop. Gain | $K_{pm}$ | 10 | - | - | - |
| MSC Current Controller Integral Gain | $K_{im}$ | 5000 | - | - | - |

**Table A.6: Utility-scale Type 4 WTG parameters.**

| **Wound-Rotor Induction Machine Parameters** | | | | | |
|---|---|---|---|---|---|
| **Quantity** | **Sym.** | **Actual Value** | | **Per-Unit Value** | |
| Power | - | 1.717 | MVA | 3 | pu |
| Voltage | $V_s$ | 575 | V | 1.7321 | pu |
| Stator Resistance | $R_s$ | 0.0014 | ohm | 0.0073 | pu |
| Stator Leakage Reactance | $X_{ls}$ | 0.0340 | ohm | 0.1766 | pu |
| Magnetizing Reactance | $X_m$ | 0.5760 | ohm | 2.9913 | pu |
| Rotor Resistance | $R_r$ | 0.0010 | ohm | 0.0052 | pu |
| Rotor Leakage Reactance | $X_{lr}$ | 0.0310 | ohm | 0.1610 | pu |
| Stator/Rotor Turns Ratio | - | 0.3353 | - | - | - |
| Inertia | $J$ | 989.45 | kg*m$^2$ | 4.55 | sec |
| Poles | - | 6 | - | - | - |
| **GSC Parameters** | | | | | |
| Filter Capacitance | $C_f$ | 500 | μF | 27.5508 | pu |
| DC-Link Capacitance | $C$ | 30,000 | μF | - | - |
| Parasitic Filter Resistance | $R_g$ | 0.0002 | ohm | 0.0010 | pu |
| Filter Inductance | $L_{gf}$ | 0.3 | mH | 0.5873 | pu |
| DC-Link Voltage | $V_{dc}$ | 1,200 | V (dc) | - | - |
| DC-Link Voltage Controller Prop. Gain | $K_{pv}$ | 0.0003 | - | - | - |
| DC-Link Voltage Controller Integral Gain | $K_{iv}$ | 6.667e-4 | - | - | - |
| GSC Current Controller Prop. Gain | $K_{pg}$ | 0.4 | - | - | - |
| GSC Current Controller Integral Gain | $K_{ig}$ | 50 | - | - | - |
| Maximum GSC Current Output | $I_{gmax}$ | 2926 | A (peak) | 1.2 | pu |
| Nominal d-axis GSC Volage | $v_{dg}$ | 469.49 | V | | |
| Low-Pass Filter Time Constant | $T_f$ | 7.958e-3 | seconds | - | - |
| Current-Limiting Turn-On Voltage | $v_{gon}$ | 422.5 | V (peak) | 0.9 | pu |
| Current-Limiting Turn-Off Voltage | $v_{goff}$ | 446.0 | V (peak) | 0.95 | pu |
| DC-Chopper Resistance | $R_{dc}$ | 2 | Ohm | - | - |
| DC-Chopper Turn-on/Turn-off Voltage | $v_{dcon}$<br>$v_{dcoff}$ | 1,500<br>1,475 | V (dc) | - | - |
| **MSC Parameters** | | | | | |
| Parasitic Filter Resistance | $R_{mf}$ | 0.0002 | ohm | 0.0010 | pu |
| Filter Inductance | $L_{mf}$ | 0.1 | mH | 0.1958 | pu |
| Rotor Speed Controller Prop. Gain | $K_{p\omega}$ | 250 | - | - | - |
| Rotor Speed Controller Integral Gain | $K_{i\omega}$ | 10 | - | - | - |
| d-axis stator current reference | $i_{ds}$* | 815 | A | 0.4727 | pu |
| MSC Current Controller Prop. Gain | $K_{pm}$ | 0.5 | - | - | - |
| MSC Current Controller Integral Gain | $K_{im}$ | 100 | - | - | - |

# APPENDIX B: CLOSED-FORM SOLUTION OF INDUCTION MACHINE SHORT-CIRCUIT CURRENTS

** The material in this Appendix has been published in [69], and is reproduced here for convenience.*

In a stationary reference frame, the stator and rotor voltage equations (neglecting the zero sequence component) are written in space vector notation as

$$\begin{aligned} \vec{v}_s &= R_s \vec{i}_s + \frac{d\vec{\lambda}_s}{dt} \\ \vec{v}_r &= R_r \vec{i}_r + \frac{d\vec{\lambda}_r}{dt} - j\omega_r \vec{\lambda}_r \end{aligned}, \tag{A.1}$$

where $R_s$ is the stator resistance, $R_r$ is the rotor resistance, and $\omega_r$ is the rotor mechanical speed. The flux linkages are written in terms of the currents as

$$\begin{aligned} \vec{\lambda}_s &= L_s \vec{i}_s + L_m \vec{i}_r \\ \vec{\lambda}_r &= L_m \vec{i}_s + L_r \vec{i}_r \end{aligned}, \tag{A.2}$$

where $L_s = L_{ls} + L_m$ and $L_r = L_{lr} + L_m$, the sum of the leakage and magnetizing inductances. Rewriting the flux linkage equations in (A.2) in terms of the stator and rotor current gives

$$\begin{aligned} \vec{i}_s &= \frac{\vec{\lambda}_s}{L_s'} - \frac{L_m}{L_r}\frac{\vec{\lambda}_r}{L_s'} \\ \vec{i}_r &= \frac{\vec{\lambda}_r}{L_r'} - \frac{L_m}{L_s}\frac{\vec{\lambda}_s}{L_r'} \end{aligned}, \tag{A.3}$$

where $L_s$' and $L_r$' are the stator and rotor transient inductances, given by

$$\begin{aligned} L_s' &= L_s - \frac{L_m^2}{L_r} = L_{ls} + \frac{L_m L_{lr}}{L_{lr} + L_m} \\ L_r' &= L_r - \frac{L_m^2}{L_s} = L_{lr} + \frac{L_m L_{ls}}{L_{ls} + L_m} \end{aligned}. \tag{A.4}$$

Inserting the current equations in (A.3) into the voltage equations in (A.1) and rearranging terms gives time derivative of the flux linkages in matrix form, given by

$$\frac{d}{dt}\begin{bmatrix}\vec{\lambda}_s\\ \vec{\lambda}_r\end{bmatrix}=\begin{bmatrix}-\dfrac{R_s}{L_s'} & \dfrac{R_s}{L_s'}\dfrac{L_m}{L_r}\\ \dfrac{R_r}{L_r'}\dfrac{L_m}{L_s} & -\dfrac{R_r}{L_r'}+j\omega_r\end{bmatrix}\begin{bmatrix}\vec{\lambda}_s\\ \vec{\lambda}_r\end{bmatrix}+\begin{bmatrix}\vec{v}_s\\ \vec{v}_r\end{bmatrix}. \tag{A.5}$$

Equation (A.5) is the general form of the induction machine electrical dynamic equations in space vector notation using flux linkages as the state variable.

In deriving the closed-form solution of the stator short-circuit currents, two key assumptions are made to make the solution more tractable:

- The rotor speed remains fixed at its pre-fault speed during the short circuit
- The stator terminal voltages of the machine are known and fixed

The first assumption is valid for a short period of time after a fault for machines with a large inertia, as in the case of a large wind turbine. The second assumption is valid if the machine is connected to a "stiff" grid, where the amount of current flowing in the machine does not significantly affect the terminal voltages. Thus it can be assumed that the voltage magnitude and angle are fixed at their rated values. For example, if a phase A to ground fault occurs at the machine terminals, the phase A terminal voltage is zero, but the magnitude and angle of the phase B and C voltage remain unchanged after the fault.

Equation (A.5) can be written more concisely if the matrix of parameters is replaced by arbitrary variables $a_1$-$a_4$, given by

$$\frac{d}{dt}\begin{bmatrix}\vec{\lambda}_s\\ \vec{\lambda}_r\end{bmatrix}=\begin{bmatrix}a_1 & a_2\\ a_3 & a_4\end{bmatrix}\begin{bmatrix}\vec{\lambda}_s\\ \vec{\lambda}_r\end{bmatrix}+\begin{bmatrix}\vec{v}_s\\ \vec{v}_r\end{bmatrix}. \tag{A.6}$$

Equation (A.6) is of the general form

$$\dot{x}=Ax+u\,, \tag{A.7}$$

where the state variable $x$ is the stator and rotor flux, $A$ is a constant matrix (if the rotor speed is assumed to remain constant) made up of elements of the machine parameters and

rotor speed, and $u$ is a vector made up of the stator and rotor applied voltages. Equation (A.7) is the general form for a set of linear differential equations with constant coefficients, in which well-established mathematical techniques can be used to find a closed-form solution. The solution to (A.7) is found by separately solving the un-driven ($u = 0$) system with given initial conditions $x_0$ and the driven system ($u \neq 0$), and then adding the two solutions together to get the total solution [68].

It can be shown that the eigenvalues $\Psi_1$ and $\Psi_2$ of the matrix $A$ in (A.7) are given by

$$\psi_{1,2} = \frac{a_1 + a_4 \pm \sqrt{a_1^2 - 2a_1a_4 + a_4^2 + 4a_2a_3}}{2}, \tag{A.8}$$

with corresponding eigenvectors given by

$$\sigma_{1,2} = \begin{bmatrix} \frac{\psi_{1,2}}{a_3} - \frac{a_4}{a_3} \\ 1 \end{bmatrix} = \begin{bmatrix} p_{1,2} \\ 1 \end{bmatrix}. \tag{A.9}$$

The eigenvalues calculated using (A.8) are complex, but their corresponding complex conjugate is not present. This is expected since, while the matrix $A$ is a 2x2 matrix, the system in (A.7) is still a *fourth-order* system, since the state variables and $A$ matrix are complex. Thus, the complex conjugate of the eigenvalues calculate in (A.8) are *implied*. The solution to (A.7) is found by first solving the un-driven ($u = 0$) system, with solution determined by the matrix exponential $e^{At}$ [67]. The general solution to this un-driven system is given by

$$x_h(t) = e^{A(t-t_0)}x_0, \tag{A.10}$$

where $x_0$ is a vector of the flux linkage initial conditions prior to the fault and $t_0$ is the time of the fault. The matrix exponential $e^{At}$ is found from the Jordan normal form of $A$ [67], given by

$$J = \begin{bmatrix} \psi_1 & 0 \\ 0 & \psi_2 \end{bmatrix}. \tag{A.11}$$

The matrix exponential can be calculated using the Jordan normal form of $A$ and a change of basis matrix $P$, given by

$$e^{At} = Pe^{Jt}P^{-1} = P\begin{bmatrix} e^{\psi_1 t} & 0 \\ 0 & e^{\psi_2 t} \end{bmatrix}P^{-1}, \tag{A.12}$$

where it can be shown that the columns of $P$ are made up of the eigenvectors in (A.9) [67], given by

$$P = \begin{bmatrix} p_1 & p_2 \\ 1 & 1 \end{bmatrix}. \tag{A.13}$$

Inserting (A.13) into (A.12) and performing the calculations gives the matrix exponential to be

$$e^{At} = \begin{bmatrix} K(p_1 e^{\psi_1 t} - p_2 e^{\psi_2 t}) & -Kp_1 p_2 (e^{\psi_1 t} - e^{\psi_2 t}) \\ K(e^{\psi_1 t} - e^{\psi_2 t}) & -K(p_2 e^{\psi_1 t} - p_1 e^{\psi_2 t}) \end{bmatrix}, \tag{A.14}$$

where $K = 1/(p_1 - p_2)$. Thus, the solution to the un-driven (homogeneous) system is given by

$$x_h = \begin{bmatrix} \vec{\lambda}_{sh} \\ \vec{\lambda}_{rh} \end{bmatrix} = e^{A(t-t_0)} \begin{bmatrix} \vec{\lambda}_s(t_0) \\ \vec{\lambda}_r(t_0) \end{bmatrix}. \tag{A.15}$$

The particular solution to (A.7) is found knowing that the stator and rotor voltages are given by

$$u = \begin{bmatrix} \vec{v}_s \\ \vec{v}_r \end{bmatrix} = \begin{bmatrix} \vec{V}_1 e^{j\omega_s t} + \vec{V}_2 e^{-j\omega_s t} \\ 0 \end{bmatrix}, \tag{A.16}$$

where the stator voltages may, in general, contain positive- and negative-sequence components. The induction machine is assumed to have short circuited rotor windings, thus the rotor voltage is zero. A good guess to the driven (particular) solution of the flux linkages follows from the form of the applied voltages given in (A.16), given by

$$x_p = \begin{bmatrix} \vec{\lambda}_{sp} \\ \vec{\lambda}_{rp} \end{bmatrix} = \begin{bmatrix} \vec{\Lambda}_{1s} e^{j\omega_s t} + \vec{\Lambda}_{2s} e^{-j\omega_s t} \\ \vec{\Lambda}_{1r} e^{j\omega_s t} + \vec{\Lambda}_{2r} e^{-j\omega_s t} \end{bmatrix}, \tag{A.17}$$

where the coefficients $\Lambda_{1s}$, $\Lambda_{2s}$, $\Lambda_{1r}$, and $\Lambda_{2r}$ are found using the method of undetermined coefficients [68]. Taking the time derivative of (A.17) gives

$$\dot{x}_p = \frac{d}{dt}\begin{bmatrix}\vec{\lambda}_{sp}\\ \vec{\lambda}_{rp}\end{bmatrix} = \begin{bmatrix} j\omega_s\vec{\Lambda}_{1s}e^{j\omega_s t} - j\omega_s\vec{\Lambda}_{2s}e^{-j\omega_s t}\\ j\omega_s\vec{\Lambda}_{1r}e^{j\omega_s t} - j\omega_s\vec{\Lambda}_{2r}e^{-j\omega_s t}\end{bmatrix}. \tag{A.18}$$

Inserting (A.16), (A.17), and (A.18) into (A.7) gives the following

$$\begin{bmatrix} j\omega_s\vec{\Lambda}_{1s}e^{j\omega_s t} - j\omega_s\vec{\Lambda}_{2s}e^{-j\omega_s t}\\ j\omega_s\vec{\Lambda}_{1r}e^{j\omega_s t} - j\omega_s\vec{\Lambda}_{2r}e^{-j\omega_s t}\end{bmatrix} - \begin{bmatrix} a_1 & a_2\\ a_3 & a_4\end{bmatrix}\begin{bmatrix}\vec{\Lambda}_{1s}e^{j\omega_s t} + \vec{\Lambda}_{2s}e^{-j\omega_s t}\\ \vec{\Lambda}_{1r}e^{j\omega_s t} + \vec{\Lambda}_{2r}e^{-j\omega_s t}\end{bmatrix} - \begin{bmatrix}\vec{V}_1e^{j\omega_s t} + \vec{V}_2e^{-j\omega_s t}\\ 0\end{bmatrix} = \begin{bmatrix}0\\0\end{bmatrix}. \tag{A.19}$$

It can be shown that a set of 4 linear equations can be extracted from (A.19), and solved to give the coefficients in (A.17). This set of equations is given by

$$\begin{bmatrix} j\omega_s - a_1 & 0 & -a_2 & 0\\ 0 & -j\omega_s - a_1 & 0 & -a_2\\ -a_3 & 0 & j\omega_s - a_4 & 0\\ 0 & -a_3 & 0 & -j\omega_s - a_4\end{bmatrix}\begin{bmatrix}\vec{\Lambda}_{1s}\\ \vec{\Lambda}_{2s}\\ \vec{\Lambda}_{1r}\\ \vec{\Lambda}_{2r}\end{bmatrix} = \begin{bmatrix}\vec{V}_1\\ \vec{V}_2\\ 0\\ 0\end{bmatrix}. \tag{A.20}$$

A solution for the terms in (A.20) can be found using any conventional solution method for a set of linear algebraic equations. Calculating the terms in (A.20) gives the particular solution to (A.7), and the final solution is found by summing the un-driven (homogeneous) and driven (particular) solutions, and calculating the initial flux values $\lambda_{si}$ and $\lambda_{ri}$ that satisfy

$$\begin{bmatrix}\vec{\lambda}_s(t_0)\\ \vec{\lambda}_r(t_0)\end{bmatrix} = e^{A(t-t_0)}\begin{bmatrix}\vec{\lambda}_{si}\\ \vec{\lambda}_{ri}\end{bmatrix} + \begin{bmatrix}\vec{\Lambda}_{1s}e^{j\omega_s t} + \vec{\Lambda}_{2s}e^{-j\omega_s t}\\ \vec{\Lambda}_{1r}e^{j\omega_s t} + \vec{\Lambda}_{2r}e^{-j\omega_s t}\end{bmatrix}. \tag{A.21}$$

Utilizing the known initial conditions of the flux linkages at time $t = t_0$, the components $\lambda_{si}$ and $\lambda_{ri}$ can be found by inserting the matrix exponential of (A.14) into (A.21) and setting $t = t_0$, given by

$$\begin{bmatrix}\vec{\lambda}_s(t_0)\\ \vec{\lambda}_r(t_0)\end{bmatrix}=\begin{bmatrix}1 & 0\\ 0 & 1\end{bmatrix}\begin{bmatrix}\vec{\lambda}_{si}\\ \vec{\lambda}_{ri}\end{bmatrix}+\begin{bmatrix}\vec{\Lambda}_{1s}e^{j\omega_s t_0}+\vec{\Lambda}_{2s}e^{-j\omega_s t_0}\\ \vec{\Lambda}_{1r}e^{j\omega_s t_0}+\vec{\Lambda}_{2r}e^{-j\omega_s t_0}\end{bmatrix}. \tag{A.22}$$

Thus, $\lambda_{si}$ and $\lambda_{ri}$ are given by

$$\begin{aligned}\vec{\lambda}_{si} &= \vec{\lambda}_s(t_0)-\vec{\Lambda}_{1s}e^{j\omega_s t_0}-\vec{\Lambda}_{2s}e^{-j\omega_s t_0}\\ \vec{\lambda}_{ri} &= \vec{\lambda}_r(t_0)-\vec{\Lambda}_{1r}e^{j\omega_s t_0}-\vec{\Lambda}_{2r}e^{-j\omega_s t_0}\end{aligned}. \tag{A.23}$$

By inserting these values for $\lambda_{si}$ and $\lambda_{ri}$ into (A.21), the general solution to the flux linkages is calculated by

$$\begin{aligned}\vec{\lambda}_s &= Kp_1(\vec{\lambda}_{si}-p_2\vec{\lambda}_{ri})e^{\psi_1(t-t_0)}+Kp_2(p_1\vec{\lambda}_{ri}-\vec{\lambda}_{si})e^{\psi_2(t-t_0)}\\ &\quad+\vec{\Lambda}_{1s}e^{j\omega_s t}+\vec{\Lambda}_{2s}e^{-j\omega_s t}\\ \vec{\lambda}_r &= K(\vec{\lambda}_{si}-p_2\vec{\lambda}_{ri})e^{\psi_1(t-t_0)}+K(p_1\vec{\lambda}_{ri}-\vec{\lambda}_{si})e^{\psi_2(t-t_0)}\\ &\quad+\vec{\Lambda}_{1r}e^{j\omega_s t}+\vec{\Lambda}_{2r}e^{-j\omega_s t}\end{aligned}. \tag{A.24}$$

The stator current is found by inserting the results of (A.24) into (A.3), given by

$$\vec{i}_s=\frac{\vec{\lambda}_s}{L_s'}-\frac{L_m}{L_r}\frac{\vec{\lambda}_r}{L_s'}=\vec{I}_{dc}e^{\psi_1(t-t_0)}+\vec{I}_t e^{\psi_2(t-t_0)}+\vec{I}_{ss}e^{j\omega_s t}, \tag{A.25}$$

where

$$\begin{aligned}\vec{I}_{dc} &= \frac{1}{L_s'}\left(Kp_1(\vec{\lambda}_{si}-p_2\vec{\lambda}_{ri})-\frac{L_m}{L_r}K(\vec{\lambda}_{si}-p_2\vec{\lambda}_{ri})\right)\\ \vec{I}_t &= \frac{1}{L_s'}\left(Kp_2(p_1\vec{\lambda}_{ri}-\vec{\lambda}_{si})-\frac{L_m}{L_r}K(p_1\vec{\lambda}_{ri}-\vec{\lambda}_{si})\right)\\ \vec{I}_{ss} &= \frac{1}{L_s'}\left(\vec{\Lambda}_{1s}-\frac{L_m}{L_r}\vec{\Lambda}_{1r}\right)-\left[\frac{1}{L_s'}\left(\vec{\Lambda}_{2s}-\frac{L_m}{L_r}\vec{\Lambda}_{2r}\right)\right]^*\end{aligned}. \tag{A.26}$$

**Derivation of Sequence-Network Representation**

In steady state, the voltage equations of the induction machine given in (A.1) become

$$\begin{aligned}\vec{v}_s &= R_s\vec{i}_s+j\omega_s\vec{\lambda}_s\\ \vec{v}_r &= R_r\vec{i}_r+j(\omega_s-\omega_r)\vec{\lambda}_r\end{aligned}, \tag{A.27}$$

where *d/dt* becomes $j\omega_s$ in steady state. The stator flux linkage can be re-written in terms of the stator voltage and current from (A.27), given by

$$\vec{\lambda}_s = \frac{\vec{v}_s - R_s\vec{i}_s}{j\omega_s}. \tag{A.28}$$

Inserting this value of the stator flux linkage into the stator current equation in (A.3) gives

$$\vec{i}_s = \frac{\vec{v}_s - R_s\vec{i}_s}{j\omega_s L_s'} - \frac{L_m}{L_r}\frac{\vec{\lambda}_r}{L_s'} = \frac{\vec{v}_s}{jX'} - \frac{R_s\vec{i}_s}{jX'} - \frac{L_m}{L_r}\frac{\vec{\lambda}_r}{L_s'}, \tag{A.29}$$

where the transient reactance $X' = \omega_s L_s'$. Eliminating the stator current from the right hand side of (A.29), the stator current is written as

$$\vec{i}_s = \frac{\frac{\vec{v}_s}{jX'} - \frac{L_m}{L_r}\frac{\vec{\lambda}_r}{L_s'}}{1+\frac{R_s}{jX'}} = \frac{\vec{v}_s - j\omega_s\frac{L_m}{L_r}\vec{\lambda}_r}{R_s + jX'} = \frac{\vec{v}_s - \vec{v}'}{R_s + jX'}. \tag{A.30}$$

Thus, the voltage behind transient reactance space vector from (A.30) is given as

$$\vec{v}' = j\omega_s\frac{L_m}{L_r}\vec{\lambda}_r. \tag{A.31}$$

Thus, the steady-state equivalent circuit of the induction machine shown in Fig. A.1(a) can be alternatively represented as the circuit shown in Fig. A.1(b) using (A.30). Equation (A.31) indicates that the voltage behind transient reactance is proportional to the rotor flux linkage. From the closed-form solution of the rotor flux linkage given in (A.24), the appropriate voltage behind transient reactance can be calculated for different types of faults.

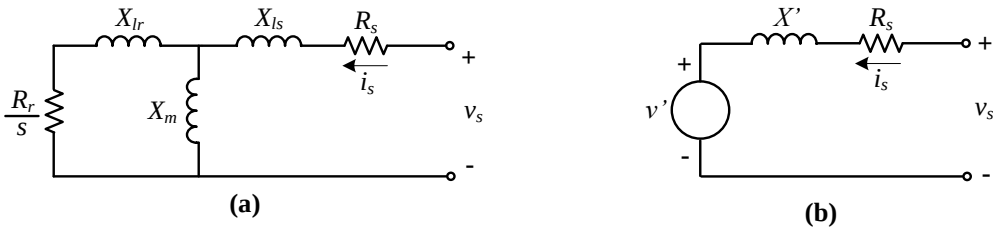


**Fig. A.1: (a) Steady-state equivalent circuit of induction machine and (b) steady-state sequence-network representation of induction machine.**

For a balanced symmetrical short circuit, the terms $\Lambda_{1s}$, $\Lambda_{2s}$, $\Lambda_{1r}$, and $\Lambda_{2r}$ in (A.17) - (A.24) are zero since the terminal voltages go to zero after the fault. Thus, the solution to the flux linkages and currents is determined entirely by the un-driven system solution. Thus, the voltage behind transient reactance at $t = t_0$ for the balanced fault case can be calculated by inserting the results of (A.23) and (A.24) for the rotor flux linkage into (A.31), given by

$$\vec{v}' = j\omega_s \frac{L_m}{L_r} K\left[p_1\vec{\lambda}_r(t_0) - \vec{\lambda}_s(t_0)\right], \tag{A.32}$$

where the low frequency component of the rotor flux linkage has been neglected. Equation (A.32) indicates that the voltage behind transient reactance is based only on the initial flux before the fault and the machine parameters. One can deduce from (A.32) that the magnitude of *v'* is independent of $t_0$ despite the rotation of the stator and rotor flux linkages, since the *relative* position between $\lambda_s$ and $\lambda_r$ for any given steady state operating point remains constant.

For the unbalanced fault, the terms $\Lambda_{1s}$, $\Lambda_{2s}$, $\Lambda_{1r}$, and $\Lambda_{2r}$ are not zero since one or two of the machine stator phases remains un-faulted. Thus the *v'* in this case at $t = t_0$ is found by inserting the results of (A.24) into (A.31), given by

$$\vec{v}' = j\omega_s \frac{L_m}{L_r}\left[K(p_1\vec{\lambda}_{ri} - \vec{\lambda}_{si}) + \vec{\Lambda}_{1r}e^{j\omega_s t_0} + \vec{\Lambda}_{2r}e^{-j\omega_s t_0}\right]. \tag{A.33}$$

Equation (A.33) indicates that for unbalanced faults, a negative-sequence voltage behind transient reactance is present due to the negative-sequence flux. This negative-sequence

voltage is caused by the solution of the driven system influencing the initial rotor flux linkage. Additionally, a positive-sequence voltage is present due to the positive sequence rotor flux, and is dependent on both the rotor flux due to the driven system and the initial rotor flux before the fault. The magnitude of this voltage varies depending on $t_0$, since the relative position between the initial stator and rotor flux and the steady-state (driven) flux is not constant.

The simple network of Fig. A.2 is used to perform an example calculation of the sequence-network parameters of the induction machine using the results of the previous paragraphs. However, a simpler approach in calculating the parameters is taken, rather than using the differential equations described previously. From the results of (A.33), one can conclude that *v'* is comprised of the post-fault steady-state rotor flux linkage and the pre-fault stator and rotor flux linkages. Therefore, knowing the steady-state solution for the flux linkages after the fault gives one "piece" of the solution. For a single phase to ground fault, the steady-state solution can be found by calculating the currents $I_A^{a+}$, $I_A^{a-}$, $I_a^{a+}$, and $I_a^{a-}$ in the steady-state sequence network shown in Fig. A.3. The slip *s* in this circuit is assumed to be the pre-fault slip. While intuitively the machine will not remain at its pre-fault slip by the time it has reached steady state after the fault, the steady-state solution affecting the *initial* short-circuit current corresponds to the solution of the currents flowing in the circuit of Fig. 4 with the pre-fault slip. Details of the current calculations of the circuit of Fig. 4 are not provided here, but the results are provided in Table A.7. The corresponding stator and rotor flux linkages after the fault are calculated by

$$\begin{aligned} \Lambda_A^{a+} &= L_s I_A^{a+} + L_m I_a^{a+}, \quad \Lambda_A^{a-} = L_s I_A^{a-} + L_m I_a^{a-} \\ \Lambda_a^{a+} &= L_m I_A^{a+} + L_r I_a^{a+}, \quad \Lambda_a^{a-} = L_m I_A^{a-} + L_r I_a^{a-} \end{aligned} . \tag{A.34}$$

The steady-state flux linkages before the fault can be calculated using the steady state, per-phase equivalent circuit of the network shown in Fig. A.2, which is displayed in Fig.

A.4. The calculated stator and rotor currents flowing in this circuit are also given in Table A.7. The pre-fault stator and rotor flux linkages are found from these currents by

$$\begin{aligned} \Lambda_A^b &= L_s I_A^b + L_m I_a^b, \\ \Lambda_a^b &= L_m I_A^b + L_r I_a^b, \end{aligned} \quad . \tag{A.35}$$

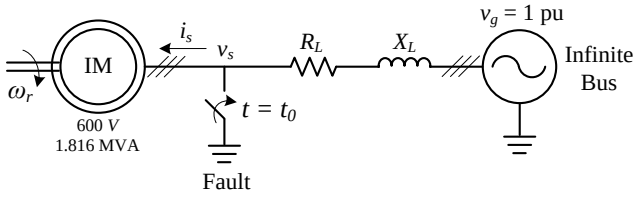


**Fig. A.2: Single induction machine network for simulation of stator short-circuit faults.**

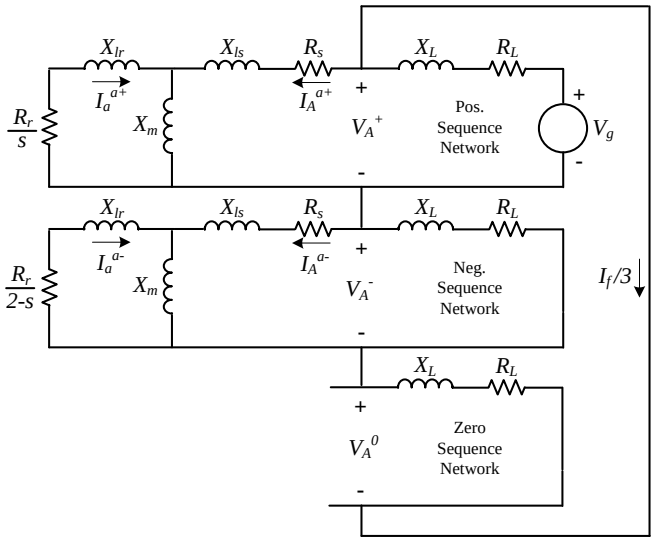


**Fig. A.3: Steady-state sequence network for a phase-A-to-ground fault on the network of Fig. A.2.**

**Table A.7: Steady State Current Calculation Results from Circuits of Fig. A.3 and Fig. A.4 (Magnitude in pu and Angle in Degrees)**

| $I_A^{a+}$ | | $I_A^{a-}$ | | $I_a^{a+}$ | | $I_a^{a-}$ | | $I_A^b$ | | $I_a^b$ | |
|---|---|---|---|---|---|---|---|---|---|---|---|
| Mag. | Ang. | Mag. | Ang. | Mag. | Ang. | Mag. | Ang. | Mag. | Ang. | Mag. | Ang. |
| 0.67 | -157 | 2.10 | 93.2 | 0.64 | 8.99 | 2.06 | -86.7 | 1.01 | -157 | 0.96 | 9.01 |

The appropriate voltage behind transient reactance can be calculated using the steady-state calculations of the pre-fault flux linkages in (A.35) and the post-fault steady state flux linkages using (A.34). From (A.33), the positive- and negative-sequence voltage behind transient reactance in terms of symmetrical components are given by

$$\begin{aligned} V'_{+} &= j\omega_s \frac{L_m}{L_r}[Kp_1(\Lambda_a^b - \Lambda_a^{a+} + \Lambda_a^{a-} * e^{-j2\delta}) \\ &\quad - K(\Lambda_A^b - \Lambda_A^{a+} + \Lambda_A^{a-} * e^{-j2\delta}) + \Lambda_a^{a+}] \quad , \\ V'_{-} &= j\omega_s \frac{L_m}{L_r} \Lambda_a^{a-} \end{aligned} \tag{A.36}$$

where $\delta = \omega_s t_0$ is defined as the fault angle and * is the complex conjugate. Specifically, $\delta$ = 0° corresponds to the phase A line-to-neutral voltage crossing zero, $\delta$ = 90° corresponds to a positive peak, etc. The calculation results shown in Table 3.3 represent calculating the voltages behind transient reactance using (A.36).

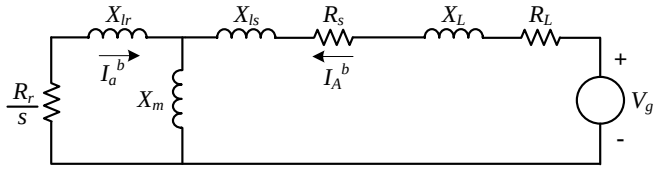


**Fig. A.4: Per-phase steady state equivalent circuit of the network in Fig. A.2.**

# APPENDIX C: COLLECTOR SYSTEM PARAMETERS

**Table A.8: Underground cable parameters used in the networks in Fig. 3.18, Fig. 3.25, Fig. 4.40, Fig. 4.47, Fig. 5.18, Fig. 5.24.**

| Quantity | Symbol | Value | Unit |
|---|---|---|---|
| Collector feeder cable Resistance | $R_c$ | 0.6362 | ohm |
| Collector feeder cable Inductance | $L_c$ | 0.0030 | H |
| Collector feeder cable capacitance* | $C_c$ | 1.6 | μF |
| WTG interconnecting cable resistance* | $R_{sc}$ | 0.1210 | ohm |
| WTG interconnecting cable inductance* | $L_{sc}$ | 0.227e-3 | H |
| WTG interconnecting cable capacitance* | $C_{sc}$ | 0.02 | μF |

*Note: these parameters are only used in the multi-machine studies in this dissertation.

**Table A.9: Generator step-up transformer parameters used in the networks in Fig. 3.18, Fig. 3.25, Fig. 4.40, Fig. 4.47, Fig. 5.18, Fig. 5.24.**

| Quantity | Symbol | Value | Unit |
|---|---|---|---|
| Rated Power | $P_{gt}$ | 1.8 | MVA |
| Primary Winding Rated Voltage (grounded wye) | $V_1$ | 575 or 600 | V |
| Secondary Winding Rated Voltage (delta) | $V_2$ | 34.5 | kV |
| Positive-Sequence Leakage Reactance | $X_{gt}$ | 0.0563 | pu |
| Winding Resistance | $R_{gt}$ | 0.0062 | pu |
| Copper Losses | $P_{cu}$ | 0.0062 | pu |
| Core Losses | $P_{core}$ | 0.0014 | pu |
| Magnetizing Current | -- | 1 % | -- |

**Table A.10: Substation step-up transformer parameters used in the networks in Fig. 3.18, Fig. 3.25, Fig. 4.40, Fig. 4.47, Fig. 5.18, Fig. 5.24.**

| Quantity | Symbol | Value | Unit |
|---|---|---|---|
| Rated Power | $P_{st}$ | 69 | MVA |
| Primary Winding Rated Voltage (grounded wye) | $V_1$ | 34.5 | kV |
| Secondary Winding Rated Voltage (grounded wye) | $V_2$ | 345 | kV |
| Tertiary Winding Rated Voltage (delta) | $V_3$ | 13.85 | kV |
| Positive-Sequence Leakage Reactance | $X_{st}$ | 0.0986 | pu |
| Primary Winding Impedance | $Z_{stl}$ | 0.00077 + j0.0124 | pu |
| Secondary Winding Impedance | $Z_{sth}$ | 0.00077 + j0.0862 | pu |
| Tertiary Winding Impedance | $Z_{st0}$ | 0.00077 + j0.0085 | pu |

| | | | |
|---|---|---|---|
| Copper Losses | $P_{cu}$ | 0.0023 | pu |
| Core Losses | $P_{core}$ | 0.000011 | pu |
| Magnetizing Current | -- | 0.01 % | -- |

**Table A.11: Transmission system parameters used in the networks in Fig. 3.18, Fig. 3.25, Fig. 4.40, Fig. 4.47, Fig. 5.18, Fig. 5.24.**

| Quantity | Symbol | Value | Unit |
|---|---|---|---|
| Transmission System Voltage | - | 345 | kV |
| X/R Ratio | - | 10 | - |
| Short-Circuit MVA (at PCC)* | - | 727 - 1000 | MVA |
| Transmission Line Impedance | $Z_L$ | 23.7 + *j*236.9 | ohm |

*The short-circuit MVA depends on the value of *k* and *m* used in the models of these particular networks. The range of these values reflects the minimum and maximum value of the short-circuit MVA for the different values of *k* and *m* used in this dissertation.

# APPENDIX D: SENSOR CALIBRATION AND MEASUREMENT UNCERTAINTY

Calibration of the current transducers was performed using the circuit shown in Fig. A.5. A DC power supply was used to inject a DC current $i_1$ into the primary conductor through the current transducer. Fifteen turns were wrapped through the current transducer to get a maximum primary conductor current of ±150 A. A digital multi-meter (DMM) was connected in series with the DC power supply to measure the supply current. The secondary current $i_2$ is nominally $i_1/2000$; thus, with a primary conductor current of 200 A, the secondary current is 0.1 A. The measuring range of the current transducer in Fig. A.5 is ±300 A; thus, the maximum secondary current is assumed to be 300/2000 = 0.15 A. The output voltage $v_2$ of the current transducer must be within the range of ±5 V for the data acquisition system used for waveform data collection. Thus, the measurement resistance $R_m$ is chosen such that 300 A in the primary conductor gives 5 V output voltage. Thus, $R_m$ is nominally given by 5 V/0.15 A = 33.33 Ω. A potentiometer was used for the measurement resistance, and was adjusted to achieve the desired output voltage at a particular primary conductor current. For example, with a DC power supply current of 5 A, the total primary conductor current is 5*15 = 75 A; thus, the potentiometer resistance $R_m$ was adjusted until the output voltage was equal to 75/2000*33.3333 = 1.25 V.

After calibration of the measurement resistor, forty measurements of the current were performed in roughly fixed intervals over the primary conductor current range from -150 A to +150 A. The measured results yielded a standard deviation of 0.48 A from their expected values.

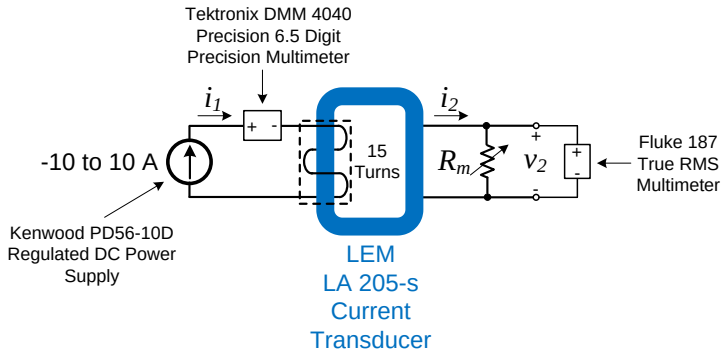


**Fig. A.5: Circuit for calibrating current transducers.**

A summary of the measurement uncertainty of the current transducers is given in Table A.12. The standard uncertainties calculated in Table A.12 are based upon the techniques given in [81]. The accuracy of all the measurement instruments was taken from the manufacturer's datasheets for these instruments. To calculate a combined uncertainty in the current measurement from all of the different sources of uncertainty, each source of uncertainty must be converted to the same units (amps in this case). For example, the Fluke 187 multi-meter is measuring the output voltage of the circuit shown in Fig. A.11. There is some uncertainty in the measurement of this voltage from this device. However, the quantity of interest is the *uncertainty in the primary conductor current due to the uncertainty of the output voltage measurement*. From the manufacturer's datasheet, the Fluke 187 DC voltage uncertainty in the range of 5 V is ±0.025% of the measured voltage. The uncertainty in the primary conductor current based on this voltage measurement is calculated to be

$$\left(\frac{0.00025*5}{33.3333}\right)2000 = 0.075 \quad A. \tag{A.37}$$

The combined standard uncertainty $U$ is given by the "root sum of the squares" of all the standard uncertainties, given by

$$U = \sqrt{a^2 + b^2 + c^2 + \ldots}, \tag{A.38}$$

where *a, b, c,* etc. are the standard uncertainties of all sources of uncertainty in the measurement. The expanded uncertainty is found by multiplying the combined standard uncertainty by a coverage factor *k*, which is chosen to be two in this case, giving a confidence level of 95%, assuming a normal distribution.

**Table A.12: Summary of Measurement Uncertainty from Current Transducers**

| Source of Uncertainty | Value (± A) | Probability Distribution | Divisor | Standard Uncertainty (± A) |
|---|---|---|---|---|
| DIMM 4040 Accuracy | 0.2370 | Normal | 2 | 0.1185 |
| DIMM 4040 Digit Resolution | 0.0005 | Uniform | 1.7321 | 0.0003 |
| LEM 205-S Accuracy | 0.2164 | Normal | 2 | 0.1082 |
| Fluke 187 Accuracy | 0.0750 | Normal | 2 | 0.0375 |
| Fluke 187 Digit Resolution | 0.0300 | Uniform | 1.7321 | 0.0173 |
| Labview Current Resolution | 0.1000 | Uniform | 1.7321 | 0.0577 |
| Standard Uncertainty of 40 Measurements | 0.0760 | Normal | 1 | 0.0760 |
| Combined Standard Uncertainty | | Normal | | 0.1912 |
| **Expanded Uncertainty (Coverage Factor k = 2)** | | Normal | | **0.3824** |

Calibration of the voltage transducers was performed using the circuit shown in Fig. A.6. A DC power supply was used to apply a DC voltage $v_1$ to the primary of the voltage transducer. A digital multi-meter (DMM) was connected in parallel with the DC power supply to measure the supply voltage. The primary resistor $R_1$ is a 25 kΩ resistor. The secondary current $i_2$ is nominally $i_1$*2.5; thus, with a primary voltage of 250 V, the secondary current is (250/25000)*2.5 = 0.025 A. The measuring range of the voltage transducer in Fig. A.6 is ±350 V with a primary resistor of 25 kΩ; thus, the maximum secondary current is assumed to be (350/25000)*2.5 = 0.035 A. The output voltage $v_2$ of the voltage transducer must be within the range of ±5 V for the data acquisition system used for waveform data collection. The measurement resistance $R_m$ is chosen such that the secondary output voltage is 0.01 times the primary voltage. Thus, $R_m$ is nominally

given by 0.01*350 V/0.035 A = 100 Ω. A potentiometer was used for the measurement resistance, and was adjusted to achieve the desired output voltage at a particular primary voltage. For example, with a DC power supply voltage of 50 V, the potentiometer was adjusted until the secondary output voltage was 50*0.01= 0.5 V.

After calibration of the measurement resistor, twenty measurements of the voltage were performed in roughly fixed intervals over the voltage range from -50 V to +50 V. The measured results yielded a standard deviation of 0.22 V from their expected values.

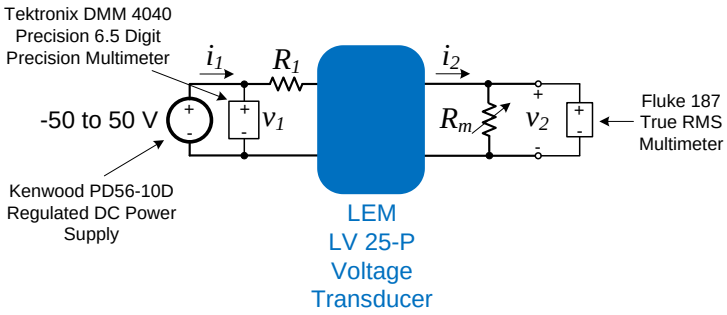


**Fig. A.6: Circuit for calibrating voltage transducers.**

A summary of the uncertainties in the voltage measurements is given in Table A.13. These tabulated values are found in a similar way described previously for the current measurements. The expanded uncertainty interval is given with a 95% confidence, assuming a normal distribution.

**Table A.13: Summary of Measurement Uncertainty from Voltage Transducers**

| Source of Uncertainty | Value (± V) | Probability Distribution | Divisor | Standard Uncertainty (± V) |
|---|---|---|---|---|
| DIMM 4040 Accuracy | 0.0051 | Normal | 2 | 0.0026 |
| DIMM 4040 Digit Resolution | 0.0005 | Uniform | 1.7321 | 0.0003 |
| LEM LV 25-P Accuracy | 2.0000 | Normal | 2 | 1.0000 |
| Fluke 187 Accuracy | 0.0031 | Normal | 2 | 0.0016 |
| Fluke 187 Digit Resolution | 0.0013 | Uniform | 1.7321 | 0.0007 |
| Labview Voltage Resolution | 0.1000 | Uniform | 1.7321 | 0.0577 |
| Standard Uncertainty of 20 Measurements | 0.0481 | Normal | 1 | 0.0481 |
| Combined Standard Uncertainty | | Normal | | 1.0028 |
| **Expanded Uncertainty (Coverage Factor k = 2)** | | Normal | | 2.0057 |

# APPENDIX E: STATOR-FLUX ESTIMATION IN TYPE 3 WTG

The induction machine voltage equations in a synchronous reference frame are given by

$$\begin{aligned} v_{ds} &= R_s i_{ds} - \omega_s \lambda_{qs} + p\lambda_{ds} \quad & v_{dr} &= R_r i_{dr} - (\omega_s - \omega_r)\lambda_{qr} + p\lambda_{dr} \\ v_{qs} &= R_s i_{qs} + \omega_s \lambda_{ds} + p\lambda_{qs} \quad & v_{qr} &= R_r i_{qr} + (\omega_s - \omega_r)\lambda_{dr} + p\lambda_{qr} \end{aligned}, \tag{A.39}$$

where the flux linkages in (A.39) are given by

$$\begin{aligned} \lambda_{ds} &= L_s i_{ds} + L_m i_{dr} \quad & \lambda_{dr} &= L_r i_{dr} + L_m i_{ds} \\ \lambda_{qs} &= L_s i_{qs} + L_m i_{qr} \quad & \lambda_{qr} &= L_r i_{qr} + L_m i_{qs} \end{aligned}. \tag{A.40}$$

The stator and rotor currents can be rewritten in terms of the flux linkages by rearranging terms in (A.40), given by

$$\begin{aligned} i_{ds} &= \frac{\lambda_{ds} - (L_m / L_r)\lambda_{dr}}{L_s'} \quad & i_{dr} &= \frac{\lambda_{dr} - (L_m / L_s)\lambda_{ds}}{L_r'} \\ i_{qs} &= \frac{\lambda_{qs} - (L_m / L_r)\lambda_{qr}}{L_s'} \quad & i_{qr} &= \frac{\lambda_{qr} - (L_m / L_s)\lambda_{qs}}{L_r'} \end{aligned}. \tag{A.41}$$

Substituting these current equations into (A.39) gives

$$\begin{aligned} v_{ds} &= \frac{R_s}{L_s'}\lambda_{ds} - \frac{R_s}{L_s'}\frac{L_m}{L_r}\lambda_{dr} - \omega_s \lambda_{qs} + p\lambda_{ds} \\ v_{qs} &= \frac{R_s}{L_s'}\lambda_{qs} - \frac{R_s}{L_s'}\frac{L_m}{L_r}\lambda_{qr} + \omega_s \lambda_{ds} + p\lambda_{qs} \\ v_{dr} &= \frac{R_r}{L_r'}\lambda_{dr} - \frac{R_r}{L_r'}\frac{L_m}{L_s}\lambda_{ds} - (\omega_s - \omega_r)\lambda_{qr} + p\lambda_{dr} \\ v_{qr} &= \frac{R_r}{L_r'}\lambda_{qr} - \frac{R_r}{L_r'}\frac{L_m}{L_s}\lambda_{qs} + (\omega_s - \omega_r)\lambda_{dr} + p\lambda_{qr} \end{aligned}. \tag{A.42}$$

Rewriting these equations in state-space form in terms of the flux linkage derivatives gives

$$p\begin{bmatrix}\lambda_{ds}\\ \lambda_{qs}\\ \lambda_{dr}\\ \lambda_{qr}\end{bmatrix}=\begin{bmatrix}-\frac{R_s}{L_s'} & \omega_s & \frac{R_s}{L_s'}\frac{L_m}{L_r} & 0\\ -\omega_s & -\frac{R_s}{L_s'} & 0 & \frac{R_s}{L_s'}\frac{L_m}{L_r}\\ \frac{R_r}{L_r'}\frac{L_m}{L_s} & 0 & -\frac{R_r}{L_r'} & \omega_s-\omega_r\\ 0 & \frac{R_r}{L_r'}\frac{L_m}{L_s} & -(\omega_s-\omega_r) & -\frac{R_r}{L_r'}\end{bmatrix}\begin{bmatrix}\lambda_{ds}\\ \lambda_{qs}\\ \lambda_{dr}\\ \lambda_{qr}\end{bmatrix}+\begin{bmatrix}v_{ds}\\ v_{qs}\\ v_{dr}\\ v_{qr}\end{bmatrix}. \quad \text{(A.43)}$$

The stator-flux linkages used in the feed-forward compensation terms of the Type 3 WTG RSC controls are calculated by integrating the (A.43). The rotor voltages $v_{dr}$ and $v_{qr}$ are taken directly from the output of the RSC controls. Thus, if the RSC enters the over-modulation region, some error in the flux calculation will result since the voltages commanded by the RSC cannot be applied due to the limitations in the RSC voltage ratings.

Calculating the stator flux linkages in this way requires an estimate of the machine inductances and resistances. Significant variation in the winding resistances occurs due to changes in temperature, and significant variation in the rotor resistance can occur due to the variation in the frequency. This method was chosen, however, because it automatically compensates for the large variation in the mutual inductance of the machine caused by mutual-flux saturation. Of the inductances used in (A.43), the transient inductances $L_r$' and $L_s$' have negligible dependence on the magnetizing inductance $L_m$. Similarly, the terms $L_m/L_r$ and $L_m/L_s$ also do not vary much with saturation, since $L_m/L_r = L_m/(L_{lr} + L_m) \approx 1$, even in saturation. Thus, the variation in $L_m$ (due to saturation) in these equations does not significantly impact the calculation results.

# APPENDIX F: EQUIVALENT IMPEDANCES FOR SHORT-CIRCUIT CALCULATIONS

**Table A.14: Equivalent Impedances for Short-Circuit Calculation in (4.65)**

| | |
|---|---|
| $Z_m = R_s + j(X_{ls} + X_m)$ | $Z_{g,eq} = \dfrac{R_g R_f}{R_g + R_f}$ |
| $Z_{s,eq} = \dfrac{R_g}{R_g + R_f Z_m / (R_f + Z_m)}$ | $Z_{r,eq} = \dfrac{jX_m(R_s + jX_{ls} + Z_{geq})}{R_s + j(X_{ls} + X_m) + Z_{geq})}$ |

# APPENDIX G: TYPE 3 WTG ROTOR OVERVOLTAGES

To demonstrate the effects of stator transients on the induced voltages on the rotor windings of a wound-rotor induction machine, take the simple example that the induction machine's rotational speed is constant at some speed $\omega_r$ and the rotor windings are open circuited. The voltage equations of the induction machine (in a rotor reference frame) in this scenario are given by

$$\begin{aligned} \vec{v}_s &= R_s\vec{i}_s + j\omega_r\vec{\lambda}_s + p\vec{\lambda}_s \\ \vec{v}_r &= p\vec{\lambda}_r \end{aligned}, \tag{A.44}$$

where $i_r = 0$ since the rotor windings are assumed to be open. The flux linkage equations are given by

$$\vec{\lambda}_s = L_s\vec{i}_s \quad \vec{\lambda}_r = L_m\vec{i}_s\,. \tag{A.45}$$

Solving for the stator current in the stator flux linkage equation in (A.45) and inserting this value into the stator voltage equation gives

$$\vec{v}_s = \left(\frac{R_s}{L_s} + j\omega_r\right)\vec{\lambda}_s + p\vec{\lambda}_s\,. \tag{A.46}$$

Equation (A.46) is a linear first-order differential equation with a solution given by the sum of a homogeneous solution ($v_s = 0$) and a particular solution ($v_s \neq 0$). The particular solution is the same as the steady-state solution; thus, steady-state analysis can be used to find the particular solution. In a rotor reference frame, the stator voltage is given by

$$\vec{v}_s = \vec{V}_1 e^{js\omega_s t}\,. \tag{A.47}$$

In steady state, the stator flux linkage is of the same form as the stator voltage given in (A.47). Thus, the steady-state voltage equation is given by

$$\vec{v}_s = \left( \frac{R_s}{L_s} + j\omega_r \right) \vec{\lambda}_{s1} + js\omega_s \vec{\lambda}_{s1}, \tag{A.48}$$

where $\lambda_{s1}$ is the particular solution of the stator flux linkage and

$$p\vec{\lambda}_{s1} = p\vec{\Lambda}_{s1} e^{js\omega_s t} = js\omega_s \vec{\Lambda}_{s1} e^{js\omega_s t} = js\omega_s \vec{\lambda}_{s1}. \tag{A.49}$$

Solving for the stator flux linkage in (A.48) gives

$$\vec{\lambda}_{s1} = \frac{\vec{v}_s}{R_s / L_s + j\omega_r + js\omega_s} = \frac{\vec{v}_s}{R_s / L_s + j\omega_s} = \frac{\vec{V}_1}{R_s / L_s + j\omega_s} e^{js\omega_s t}. \tag{A.50}$$

In [68], it is shown that the homogeneous solution to a linear first order differential equation of the form

$$\frac{dy}{dx} + P(x)y = 0, \tag{A.51}$$

is given by

$$y = Ce^{-\int P(x)dx}, \tag{A.52}$$

where $C$ is a constant of integration. Equation (A.46) is of the same form as (A.51) and, therefore, has a solution of the same form as (A.52). Thus, the homogenous solution to (A.46) is given by

$$\vec{\lambda}_{s2} = Ce^{-(R_s / L_s + j\omega_r)t}. \tag{A.53}$$

The total solution of the stator flux linkage is given by

$$\vec{\lambda}_s = \vec{\lambda}_{s1} + \vec{\lambda}_{s2} = Ce^{-(R_s / L_s)t} e^{-j\omega_r t} + \frac{\vec{V}_1}{R_s / L_s + j\omega_s} e^{js\omega_s t}. \tag{A.54}$$

The value $C$ is determined by the initial conditions at $t = 0$, given by

$$\vec{\lambda}_s(0) = C + \frac{\vec{V}_1}{R_s / L_s + j\omega_s}. \tag{A.55}$$

Thus, the total solution of the stator flux linkage is given by

$$\vec{\lambda}_s = \left[ \vec{\lambda}_s(0) - \frac{\vec{V}_1}{R_s / L_s + j\omega_s} \right] e^{-(R_s / L_s)t} e^{-j\omega_r t} + \frac{\vec{V}_1}{R_s / L_s + j\omega_s} e^{js\omega_s t}. \tag{A.56}$$

From (A.44), the rotor voltage is given by

$$\vec{v}_r = p\vec{\lambda}_r = \frac{L_m}{L_s} p\vec{\lambda}_s . \tag{A.57}$$

Taking the time derivative of (A.56) and inserting into (A.57) gives the rotor voltage to be

$$\vec{v}_r = \vec{V}_{0r} e^{-(R_s / L_s)t} e^{-j\omega_r t} + \vec{V}_{1r} e^{js\omega_s t}, \tag{A.58}$$

where

$$\vec{V}_{0r} = \left[ \frac{\vec{V}_1}{R_s / L_s + j\omega_s} - \vec{\lambda}_s(0) \right] (R_s / L_s + j\omega_r), \tag{A.59}$$

and

$$\vec{V}_{1r} = \frac{js\omega_s \vec{V}_1}{R_s / L_s + j\omega_s} . \tag{A.60}$$

# APPENDIX H: AC-CROWBAR AND DC-CHOPPER CONTROL LOGIC

The AC crowbar circuit used in both the hardware testbed and utility-scale simulation model of the Type 3 WTG is shown in Fig. A.7. This AC crowbar circuit consists of a three-phase diode rectifier with a crowbar resistance $R_{cb}$ and an insulated-gate bipoloar transistor (IGBT) module with gating signal $G_{cb}$. The control logic for the turn-on/turn-off of this AC crowbar circuit is shown in Fig. A.8. This control logic takes the three-phase instantaneous rotor current measurements as inputs and outputs a gating signal for the AC crowbar IGBT module. When the gating signal is high, the AC crowbar circuit is turned on, and vice versa. The gating signal goes high when the instantaneous magnitude of one of the rotor current measurements exceeds a threshold set point $I_{cb}$. This logic is acheived with the comparator block in Fig. A.8. The output of the comparator block is a digital logic signal (1 or 0). The timer block in Fig. A.8 is a positive-edge triggered block, in which $G_{cb}$ goes high on the positive edge of the input from the comparator, and remains high for some amount of time specified by the crowbar on-time $T_{cb}$. These setpoints used in the experimental testbed and utility-scale simulation model of the Type 3 WTG are given in Appendix A. In each case, the crowbar on time is set to 1 cycle (16.7 milliseconds). When $G_{cb}$ is high, the gating signals of the RSC are blocked; thus, when the AC crowbar is turned on, the RSC is turned off simultaneously. Note that some time delay exists between a measured over current and the application of the crowbar due to the finite sampling frequency and control delays. For a switching frequency of 10 kHz, this time delay is at least 200 microseconds (2/10,000 Hz). Thus, the rotor current threshold $I_{cb}$ at which the AC crowbar turns on should be set low enough

such that this time delay does not result in currents that might exceed the RSC IGBT ratings.

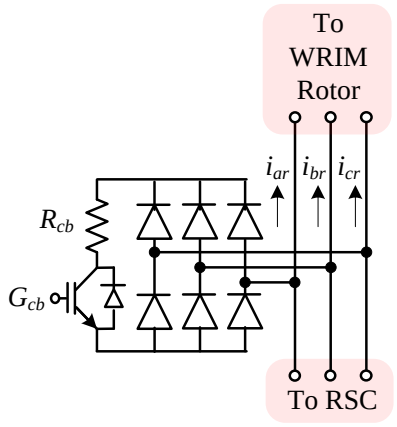


**Fig. A.7: AC crowbar circuit used in Type 3 WTG.**

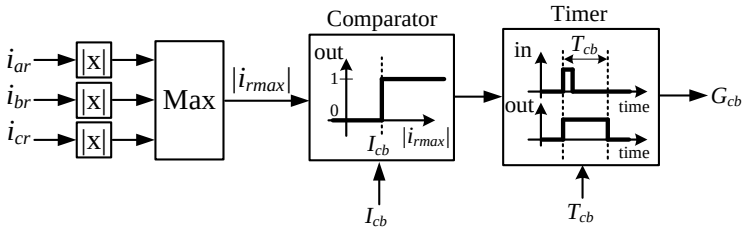


**Fig. A.8: Control logic for AC crowbar IGBT gate signal.**

The DC-link circuit between the RSC and GSC of the Type 3 WTG (and in between the MSC and GSC of the Type 4 WTG) is shown in Fig. A.9. The DC-chopper circuit consists and an IGBT module and resistance connected in series across the DC-link bus voltages. The DC-chopper gating signal $G_{dc}$ turns-on/turns-off the DC-chopper circuit. This gating signal is determined using the control logic shown in Fig. A.10. The DC-chopper turns on when the DC-link voltage $v_{dc}$ exceeds a specified voltage threshold $v_{dcon}$. The DC-chopper remains on until the DC-link voltage drops below the specified voltage threshold $v_{dcoff}$. The turn-on voltage $v_{dcon}$ should be set so that the DC-link

voltage does not exceed the voltage ratings of the DC-link capacitor and the IGBT modules of the RSC (MSC) and GSC.

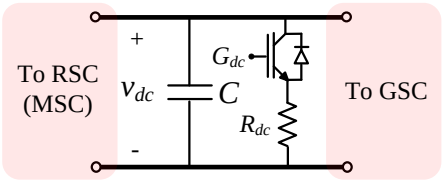


**Fig. A.9: DC-link circuit for Type 3 and Type 4 WTG.**

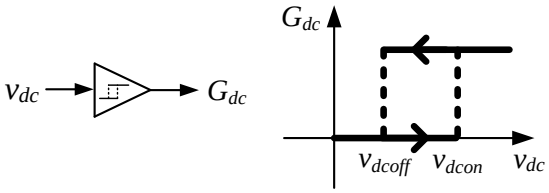


**Fig. A.10: Control logic of the DC-chopper in the Type 3 and Type 4 WTG.**

# APPENDIX I: COMPARISON OF AVERAGED AND SWITCHING WTG MODELS

The circuit diagram of the power electronic converter used in the simulation of the Type 3 and Type 4 wind-turbine generators (WTGs) is shown in Fig. A.11. An "averaged" model of this power electronic converter was used in the multi-machine network studies in this dissertation so that a larger simulation time-step could be used. The definition of an "averaged" model indicates that the switching of the power electronic converters is not modeled in detail. This is achieved using the circuit show in Fig. A.12 (note that the labels in Fig. A.11 and Fig. A.12 are specific to the Type 3 WTG, but the same circuit is used for the Type 4 WTG except the voltage source for the rotor-side converter (RSC) is used for the machine-side converter (MSC) of the Type 4 WTG). Both the RSC and GSC are represented with a controlled-current source and three single-phase controlled-voltage sources. These components are available in the built-in PSCAD component library. The controlled-current sources $i_{rdc}$ and $i_{sdc}$ are calculated from the instantaneous simulated phase currents, given by

$$i_{rdc} = D_{ar} i_{ra} + D_{br} i_{rb} + D_{cr} i_{rc}\,, \tag{A.61}$$

where $D_{ar}$, $D_{br}$, and $D_{cr}$ are the duty cycles determined from the space-vector modulation routine [79]. The controlled current source of the GSC $i_{sdc}$ is calculated in a similar way using the duty cycles of the GSC space vector routine. Calculating the currents in the DC-link circuit provides a good model for representing the DC-link voltage dynamics during short-circuit transients. The controlled-voltage sources of the RSC are calculated from the instantaneous simulated DC-link voltage, given by

$$v_{ra} = (D_{ar} - 0.5)v_{dc},\;\; v_{rb} = (D_{br} - 0.5)v_{dc},\;\; v_{rc} = (D_{cr} - 0.5)v_{dc} \tag{A.62}$$

where 0.5 is subtracted from the duty cycles to remove the offset.

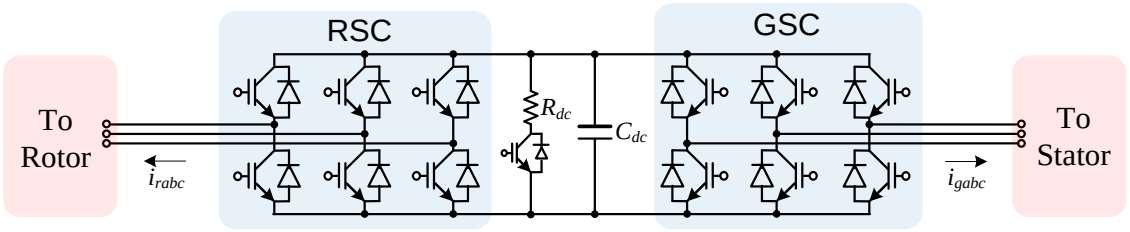


**Fig. A.11: Circuit diagram of power electronics converter used in Type 3 and 4 WTGs.**

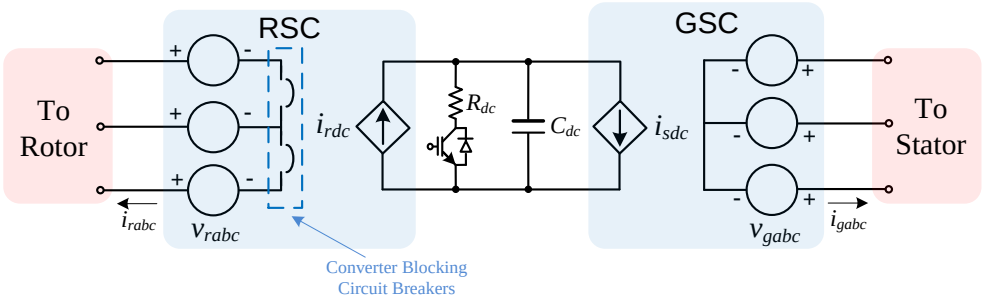


**Fig. A.12: Circuit diagram of averaged power electronics converter.**

The averaged model of the power electronics converter shown in Fig. A.12 has the disadvantage that converter losses (such as the IGBT and Diode conduction losses, switching losses, etc.) are not represented. Additionally, the behavior of the power-electronic converter when the IGBT gating signals are blocked are not modeled. However, this behavior is imitated using the converter-blocking circuit breakers shown in Fig. A.12. Within PSCAD, these are ideal circuit breakers which can open at any level of current flowing. These circuit breakers are used to imitate the converter blocking while the AC crowbar circuit is activated. It is assumed that the AC crowbar resistance is small enough such that anti-parallel diodes in the RSC do not conduct when the AC crowbar circuit is activated. Thus, these converter-blocking circuit breakers prevent current from flowing in the RSC while the AC crowbar is activated.

Simulation results comparing the switching model of the Type 3 WTG to the averaged model are shown in Fig. A.13 - Fig. A.15. In each of these sets of simulation results, the network shown in Fig. 4.40 is the simulated network. In each simulation case, identical simulation parameters are used with the exception that the switching power electronics converter is replaced with the averaged model of the converter shown in Fig. A.12. The simulation results for a three-phase fault on the transmission system, single-phase fault on the transmission system, and a single-phase fault on the collector cable are shown in Fig. A.13, Fig. A.14, and Fig. A.15, respectively. In each case, good agreement between the switching and averaged models can be seen.

Simulation results comparing the switching and averaged models of the Type 4 WTG are shown in Fig. A.16 and Fig. A.17. The network shown in Fig. 5.18 is used for the simulation results. The results shown in Fig. A.16 are for a three-phase fault on the transmission system and the results in Fig. A.17 are for a single-phase fault on the transmission system. In each case, good agreement between the switching and averaged models can be seen.

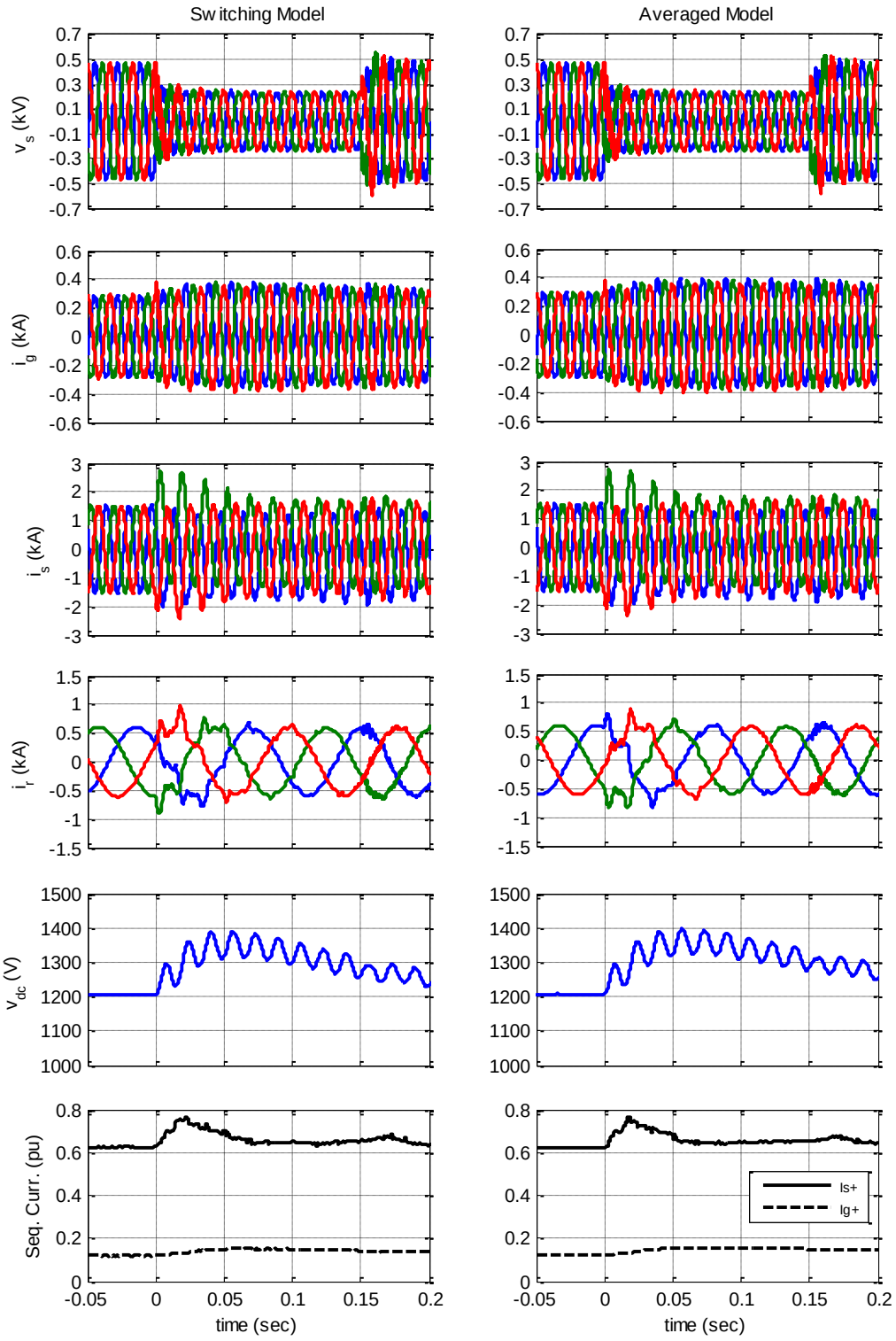


**Fig. A.13: Comparison of averaged and switching models of the Type 3 WTG for a three-phase fault.**

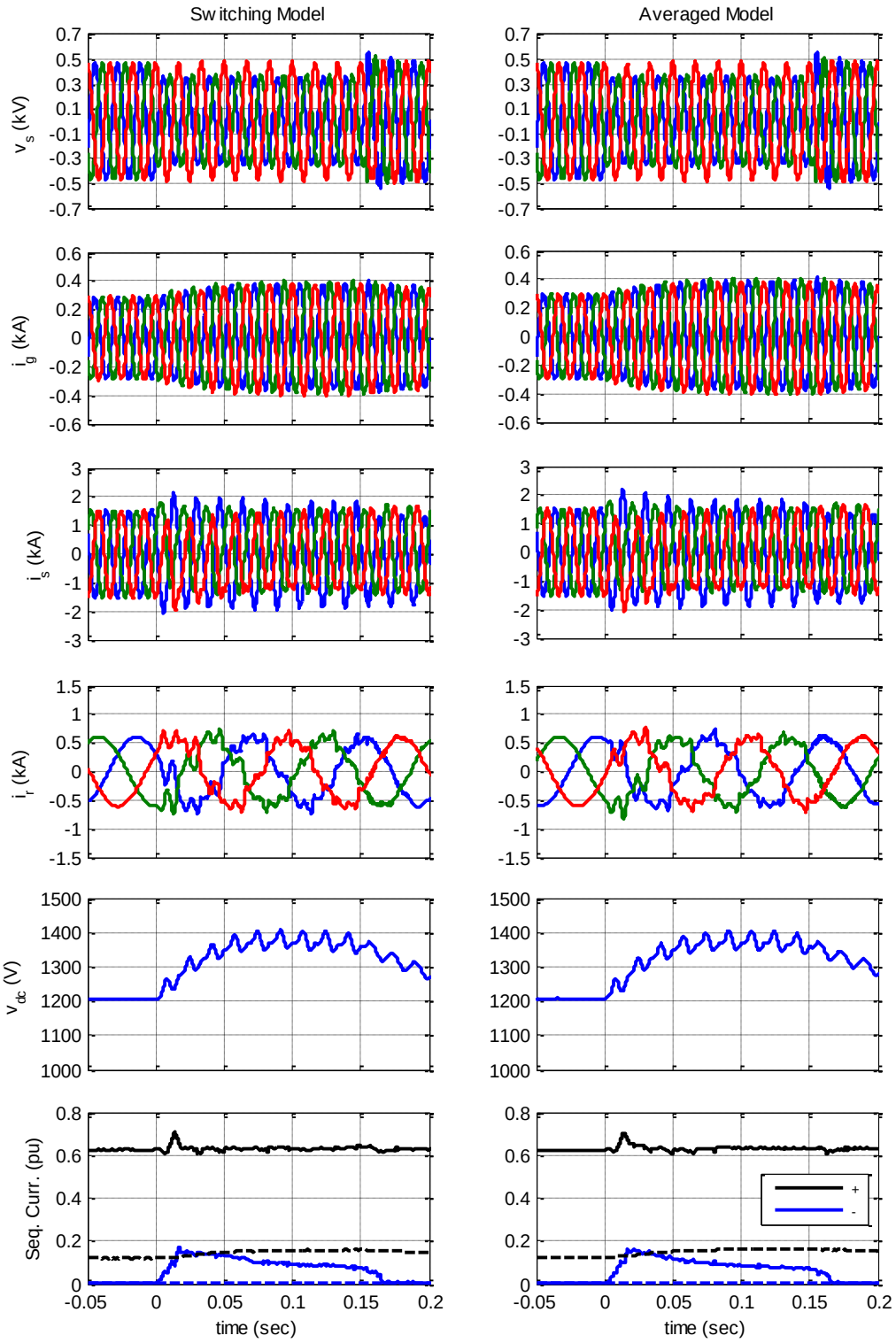


**Fig. A.14: Comparison of averaged and switching models of the Type 3 WTG for a single-phase fault.**

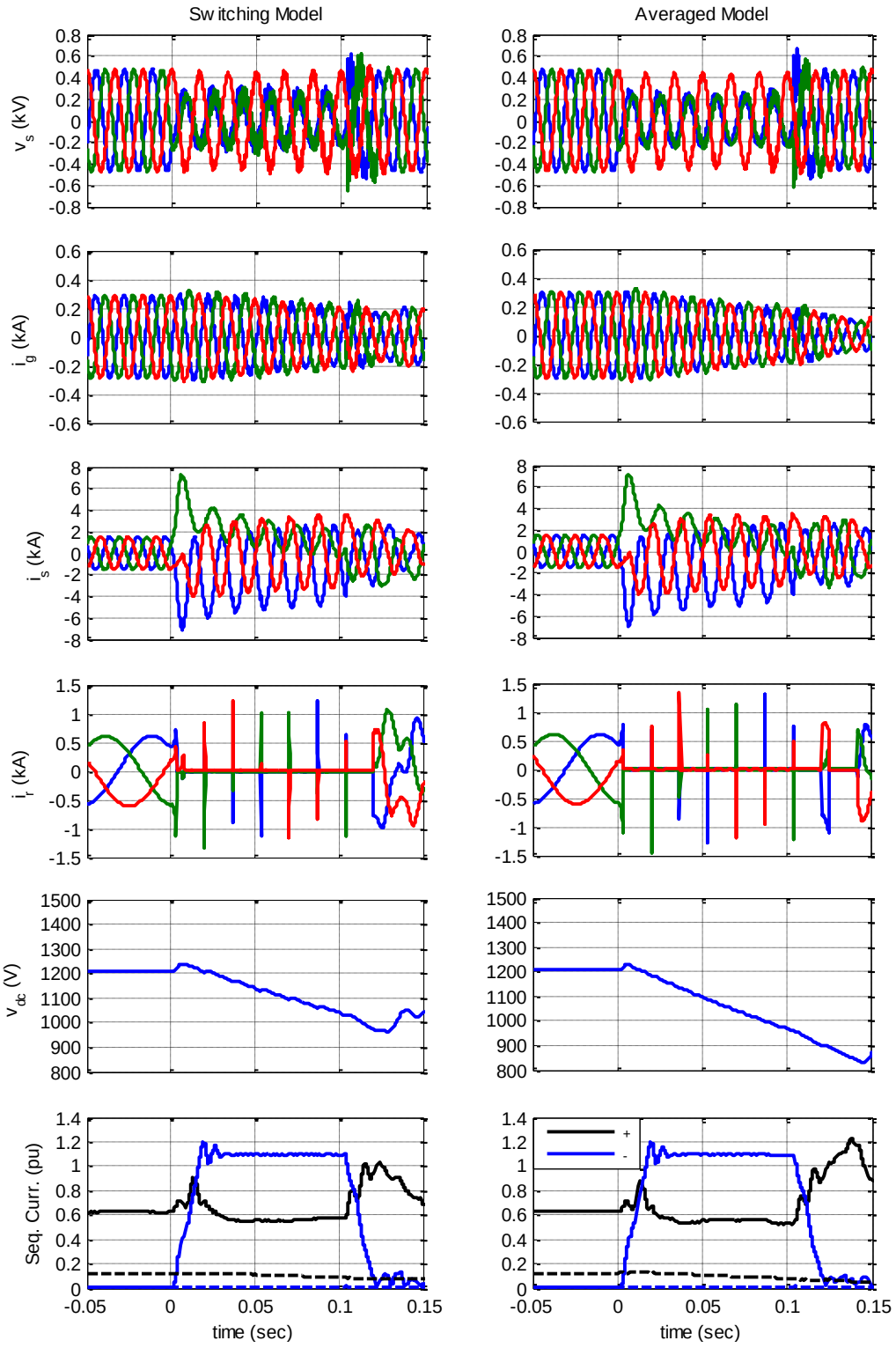


**Fig. A.15: Comparison of averaged and switching models of the Type 3 WTG for a single-phase fault.**

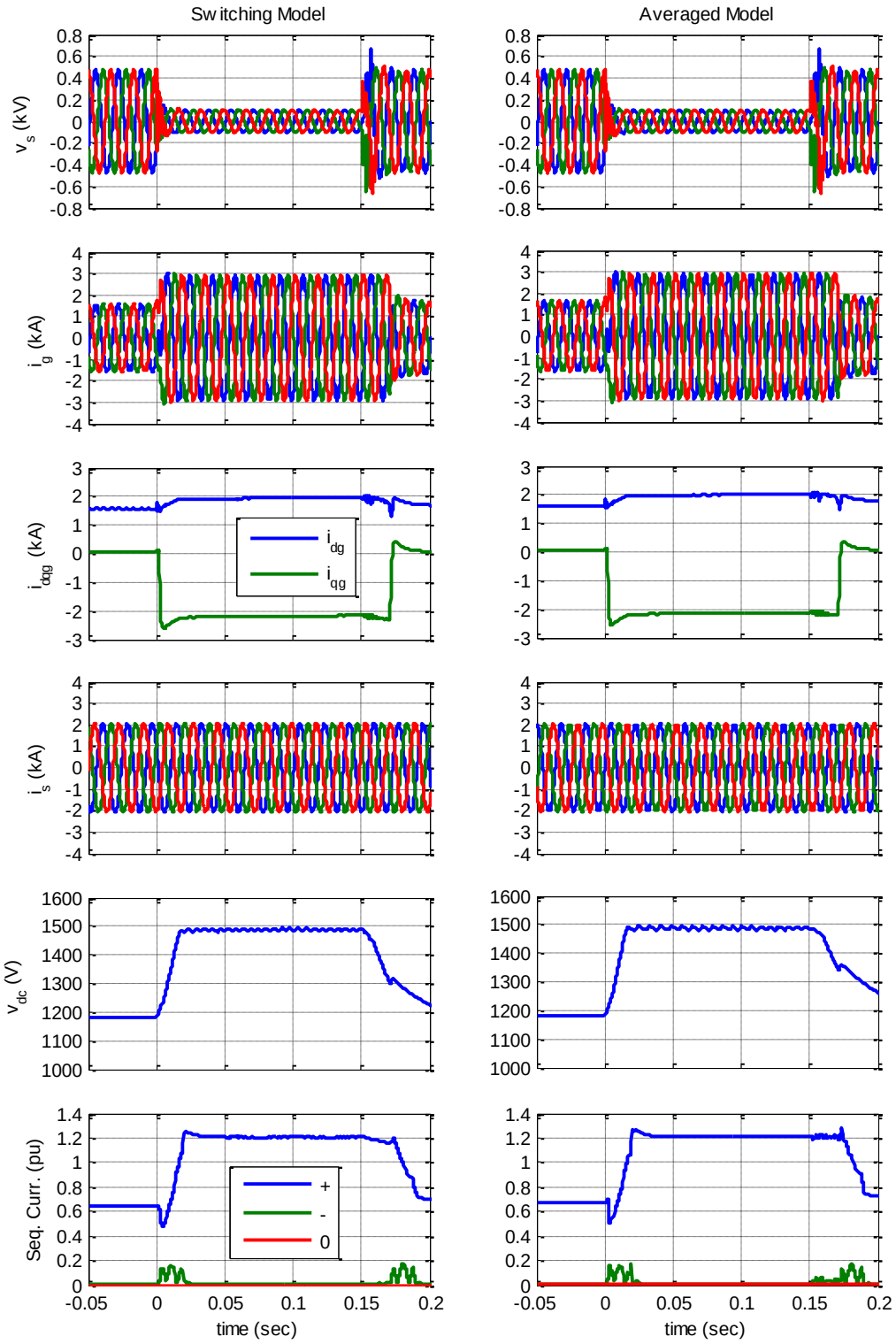


**Fig. A.16: Comparison of averaged and switching models of the Type 4 WTG for a three-phase fault.**

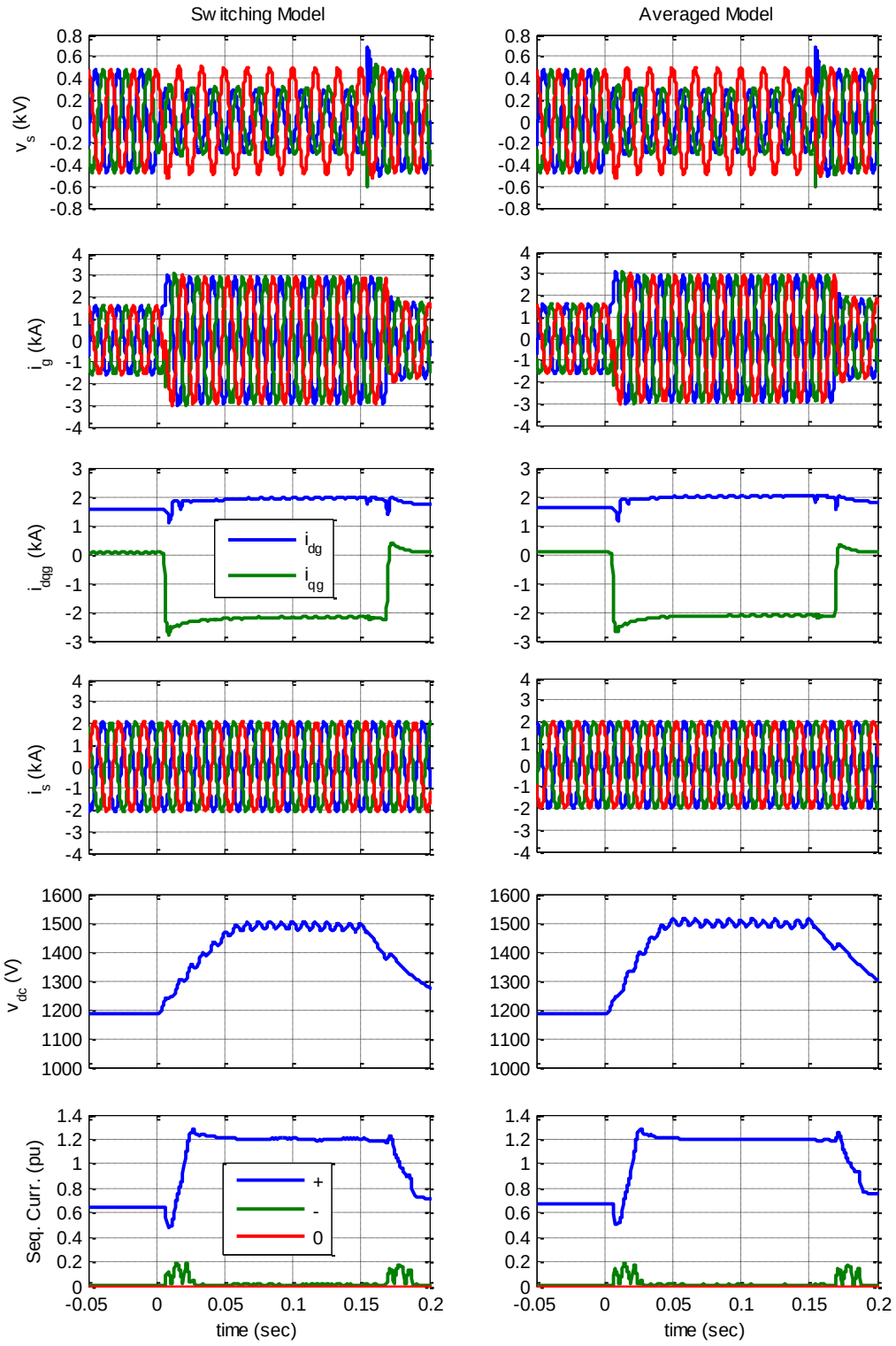


**Fig. A.17: Comparison of averaged and switching models of the Type 4 WTG for a single-phase fault.**

# REFERENCES


[1] "World Wind Energy Report 2010," World Wind Energy Association, April 2011. [Online]. Available: http://www.wwindea.org.

[2] "20% Wind Energy by 2030," U.S. Department of Energy, Report DOE/GO-102008-2567, July 2008. [Online]. Available: http://www.20percentwind.org.

[3] "Interconnection for Wind Energy," Federal Energy Regulatory Commission, Report 18 CFR Part 35, Order No. 661-A, 2005. [Online]. Available: http://www.ferc.gov.

[4] B. Singh and S. N. Singh, "Wind Power Interconnection into the Power System: A Review of Grid Code Requirements," *The Electricity Journal*, vol. 22, pp. 54-63, 2009.

[5] C. Feltes, S. Engelhardt, J. Kretschmann, J. Fortmann, and I. Erlich, "Dynamic performance evaluation of DFIG-based wind turbines regarding new German grid code requirements," in *Proc. 2010 IEEE Power and Energy Society General Meeting*, Minneapolis, MN, July 25-29, 2010.

[6] P. Kundur, *Power System Stability and Control*. New York: McGraw-Hill, Inc., 1994.

[7] A. R. Bergen and V. Vittal, *Power Systems Analysis (2nd Ed.)*. New Jersey: Prentice Hall, 2000.

[8] M. S. Sarma, *Electric Machines: Steady-State Theory and Dynamic Performance (2nd Ed.)*. Florence, KY: Nelson Engineering, 1994.

[9] "Large Generator Interconnection Procedure," Federal Energy Regulatory Commission, Report 18 CFR Part 35, Order No. 2003-C, 2005. [Online]. Available: http://www.ferc.gov.

[10] "IEEE Recommended Practice for Calculating Short-Circuit Currents in Industrial and Commercial Power Systems," *IEEE Std 551-2006 [The Violet Book]*, 2006.

[11] D. Hornak and N. H. J. Chau, "Green Power - Wind Generated Protection and Control Considerations," in *Proc. IEEE 57th Annual Conference for Protective Relay Engineers*, College Station, TX, Mar. 30 - Apr. 1, 2004.

[12] E. H. Camm, et. al., "Wind Power Plant Collector System Design Considerations," in *Proc. 2009 IEEE Power and Energy Society General Meeting*, Calgary, Canada, July 26-30, 2009.

[13] C. Zhe, J. M. Guerrero, and F. Blaabjerg, "A Review of the State of the Art of Power Electronics for Wind Turbines," *IEEE Transactions on Power Electronics*, vol. 24, pp. 1859-1875, 2009.

[14] E. Muljadi and V. Gevorgian, "Short-Circuit Modeling of a Wind Power Plant," in *Proc. 2011 IEEE Power and Energy Society General Meeting*, Detroit, MI, July 24-29, 2011.

[15] E. H. Camm, et. al., "Characteristics of Wind Turbine Generators for Wind Power Plants," in *Proc. 2009 IEEE Power and Energy Society General Meeting*, Calgary, Canada, July 26-30, 2009.

[16] J. Martinez, P. C. Kjar, P. Rodriguez, and R. Teodorescu, "Short Circuit Signatures from Different Wind Turbine Generator Types," in *Proc. 2011 IEEE Power Systems Conference and Exposition*, Phoenix, AZ, Mar. 20-23, 2011.

[17] R. A. Walling and M. L. Reichard, "Short Circuit Behavior of Wind Turbine Generators," in *Proc. 2009 IEEE Annual Conference for Protective Relay Engineers*, College Station, TX, Mar. 30 - Apr. 2, 2009.

[18] H. Li and Z. Chen, "Overview of Different Wind Generator Systems and their Comparisons," *IET Renewable Power Generation*, vol. 2, pp. 123-138, 2008.

[19] A. D. Hansen and L. H. Hansen, "Wind Turbine Concept Market Penetration Over 10 Years (1995–2004)," *Wind Energy*, vol. 10, pp. 81-97, 2007.

[20] M. A. Abdullah, A. H. M. Yatim, C. W. Tan, and R. Saidur, "A Review of Maximum Power Point Tracking Algorithms for Wind Energy Systems," *Renewable and Sustainable Energy Reviews*, vol. 16, pp. 3220-3227, 2012.

[21] P. M. Anderson, *Analysis of Faulted Power Systems*. New York: IEEE Press, 1995.

[22] M. Z. Kamh and R. Iravani, "Three-Phase Steady-State Model of Type-3 Wind Generation Unit-Part I: Mathematical Models," *IEEE Transactions on Sustainable Energy*, vol. 2, pp. 477-486, 2011.

[23] P. C. Krause, O. Wasynczuk, and S. D. Sudhoff, *Analysis of Electric Machinery and Drive Systems (2nd Ed.)*. New Jersey: IEEE Press, 2002.

[24] D. W. Novotny and T. A. Lipo, *Vector Control and Dynamics of AC Drives*. Oxford: Oxford University Press, 1996.

[25] S. S. Kalsi, B. Adkins, and D. D. Stephen, "Calculation of system-fault currents due to induction motors," *Proceedings of the Institution of Electrical Engineers,* vol. 118, pp. 201-215, 1971.

[26] J. Morren and S. W. H. de Haan, "Short-Circuit Current of Wind Turbines With Doubly Fed Induction Generator," *IEEE Transactions on Energy Conversion,* vol. 22, pp. 174-180, 2007.

[27] F. Sulla, J. Svensson, and O. Samuelsson, "Symmetrical and unsymmetrical short-circuit current of squirrel-cage and doubly-fed induction generators," *Electric Power Systems Research,* vol. 81, pp. 1610-1618, 2011.

[28] N. Samaan, R. Zavadil, J. C. Smith, and J. Conto, "Modeling of Wind Power Plants for Short Circuit Analysis in the Transmission Network," in *Proc. 2008 IEEE Transmission and Distribution Conference and Exposition*, Chicago, IL, Apr. 21-24, 2008.

[29] E. Muljadi, N. Samaan, V. Gevorgian, L. Jun, and S. Pasupulati, "Short Circuit Current Contribution for Different Wind Turbine Generator Types," in *Proc. 2010 IEEE Power and Energy Society General Meeting*, Minneapolis, MN, July 25-29, 2010.

[30] S. M. Brahma, M. Chaudhary, and S. J. Ranade, "Some Findings About Equivalencing Windfarms with Type 1 and Type 2 Induction Generators," in *Proc. 2011 IEEE North American Power Symposium*, Boston, MA, Aug. 4-6, 2011.

[31] S. Muller, M. Deicke, and R. W. De Doncker, "Doubly Fed Induction Generator Systems for Wind Turbines," *IEEE Industry Applications Magazine,* vol. 8, pp. 26-33, 2002.

[32] N. Mohan, T. M. Undeland, and W. P. Robbins, *Power Electronics Converters, Applications, and Designs (3rd Ed.)*: John Wiley & Sons, Inc., 2003.

[33] J. Liang, W. Qiao, and R. G. Harley, "Feed-Forward Transient Current Control for Low-Voltage Ride-Through Enhancement of DFIG Wind Turbines," *IEEE Transactions on Energy Conversion,* vol. 25, pp. 836-843, 2010.

[34] J. Lopez, P. Sanchis, X. Roboam, and L. Marroyo, "Dynamic Behavior of the Doubly Fed Induction Generator During Three-Phase Voltage Dips," *IEEE Transactions on Energy Conversion,* vol. 22, pp. 709-717, 2007.

[35] F. K. A. Lima, A. Luna, P. Rodriguez, E. H. Watanabe, and F. Blaabjerg, "Rotor Voltage Dynamics in the Doubly Fed Induction Generator During Grid Faults," *IEEE Transactions on Power Electronics*, vol. 25, pp. 118-130, 2010.

[36] S. Engelhardt, J. Kretschmann, J. Fortmann, F. Shewarega, I. Erlich, and C. Feltes, "Negative sequence control of DFG based wind turbines," in *Proc. 2011 IEEE Power and Energy Society General Meeting*, San Diego, CA, July 24-29, 2011.

[37] S. Engelhardt, J. Kretschmann, J. Fortmann, F. Shewarega, I. Erlich, and T. Neumann, "Capability and Limitations of DFIG based Wind Turbines concerning Negative Sequence Control," in *Proc. IEEE Power and Energy Society General Meeting*, Vancouver, BC, July 21-25, 2013.

[38] R. A. Walling, E. Gursoy, and B. English, "Current Contribution from Type 3 and Type 4 Wind Turbine Generators During Faults," in *Proc. IEEE Transmission and Distribution Conference & Exposition*, Orlando, FL, May 7-10, 2012.

[39] G. Pannell, D. J. Atkinson, and B. Zahawi, "Minimum-Threshold Crowbar for a Fault-Ride-Through Grid-Code-Compliant DFIG Wind Turbine," *IEEE Transactions on Energy Conversion*, vol. 25, pp. 750-759, 2010.

[40] J. Liang and R. G. Harley, "Feed-forward transient compensation control for DFIG wind generators during both balanced and unbalanced grid disturbances," in *Proc. 2011 IEEE Energy Conversion Congress and Exposition*, Phoenix, AZ, Sept. 17-22, 2011.

[41] W. Qiao, "Dynamic Modeling and Control of Doubly Fed Induction Generators Driven by Wind Turbines," in *Proc. 2009 IEEE Power Systems Conference and Exposition*, Seattle, WA, Mar. 15-18, 2009.

[42] R. Pena, J. C. Clare, and G. M. Asher, "Doubly fed induction generator using back-to-back PWM converters and its application to variable-speed wind-energy generation," *IEE Proceedings - Electric Power Applications*, vol. 143, pp. 231-241, 1996.

[43] T. K. A. Brekken and N. Mohan, "Control of a Doubly Fed Induction Wind Generator Under Unbalanced Grid Voltage Conditions," *IEEE Transactions on Energy Conversion*, vol. 22, pp. 129-135, 2007.

[44] O. Gomis-Bellmunt, A. Junyent-Ferre, A. Sumper, and J. Bergas-Jan, "Ride-Through Control of a Doubly Fed Induction Generator Under Unbalanced Voltage Sags," *IEEE Transactions on Energy Conversion*, vol. 23, pp. 1036-1045, 2008.

[45] X. Lie, "Coordinated Control of DFIG's Rotor and Grid Side Converters During Network Unbalance," *IEEE Transactions on Power Electronics,* vol. 23, pp. 1041-1049, 2008.

[46] J. Hu, Y. He, L. Xu, and B. W. Williams, "Improved Control of DFIG Systems During Network Unbalance Using PI-R Current Regulators," *IEEE Transactions on Industrial Electronics,* vol. 56, pp. 439-451, 2009.

[47] L. Xu and Y. Wang, "Dynamic Modeling and Control of DFIG-Based Wind Turbines Under Unbalanced Network Conditions," *IEEE Transactions on Power Systems,* vol. 22, pp. 314-323, 2007.

[48] R. S. Semken, et. al., "Direct-Drive Permanent Magnet Generators for High-Power Wind Turbines: Benefits and Limiting Factors," *IET Renewable Power Generation,* vol. 6, pp. 1-8, 2012.

[49] M. Fischer and A. Mendonca, "Representation of Variable Speed Full Conversion Wind Energy Converters for Steady-State Short Circuit Calculations," in *Proc. IEEE PES Transmission & Distribution Conference & Exposition*, Orlando, FL, May 7-10, 2012.

[50] R. J. Nelson and H. Ma, "Short-Circuit Contributions of Full-Converter Wind Turbines," in *Proc. 2011 IEEE Power and Energy Society General Meeting*, Detroit, MI, July 24-29, 2011.

[51] C. H. Ng, R. Li, and J. Bumby, "Unbalanced-Grid-Fault Ride-Through Control for a Wind Turbine Inverter," *IEEE Transactions on Industry Applications,* vol. 44, pp. 845-856, 2008.

[52] M. E. Haque, M. Negnevitsky, and K. M. Muttaqi, "A Novel Control Strategy for a Variable-Speed Wind Turbine With a Permanent-Magnet Synchronous Generator," *IEEE Transactions on Industry Applications,* vol. 46, pp. 331-339, 2010.

[53] S. Li, T. A. Haskew, R. P. Swatloski, and W. Gathings, "Optimal and Direct-Current Vector Control of Direct-Driven PMSG Wind Turbines," *IEEE Transactions on Power Electronics,* vol. 27, pp. 2325-2337, 2012.

[54] N. D. Caliao, "Dynamic modelling and control of fully rated converter wind turbines," *Renewable Energy,* vol. 36, pp. 2287-2297, 8// 2011.

[55] J. Brochu, C. Larose, and R. Gagnon, "Generic Equivalent Collector System Parameters for Large Wind Power Plants," *IEEE Transactions on Energy Conversion,* vol. 26, pp. 542-549, 2011.

[56] M. Bradt and e. al., "Power Transformer Application for Wind Plant Substations," in *Proc. 2010 IEEE Transmission and Distribution Conference and Exposition*, 2010.

[57] R. Walling, "Power Transformer Application for Wind Plant Substations," presented at the IEEE PES Wind Plant Collector System Design Working Group Meeting, New Orleans, LA, April 19-22, 2010. [Online]. Available: http://grouper.ieee.org/groups/td/wind/Presentation8.pdf.

[58] C. Feltes, R. van de Sandt, F. Koch, F. Shewarega, and I. Erlich, "Neutral grounding in wind farm medium voltage collector grids," in *Proc. 2011 IEEE PES Power Systems Conference and Exposition*, Phoenix, AZ, March 20-23, 2011.

[59] M. Bradt, et. al., "Wind Plant Collector System Fault Protection and Coordination," in *Proc. 2010 IEEE Transmission and Distribution Conference and Exposition*, April 19-22, 2010.

[60] L. L. Henriksen and J. J. Kumm, "Protective relaying applied to large wind plant collector systems," in *Proc. 2008 IEEE PES Transmission and Distribution Conference and Exposition*, Chicago, IL, April 21-24, 2008.

[61] T. Kawady, C. Feltes, I. Erlich, and A. I. Taalab, "Protection system behavior of DFIG based wind farms for grid-faults with practical considerations," in *Proc. 2010 IEEE Power and Energy Society General Meeting*, Minneapolis, MN, July 25-29, 2010.

[62] E. H. Camm, et. al., "Wind power plant grounding, overvoltage protection, and insulation coordination," in *Proc. 2009 IEEE Power & Energy Society General Meeting*, Calgary, AB, July 26-30, 2009.

[63] D. Hou, "Relay Element Performance During Power System Frequency Excursions," in *Proc. 2008 IEEE 61st Annual Conference for Protective Relay Engineers*, College Station, TX, Apr. 1-3, 2008.

[64] E. O. Schweitzer and D. Hou, "Filtering for Protective Relays," in *Proc. 1993 IEEE WESCANEX Conference*, May 17-18, 1993.

[65] D. F. Howard, J. Restrepo, T. Smith, M. Starke, J. Dang, and R. G. Harley, "Calculation of Fault Current Contribution of Type I Wind Turbine-Generators," in *Proc. 2011 IEEE Power and Energy Society General Meeting*, Detroit, MI, July 24-29, 2011.

[66] D. F. Howard, T. M. Smith, M. Starke, and R. G. Harley, "Short Circuit Analysis of Induction Machines - Wind Application," in *Proc. 2012 IEEE Transmission and Distribution Conference and Exposition*, Orlando, FL, May 7-10, 2012.

[67] J. P. Hespanha, *Linear Systems Theory*. New Jersey: Princeton University Press, 2009.

[68] D. G. Zill and M. R. Cullen, *Advanced Engineering Mathematics (3rd Ed.)*. Sudbury, Massachusetts: Jones and Bartlett Publishers, 2006.

[69] D. F. Howard, T. G. Habetler, and R. G. Harley, "Improved Sequence Network Model of Wind Turbine-Generators for Short Circuit Studies," *IEEE Transactions on Energy Conversion (Under Review)*, 2012.

[70] "IEEE Standard Test Procedure for Polyphase Induction Motors and Generators," *IEEE Std 112-1996*, 1997.

[71] H. M. Jabr and N. C. Kar, "Effects of main and leakage flux saturation on the transient performances of doubly-fed wind driven induction generator," *Electric Power Systems Research*, vol. 77, pp. 1019-1027, 2007.

[72] T. A. Lipo and A. Consoli, "Modeling and Simulation of Induction Motors with Saturable Leakage Reactances," *IEEE Transactions on Industry Applications*, vol. IA-20, pp. 180-189, 1984.

[73] D. F. Howard, T. G. Habetler, and R. G. Harley, "Experimental Study on the Short-Circuit Contribution of Induction Machines," in *Proc. 2013 IEEE International Electric Machines and Drives Conference*, Chicago, IL, May 12-15, 2013.

[74] R. Krishnan, *Electric Motor Drives: Modeling, Analysis, and Control*. New Jersey: Prentice Hall, 2001.

[75] V. Akhmatov, "Analysis of dynamic behaviour of electric power systems with large amount of wind power," PhD Thesis, Electric Power Engineering, Technical University of Denmark, 2003.

[76] F. Lingling, R. Kavasseri, M. Zhixin Lee, and Z. Chanxia, "Modeling of DFIG-Based Wind Farms for SSR Analysis," *IEEE Transactions on Power Delivery*, vol. 25, pp. 2073-2082, 2010.

[77] S. Engelhardt, I. Erlich, C. Feltes, J. Kretschmann, and F. Shewarega, "Reactive Power Capability of Wind Turbines Based on Doubly Fed Induction Generators," *IEEE Transactions on Energy Conversion*, vol. 26, pp. 364-372, 2011.

[78] N. W. Miller, J. J. Sanchez-Gasca, W. W. Price, and R. W. Delmerico, "Dynamic modeling of GE 1.5 and 3.6 MW wind turbine-generators for stability simulations," in *Proc. 2003 Power Engineering Society General Meeting*, July 13-17, 2003.

[79] J. Restrepo, J. M. Aller, A. Bueno, V. M. Guzman, and M. I. Gimenez, "Generalized Algorithm for Pulse Width Modulation using a Two-Vectors Based Technique," *European Power Electronics and Drives Journal*, vol. 21, pp. 30-39, 2011.

[80] J. Liang, "Wind Energy and Power System Interconnection, Control, and Operation for High Penetration of Wind Energy," Ph.D. Dissertation, Georgia Institute of Technology, 2012.

[81] S. Bell, "A Beginner's Guide to Uncertainty of Measurement," Measurement Good Practice Guide No. 11 (Issue 2), National Physical Laboratory, 2001.

# VITA

## DUSTIN F. HOWARD

DUSTIN F. HOWARD was born in Cairo, GA in 1985. He received his Bachelor's and Master's degree in Electrical Engineering from Georgia Institute of Technology in 2008 and 2010, respectively. Since 2010, he has been working toward a Ph.D. in the same discipline at Georgia Institute of Technology.

Dustin has worked as a graduate teaching assistant at Georgia Institute of Technology in the Electrical and Computer Engineering department, and has lectured on numerous occasions in both undergraduate and graduate classes on electric machinery analysis. He has participated in numerous internships, including summer engineering positions at Progress Energy (Crystal River, FL), General Electric (Norcross, GA), and Oak Ridge National Laboratory (Oak Ridge, TN). He has supervised and provided mentoring to three students as a part of the Opportunity Research Scholar's undergraduate research program at Georgia Institute of Technology in 2012. His research interests include the grid integration of renewable energy sources, control of electric machines, and power electronics.